



Organic Based Solar Cells with Morphology Control

Andersen, Thomas Rieks

Publication date:
2013

Document Version
Publisher's PDF, also known as Version of record

[Link back to DTU Orbit](#)

Citation (APA):
Andersen, T. R. (2013). *Organic Based Solar Cells with Morphology Control*. Department of Energy Conversion and Storage, Technical University of Denmark.

General rights

Copyright and moral rights for the publications made accessible in the public portal are retained by the authors and/or other copyright owners and it is a condition of accessing publications that users recognise and abide by the legal requirements associated with these rights.

- Users may download and print one copy of any publication from the public portal for the purpose of private study or research.
- You may not further distribute the material or use it for any profit-making activity or commercial gain
- You may freely distribute the URL identifying the publication in the public portal

If you believe that this document breaches copyright please contact us providing details, and we will remove access to the work immediately and investigate your claim.

Organic Based Solar Cells with Morphology Control

Ph.D. Thesis

Thomas Rieks Andersen

September 2013

September 2013

By

Thomas Rieks Andersen

Sponsorship: The project was financed by Danish National Research Foundation and the National Natural Science Foundation of China (Grant no. 51011130028)

Academic advisor: Senior scientist Eva Bundgaard
Functional Organic Materials, Department of Energy Conversion and Storage, Danish Technical University.

Senior scientist Mikkel Jørgensen
Functional Organic Materials, Department of Energy Conversion and Storage, Danish Technical University.

Copyright: Reproduction of this publication in whole or in part must include the customary bibliographic citation, including author attribution, report title, etc.

Cover photo: Images shows: TEM-image of Nanoparticles as presented in Chapter 2; STXM reconstruction , as presented in Chapter 2; Mirror setup for double sided illumination , as presented in Chapter 4; Polymer tandem solar cell module, as presented in Chapter 4;

Published by: Department of Energy Conversion and Storage, Frederiksborgvej 399, Building 775, 4000 Roskilde, Denmark

ISBN: 978-87-92986-09-2

Preface

Roskilde 2013-09-26

This PhD thesis represents the main results of my work carried out as a PhD-student at Technical University of Denmark in the period from October 2010 to October 2013 in the section Functional Organic Materials under Department of Energy Conversion and Storage. This work has been conducted as part of the Danish-Chinese center for Organic-based photovoltaic cells with morphology control which consists of four partners two Danish (Technical University of Denmark and Aalborg University) and two Chinese (Zhejiang University and Institute of Chemistry, Chinese Academy of Science) the center is financed by the Danish National Research Foundation and the National Natural Science Foundation of China (Grant no. 51011130028) under the supervision of senior scientists Eva Bundgaard and Mikkel Jørgensen. The thesis is based in a number of papers which I have authored/co-authored during the project. During the past three years I have had the opportunity to work on different subjects which gave me a profound energy for that I am very thankful.

As PhD student it is required that you study in different research environments during the PhD, preferably a longer stay outside Denmark. My external stay took place from April to October 2011 in the research group of Professor Hongzheng Chen at Zhejiang University placed in Hangzhou, China. They gave me the opportunity and experience to work with fabrication of silicon nanoparticles. My work done during my stay at Zhejiang University will be described in Chapter 3, although the description of this part is relatively short it still includes around a year of work from arrival in China to submission of paper.

Acknowledgments

First and foremost I want to thank my supervisors Mikkel Jørgensen and especially Eva Bundgaard for always taken the time to help me and for their guidance and encouragement of my work and for the correction and proofreading of this thesis. A special

thanks should go to Prof. Frederik C. Krebs for optimism and energy of spirit. I would also like to thank the people in the “china-group”: Frederik, Mikkel, Eva, Kion, Jens, Thue, Birgitta, and Arvid. For all the joint project we have been involved in. Last but not least a special thanks to Henrik Friis Dam for being my faithful lab-partner through the last year of the PhD, keeping up each others spirit during the preparation of thousands of solar cells.

I will also give thanks the synthetic team Eva, Ole, Martin, and Jon for their supply of polymers, without most of the work in this thesis would not have been possible as well at the R2R-coating team Mikkel, Markus, Roar, and Frederik for providing substrates, and to the rest of the solar cell group which for sure has also been helping out through the last 3 years.

I would also like to thank Prof. Hongzheng Chen for allowing me to work in her group at Zhejiang University. Moreover, a thanks goes to the rest of the people in her group for help and support during my stay.

Additional thanks should go to Natalie Patrice Holmes for help with the TEM and STXM analysis.

Finally, I would like to thank Karsten Hansgaard Nielsen and Natalia Klaudia Zawacka for proofreading of this thesis.

List of publications:

2011

T. R. Andersen, T. T. Larsen-Olsen, B. Andreasen, A. P. L. Böttiger, J. E. Carlé, M. Helgesen, E. Bundgaard, K. Norrman, J. W. Andreasen, M. Jørgensen, and F. C. Krebs, *Aqueous processing of low-band-gap polymer solar cells using roll-to-roll methods*, ACS NANO, **2011**, 5, 4188-4196, DIO: 10.1021/nn200933r.

2012

T. T. Larsen-Olsen, T. R. Andersen, B. Andreasen, A. P. L. Böttiger, E. Bundgaard, K. Norrman, J. W. Andreasen, M. Jørgensen, and F. C. Krebs, *Roll-to-roll processed polymer tandem solar cells partially processed from water*, Solar Energy Materials and Solar Cells, **2012**, 97, 43-49, DIO: 10.1016/j.solmat.2011.08.025.

T. T. Larsen-Olsen, B. Andreasen, T. R. Andersen, A. P. L. Böttiger, E. Bundgaard, K. Norrman, J. W. Andreasen, M. Jørgensen, and F. C. Krebs, *Simultaneous multilayer formation of the polymer solar cell stack using roll-to-roll double slot-die coating from water*, Solar Energy Materials and Solar Cells, **2012**, 22-27, DIO: 10.1016/j.solmat.2011.08.026 .

T. R. Andersen, Q. Yan, T. T. Larsen-Olsen, R. Søndergaard, Q. Li, B. Andreasen, K. Norrman, M. Jørgensen, W. Yue, D. Yu, F. C. Krebs, H. Chen, and E. Bundgaard, *A Nanoparticle Approach towards Morphology Controlled Organic Photovoltaics (OPV)*, Polymers, **2012**, 4, 1242-1258. DOI:10.3390/polym4021242

L. Fu, H. Pan, T. T. Larsen-Olsen, T. R. Andersen, E. Bundgaard, F. C. Krebs, and H. Chen, *Synthesis and characterization of new electron-withdrawing moiety thieno [2, 3-c] pyrrole-4, 6-dione-based molecules for small molecule solar cells*, Dyes and Pigments, **2012**, 97, 141-147, DOI: 10.1016/j.dyepig.2012.12.009.

L.-J. Zuo, X.-L. Hu, T. Ye, T. R. Andersen, H.-Y. Li, M.-M. Shi, M. Xu, J. Ling, Q. Zheng, J.-T. Xu, E. Bundgaard, F. C. Krebs, and H.-Z. Chen, *Effect of Solvent-Assisted Nanoscaled Organo-Gels on Morphology and Performance of Organic Solar Cells*, The Journal of Physical Chemistry C, **2012**, 116, 16893-16900, DIO: 10.1021/jp3049444.

2013

T. R. Andersen, H. F. Dam, B. Andreasen, M. Hösel, M. V. Madsen, S. A. Gevorgyan, R. Søndergaard, M. Jørgensen, and F. C. Krebs, *A rational method for developing and testing stable flexible indium-and vacuum-free multilayer tandem polymer solar cells comprising up to twelve roll processed layers*, Solar Energy Materials and Solar Cells, **2013**, DOI: 10.1016/j.solmat.2013.07.006.

J. E. Carlé, T. R. Andersen, M. Helgesen, E. Bundgaard, M. Jørgensen, and F. C. Krebs, *A laboratory scale approach to polymer solar cells using one coating/printing machine, flexible substrates, no ITO, no vacuum and no spincoating*, Solar Energy Materials and Solar Cells, **2013**, 108, 126-128, DOI: 10.1016/j.solmat.2012.09.008.

M. Jørgensen, J. E. Carlé, R. R. Søndergaard, M. Lauritzen, N. A. Dagnæs-Hansen, S. L. Byskov, T. R. Andersen, T. T. Larsen-Olsen, A. P. L. Böttiger, B. Andreasen, L. Fu, L. Zuo, Y. Liu, E. Bundgaard, X. Zhan, H. Chen, and F. C. Krebs, *The state of organic solar cells—*

A meta analysis, Solar Energy Materials and Solar Cells, **2013**, DOI:
10.1016/j.solmat.2013.05.034.

Abstract

The field of organic solar cells has in the last years gone through an impressive development with efficiencies reported up to 12 %. For organic solar cells to take the leap from primarily being a laboratory scale technology to being utilized as renewable energy source, several issues need to be addressed. Among these are a more direct transfer of new materials tested on a laboratory scale to large scale production than offered by spincoating, a method offering direct control of the morphology in the active layer, and a more environmental friendly processing, where the vast use of organic solvents offers a great challenge.

In this thesis the development of inks with a pre-arranged morphology was attempted by two methods. First by grafting of silicon nanoparticles with an organic phenylene vinylene oligomer, the resulting particles were analyzed by $^1\text{H-NMR}$, absorption spectroscopy, Atomic Force Microscopy and as solar cells in a blend with PCBM. It was concluded that these particles did not show a potential large enough for continuous work due to a high material loss and low efficiency when applied in solar cells. The second method to achieve was preparation of pre-arranged morphology organic nanoparticles consisting of a blend of donor and acceptor in an aqueous dispersion, thereby addressing two of the issues remaining in the field of organic solar cells. This approach was used on six different polymers, which all had the ability to prepare aqueous nanoparticle inks. The morphology of the nanoparticles was investigated both internally and externally, both were attempted to be controlled by variation in preparation solvent and particle sizes. The inks were slot-die coated on both the R2R coater and mini roll coater but only after a number of inks modifications and adjustments of the coating parameters. Solar cell prepared by large scale R2R-coating with an active layer consisting of these nanoparticles had an efficiency of up to 0.55 %.

In order to shorten the distance from laboratory scale testing of solar cells to R2R production a mini roll coater was invented. This roll coater uses film deposition techniques which have been downscaled from the R2R coater i.e. slot-die coating and flexographic printing. Thereby allowing the device optimizations to be transferred almost

directly from small to large scale. This is in contrast to devices prepared by spincoating. Another advantage with the laboratory roll coater is that, it enables the preparation of 250-300 solar cells in an hour from as little as 15-20 mg of polymer. This means that a number of parameters can be optimized with very little material compared to the amount necessary for optimization directly on the R2R equipment.

The laboratory roll coater was used in the search of the high efficient organic solar cells by optimizing new electrodes and preparing a number of solar cells from different polymers with various optimization parameters such as thickness of the active layer, ratio between donor and acceptor, and coating temperature. Further small molecule inks were slot-die coated on this coater with a variation in ink formulations enabling the coating of films of a higher quality and coating of ink employing molecules with cross-linkable side chains to avoid dissolution of the active layer when coating subsequent layers.

The mini roll coater was also used to develop a procedure for preparation of tandem devices where all layers were deposited by wet-processing on an ITO-free flexible substrate. The challenging part was the preparation of an intermediate layer, which was both easy to coat and had a good solvent resistance. Thus by pure intermediate optimizations the efficiency increased from 0.067 % to 1.7 %.

Main aspects of this thesis worth of further investigation includes pre-arranged morphology by aqueous inks, the use of the mini roll coater to investigate and optimize new polymer, and the preparation of tandem devices with high efficiency.

Resume

Organiske solceller har gennem de sidste år gennemgået en imponerende udvikling med rapporterede effektiviteter på op til 12 %. For at organiske solceller kan tage det næste skridt fra primært at være en teknologi på laboratorie skala til at blive benyttet som bæredygtig energikilde skal adskillige problematikker adresseres. Blandt dem er en mere direkte overførsel af nye materialer fra laboratorie tests til stor skala produktion end det er muligt med spincoating, en metode der tilbyder en direkte kontrol over morfologien af det aktive lag, og en mere miljøvenlig processering, hvor den enorme brug af organiske solventer er en stor udfordring.

I denne afhandling er udviklingen af blækker med pre-organiseret morfologi forsøgt gennemført på to måder. Først ved at "koble" silicon nanopartikler med en organisk phenylen vinylen oligomer. De fremstillede partikler blev analyseret med $^1\text{H-NMR}$, absorption spektroskopi, Atomic Force Mikroskopi og som solceller i en blanding med PCBM. Det blev konkluderet, at disse partikler ikke fremviste potentiale nok til at fortsætte udvikling af denne metode. Dette skyldes et stort materiale tab og en lav effektivitet i de fremstillede solceller. Den anden metode var at fremstille organiske nanopartikler bestående af en blanding af donor og accepter i en vandig opløsning. Denne metode adressere derved to af de tilbageværende problemstillinger indenfor organiske solceller. Denne fremgangsmåde blev benyttet på seks forskellige polymere, som alle har evnen til at danne vandige nanopartikel blække. Morfologien af disse nanopartikler blev undersøgt både internt og eksternt, begge blev forsøgt kontrolleret ved at variere forberedelse solventet og partikelstørrelsen. Disse blækker blev slot-die coatet både i stor (rulle-til-rulle (R2R)) og lille skala dog først efter ændring af blækformuleringerne og justeringer af coating parametre. Solceller fremstillet ved R2R coating med et aktivt lag bestående af disse nanopartikler havde en effektivitet på op til 0.55 %.

For at forkorte afstanden fra laboratorie skala forberedelse til fuldskala R2R fabrikation af solceller blev en mini rulle coater udviklet. Denne rulle coater anvender trykemetoder som er nedskaleret fra R2R. Derved tillader den at solcelle optimeringer

kan overføres næsten direkte fra lille til stor skala, hvilket er i kontrast til celler forberedt ved spincoating. En anden fordel ved mini rulle coateren er, at den muliggøre forberedelsen af 250-300 solceller på 1 time ud fra så lidt som 15-20 mg polymer. Dette betyder at flere parametre kan blive optimeret med en meget lille mængde af materiale i forhold til den mængde det ville kræve at optimere direkte på R2R udstyret.

Mini rulle coateren blev benyttet til studiet af solceller med en høj effektivitet ved at optimere nye elektroder og ved at forberede solceller med forskellige optimeringsparametre så som tykkelse af det aktive lag, forholdet mellem donor og accepter og coating temperatur. Blækker indeholdende små molekyler blev slot-die coatet på denne coater med variation i blækformuleringerne for at muliggøre coating af film med en høj kvalitet. Ligeledes coater blækker indeholdende molekyler med krydsbindende sidekæder for at undgå genopløsning af det aktive lag når efterfølgende lag coates.

Mini rulle coateren blev også anvendt til at udvikle en fremgangsmåde til at fremstille tandem solceller, hvor alle lag blev deponeret ved våd-processering på et ITO-frit fleksibelt substrat. Den udfordrende del var at fremstille et intermediat lag, som var både nemt at coate og var solvent resistent. Ved intermediat lag optimering blev effektiviteten forbedret fra 0,073 % til 1,7 %.

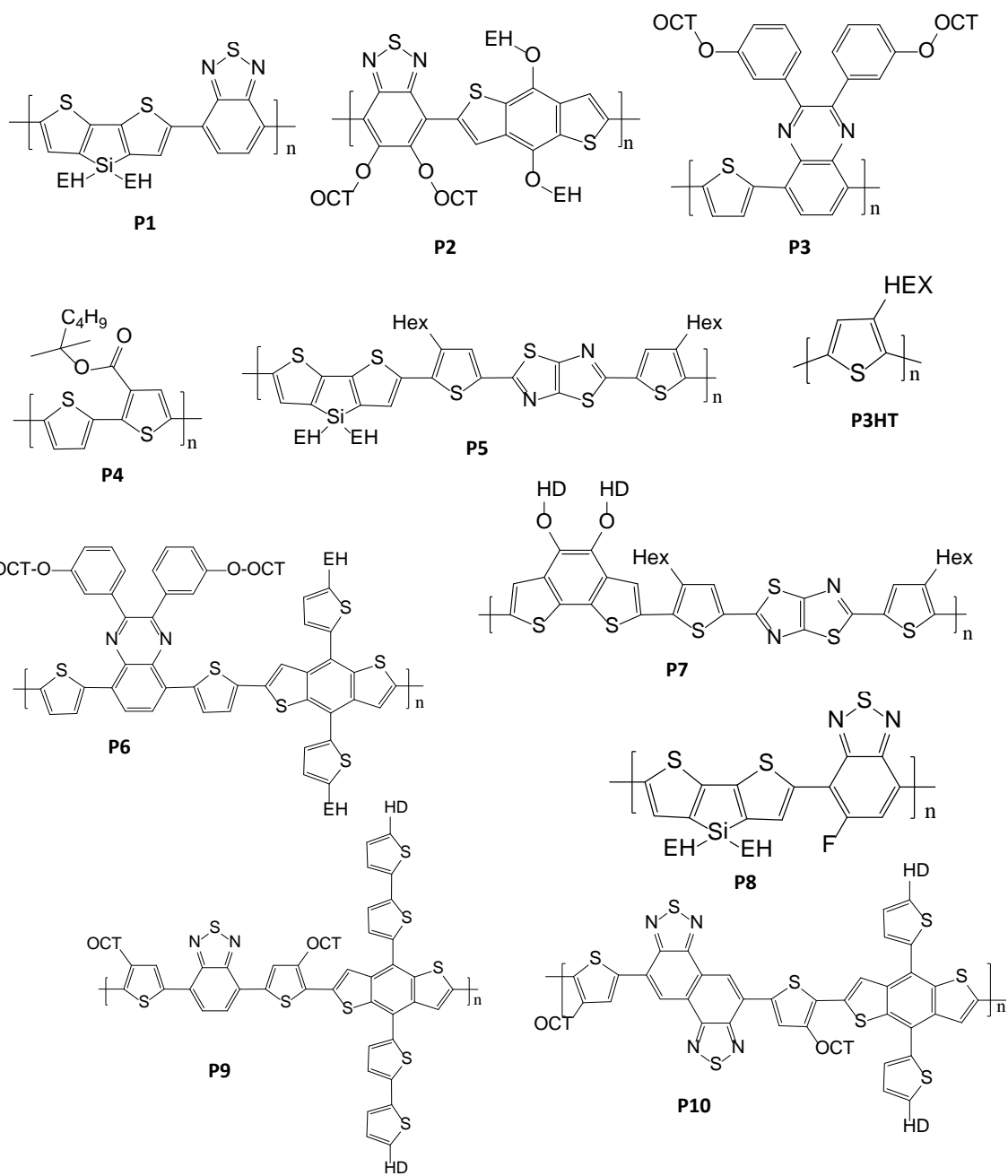
Hoveddelene af denne afhandling som er værd at undersøge yderligere inkludere pre-organiseret morfologi med vandige blække, undersøgelser og optimering af nye polymere med den mini rulle coateren og forberedelsen af tandem solceller med høj effektivitet.

List of abbreviations

AFM	Atomic Force Microscopy
AM1.5	Air mass 1.5
A.U.	Arbitrary units
BHJ	Bulk heterojunction
CB	Chlorobenzene
CF	Chloroform
CN	Chloronaphthalene
D-A interface	Donor-acceptor interface
DIO	Diiodooctane
EH	2-Ethylhexyl
EPBT	Energy payback time
ETL	Electron transport layer
FF	Fill factor
F8BT	Poly(9,9-dioctylfluorene-co-benzothiadiazole)
HBG	High band gap
HEX	Hexyl
HOMO	Highest occupied molecular orbital
HTL	Hole transport layer
I-V	Current-Voltage
ICBA	Indene-C ₆₀ bisadduct
IPA	Isopropanol
IPCE	Incident photon to current efficiency
ITO	Indium Tin Oxide
J _{sc}	Short circuit current density
LBIC	Light Beam Induced Current
LBG	Low band gap
LUMO	Lowest unoccupied molecular orbital
MRC	Mini Roll Coater
NEXAFS	Near-Edge X-ray Absorption Fine Structure

NMR	Nuclear magnetic resonance
<i>o</i> -DCB	<i>Ortho</i> -dichlorobenzene
OCT	Octyl
OSC	Organic solar cell
PCBM	[6,6]-phenyl C ₆₁ butyric acid methyl ester
C ₇₀ -PCBM	[6,6]-phenyl C ₇₁ butyric acid methyl ester
PCE	Power conversion efficiency
PEDOT:PSS	Poly(3,4-ethylenedioxythiophene):poly(styrenesulfonate)
PFB	Poly(9,9-dioctylfluorene-co-N,N-bis(4-butylphenyl)-N,N-diphenyl-1,4-phenylenediamine)
PFN	Poly[(9,9-bis(3'-(N,N-dimethylamino)propyl)-2,7-fluorene)-alt-2,7-(9,9-dioctylfluorene)]
P _{in}	Power of incoming light
P _{max}	Maximum power point
PSBTBT	Poly(4,4-dioctyldithieno(3,2-b:2',3'-d)silole)-2,6-diyl-alt-(2,1,3-benzothiadiazole)-4,7-diyl)
P3HT	Poly(3-hexylthiophene)
PV	Photovoltaic
R2R	Roll-to-roll
SAXS	Small Angle X-ray Scattering
SDS	Sodium dodecyl sulfate
STXM	Scanning Transmission X-ray Microscopy
TEM	Transmission Electron Microscopy
V _{oc}	Open circuit voltage
VTIP	Vanadium triisopropoxide

List of polymers



Content

1. INTRODUCTION.....	1
1.1. Background.....	1
1.2. OSC architecture and working principle.....	3
1.3. Defining the limits and how to overcome them.....	9
1.4. Energy payback time (EPBT).....	13
1.5. Aim and scope of this thesis	15
1.6. References.....	17
2. FABRICATION OF INKS WITH A PRE-ARRANGED MORPHOLOGY	23
2.1. Introduction.....	23
2.2. Aqueous nanoparticle inks.....	25
2.3. Grafting of nanoparticles for morphology control	37
2.4. Summary	43
2.5. References.....	44
3. PROCESSING.....	51
3.1. Introduction.....	51
3.2. Mini roll-coater.....	57
3.3. Small molecule OSCs.....	69
3.4. Preparation of OSCs from aqueous inks.....	74
3.5. Summary	79
3.6. References.....	81

4. TANDEM OSC PROCESSING	85
4.1. Introduction	85
4.2. Tandem OSC prepared by wet-processing	88
4.3. Summary	105
4.4. References.....	106
5. SUMMARY AND OUTLOOK	111
APPENDIX 1	115
APPENDIX 2	116

1. Introduction

1.1. Background

In a world challenged by an increasing energy consumption and decreasing stockpiles of fossil fuels, the search for renewable energy sources is attracting great attention from politicians and scientists. There is no other renewable energy source that exhibits the same potential as found in solar energy, since the other energy sources, such as wind, are secondary energy sources generated by the energy from the sun. There are only two methods for direct conversion today: solar heating systems, mainly used for heating of houses and water, and solar cells which allows sunlight to be directly transformed into electricity.

The first commercial solar cell was presented by “Bell Telephone Laboratories” in 1954 with an efficiency of 6 % prepared from inorganic silicon.[1] The technology has been further developed to achieve an efficiency of 25 % on small scale,[2] module efficiencies are generally around 12 %,[3] with a lifetime of 25 years.[4] Even though the efficiency is high and the lifetime is long, electricity produced by 1st generation solar cells is still more expensive than electricity produced by fossil fuels. This is due to a high energy consumption during fabrication, which is also the reason why silicon solar cells in 2012 only provided less than 0.5 % of the electricity consumption.[5]

A 2nd generation of solar cells have been developed. They are still produced from inorganic materials but address the cost issues found in the 1st generation. They are prepared as a thin-film from amorphous silicon, cadmium sulphide, or cadmium telluride, by sputtering or vapor deposition. Efficiencies of up to 20 % has been achieved on laboratory scale,[2] module efficiencies are generally around 7-10 % [3,6] with a lifetime of 20-25 years.[7]

In order to reduce the cost issues even further a 3rd generation of solar cells has been explored. It prepares solar cell with new architectures and changing the materials from inorganic to organic materials. 3rd generation organic solar cells (OSCs) possess attractive advantages such as flexible substrates, fast solution processing, and the potential for low cost large scale production by roll-to-roll (R2R).

Despite a decade of intensive research within OSCs, the field has not yet fulfilled its overwhelming potential as a renewable energy source. Even though the top performance of OSCs in a period from 2001 to 2011 have increased from around 3 % to 10 %, [2] the field is still on an academic level with only a few research-groups working intensively to bring it to the next level. [8] The majority of researchers are studying small area devices prepared by spin-coating in a glovebox with vacuum deposited electrodes containing scarce materials such as indium tin oxide (ITO). None of these appears to be compatible with large-scale fabrication of OSC. [8] OSC modules prepared by R2R processing generally do not achieve an efficiency higher than 2.5-4 %, which is significantly lower than what is obtained on laboratory scale spin coated OSC. [2] Understandably, new materials cannot be tested in large-scale R2R production for preliminary studies, it would, however, make the route from laboratory scale to large-scale production significantly shorter if only coating and printing methods compatible with R2R were used.

For OSC to take the leap from laboratory scale technology to actual energy production either the performance of the module need to be increased or the embodied energy in the modules needs to be reduced. [9] The performance can among other be increased by better utilization of the photon flux from the solar irradiation spectrum. Most materials used in OSCs nowadays have a rather narrow absorption, reducing the current from the otherwise theoretical maximum given by the solar irradiating spectrum. [10] There are two main approaches to overcome the narrow absorption 1) expanding the absorption by preparing low band gap random co-polymer containing more chromophores, or 2) by stacking OSC containing polymers with narrow absorptions band on top of each other known as a tandem OSC. Other loss mechanisms/efficiency reductions are decay of excitons caused by insufficient morphology. [11] A loss of voltage as a result of poor alignment between LUMO levels of donor and acceptor. And thermalization caused by absorption of photons containing a higher energy than the band gap of the polymer. The embodied energy is all the energy that goes into the production of the OSC module. A reduction of the embodied energy could be a large step towards commercialization since it simply would allow poorer efficiency of the OSC. Reduction of the embodied energy have already taken a leap forward by substituting the ITO electrode with low energy containing ones such as a silver and poly(3,4-

ethylenedioxythiophene) poly(styrenesulfonate) (PEDOT:PSS) electrode. There is, however, still a great potential for decreasing the energy investment.[9,12]

Another great challenge on the path towards utilizing OSC as energy source is the vast usage of organic solvents for fabrication.[13] This has not attracted the same amount of attention as the efficiency or stability of the OSC, it might, however, be just as important if the manufacturers are to obey environmental laws throughout the western world.

1.2. OSC architecture and working principle

The general OSC architecture is comprised of a layered stack, with an active layer sandwiched in between two electrodes. The front electrode needs to be transparent to allow illumination of the photoactive layer, and usually buffer layers are applied at the interface between the electrodes and the active layer to ensure a selective charge transport from the active layer to the electrode. OSCs can be prepared in two main geometries known as “normal” and “inverted” geometry (found in Figure 1.1).[14] The distinction between the two is the polarity of the device, it determines at which electrodes the electrons and holes are to be extracted. The polarity is determined by the work function of the electrode materials and the buffer layers. A typical buildup of an OSC would start with a transparent electrode, often ITO but alternatively a highly conductive PEDOT:PSS. On top a layer of either PEDOT:PSS as hole transport layer (HTL) or ZnO as electron transport layer (ETL) would be deposited for normal and inverted geometry, respectively, these would function as buffer layers. Subsequently a mixture of donor and acceptor materials are coated from an appropriate solvent. During solvent evaporation an interpenetrating network is formed in the film due to phase separation of the donor and acceptor materials. To finish the devices another buffer layer is applied prior to the back electrode. In normal geometry the back electrode would usually consist of an aluminum layer whereas silver is used in inverted geometry.

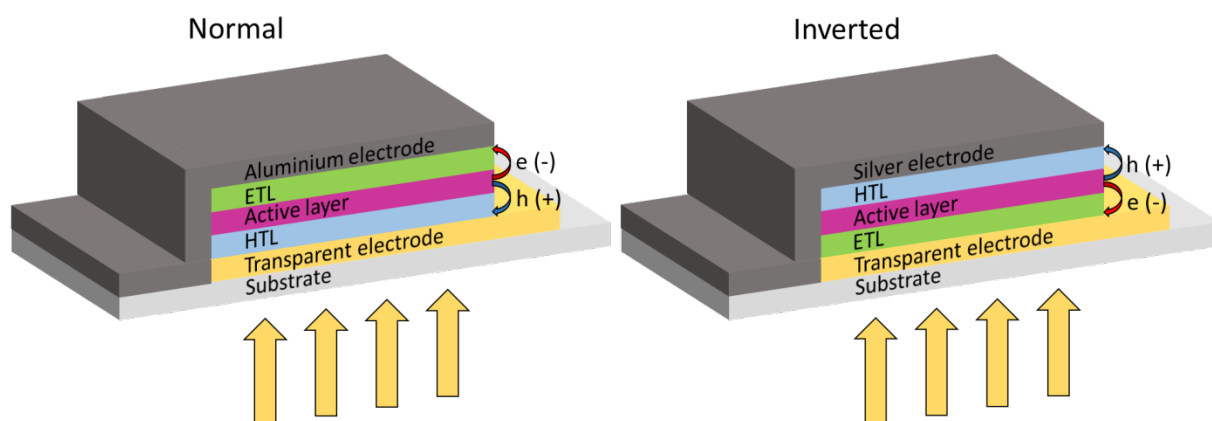


Figure 1.1: Schematic build-up of an OSC in the two different geometries: Normal geometry (on the left) where electrons are collected at the back Al-electrode and Inverted geometry (on the right) where collection of electrons is at the transparent electrode. HTL = hole transport layer, ETL = electron transport layer, e = electrons, and h = holes.

OSC functions, like all other photovoltaic technologies, by transforming incoming light, i.e. photons, to electricity. In contrast, to inorganic photovoltaics where excitation of an electron from valence to conduction band results in the formation of a free charge carrier, free charge carriers are not formed as easily in OSC.[15] This is due to the relatively low dielectric constant of organic materials, the excitation instead leads to the formation of a bound state known as an “exciton”, which consists of a negatively charge electron and a positively charged hole.[15,16] To extract the power the exciton needs to be dissociated into free charge carriers, this is carried out by applying a so-called heterojunction that may be either the bulk or bilayer type (Figure 1.2A).[17] A heterojunction consists of two materials a donor and an acceptor (Figure 1.2B). The acceptor has the ability to accept excited electrons from the donor due to a difference in energy offset in the molecular orbitals, if the energy offset is large enough the exciton willingly breaks into free charge carrier. Empirically it has been determined that an offset of 0.3 eV is sufficient to ensure efficient exciton dissociation.[17] The most commonly used acceptors are fullerene based acceptors such as [6,6]-phenyl C₆₁ butyric acid methyl ester (PCBM) or [6,6]-phenyl C₇₁ butyric acid methyl ester (C₇₀-PCBM). Fullerene based acceptor have several very attractive properties to the use in OSC such as high electron mobility, the ability to pack in crystalline structures, which favors transport of electron to the electrode, and from a practical view they are easy to process due to solubility in

common organic solvents. The donor material is usually a conjugated polymer. This class of materials are generally electron rich, readily undergoes oxidation, have a high highest occupied molecular orbital (HOMO) orbital energy level and typically a high hole transport.

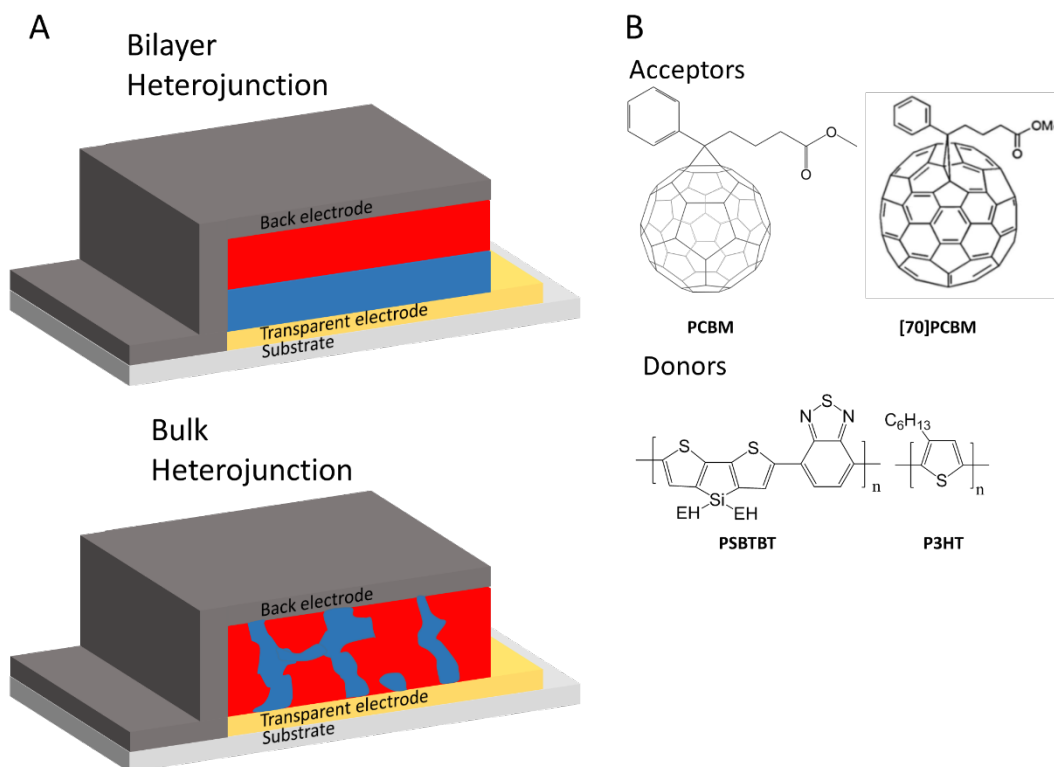


Figure 1.2: A) Two types of heterojunction OSC. Bilayer heterojunction consists of two pure phases of donor and acceptor stacked on top of each other. Bulk heterojunction consists of a blend of donor and acceptor. B) Structures of the most widely used acceptors phenyl-C61-butyric acid methyl ester (PCBM) and phenyl-C71-butyric acid methyl ester (C_{70} -PCBM), and of two donor polymers; a high band gap polymer poly(3-hexylthiophene) (P3HT) and a low band gap polymer poly(4,4'-diocylthiopheno(3,2-b:2',3'-d)silole)-2,6-diyl-alt-(2,1,3-benzothiadiazole)-4,7-diyl (PSBTBT).

A schematic illustration of the basic mechanism for converting photons to electricity in a heterojunction OSC is found in Figure 1.3.[18-20] The conversion mechanism from photon to electricity consists of four steps; A) absorption of photons, B) exciton diffusion, C) exciton dissociation, and D) charge carrier transport and collection.

- A) Absorption of photons in the active layer causes an electron to be excited from the HOMO to the lowest unoccupied molecular orbital (LUMO), leaving behind a hole in the HOMO-level.

- B) This leads to the formation of an exciton that diffuses through the polymer phase and may reach a donor-acceptor interface (D-A interface).
- C) At the interface, the exciton dissociate into free charge carriers, leaving the positively charged hole in the donor material whereas the negatively charged electron will be relocated to the acceptor material. For the exciton dissociation to occur a driving force is needed to overcome the coulombic forces. The driving force is created by having a lower lying LUMO-level for the acceptor than for the donor, usually a difference of 0.3 eV is required to ensure the dissociation.[17]
- D) The separated charge carriers are transported through the respective phases of the active layer and collected at the electrodes.

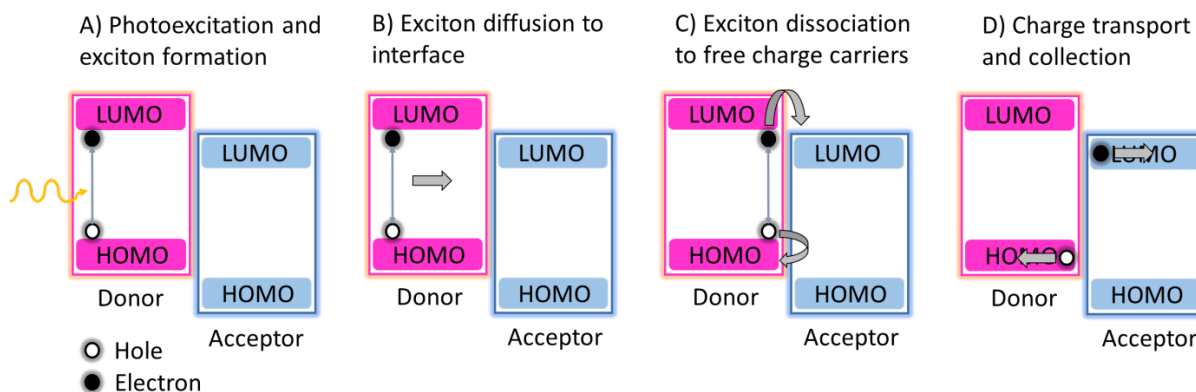


Figure 1.3: Schematic illustration of the mechanism for OSC to convert photons to electricity in the active layer.

Generally, all four of the above mentioned steps are crucial for the efficiency of the prepared OSC, there is a number of loss mechanisms involved in the sequence. One of the most pronounced is the limited diffusion length of excitons in organic material which is typically 10-20 nm.[21] Excitons created further away from a D-A interface will therefore have a low probability of being dissociated into free charge carriers, and thereby be lost due to recombination of the excited electron and hole. Ideally, the heterojunction should be formed in such a manner that all generated excitons have the possibility of reaching an interface, this makes OSC prepared with a bilayer heterojunction insufficient (Figure 1.2A). A major breakthrough came with the introduction of the bulk heterojunction (BHJ) in which the active lay-

er consist of a heterogenic blend of donor and acceptor materials (Figure 1.2A).[18,22] The introduction of BHJ led to an increase in the amount of excitons reaching a D-A interface and thereby dissociating into free charge carriers. An optimal morphology for the heterojunction could therefore be a nanoscale interpenetrating bicontiguous network of donor and acceptor, which ensures all excitons to be generated in vicinity of a D-A interface while still having pure phases to ensure transport of the free charge carriers (Figure 1.4). [23]

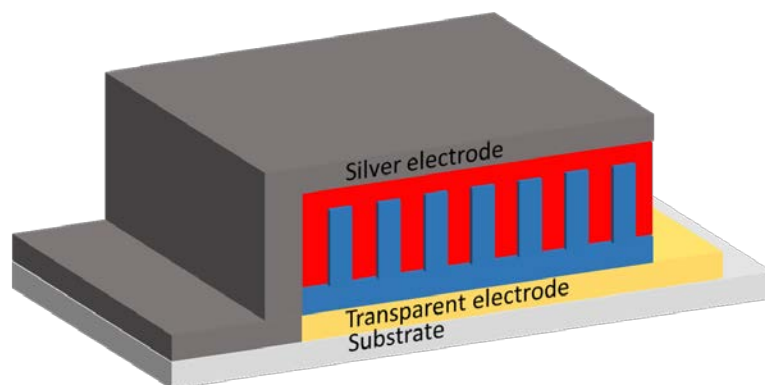


Figure 1.4: An example of how the optimal morphology of the heterojunction could look like.

1.2.1. Device characterization

1.2.1.1. Power conversion efficiency

The efficiency of an OSC is examined through the power conversion efficiency (PCE). It can be calculated from a generated current-voltage (I-V) curve, which is obtained by measuring the current at a forced voltage thereby resulting in a curve as seen in Figure 1.5. V_{OC} is the open circuit voltage being the maximum voltage that can be extracted from the OSC. The maximum V_{OC} is defined by the position of the molecular orbitals of the active materials as being the energy-difference between the HOMO of the donor and the LUMO of the acceptor.[24] J_{SC} is the short circuit current density, it is the current flowing through the OSC under illumination at short circuit condition.[25] From an I-V curve a third important parameter known as the fill factor (FF) can be calculated by Equation 1.1.[26] The FF is the percentage

of the maximum achievable power that can actually be extracted by the OSC, it describes the quality of the diode.[24]

$$FF = \frac{V_{mpp} \times J_{mpp}}{V_{OC} \times J_{SC}} \times 100 \% \quad (\text{Equation 1.1})$$

V_{mpp} and J_{mpp} are the voltage and current density at the maximum power point in V and mA cm⁻², respectively. (Figure 1.5)

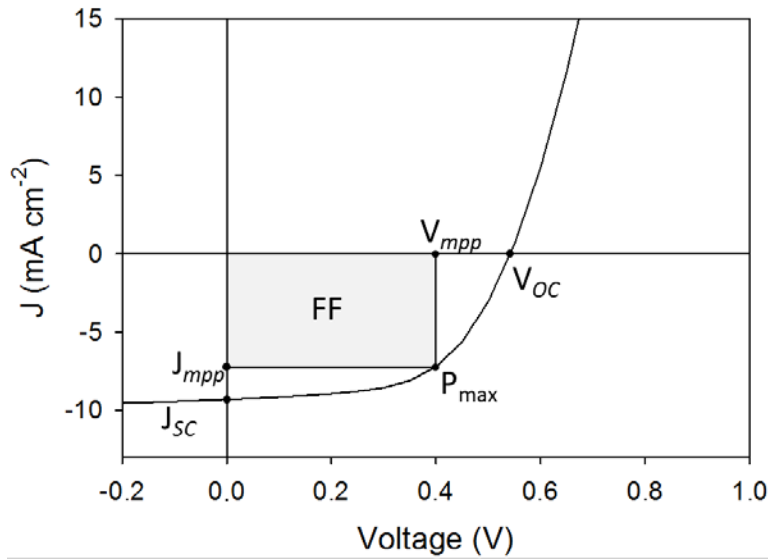


Figure 1.5: I-V curve of an OSC under illumination. Illustrating the device characterization parameters J_{SC} , V_{OC} , P_{max} , J_{mpp} and V_{mpp} .

The PCE is given by Equation 1.2, it is the ratio between the power produced at the maximum power point and the power of the incoming light.

$$PCE = \frac{V_{OC} \times J_{SC} \times FF}{P_{in}} \times 100 \% \quad \text{Equation 1.2}$$

P_{in} is the power of the incoming light; normally the air mass 1.5 (AM1.5) irradiation spectrum is used, which have an intensity of 1000 W m⁻².

1.2.1.2. Incident photon to current efficiency

Incident photon to current efficiency (IPCE) is another important measure for investigating the performance of the OSC. IPCE is defined by Equation 1.3 and indicates if the emitted photons are being efficiently converted to charge carriers and collected at the electrodes at

a given wavelength. The usual method for determining the IPCE are by shining monochromatic light with controlled intensity (number of photons) at the OSC and then measuring the response of generated current (number of electron and hole pairs) at the electrode. These measurements are conducted while changing the wavelength of the emitted light throughout the wanted spectrum range.[21]

$$IPCE = \frac{1240 \times I_{SC}}{\lambda \times P_{in}} \times 100 \% \quad \text{Equation 1.3}$$

λ is the wavelength in nm, I_{SC} is the current in ampere pr. meter squared, and P_{in} is the power of the incoming light.[27]

1.3. Defining the limits and how to overcome them

In order to increase the efficiency of OSC to the optimal value it is necessary to tune the band gap of the polymers to obtain a better match with the solar irradiation spectrum and thereby increase the number of collected photons. Simultaneously, it is necessary to take the decrease in maximum V_{OC} as a function of a decreasing band gap into account. Thus, a decreasing band gap might cause an increase in the maximum obtainable current but it simultaneously causes a decrease in the maximum obtainable voltage. These counter acting processes were in 1961 investigated theoretically by Shockley and Queisser,[28] they put forward a model in which they determined the so-called “*ultimate efficiency*” of an inorganic photovoltaic (PV) device. In this model, they only considered two performance reduction parameters (Figure 1.6).

- Only photons having a higher energy than the band gap of the active material can be absorbed and contribute to the performance.
- Hot charge carriers created by absorption of photons containing a higher energy than band gap will relax down to the conduction band of the active material, also known as “thermalization”

Applying these parameters to the AM1.5 solar irradiation spectrum, they came up with the scheme seen in Figure 1.7 by calculating the power from the maximum achievable voltages and currents densities at each wavelength. The theoretical maximum power peaked at

approx. 48 % around 1100 nm translating into an E_g of 1.1. The decrease in theoretical power on both sides of the peak around 1100 nm is due to current or voltage limitations. Shockley and Queisser[28] also display a more realistic model where they included more loss mechanisms such as radiative and non-radiative recombination of hole and electron pairs, thereby reducing the maximum PCE to 30.1 % for a single junction inorganic PV.

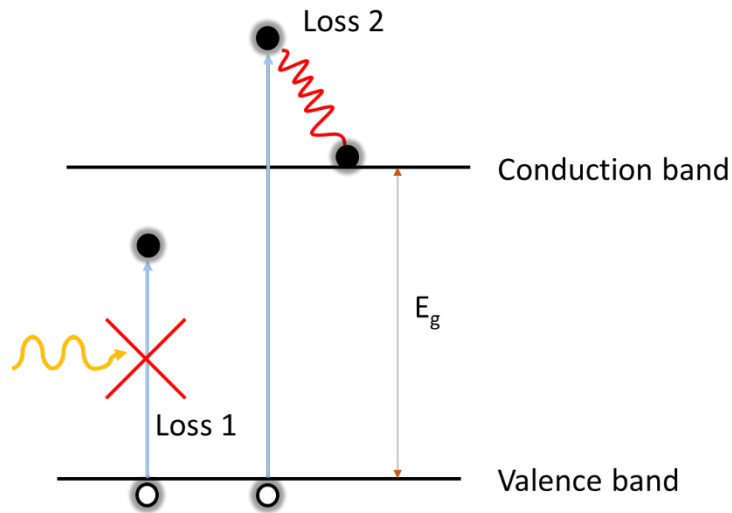


Figure 1.6: Description of the absorption (Loss 1) and thermalization (Loss 2) performance reductions occurring in a solar cell.[29]

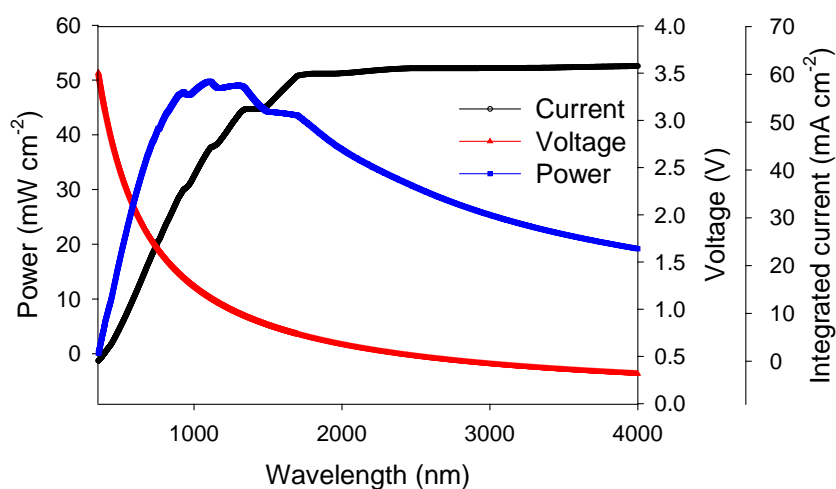


Figure 1.7: Maximum power obtainable in inorganic PVs as a function of wavelength based on the Shockley-Queisser model and the AM 1.5G emission spectrum. The power is calculated as the product of the integrated current (assuming an EQE of 100%) and the voltage of a device taken as the value of the band gap. The power is thus the maximum theoretical value, neglecting thermodynamic effects and losses on the final solar cell displaying a perfect diode (FF=100%).

This simple model cannot be applied directly to OSC, since it is necessary to consider the exciton dissociation as well. Optimal exciton dissociation requires an offset between the LUMO-levels of the donor and acceptor of at least 0.3 eV, thus reducing the maximum voltage to a value lower than the band gap of the active material. The lower voltage influences the diagram of maximum power in two ways, firstly it reduces the *ultimate efficiency* from 48 % to 36 %, and secondly it pushes the optimal E_g from 1.1 eV to around 1.4 eV (Figure 1.8 number 2). Further reductions in the theoretical efficiency and changes in the optimal band gap can be found by adding other known losses in to the model. One of them being an additional drop in V_{OC} from the energy difference between the HOMO of the donor and the LUMO of the acceptor empirically determined to be 0.3 eV.[30] This results in a maximum PCE of 26 % and optimal band gap around 1.45 eV. These theoretical considerations assuming a perfect diode (FF=100 %) and an IPCE of 100 % of photons containing an energy higher than the band gap, changing these to a more realistic values could decrease the *ultimate efficiency* even further.

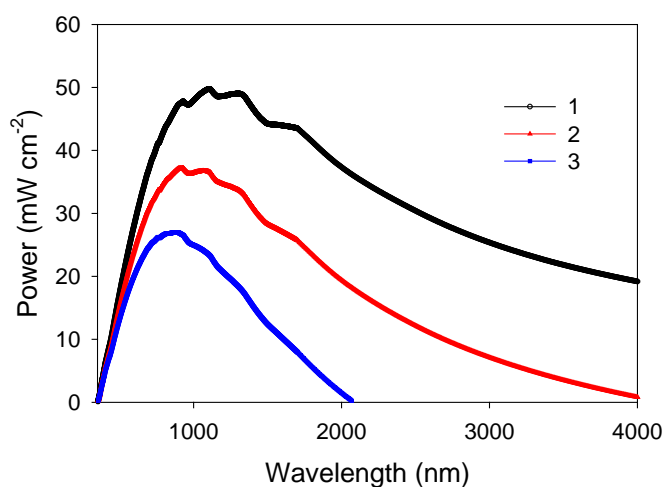


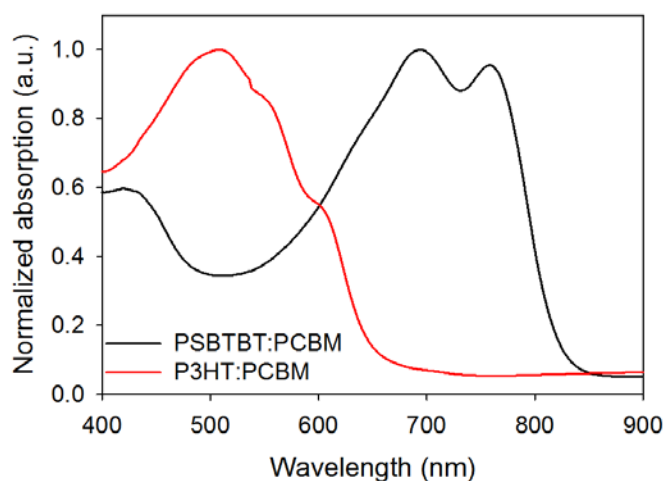
Figure 1.8: Maximum power obtainable in PVs based on the AM 1.5G emission spectrum. The power is calculated as the product of the integrated current (assuming an EQE of 100%) and the voltage varied to include OSC. 1: theoretical maximum for inorganic solar cells, 2: band gap-0.3 eV to ensure exciton dissociation, and 3: band gap-0.6 eV to ensure exciton dissociation and to include an empirical loss of 0.3 eV. The power is thus the maximum theoretical value, neglecting thermodynamic effects and losses on the final solar cell displaying a perfect diode (FF=100%).

Given by the boundaries for Shockley and Queisser's model two of the largest reductions in PV is the transmission of photon contain a lower energy than the band gap and the thermalization of hot carriers. Both of these losses can be circumvented by the application of a tandem PV. The theoretical limits of performance was studied by De Vos[31]. The author demonstrates that it should be possible to achieve performance that surpasses the limits otherwise presented by Shockley and Queisser[24]. The theoretical efficiency for a single junction device is approx. 30 %, this increases to 42 % for a tandem device comprised of two sub-cells having band gaps of 1.9 and 1.0 eV, respectively (Table 1.1). The theoretical maximum continuous to increase with increasing number of sub-cells it can go as high as 53 % when applying four sub-cells.

Table 1.1: The optimal set of band gaps for tandem structures with n stacked cells in nonconcentrated sunlight based on inorganic materials.[31]

N	PCE (%)	BG_1 (eV)	BG_2 (eV)	BG_3 (eV)	BG_4 (eV)
1	30	1.3	-	-	-
2	42	1.9	1.0	-	-
3	49	2.3	1.4	0.8	-
4	53	2.6	1.8	1.2	0.8

In the case of OSC the application of the tandem approach have the additional advantage to tackle one more issue, concerned with the nature of light absorption in organic semiconductors. The absorption spectrum is unlike inorganic semiconductors not a continuum, but rather a narrow and discrete peak (Figure 1.9). Thus, combining organic semiconductors with different band gap will give a more efficient coverage of the light spectrum.

**Figure 1.9: Film absorption of P3HT and PSBTBT in a blend with PCBM.**

1.4. Energy payback time (EPBT)

The EPBT is an essential parameter to evaluate for a new energy technology. It is the time required for the technology to produce the equivalent amount of energy as was and will be

invested in the installed device.[32] For OSC this includes the energy investments all the way from mining of the raw materials, synthesis, OSC fabrication, installation, to decommissioning, as shown in Figure 1.10. Even though there are these five steps to consider, only two will be described below, Synthesis/ink fabrication and ink deposition/drying since it is the two that will be in focus in this thesis. The energy investment is generally divided into two categories, 1) embodied energy of the materials used during fabrication, and 2) direct processing energy.[12]

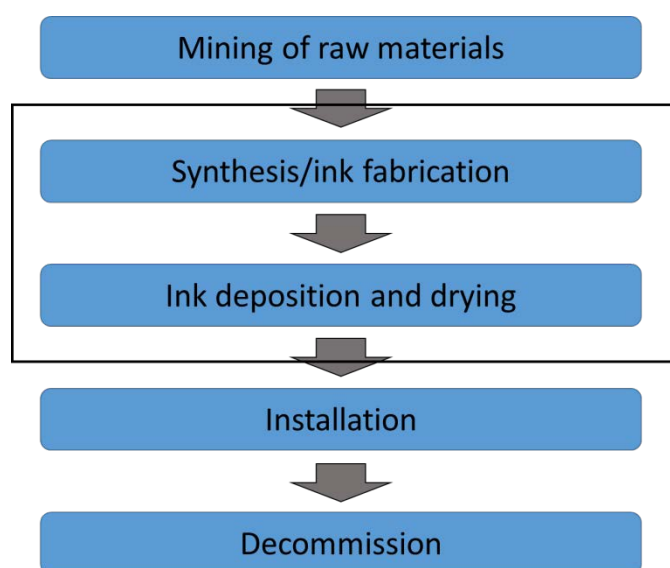


Figure 1.10: The steps to consider when examining the EPBT of OSC. The two steps (synthesis/ink fabrication and ink deposition and drying) in the black box are the steps described in the thesis.

Synthesis/ink fabrication: Reducing the EPBT on the basis of synthesis and ink fabrication represents a trade-off between preparation of simpler molecules, to reduce the number of synthesis steps, and maintaining the performance of the prepared OSC. State of the art polymers for OSC are usually quite complex with more than 10 synthetic steps needed to arrive at the wanted polymer.[33-36] Each step often require purification before further synthesis and have a loss of material due to a yield lower than 100 %, thus causing an increase in the embodied energy in the polymer.[37] Alternative reductions can be found in the used solvents due to a large variation in embodied energy of commonly used solvent.[12] Therefore, it should be taken in to account how extraordinary the performance of a new polymer needs to be before requiring 20 synthetic steps to arrive at the wanted polymer.

Ink deposition and drying: The deposition method of OSC must be chosen such that the processing energy does not add unnecessary time to the EPBT. The primarily used deposition method is nowadays still spin-coating even though the ink losses are extensive and it does not provide the ability to produce OSC with a high throughput.[38] Alternative methods, which can be applied using a R2R coater is for example slot-die coating, and flexographic printing, these are of interest because of a potentially high throughput and a minimum of ink waste both of which will lower the EPBT.

Additional techniques to avoid are vacuum deposition and glovebox.[37] It has been estimated that the deposition of a back-electrode consisting of calcium and aluminum is responsible for around 34 % of the direct energy invested in small scale OSC prepared by spin-coating in a glovebox.[37] Admittedly the thickness of the applied materials is usually reduced when using vacuum deposition as compared to other techniques such as flexographic printing and screen printing. The use of glovebox during fabrication is of interest due to the use and purification of nitrogen, that is responsible for 48 % of the embodied energy and 39 % of the direct processing energy in small scale OSC preparation.[37]

1.5. Aim and scope of this thesis

The aim of this project has been to shorten the distance for organic solar cells (OSC) to reach production level through developing methods to enhance the performance of OSC or reducing the energy payback time (EPBT). The research presented in this thesis is divided into three areas:

- 1) Preparation of inks with a prearranged morphology, thereby obtaining control by a pre-treatment instead of the commonly used post-treatments. The prearranging was obtained through nano-structuring of the ink using two different nanoparticle approaches, i.e. by nanoparticles prepared from a blend of donor and acceptor material in an aqueous ink or by grafting of silicon nanoparticles with an organic oligomer, where the morphology can be tuned by controlling the sizes of the nanoparticles. The first method has the major advantage of also lowering the embodied energy due to the use of water as coating solvent.

- 2) Improving the compatibility between device preparation by laboratory scale techniques and roll-to-roll (R2R) techniques by developing a roll coater, specially developed for small scale testing using only coating methods which can also be mounted and used on the R2R coater.
- 3) Improving the utilization of the light spectrum and reducing the thermalization by developing a tandem stack that can be prepared by coating and printing methods that can also be used on the R2R coater.

These three subjects are described in this thesis as follows:

Chapter 2 – Ink fabrication: The optimal morphology is for OSC an important factor due to its impact on the efficiency of the OSC influencing both the J_{sc} and the FF. The most common method for improving the morphology is through self-assembly of the components in the active layer, which unfortunately does not offer direct morphology control. In this chapter a description of the formulation of aqueous nanoparticle inks with a pre-arranged internal structure will be presented. Then, the internal structure is investigated and size control of the nanoparticles is attempted by varying the formulation parameters. The second part of the chapter describes the synthesis and grafting of silicon nanoparticles with an organic phenylene vinylene oligomer these are then characterized by $^1\text{H-NMR}$, absorption, Atomic Force Microscopy (AFM), and as OSCs. This chapter is based on work published in four papers [13,39-41] (see Appendix 2) and unpublished work.

Chapter 3 – Processing: The major advantage of OSCs in comparison to other photovoltaic technologies is that they can be processed using coating and printing methods on large scale R2R coaters. There is, however, a leap from laboratory scale testing using spincoating to large area coating/printing, which makes it necessary to overcome a number of adaptations. In this chapter a mini roll coater (MRC) is presented and further developed for the purpose of narrowing the gap between laboratory scale testing and R2R production. The MRC enables preparation of OSCs, which are almost directly scalable R2R but on a much smaller scale. Furthermore, the MRC was used to optimize a new ITO-free substrate, for preparation of OSC with an active layer consisting of small molecules, and for coating of the aqueous inks presented in chapter 2. This chapter is based on work

published in three papers [13,40,42] (see Appendix 2), three manuscripts under preparation, and unpublished work.

Chapter 4 – tandem processing: The real pinnacle in OSC processing is the preparation of tandem OSC by wet-processing of all layers on flexible substrates. Tandem OSCs have the possibility of reducing the thermalization and to give a better coverage of the solar irradiation spectrum as described above. In this chapter, a newly developed intermediate layer for tandem OSCs is presented and optimized on the MRC. Tandem OSCs with various polymers as 1st and 2nd sub-cell were prepared to find an optimum polymer match. This chapter is based on work published in one paper[43] and unpublished work.

Chapter 5 – outlook: This chapter presents a summary of the project and the future aspects.

1.6. References

- [1] D. M. Chapin, C. S. Fuller, and G. L. Pearson, "A New Silicon p-n Junction Photocell for Converting Solar Radiation into Electrical Power," *Journal of Applied Physics*, vol. 25, no. 5, p. 676-677, 1954.
- [2] M. A. Green, K. Emery, Y. Hishikawa, W. Warta, and E. D. Dunlop, "Solar cell efficiency tables (version 39)," *Progress in Photovoltaics: Research and Applications*, vol. 20, pp. 12–20, 2012.
- [3] "Direct solar." [Online]. Available: <http://www.solardirect.com/pv/pvlist/pvlist.htm>. [Accessed: 06-Sep-2013].
- [4] A. Stoppato, "Life cycle assessment of photovoltaic electricity generation," *Energy*, vol. 33, no. 2, pp. 224–232, Feb. 2008.
- [5] I. E. Agency, "PVPS Report A Snapshot of Global PV 1992-2012," 2013, ISBN: 978-3-906042-10-7.
- [6] K. L. Chopra, P. D. Paulson, and V. Dutta, "Thin-film solar cells: an overview," *Progress in Photovoltaics: Research and Applications*, vol. 12, no. 23, pp. 69–92, Mar. 2004.
- [7] "First solar." [Online]. Available: www.firstsolar.com. [Accessed: 10-Sep-2013].
- [8] F. C. Krebs and M. Jørgensen, "Polymer and organic solar cells viewed as thin film technologies: What it will take for them to become a success outside academia," *Solar Energy Materials and Solar Cells*, pp. 1–4, 2013, DOI: 10.1016/j.solmat.2013.05.032.

- [9] N. Espinosa, M. Hösel, D. Angmo, and F. C. Krebs, "Solar cells with one-day energy payback for the factories of the future," *Energy & Environmental Science*, vol. 5, no. 1, pp. 5117–5132, 2012.
- [10] P. P. Khlyabich, B. Burkhart, C. F. Ng, and B. C. Thompson, "Efficient Solar Cells from Semi-random P3HT Analogues Incorporating Diketopyrrolopyrrole," *Macromolecules*, vol. 44, no. 13, pp. 5079–5084, 2011.
- [11] J. Zhao, S. Bertho, J. Vandenberghe, G. Van Assche, J. Manca, D. Vanderzande, X. Yin, J. Shi, T. Cleij, L. Lutsen, and B. Van Mele, "Phase behavior of PCBM blends with different conjugated polymers," *Physical chemistry chemical physics : PCCP*, vol. 13, no. 26, pp. 12285–12292, 2011.
- [12] N. Espinosa, R. García-Valverde, A. Urbina, and F. C. Krebs, "A life cycle analysis of polymer solar cell modules prepared using roll-to-roll methods under ambient conditions," *Solar Energy Materials and Solar Cells*, vol. 95, no. 5, pp. 1293–1302, 2011.
- [13] T. R. Andersen, T. T. Larsen-Olsen, B. Andreasen, A. P. L. Böttiger, J. E. Carlé, M. Helgesen, E. Bundgaard, K. Norrman, J. W. Andreasen, M. Jørgensen, and F. C. Krebs, "Aqueous Processing of Low-Band-Gap Polymer Solar Cells Using Roll-to-Roll Methods," *ACS nano*, vol. 5, no. 5, pp. 4188–4196, 2011.
- [14] B. C. Thompson, P. P. Khlyabich, B. Burkhart, A. E. Aviles, A. Rudenko, G. V. Schultz, C. F. Ng, and L. B. Mangubat, "Polymer-Based Solar Cells: State-of-the-Art Principles for the Design of Active Layer Components," *Green*, vol. 1, pp. 29–54, 2011.
- [15] B. A. Gregg and M. C. Hanna, "Comparing organic to inorganic photovoltaic cells: Theory, experiment, and simulation," *Journal of Applied Physics*, vol. 93, no. 6, p. 3605-3615, 2003.
- [16] V. I. Arkhipov and H. Bässler, "Exciton dissociation and charge photogeneration in pristine and doped conjugated polymers," *Physica Status Solidi (a)*, vol. 201, no. 6, pp. 1152–1187, May 2004.
- [17] J. J. M. Halls, J. Cornil, R. Silbey, A. B. Holmes, J. L. Bre, and R. H. Friend, "Charge- and energy-transfer processes at polymer / polymer interfaces : A joint experimental and theoretical study," *Physical Review B*, vol. 60, no. 8, pp. 5721–5727, 1999.
- [18] G. Yu and a. J. Heeger, "Charge separation and photovoltaic conversion in polymer composites with internal donor/acceptor heterojunctions," *Journal of Applied Physics*, vol. 78, no. 7, p. 4510-4516, 1995.

- [19] N. S. Sariciftci, L. Smilowitz, A. J. Heeger, and F. Wudl, "Photoinduced electron transfer from a conducting polymer to buckminsterfullerene.," *Science*, vol. 258, no. 5087, pp. 1474–1476, 1992.
- [20] J.-L. Brédas, D. Beljonne, V. Coropceanu, and J. Cornil, "Charge-transfer and energy-transfer processes in pi-conjugated oligomers and polymers: a molecular picture.," *Chemical reviews*, vol. 104, no. 11, pp. 4971–5004, 2004.
- [21] S. Günes, H. Neugebauer, and N. S. Sariciftci, "Conjugated polymer-based organic solar cells.," *Chemical reviews*, vol. 107, no. 4, pp. 1324–1338, 2007.
- [22] G. Yu, J. Gao, J. C. Hummelen, F. Wudl, and A. J. Heeger, "Polymer Photovoltaic Cells - Enhanced Efficiencies Via A Network of Internal Donor-Acceptor Heterojunctions," *Science*, vol. 270, no. 5243, pp. 1789–1791, 1995.
- [23] Y. Yang, K. Mielczarek, M. Aryal, A. Zakhidov, and W. Hu, "Nanoimprinted polymer solar cell.," *ACS nano*, vol. 6, no. 4, pp. 2877–92, Apr. 2012.
- [24] C. Winder and N. S. Sariciftci, "Low bandgap polymers for photon harvesting in bulk heterojunction solar cells," *Journal of Materials Chemistry*, vol. 14, no. 7, pp. 1077–1086, 2004.
- [25] H. Spanggaard and F. C. Krebs, "A brief history of the development of organic and polymeric photovoltaics," *Solar Energy Materials and Solar Cells*, vol. 83, no. 2–3, pp. 125–146, 2004.
- [26] M.-S. Kim, B.-G. Kim, and J. Kim, "Effective variables to control the fill factor of organic photovoltaic cells," *ACS applied materials & interfaces*, vol. 1, no. 6, pp. 1264–1269, 2009.
- [27] G. Dennler, N. S. Sariciftci, and C. J. Brabec, "Conjugated Polymer-Based Organic Solar Cells," in in *Semiconducting Polymers: Chemistry, Physics and Engineering*, 2nd ed., G. Hadziioannou and G. G. Malliaras, Eds. Weinheim: WILEY-VCH Verlag GmbH & Co. KGaA, pp. 455–530, 2006, ISBN: 3-527-31271-4.
- [28] W. Shockley and H. J. Queisser, "Detailed Balance Limit of Efficiency of p-n Junction Solar Cells," *Journal of Applied Physics*, vol. 32, no. 3, p. 510-519, 1961.
- [29] T. Ameri, G. Dennler, C. Lungenschmied, and C. J. Brabec, "Organic tandem solar cells: A review," *Energy & Environmental Science*, vol. 2, no. 4, pp. 347–363, 2009.
- [30] M. C. Scharber, D. Mühlbacher, M. Koppe, P. Denk, C. Waldauf, A. J. Heeger, and C. J. Brabec, "Design Rules for Donors in Bulk-Heterojunction Solar Cells—Towards 10 % Energy-Conversion Efficiency," *Advanced Materials*, vol. 18, no. 6, pp. 789–794, 2006.

- [31] A. De Vos, "Detailed balance limit of the efficiency of tandem solar cells," *Journal of Physics D: Applied Physics*, vol. 13, no. 5, pp. 839–846, 1980.
- [32] A. L. Roes, E. A. Alsema, K. Blok, and M. K. Patel, "Ex-ante Environmental and Economic Evaluation of Polymer Photovoltaics," vol. 17, pp. 372–393, 2009.
- [33] J. Hou, H.-Y. Chen, S. Zhang, G. Li, and Y. Yang, "Synthesis, characterization, and photovoltaic properties of a low band gap polymer based on silole-containing polythiophenes and 2,1,3-benzothiadiazole," *Journal of the American Chemical Society*, vol. 130, no. 48, pp. 16144–16145, 2008.
- [34] M. Helgesen, J. E. Carlé, and F. C. Krebs, "Slot-Die Coating of a High Performance Copolymer in a Readily Scalable Roll Process for Polymer Solar Cells," *Advanced Energy Materials*, 2013, DIO: 10.1002/aenm.201300324.
- [35] N. Blouin, a. Michaud, and M. Leclerc, "A Low-Bandgap Poly(2,7-Carbazole) Derivative for Use in High-Performance Solar Cells," *Advanced Materials*, vol. 19, no. 17, pp. 2295–2300, 2007.
- [36] S. K. Lee, M. Cho, Y. Goo, S. Shin, and J. Lee, "Synthesis and characterization of a thiazolo [5 , 4-d] thiazole-based copolymer for high performance polymer solar cells," *chemical communications*, vol. 47, pp. 1791–1793, 2011.
- [37] R. García-Valverde, J. A. Cherni, and A. Urbina, "Life cycle analysis of organic photovoltaic technologies," *Progress in Photovoltaics: Research and Applications*, vol. 18, no. 7, pp. 535–558, 2010.
- [38] F. C. Krebs, "Fabrication and processing of polymer solar cells: A review of printing and coating techniques," *Solar Energy Materials and Solar Cells*, vol. 93, no. 4, pp. 394–412, 2009.
- [39] T. R. Andersen, Q. Yan, T. T. Larsen-Olsen, R. Søndergaard, Q. Li, B. Andreasen, K. Norrman, M. Jørgensen, W. Yue, D. Yu, F. C. Krebs, H. Chen, and E. Bundgaard, "A Nanoparticle Approach towards Morphology Controlled Organic Photovoltaics (OPV)," *Polymers*, vol. 4, no. 4, pp. 1242–1258, 2012.
- [40] T. T. Larsen-Olsen, B. Andreasen, T. R. Andersen, A. P. L. Böttiger, E. Bundgaard, K. Norrman, J. W. Andreasen, M. Jørgensen, and F. C. Krebs, "Simultaneous multilayer formation of the polymer solar cell stack using roll-to-roll double slot-die coating from water," *Solar Energy Materials and Solar Cells*, vol. 97, pp. 22–27, 2011.
- [41] T. T. Larsen-Olsen, T. R. Andersen, B. Andreasen, A. P. L. Böttiger, E. Bundgaard, K. Norrman, J. W. Andreasen, M. Jørgensen, and F. C. Krebs, "Roll-to-roll processed polymer tandem solar

- cells partially processed from water,” *Solar Energy Materials and Solar Cells*, vol. 97, pp. 43–49, 2011.
- [42] J. E. Carlé, T. R. Andersen, M. Helgesen, E. Bundgaard, M. Jørgensen, and F. C. Krebs, “A laboratory scale approach to polymer solar cells using one coating/printing machine, flexible substrates, no ITO, no vacuum and no spincoating,” *Solar Energy Materials and Solar Cells*, vol. 108, pp. 126–128, 2013.
- [43] T. R. Andersen, H. F. Dam, B. Andreasen, M. Hösel, M. V. Madsen, S. a. Gevorgyan, R. R. Søndergaard, M. Jørgensen, and F. C. Krebs, “A rational method for developing and testing stable flexible indium- and vacuum-free multilayer tandem polymer solar cells comprising up to twelve roll processed layers,” *Solar Energy Materials and Solar Cells*, 2013, DIO: 10.1016/j.solmat.2013.07.006.

2. Fabrication of inks with a pre-arranged morphology

2.1. Introduction

The optimal morphology of the active layer is of the utmost importance for the exciton dissociation into free charge carriers because of the limited diffusion length of excitons in organic materials as described in Section 1.2. Yang *et al.*[1], Coakley *et al.* [2] and Gonzalez-Valls *et al.*[3] presented two methods to obtain a promising morphology. Yang *et al.*[1] uses nano-imprinting of one of the components after which the other component is deposited on top ensuring an optimal phase separation, whereas Coakley *et al.* [2] and Gonzalez-Valls *et al.*[3] grew inorganic crystallites on the surface of the substrate in the optimal dimensions to be used as acceptor or transport pathways. These methods represent promising ways to obtain morphology control. They are, however, at this time not compatible with high-throughput R2R processing. The most commonly used method for improving the morphology is by self-assembly meaning that the two components are allowed to phase-separate without any direct control of the domain sizes. Self-assembly is usually achieved by 1) choice of coating solvent, [4-6] 2) thermal annealing, [4] 3) addition of additives to the coating ink, [7-9] and/or 4) solvent annealing.[10,11] Methods 1-3 are scalable with R2R coating whereas method 4 is more difficult since it requires the film to be subjected to solvent vapors for a longer period thereby decreasing the throughput.[11] A disadvantage with morphology optimizations by self-assembly is that they are basically working by controlling the diffusion rate in the film and therefore do not offer any direct control of the morphology in the film. Direct morphology control can be obtained by use of inks with a pre-organized structure. Previously, these have been prepared by two nanoparticle approaches first presented by Landfester[12] and Tkachov *et al.*[13]

A nanoparticle approach for preparation of OSC was presented by Landfester *et al.*[12,14,15] They prepared nanoparticles from a blend of two polymers via a micro-emulsion route where a polymer solution was mixed with an aqueous solution of sodium dodecyl sulfate (SDS), then treated with ultrasound and subsequently heated to remove residual organic solvent. The prepared nanoparticles offer morphology control on two levels.

Firstly the size of the particles can be controlled by varying the three main components in the particle formation i.e. SDS concentration, solvent volume, and polymer/PCBM concentration. Secondly, it offers the possibility to control the internal morphology in the particles between the donor and acceptor materials by changing either the polymer/acceptor system or possibly the solvent. The internal morphology of the nanoparticles have previously been determined to occur from the surface energy of the two components.[16,17] The photovoltaic performance of OSCs prepared from these inks were very poor with a maximum IPCE of 4.2 %.[15] The materials (Poly(9,9-dioctylfluorene-co-N,N-bis(4-butylphenyl)-N,N-diphenyl-1,4-phenylenediamine) (PFB) and Poly(9,9-dioctylfluorene-co-benzothiadiazole (F8BT)) used in these experiments are, however, not known for high-performing OSCs with PCEs of only 0.2 % in regular OSCs.[17]

A different approach was presented by Tkachov *et al.*[13,18] They prepare silica nanoparticles grafted by known organic polymers via polymerization directly from the surface of the silica nanoparticle by a Kumada polymerization. OSCs were prepared with silica particles grafted with P3HT together with PCBM (ratio 1:1) obtaining a PCE of 1.8-2.3 % for a 1 cm² device[18]. This efficiency is lower than the PCE usually obtained from a P3HT:PCBM device, especially the J_{sc} (between -5.5 and -6.8 mA cm⁻²) is reduced. A reason might be that a volume of the active material is lost due to the non-absorptive silica cores. It is responsible for 4.3 % of the weight of the grafted nanoparticles.[18] This could be compensated by coating a thicker film, which, however, can lead to a decrease in FF because of an increase in series resistance. Another reason could be the blue shift in the film absorption of the grafted polymers compared to “free” polymers, thereby reducing the photon absorption. One way to overcome the lower performance of the OSC would be to change the silica nanoparticle to a particle with a broader absorption thereby enhancing the J_{sc} . Silicon nanoparticles have a broader absorption than what is observed for silica and they can be synthesized through known pathway making them suitable for the exchange.[19-21]

In this chapter preparation of inks containing nanoparticles using these two different methods is presented: 1) Formation of organic nanoparticles containing both donor and acceptor in an aqueous dispersion, and 2) by grafting of organic molecules to silicon nanoparticles.

2.2. Aqueous nanoparticle inks

In addition to the promised morphology control the polymer nanoparticles also have the advantage of being formulated as an aqueous ink. This could help to overcome one of the challenges for the utilization of OSCs as energy source, i.e. the vast use of organic solvents during the fabrication process. State of the art OSC production uses chloroform, chlorobenzene etc. as coating solvents and they are considered not only harmful but also possibly carcinogenic, thus they need to be avoided. The elimination of organic solvents will additionally result in a lowering of the embodied energy of the OSCs. In Table 2.1 the embodied energies for five different solvents are listed. As seen chlorobenzene and acetone have by far the largest embodied energy and demineralized water have with 1 kilojoule per kilogram practically no embodied energy. Therefore a change from organic solvents to water is preferable.

Table 2.1. The embodied energy in kilojoule for demineralized water, acetone, isopropanol, methanol, and chlorobenzene. [22,23]

<i>Solvent</i>	<i>Volume/weight</i>	<i>Embodied energy (kJ)</i>
<i>Dem. Water</i>	1 kg	1.0-19.0
<i>Acetone</i>	1 kg	51,141.00
<i>Isopropanol</i>	1 kg	12,865.53
<i>Methanol</i>	1 kg	12,865.53
<i>Chlorobenzene</i>	1 kg	49,962.50

Yet another advantage of this nanoparticle approach compared to other methods for preparing aqueous inks, is that, it allows one to prepare nanoparticle inks from already known polymers without further modification. In other methods it is necessary to modify the side-chains of the polymers to enhance the polymers solubility in water with groups such as sulfonic acid, pyridinum, ammonium, nonionic alcohol or glycol side-chains.[24-27].

2.2.1. Ink formulation and characterization

2.2.1.1. General procedure for formulating aqueous nanoparticle inks

The aqueous inks were prepared according to the procedure presented by Landfester *et al.* [12,14,15,28] with minor variations. The materials (polymer and PCBM) was dissolved in an organic solvent to which an aqueous solution of SDS was added and the phases were allowed to form an emulsion for an hour with vigorous stirring. The emulsion was treated with ultrasound to form a micro-emulsion which was subsequently heated to remove the organic solvent. This resulted in an aqueous dispersion of organic nanoparticles, as illustrated in Figure 2.1. The dispersion was then dialyzed against demineralized water to remove excess SDS. The remaining dispersion was concentrated either by centrifugation in a dialysis centrifugation tube or concentrated by dialysis using large scale equipment, seen in Figure 2.2A and B, to a concentration of approximately 55-60 mg mL⁻¹. The sizes of the prepared nanoparticles were determined by either Small Angle X-ray Scattering (SAXS) in a capillary (measurements and data analysis were conducted by Arvid Pihl Lauritzen Böttiger and Jens Wenzel Andreassen from DTU Energy Conversion) or by Atomic Force Microscopy (AFM) on a sample prepared by spin-coating of a dilute dispersion on a mica-slide and measuring the height difference between the top of the nanoparticle and the mica-surface (measurements were conducted by Birgitta Andreasen (DTU) or myself).

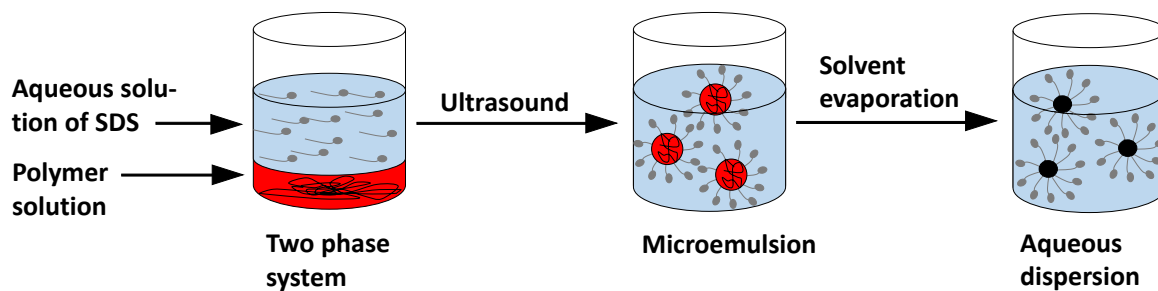


Figure 2.1: Schematic overview of the preparation of polymer nanoparticles dispersed in water. First a solution of polymer and/or PCBM is mixed with an aqueous solution of SDS. After a pre-emulsion by stirring, a micro-emulsion is formed upon ultrasonic treatment, and finally the solvent is removed by evaporation resulting in the nanoparticle dispersion.

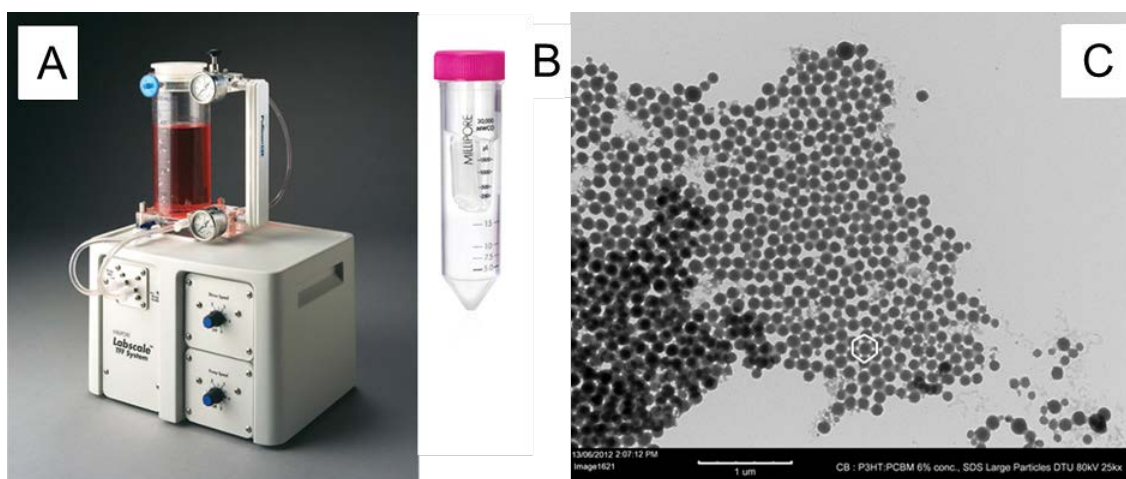


Figure 2.2. A) Shows a Transmission Electron Microscopy (TEM) image taken on an organic nanoparticle dispersion spin-coated on silicon nitride. (Picture taken by Natalie Patricia Holmes, University of Newcastle) B) Shows Millipore labScale tff system used for SDS-removal and concentration of large scale water based ink batches. C) Displays the centrifuge tube used for concentration of small ink batches, it contains a filter through which water can be removed (Pictures B and C are taken from <http://www.millipore.com>).

The structure of the organic nanoparticles was investigated by Transmission Electron Microscopy (TEM) of a spin-coated particle dispersion, the TEM image was prepared by Natalie Patricia Holmes from University of Newcastle. From the image in Figure 2.2C it can be seen that the nanoparticles (entry 6 in Table 2.2) appears as spherical with the ability to pack densely in a hexagonal structure as marked by the white line.

2.2.1.2. Preparation of aqueous nanoparticle inks with different polymers

The aim of this study was to prepare aqueous inks containing nanoparticles consisting of six different polymers each of them in a blend with PCBM as acceptor. The structures of the polymer, from now known as **P1-P5** and P3HT, are represented in Figure 2.3.

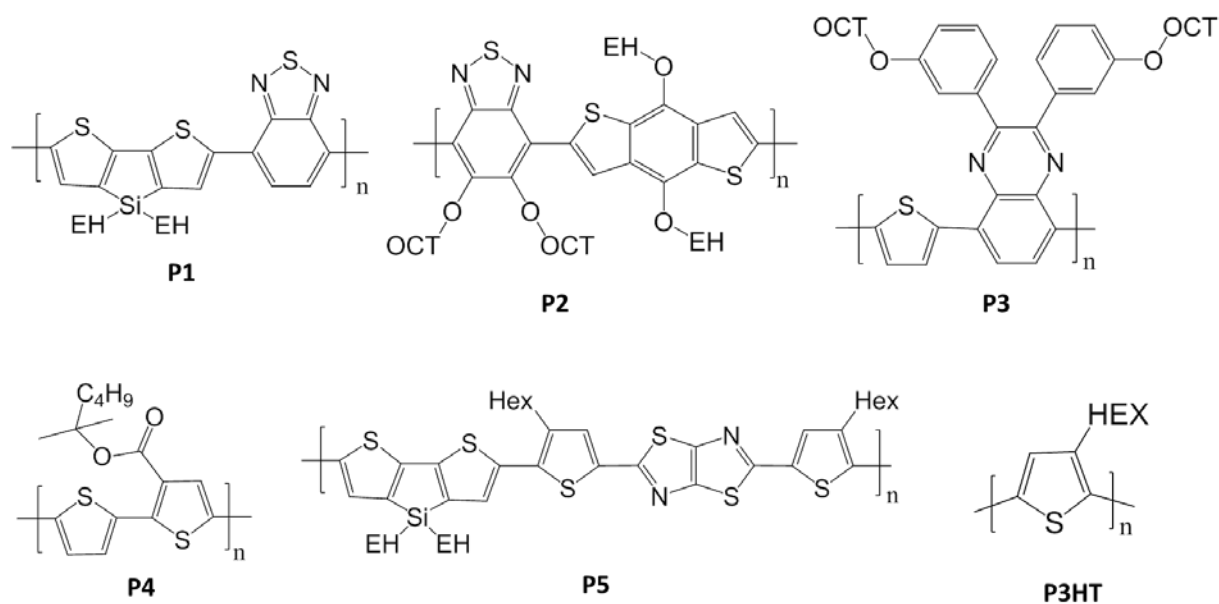


Figure 2.3. Schematic presentation of the six polymers, P1 [29], P2 [30], P3 [31], P4 [32], P5 [33], and P3HT from which nanostructured aqueous inks have been prepared. EH= 2-Ethylhexyl, OCT=Octyl, HEX=Hexyl.

The precise specifications for the prepared inks are shown in Table 2.2. Nanoparticles have been prepared using a variety of organic solvents from chloroform to a solvent mixture of *ortho*-dichlorobenzene and chloronaphthalene. Chloroform is the preferred solvent since the removal after sonication is significantly easier than experienced with a high boiling point solvent. However, the solubility of some polymers is in chloroform very limited, therefore use of other organic solvents were be a necessity.

During fabrication a large increase in temperature caused by the energy delivered by the booster horn during the ultrasonic treatment resulted in evaporation of the organic solvent. Evaporation of the solvent was mainly a problem when using chloroform as preparation solvent. This evaporation was counteracted by decreasing the effect of the booster horn from

900 W to 650 W for nanoparticles prepared in later batches. An operational effect at 650 W was, however, found to be inadequate to obtain homogenous ultrasonic treatment when preparing large scale nanoparticle dispersions such as the last entry in Table 2.2. The size of the obtained nanoparticles varies even though similar formulation parameters were used. This variation is ascribed to physical properties of the different polymers such as the ability to form coils, which is the case for P3HT,[34-37] or the molecular weight of the polymers.

Table 2.2. Production specifications of the ink batches prepared. These batches are selected because it was possible to prepare functioning OSC from them. SDS concentration was unless stated otherwise 30 g/L, sizes were determined by SAXS, solvent abbreviations are chloroform (CF), chlorobenzene (CB), *ortho*-dichlorobenzene (*o*-DCB), and chloronaphthalene (CN).

<i>Polymer</i>	<i>Solid weight (mg)</i>	<i>Solvent</i>	<i>Volume solvent (mL)</i>	<i>Aqueous SDS solution (mL)</i>	<i>Ultrasonic treatment</i>	<i>Size (nm)</i>
P1	730	CF	17.5	50	5.0 min, 900 W	32
P1¹	100	CF	5.3	9.3	5.0 min, 650 W	NA
P2	380	CF	8.9	25	5.0 min, 900 W	130
P3	650	CF	15.5	50	5.0 min, 900 W	87
P4	2,000	CF	45.2	133	2.5 min, 900 W	59
P5	400	CB	20	40	5.0 min, 650 W	NA
<i>P3HT</i>	8,000	CF	181	480	6.5 min, 900 W	46
<i>P3HT</i>	600	CB	15	50	4.0 min, 650 W	NA
<i>P3HT</i>	600	<i>o</i> -DCB	15	50	4.0 min, 650 W	NA
<i>P3HT</i>	10,000	<i>o</i> -DCB ² (CN)	500 (10)	1,000	1 min, 650 W +4 min, 1000 W	NA

¹particles prepared to have a wide size distribution to be used for studies of the internal morphology. Concentration of the aqueous SDS solution was 0.36 g L⁻¹.

²solvent mixture of *ortho*-dichlorobenzene (500 mL) and chloronaphthalene (10 mL)

2.2.1.3. Internal morphology of the nanoparticles

The internal morphology of nanoparticles prepared with a blend of **P1** or P3HT with PCBM were investigated by X-ray and TEM analysis. Nanoparticles used for the morphology investigations were prepared at DTU whereas preparation of samples, conduction of experiments and data-analysis of the X-ray experiments were prepared by Henrik Friis Dam (DTU) and Natalie Patricia Holmes (University of Newcastle).

The particles presented in section 2.2.1.2 consists of two different materials a donor and an acceptor component, which give them a structured internal morphology. Two main theories have been introduced regarding the internal morphology of particles of this kind; 1) a Janus structure morphology[38] or 2) a core-shell structure.[16,39] The phrase Janus structure comes from the ancient Roman religion where Janus is a two faced God, having a Janus structure is therefore an expression for the two components forming two pure phases in the nanoparticles. The Janus structured morphology was presented by Kietze *et al.*[15], their theories were built on TEM images of particles containing a polystyrene and poly(propylene carbonate) blend. Particular systems containing PFB:F8BT and P3HT:PCBM were investigated using Scanning Transmission X-ray Microscopy (STXM) by Dastoor *et al.* [16,39] They suggested a core-shell structure for both systems, meaning that the core is enriched by one component and the shell of the particle by the other component. Since the blended particles presented in this thesis do not contain materials which exhibits a large contrast in TEM, the internal morphology was investigated by STXM.[16,40]

A Near-Edge X-ray Absorption Fine Structure (NEXAFS) spectrum was taken of pure sample of each material to detect the absorption peaks for the components in order to separate the main components in the nanoparticle from each other. Characterization of the main components in the nanoparticles was done on the basis of a STXM image acquired with the two different energies from the NEXAFS experiment chosen for maximum contrast. The image was then analyzed by deconvoluting the amount of each component in each pixel.

NEXAFS spectra

After the NEXAFS line scan across the edge of the sample, the intensities were normalized to account for the background, the resulting spectra was further normalized based on a calculated absorption spectra for the components, obtained from online solid X-ray filter tables.[41,42]

The normalized spectra from **P1** and P3HT are plotted in Figure 2.4A and B, together with the PCBM reference. From the two spectra, energies with a suitable contrast between polymer and PCBM can be found. The energies for STXM were chosen to be 284.5 eV and 287.4 eV for both nanoparticle inks.

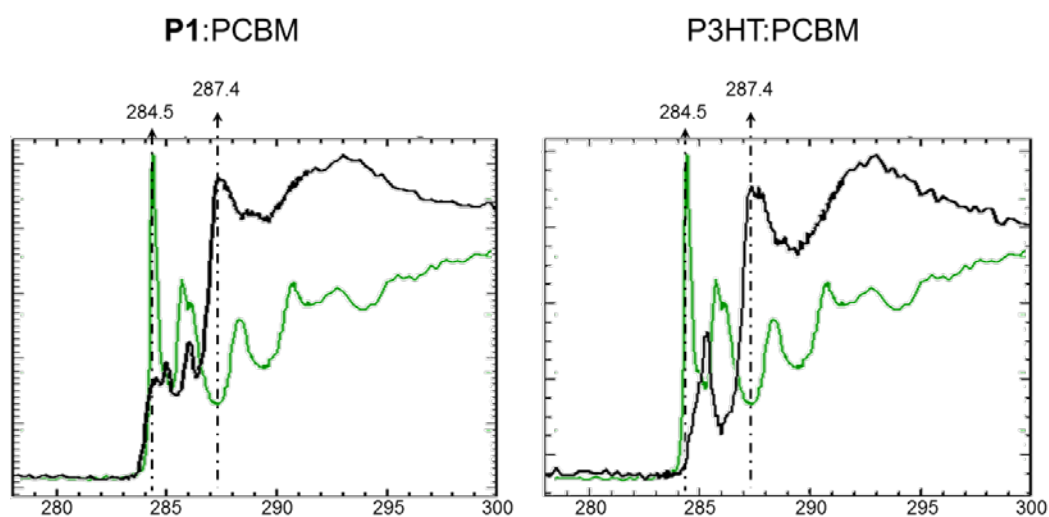


Figure 2.4. Normalized absorption spectra for the reference samples prepared and the two selected energies used for the STXM scan. A) Black is the P1 reference, B) Black is the P3HT reference, and green is the PCBM reference for both spectra.

STXM

STXM measurements were conducted on nanoparticle clusters by scanning with one of the chosen energies, changing to the other energy and then scanning the same cluster. The analysis of the nanoparticle-clusters was completed using the techniques described by Burke *et al.*[16]

The relative mass densities obtained from the STXM measurement for **P1** and PCBM are shown in Figure 2.5, together with a TEM image of the same cluster taken after the X-ray studies. The TEM image shows spherical particles that can easily be distinguished from each other (Figure 2.5C). The relative mass compositions of the cluster show a sample with an indication of a core-shell structure, as seen by the high-intensity areas in the rim of the particles in Figure 2.5A. The intensity is seen primarily being in the center of the particles in Figure 2.5B. This indicates a nanoparticle where the shell have a high concentration of **P1** and the core consists primary of PCBM.

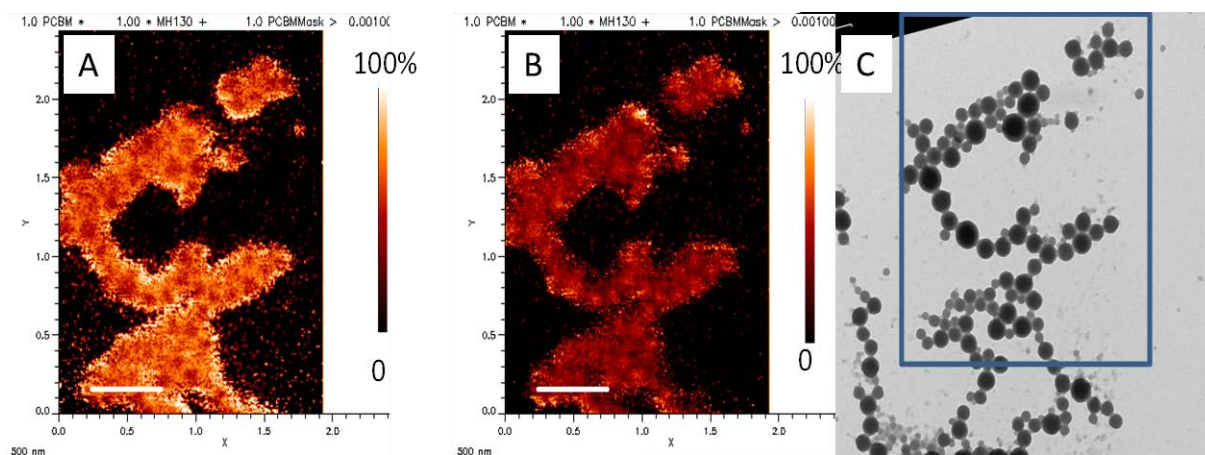


Figure 2.5. Cluster 1: Composition of P1:PCBM nanoparticles from STXM. A) Relative mass composition of P1 to the total mass. B) Relative mass composition of PCBM to the total mass. C) TEM image of nanoparticle cluster taken after STXM imaging. Mass composition plots are shown on a black to white color scale.

STXM images of two different clusters consisting of P3HT:PCBM, using chlorobenzene as preparation solvent, are presented in Figure 2.6 and Figure 2.7. The TEM-image in Figure 2.6C shows a cluster of nanoparticles with a few larger particles surrounded by a number of smaller particles. The particles are fused together which is different from the nanoparticles of **P1**:PCBM shown in Figure 2.5C. The mass content of the components P3HT and PCBM can be seen in Figure 2.6A and B, respectively. The images shows signs of core-shell structure with a higher concentration of P3HT in the shell and a core consisting primarily of PCBM.

The images in Figure 2.7 show another nanoparticle-cluster with a greater size variation than the cluster in Figure 2.6 and in a larger view. The TEM image captures the same ten-

density where nanoparticles are fused together. The relative mass composition images (Figure 2.7A and B) shows, unlike the previous cluster, no clear signs of a core-shell structure, with the relative density of the components more evenly distributed.

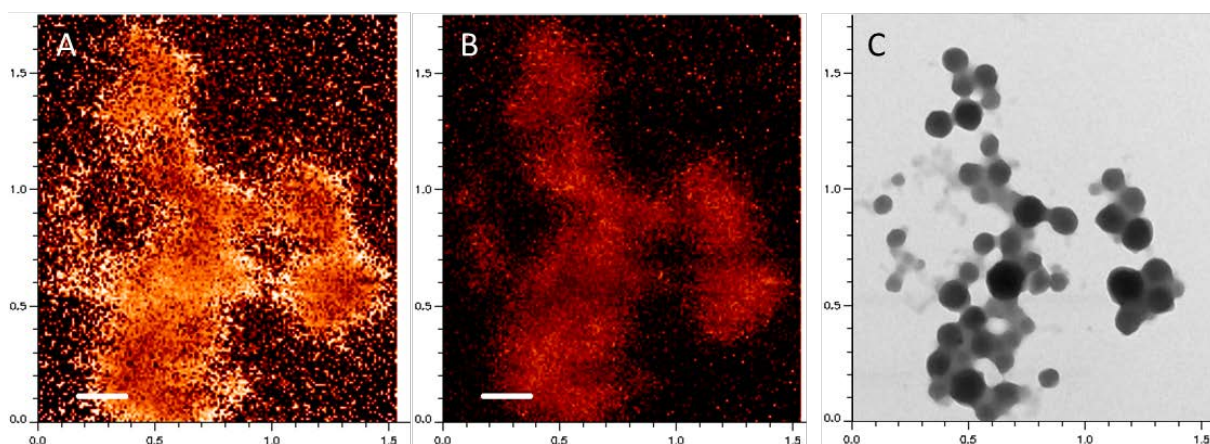


Figure 2.6: Cluster 1: Composition of P3HT:PCBM nanoparticles from STXM. A) Relative mass composition of P3HT to the total mass. B) Relative mass composition of PCBM to the total mass. C) TEM image of nanoparticle cluster taken after STXM imaging. Mass composition plots are shown on a black to white color scale.

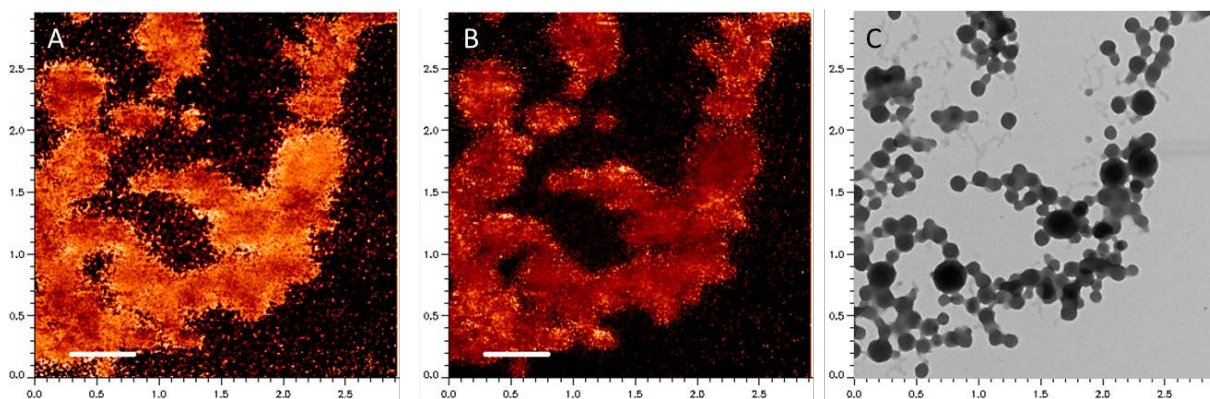


Figure 2.7. Cluster 2: Composition of P3HT:PCBM nanoparticles from STXM. A) Relative mass composition of P3HT to the total mass. B) Relative mass composition of PCBM to the total mass. C) TEM image of nanoparticle cluster taken after STXM imaging. Mass composition plots are shown on a black to white color scale.

The STXM images, based on the experiments and analysis conducted by Natalie Holmes and Henrik Friis Dam, indicated both nanoparticles formulations to have obtained a core-shell morphology with a core consisting primarily of PCBM and the shell having a high concentration of polymer. A more detailed schema presenting the actual ratio between the two components are at this time under development.

2.2.1.4. Size-control experiments

The ability to control the size of the prepared nanoparticles is important for two reasons; 1) it can be a method to control the maximum domain size for the components within the particle thereby allowing all generated excitons to reach a donor/acceptor interface for dissociation into free charge carriers. 2) It can be a method to ensure that the number of particle “monolayers” stacked on top of each other is large enough for the film to be completely covering without the film thickness surpassed a reasonable range (below 1 μm).

The size of the prepared nanoparticles should in general be determined by the micelle size and the concentration of the organic material inside the formed micelle. A micelle is the structure formed by SDS dissolved in water in order to diminish the interaction between water and the aliphatic chains. The micelle size and form can be controlled by the concentration of SDS, temperature, pH, and ionic strength of the solution.[43] In order to vary the micelle sizes the focus was decided to be on SDS concentration since it is the parameter easiest to control. Temperature control is more difficult since ultra-sonication causes the temperature of the dispersion to increase which may increase the size of the micelle. The PH and the ionic strength of the solution was assumed to be similar when preparing the SDS-solutions within minutes from demineralized water prepared at the set up at DTU.

Micelles with varying concentration of organic material was prepared by two different methods; 1) controlling the volume of the organic solvent and assuming that the size of the micelles remains constant and that the solid particles shrinks into a dense “ball”. 2) Varying the solid concentration while keeping a constant ratio between solvent and SDS solution. Thereby lowering the risk of size variation in the formed micelles between experiments. Results from the size-control experiments are shown in Table 2.3 to Table 2.5.

The concentration of SDS has an influence on the size of the micelle because the micelle is only formed when there is at least a monolayer of SDS on the surface of the “oil” component (organic solution). Therefore, a higher SDS content will have the possibility for SDS to cover a larger surface area thereby reducing the diameter of each micelle. When the SDS concentration is varied between 18 g L^{-1} and 35 g L^{-1} using 6 g L^{-1} steps, there appears to be no variation in the obtained sizes, which are between 65 nm and 69 nm without a specific tendency (Table 2.3). This can be ascribed to the development of the average aggregation number. It describes the number of the SDS molecules used to form each micelle and it is increasing along with the SDS concentration.[43] Taking this into account this experiment revealed that the SDS concentrations could have been over the threshold where the SDS-concentration has great influence, although Landfester previously have claimed otherwise[28].

Table 2.3. Specifications for the nanoparticles fabricated with varying SDS concentration while keeping amount of organic material and volume of chloroform and aqueous SDS solution constant. Sizes of the obtained nanoparticles measured by SAXS.

<i>SDS concentration (g/L)</i>	<i>P3HT :PCBM (mg)</i>	<i>Chloroform (mL)</i>	<i>Aqueous SDS solution (mL)</i>	<i>Ultrasonic treatment</i>	<i>Size (nm) SAXS</i>
18	600	15	50	4 min, 650 W	65
24	600	15	50	4 min, 650 W	66
30	600	15	50	4 min, 650 W	69
35	600	15	50	4 min, 650 W	67

In Table 2.4 the formulation parameters and sizes for nanoparticles prepared with a variation in the volume of chloroform. The variation resulted only in a small difference in the obtained sizes, i.e. when using a small amount of solvent an increase in size of the obtained nanoparticles is observed. The size increases from between 42-45 nm to 61 nm when decreasing the volume of chloroform from 5-10 mL to 2.5 mL as seen in

Table 2.4. This indicates that there might be a correlation between particle size and volume of chloroform used. Further, a threshold might be present after which the particle size becomes independent.

Table 2.4. Specifications for the nanoparticles fabricated with varying amount of chloroform while keeping a constant volume and concentration of aqueous SDS solution. Sizes of the obtained nanoparticles measured by SAXS.

<i>Chloroform (mL)</i>	<i>PCBM (mg)</i>	<i>Aqueous SDS so- lution(mL)</i>	<i>Ultrasonic treatment</i>	<i>Size (nm) SAXS</i>
2.5	100	15	4 min, 650 W	61
5.0	100	15	4 min, 650 W	43
7.5	100	15	4 min, 650 W	45
10.0	100	15	4 min, 650 W	42

The parameter, which seems to have the largest effect on the particle size, is the variation of the amount of organic material while keeping the ratio between chloroform and the aqueous SDS solution constant. There were an increase in particle size from 7 nm to 18 nm when keeping the amount of solid constant while decreasing the chloroform volume from 20 to 10 mL and SDS volumes from 40 to 20 mL, respectively as seen in Table 2.5 (AFM images can be found in Appendix 1). The size given in this experiment was determined by AFM instead of SAXS. This change in method for size determination makes it impossible to compare the size with sizes obtained from the other experiments.

Table 2.5. Specifications for the nanoparticles fabricated with varying concentration of organic material while keeping a constant ratio between chloroform and aqueous SDS solution. Sizes of the obtained nanoparticles measured by AFM.

<i>P3HT:PCBM</i> (mg)	<i>Chloroform</i> (mL)	<i>Aqueous SDS</i> <i>solution(mL)</i>	<i>Ultrasonic</i> <i>treatment</i>	<i>Size (nm)</i> <i>AFM</i>
200	5	10	5 min, 650 W	NA
200	10	20	5 min, 650 W	18
200	15	30	5 min, 650 W	12
200	20	40	5 min, 650 W	7

From the experiments and results introduced in Table 2.4 and especially Table 2.5 it is shown that it is possible to vary the size of the obtained particles by varying the concentration of organic material inside the micelle. Trying to prepare smaller micelle by increasing the SDS concentration did not seem to have any effect, therefore, the micelle size is either already at a minimum or there is another unknown parameter controlling the size possibly connected to physical properties of the organic solution such as surface tension.

2.3. Grafting of nanoparticles for morphology control

Grafting of organic polymers onto the surface of inorganic nanoparticles as a method to achieve morphology control in OSCs was originally presented by Tkachov *et al.*[13,18,44]. As described in section 2.1 OSCs prepared from inks containing these particles performed worse compared to “normal” P3HT:PCBM device, due to a lower J_{SC} . This could be overcome by enhancing the absorption by changing the nanoparticle from silica to silicon. The band gap of a silicon nanoparticles is largely depended on the size, increasing the size pushes the absorption towards longer wavelengths (decreases the band gap).[19] From this size dependence one might be encouraged to prepare large silicon nanoparticles (100 nm) and thereby ensure a higher absorption. This would however just introduce a new set of problems since densely packed films are necessary to avoid possible shorting. For a densely

packed film to be formed a number of particles to be stacked on top of each other is required.

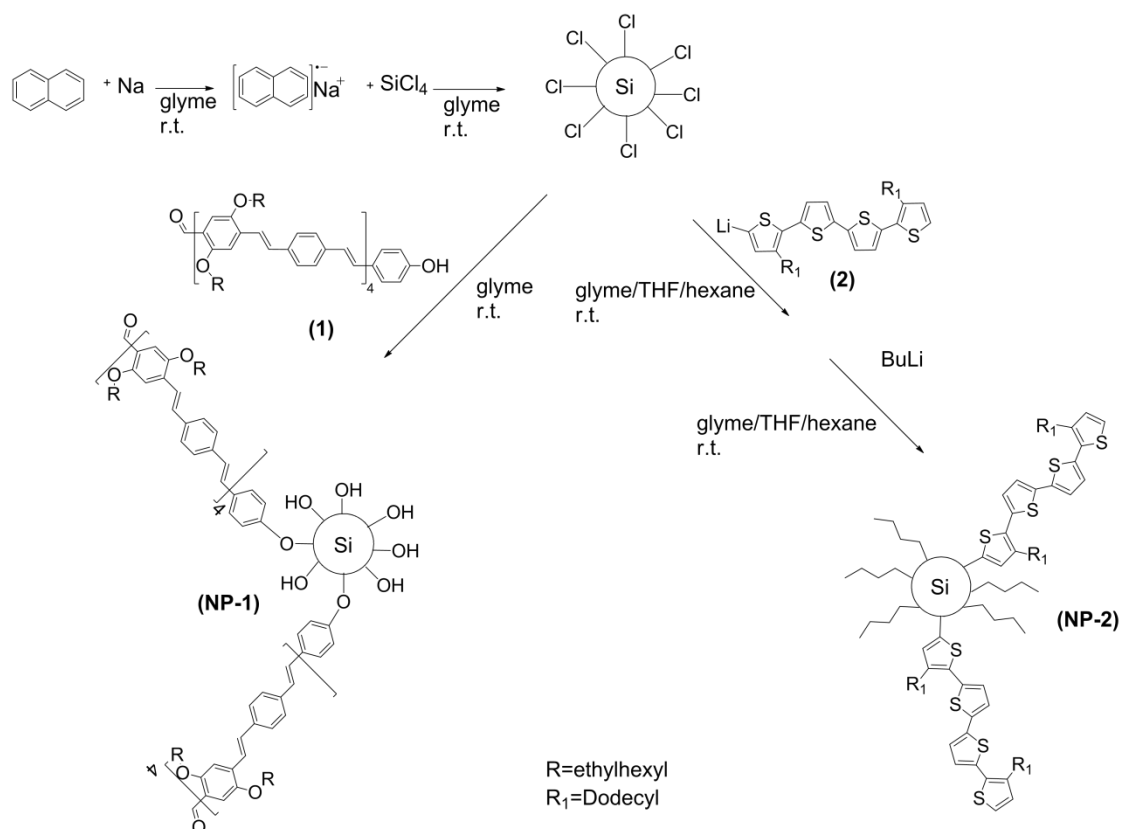
The following section describes the synthesis and grafting of silicon nanoparticles with an organic phenylene vinylene oligomer, characterization of the grafted nanoparticles and OSC performance. The nanoparticles grafted with tetrathiophene, **NP-2**, were provided by Yan Quanziang (Zhejiang University).

2.3.1. Synthesis and grafting of silicon nanoparticles

The synthesis of silicon nanoparticles were conducted by a Würtz reaction of tetrachlorosilane with sodium-naphthalene similar to that used by others.[19-21,45] Size control of silicon nanoparticles prepared via this reaction can be obtained by controlling the (tetrachlorosilane)/(sodium-naphthalene) ratio. It is expected that a higher ratio will result in larger particles. [19] The preparation procedure was based on a procedure described by Baldwin *et al.*[20] where they prepare tetrahedrally shaped nanoparticles with a length of around 50-70 nm and a width of 25 nm.

Grafting of organic molecules onto the surface of a silicon nanoparticle have previously been carried out by adding the organic grafting agent at the end of the nanoparticles synthesis. Different active groups have been used for this grafting procedure, such as hydroxy-groups and organic lithium molecules.[20,21] Hydroxy-groups have previously been used for grafting aliphatic molecules on the surface as a stabilizer.[21] It has, however, not been possible to find literature where aromatic molecules have been grafted to the surface using a hydroxy-group. Therefore, preliminary experiments using meta-cresol as grafting agent was conducted to ensure the possibility of grafting with a phenol as the active group. A detailed description and results from these experiments can be found in Appendix 2.4 including purification experiments. $^1\text{H-NMR}$ (nuclear magnetic resonance) spectra was used to ensure that meta-cresol was covalently linked to the silicon particles by the disappearance of the hydroxy signal from the phenol-group after grafting.

Early experiments with preparing grafted silicon nanoparticles for OSCs were conducted with an in-house prepared organic phenylene-vinylene oligomer **1**[46] shown in Scheme 2.1 together with the preparation steps. During purification of the nanoparticles a large amount was lost due to irreversible precipitation.



Scheme 2.1. Preparation of silicon nanoparticles and the grafting using organic oligomers. NP-2 was prepared by Yan Quanziang from ZJU.

2.3.2. Characterization

The grafted particles **NP-1** have been submitted to a structural, optical and photovoltaic characterization by means of ¹H-NMR, absorption spectroscopy, and AFM microscopy.

As shown in Figure 2.8 the ¹H-NMR for **NP-1** contains the same main signals as for **1**, both the aromatic (6.5-7.5 ppm) and aliphatic (0.75-2 ppm) protons can be found. The hydroxy group at the end of **1** is found at 4.75 ppm as a singlet which as expected had the same integrated area as the aldehyde peak around 10.5 ppm. The shift of a phenol proton in ¹H-NMR can in general be found between 4.2 and 9 ppm[47] it is largely depended on the solvent and

neighboring groups. This shift have for 4-phenylphenol dissolved in CDCl_3 previously been reported at 4.80 ppm[48] it is therefore a distinct possibility that the peak at 4.75 ppm is the shift from the phenol. Evaluating the $^1\text{H-NMR}$ obtained from **NP-1** reveals a similar signal at 4.85 ppm, integrating the area under the peak gave an area of 15 % of that from the aldehyde signal. There is a number of other peaks from 4 to 7 ppm which was also examined none of these showed the expected singlet splitting, it is therefore unlikely that these peaks results from the hydroxy-group. From the obtained $^1\text{H-NMR}$ spectra it is therefore concluded that the grafting process was successful but also that the purification may have been less successful in removing excess oligomers.

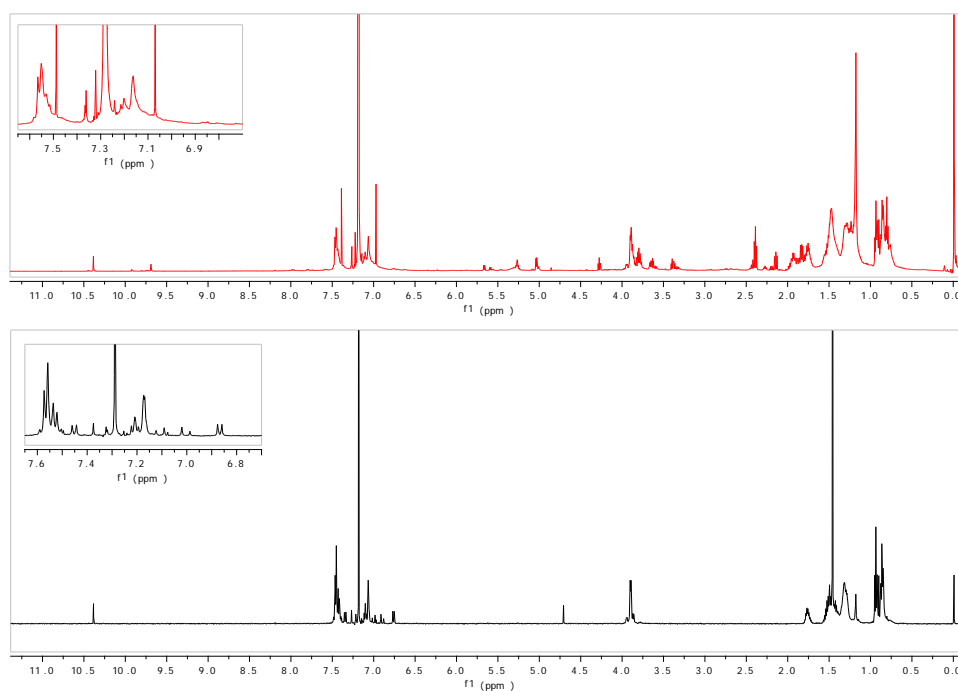


Figure 2.8 . $^1\text{H-NMR}$ spectra of the **1 (bottom/black) and **NP-1** (top/red).**

Absorption spectra obtained from a chloroform solution, reveal a small blue-shift from 460 nm to 456 nm (Figure 2.9) after grafting of oligomer **1** onto the nanoparticles. Senkovskyy *et al.*[18] had previously presented absorption data where they observed a red shift in the absorption for P3HT after grafting on to silica particles also obtained from a chloroform solution. This was, however, on larger particles (460 nm). Absorption data for small nanoparticles (4 nm) on a film had a blue shift in comparison to the ungrafted P3HT film. They as-

cribed this blue-shift to polymer packing issues when using smaller nanoparticles. A schematic illustration of the packing issues is shown in Figure 2.9 where molecules grafted on the surface of a smaller nanoparticle have a larger distance to their neighbour than when grafted on to a larger nanoparticle, thereby having less π stacking.

Another difference in absorption between **1** and **NP-1** is observed when going towards shorter wavelengths. The absorption for **1** decreases towards 250 nm, whereas the absorption for **NP-1** continues to increase in this region, this effect is due to silicon nanoparticles absorption.[45]

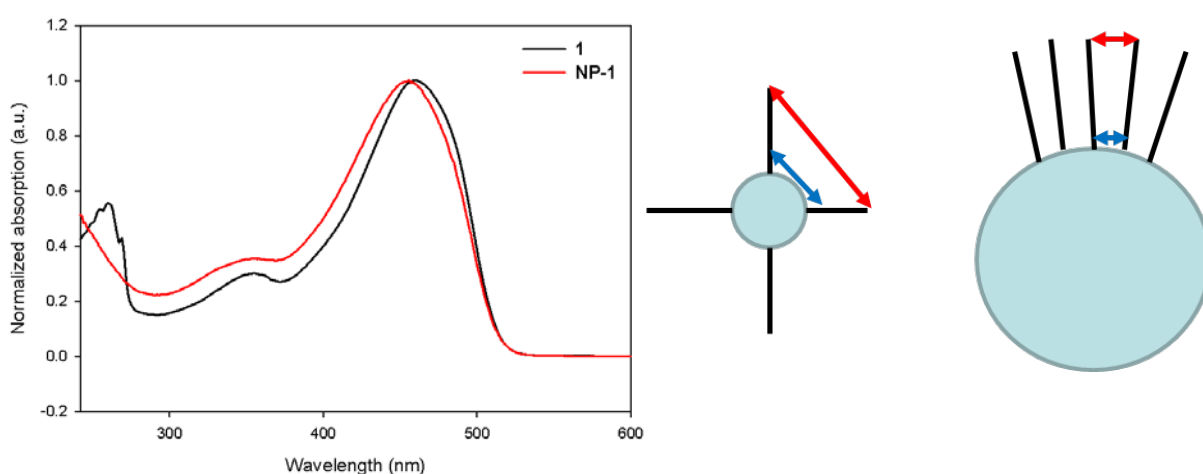


Figure 2.9. Normalized absorption spectra of the pure oligomer (black line) and the grafted oligomer (red line) both dissolved in chloroform (left). Packing of grafted molecules on to particles of two different sizes (right).

A film of **NP-1** coated on mica-slides was mapped out by AFM and the size was determined by measuring the height of the particles. On the AFM image (Figure 2.10A) a monolayer of particles is seen, this makes the size determination by height valid. The size distribution of the two different types of particles (**NP-1** and **NP-2**) is shown in Figure 2.10B. The average particle size for **NP-1** is around 7 nm with a narrow size distribution with most particles being below 10 nm. These particles are much smaller than what was previously observed by Baldwin *et al.* presenting tetrahedrally shaped nanoparticles as large as 60x25 nm.[20] The sizes measured for **NP-1** agrees with the observed blue-shift in Figure 2.9.

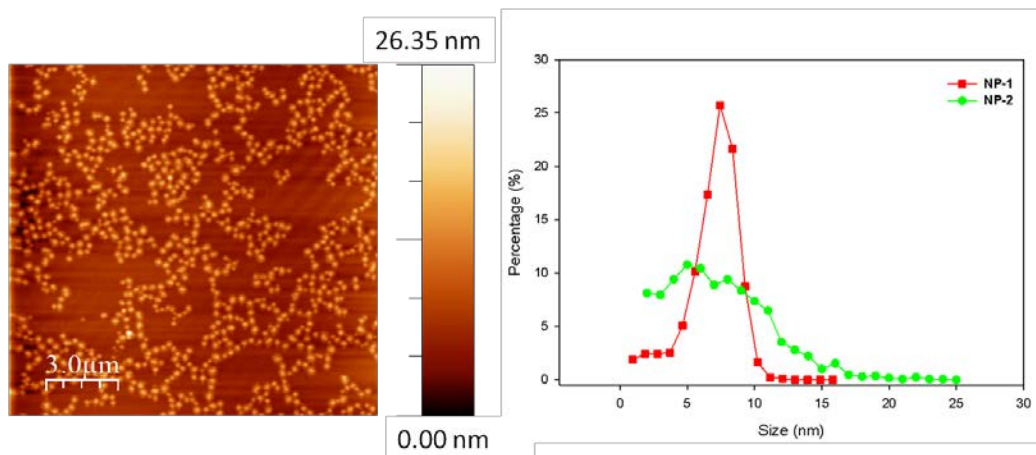


Figure 2.10. A) An AFM image of NP-1 on mica (prepared by Donghong Yu, AAU), B) The size distribution obtained from the AFM images of NP-1 and NP-2 (analysis prepared by Birgitta Andreasen, DTU Energy Conversion).

OSCs were prepared by spin-coating with the pure oligomer (**1** or **2**), **NP-1**, or **NP-2** in a 1:1 ratio with PCBM. The efficiency for **NP-1** was lower than what was obtained with **1** giving PCE of 0.27 % and 0.71 %, respectively, whereas functional devices were not obtained for **NP-2** and **2**.

The macroscopic morphology of the obtained film was investigated by AFM of a spin-coated film of **NP-1** or **1** with PCBM (ratio 1:1). The film shown in Figure 2.11A consists of **1** and PCBM and shows a rather smooth film having a Z-range of 33 nm with few defects. The AFM-analysis shown in Figure 2.11B is on a **NP-1**:PCBM film, it shows a film containing a number of pinholes in the coated film making preparation of well-functional OSCs difficult.

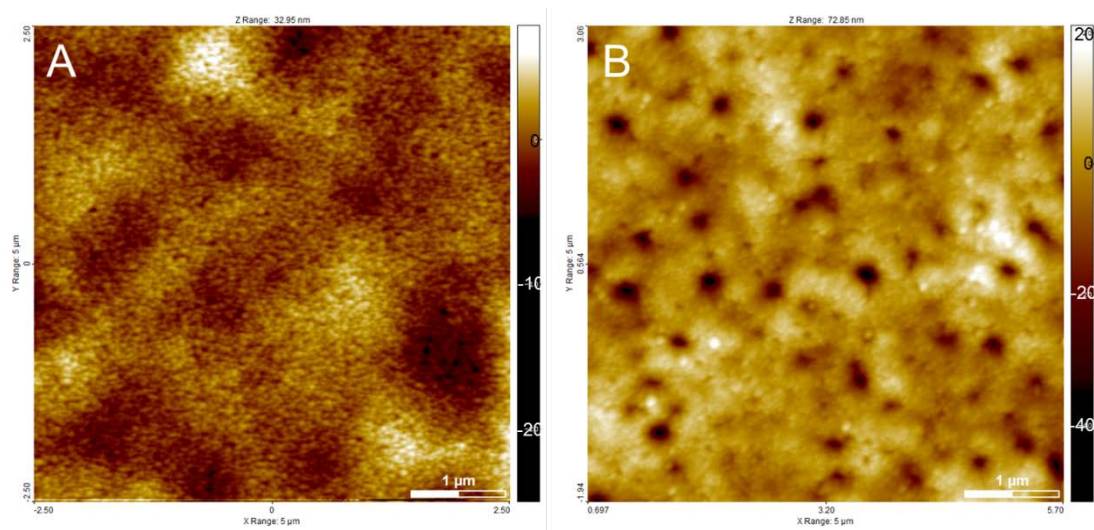


Figure 2.11. AFM images of a spin coated film of A) 1 in a 1:1 ratio with PCBM, B) NP-1 in a 1:1 ratio with PCBM.

2.4. Summary

Preparation of aqueous inks have been further developed from the first papers by Landfester *et al.* to be applied on several polymer:PCBM systems all of them resulting in a nanoparticles dispersion in water. Particles prepared using different polymers, but with the similar preparation conditions gave very different sizes (32-132 nm) indicating that physical properties of the polymer have great influence on the particle size.

The morphology of the nanoparticles were studied on particles prepared from two of the polymers (**P1** and P3HT) otherwise used to prepare aqueous inks in a 1:1 ratio with PCBM. The morphology study was conducted by STXM. The resulting image for a **P1**:PCBM blend prepared from chloroform shows signs of a core-shell structure with a **P1** rich shell and a PCBM rich core. Similar results were obtained for a P3HT:PCBM blend prepared from chlorobenzene, although the results were less clear, and these nanoparticles displayed a tendency towards agglomeration. The morphology studies shows that it is possible to prepare nanoparticles with a pre-arranged internal morphology.

Size control of the prepared nanoparticles can be essential to obtain the optimal internal morphology, this led to investigations of particles sizes using different preparation parame-

ters i.e. SDS-concentration, amount of organic solvent, and concentration of organic material. Nanoparticles prepared with four different SDS-concentrations showed no difference in the size for the prepared particles. Varying either the amount of organic solvent or the concentration of organic material resulted in particles with a variation in size. Nanoparticles prepared with a decreasing amount of organic solvent while keeping the same amount of both aqueous SDS solution and organic material constant, seemed only to have an effect i.e. increases size, when using a small amount of organic solvent. Preparation of nanoparticles with a variation in concentration of organic material on the other hand resulted in particles with decreasing size when decreasing the concentration of the organic material.

Silicon-nanoparticles were grafted with a small organic molecule with the aim to fabricate OSCs with a controlled morphology. The grafting process of the organic molecules onto the silicon-nanoparticles was successful as shown by $^1\text{H-NMR}$. The size of the grafted nanoparticles were measured to be around 7 nm which is smaller than expected with the preparation conditions applied. The OSC performance for the prepared materials in a 1:1 blend PCBM were low with a PCE of 0.27 % for **NP-1** compared to 0.71 % for **1**. Based on the low efficiency of the OSC and the loss of material during purification, it was concluded that this method is not compatible with large scale OSC fabrication.

2.5. References

- [1] Y. Yang, K. Mielczarek, M. Aryal, A. Zakhidov, and W. Hu, "Nanoimprinted polymer solar cell.," *ACS nano*, vol. 6, no. 4, pp. 2877–2892, 2012.
- [2] K. M. Coakley and M. D. McGehee, "Photovoltaic cells made from conjugated polymers infiltrated into mesoporous titania," *Applied Physics Letters*, vol. 83, no. 16, p. 3380-3382, 2003.
- [3] I. Gonzalez-Valls, D. Angmo, S. A. Gevorgyan, J. Sebastián Reparaz, F. C. Krebs, and M. Lira-Cantu, "Comparison of two types of vertically aligned ZnO NRs for highly efficient polymer solar cells," *Journal of Polymer Science Part B: Polymer Physics*, vol. 51, no. 4, pp. 272–280, 2013.
- [4] A. J. Moulé and K. Meerholz, "Morphology Control in Solution-Processed Bulk-Heterojunction Solar Cell Mixtures," *Advanced Functional Materials*, vol. 19, no. 19, pp. 3028–3036, 2009.

- [5] M. T. Rispens, A. Meetsma, R. Rittberger, C. J. Brabec, and N. S. Sariciftci, "Influence of the solvent on the crystal structure of PCBM and the efficiency of MDMO-PPV : PCBM ' plastic ' solar cells," *chemical communications*, pp. 2116–2118, 2003.
- [6] M. Al-Ibrahim, O. Ambacher, S. Sensfuss, and G. Gobsch, "Effects of solvent and annealing on the improved performance of solar cells based on poly(3-hexylthiophene): Fullerene," *Applied Physics Letters*, vol. 86, no. 20, p. 201120-201123, 2005.
- [7] B. R. Aïch, J. Lu, S. Beaupré, M. Leclerc, and Y. Tao, "Control of the active layer nanomorphology by using co-additives towards high-performance bulk heterojunction solar cells," *Organic Electronics*, vol. 13, no. 9, pp. 1736–1741, 2012.
- [8] F. Zhang, K. G. Jespersen, C. Björström, M. Svensson, M. R. Andersson, V. Sundström, K. Magnusson, E. Moons, a. Yartsev, and O. Inganäs, "Influence of Solvent Mixing on the Morphology and Performance of Solar Cells Based on Polyfluorene Copolymer/Fullerene Blends," *Advanced Functional Materials*, vol. 16, no. 5, pp. 667–674, 2006.
- [9] Y. Yao, J. Hou, Z. Xu, G. Li, and Y. Yang, "Effects of Solvent Mixtures on the Nanoscale Phase Separation in Polymer Solar Cells," *Advanced Functional Materials*, vol. 18, no. 12, pp. 1783–1789, 2008.
- [10] H. Li, H. Tang, L. Li, W. Xu, X. Zhao, and X. Yang, "Solvent-soaking treatment induced morphology evolution in P3HT/PCBM composite films," *Journal of Materials Chemistry*, vol. 21, no. 18, p. 6563-6568, 2011.
- [11] J. Peet, M. L. Senatore, A. J. Heeger, and G. C. Bazan, "The Role of Processing in the Fabrication and Optimization of Plastic Solar Cells," *Advanced Materials*, vol. 21, no. 14–15, pp. 1521–1527, 2009.
- [12] K. Landfester, "The Generation of Nanoparticles in Miniemulsions," *Advanced Materials*, vol. 13, no. 10, pp. 765–768, 2001.
- [13] R. Tkachov, V. Senkovskyy, M. Horecha, U. Oertel, M. Stamm, and A. Kiriya, "Surface-initiated Kumada catalyst-transfer polycondensation of poly(9,9-dioctylfluorene) from organosilica particles: chain-confinement promoted beta-phase formation.," *Chemical communications (Cambridge, England)*, vol. 46, no. 9, pp. 1425–7, 2010.
- [14] T. Kietzke, D. Neher, K. Landfester, R. Montenegro, R. Güntner, and U. Scherf, "Novel approaches to polymer blends based on polymer nanoparticles.," *Nature materials*, vol. 2, no. 6, pp. 408–12, 2003.

- [15] T. Kietzke, D. Neher, M. Kumke, R. Montenegro, K. Landfester, and U. Scherf, "A Nanoparticle Approach To Control the Phase Separation in Polyfluorene Photovoltaic Devices," *Macromolecules*, vol. 37, no. 13, pp. 4882–4890, 2004.
- [16] K. B. Burke, A. J. Stapleton, B. Vaughan, X. Zhou, a L. D. Kilcoyne, W. J. Belcher, and P. C. Dastoor, "Scanning transmission x-ray microscopy of polymer nanoparticles: probing morphology on sub-10 nm length scales.," *Nanotechnology*, vol. 22, no. 26, p. 265710-265715, 2011.
- [17] A. Stapleton, B. Vaughan, B. Xue, E. Sesa, K. Burke, X. Zhou, G. Bryant, O. Werzer, A. Nelson, D. Kilcoyne, L. Thomsen, E. Wanless, W. Belcher, and P. Dastoor, "A multilayered approach to polyfluorene water-based organic photovoltaics," *Solar Energy Materials and Solar Cells*, vol. 102, pp. 114–124, 2012.
- [18] V. Senkovskyy, R. Tkachov, T. Beryozkina, H. Komber, U. Oertel, M. Horecha, V. Bocharova, M. Stamm, S. A. Gevorgyan, F. C. Krebs, and A. Kiriy, "'Hairy' poly(3-hexylthiophene) particles prepared via surface-initiated Kumada catalyst-transfer polycondensation.," *Journal of the American Chemical Society*, vol. 131, no. 45, pp. 16445–16453, 2009.
- [19] J. Zou, P. Sanelle, K. A. Pettigrew, and S. M. Kauzlarich, "Size and Spectroscopy of Silicon Nanoparticles Prepared via Reduction of SiCl₄," *Journal of Cluster Science*, vol. 17, no. 4, pp. 565–578, 2006.
- [20] R. K. Baldwin, K. A. Pettigrew, J. C. Garno, P. P. Power, G. Liu, and S. M. Kauzlarich, "Room temperature solution synthesis of alkyl-capped tetrahedral shaped silicon nanocrystals.," *Journal of the American Chemical Society*, vol. 124, no. 7, pp. 1150–1151, 2002.
- [21] R. K. Baldwin, K. A. Pettigrew, E. Ratai, M. P. Augustine, and S. M. Kauzlarich, "Solution reduction synthesis of surface stabilized silicon nanoparticles.," *Chemical communications (Cambridge, England)*, no. 17, pp. 1822–1823, 2002.
- [22] N. Espinosa, R. García-Valverde, A. Urbina, and F. C. Krebs, "A life cycle analysis of polymer solar cell modules prepared using roll-to-roll methods under ambient conditions," *Solar Energy Materials and Solar Cells*, vol. 95, no. 5, pp. 1293–1302, 2011.
- [23] Swiss Centre for Life Cycle Inventories, "ecoinven." [Online]. Available: <http://www.ecoinvent.ch/>. [Accessed: 11-Sep-2013].
- [24] F. Tran-Van, M. Carrier, and C. Chevrot, "Sulfonated polythiophene and poly(3,4-ethylenedioxythiophene) derivatives with cations exchange properties," *Synthetic Metals*, vol. 142, no. 1–3, pp. 251–258, 2004.

- [25] D. A. Rider, B. J. Worfolk, K. D. Harris, A. Lalany, K. Shahbazi, M. D. Fleischauer, M. J. Brett, and J. M. Buriak, "Stable Inverted Polymer/Fullerene Solar Cells Using a Cationic Polythiophene Modified PEDOT:PSS Cathodic Interface," *Advanced Functional Materials*, vol. 20, no. 15, pp. 2404–2415, 2010.
- [26] V. Sgobba, A. Troeger, R. Cagnoli, A. Mateo-Alonso, M. Prato, F. Parenti, A. Mucci, L. Schenetti, and D. M. Guldi, "Electrostatic layer-by-layer construction and characterization of photoelectrochemical solar cells based on water soluble polythiophenes and carbon nanotubes," *Journal of Materials Chemistry*, vol. 19, no. 25, pp. 4319–4324, 2009.
- [27] R. Søndergaard, M. Helgesen, M. Jørgensen, and F. C. Krebs, "Fabrication of Polymer Solar Cells Using Aqueous Processing for All Layers Including the Metal Back Electrode," *Advanced Energy Materials*, vol. 1, no. 1, pp. 68–71, 2011.
- [28] K. Landfester, R. Montenegro, U. Scherf, R. Güntner, U. Asawapirom, S. Patil, D. Neher, and T. Kietzke, "Semiconducting Polymer Nanospheres in Aqueous Dispersion Prepared by a Miniemulsion Process," *Advanced Materials*, vol. 14, no. 9, pp. 651–655, 2002.
- [29] J. Hou, H.-Y. Chen, S. Zhang, R. I. Chen, Y. Yang, Y. Wu, and G. Li, "Synthesis of a low band gap polymer and its application in highly efficient polymer solar cells.," *Journal of the American Chemical Society*, vol. 131, no. 43, pp. 15586–15587, 2009.
- [30] E. Bundgaard, O. Hagemann, M. Jørgensen, and F. Krebs, "Low Band Gap Polymers for Roll-to-Roll Coated Organic Photovoltaics—Design, Synthesis and Characterization," *Green*, vol. 1, pp. 55–64, 2011.
- [31] E. Wang, L. Hou, Z. Wang, S. Hellström, F. Zhang, O. Inganäs, and M. R. Andersson, "An Easily Synthesized Blue Polymer for High-Performance Polymer Solar Cells," *Advanced Materials*, vol. 22, pp. 5240–5244, 2010.
- [32] S. A. Gevorgyan and F. C. Krebs, "Bulk Heterojunctions Based on Native Polythiophene," *Chemistry of Materials*, vol. 20, no. 13, pp. 4386–4390, 2008.
- [33] Z.-G. Zhang, J. Min, S. Zhang, J. Zhang, M. Zhang, and Y. Li, "Alkyl chain engineering on a dithieno[3,2-b:2',3'-d]silole-alt-dithienylthiazolo[5,4-d]thiazole copolymer toward high performance bulk heterojunction solar cells," *Chemical communications (Cambridge, England)*, vol. 47, no. 33, pp. 9474–9476, 2011.
- [34] C. Scharsich, R. H. Lohwasser, M. Sommer, U. Asawapirom, U. Scherf, M. Thelakkat, D. Neher, and A. Köhler, "Control of aggregate formation in poly(3-hexylthiophene) by solvent,

- molecular weight, and synthetic method," *Journal of Polymer Science Part B: Polymer Physics*, vol. 50, no. 6, pp. 442–453, 2012.
- [35] P. V Shibaev, K. Schaumburg, T. Bjornholm, and K. Norgaard, "Conformation of polythiophene derivatives in solution," *Synthesis*, vol. 97, pp. 97–104, 1998.
- [36] D. Moerman, R. Lazzaroni, and O. Douhéret, "Efficient bulk heterojunction photovoltaic cells with a pre-organized poly(3-hexylthiophene) phase," *Applied Physics Letters*, vol. 99, no. 9, p. 093303-093306, 2011.
- [37] M. Giulianini, E. R. Waclawik, J. M. Bell, M. Scarselli, P. Castrucci, M. De Crescenzi, and N. Motta, "Poly(3-hexyl-thiophene) coil-wrapped single wall carbon nanotube investigated by scanning tunneling spectroscopy," *Applied Physics Letters*, vol. 95, no. 14, p. 143116-143118, 2009.
- [38] T. Kietzke, D. Neher, M. Kumke, O. Ghazy, U. Ziener, and K. Landfester, "Phase separation of binary blends in polymer nanoparticles.," *Small*, vol. 3, no. 6, pp. 1041–1048, 2007.
- [39] S. Ulum, N. Holmes, D. Darwis, K. Burke, D. Kilcoyne, X. Zhou, W. Belcher, and P. Dastoor, "Determining the structural motif of P3HT:PCBM nanoparticulate organic photovoltaic devices," *Solar Energy Materials and Solar Cells*, vol. 110, pp. 43–48, 2013.
- [40] Y. Lee, S. H. Lee, K. Kim, J. W. Lee, K.-Y. Han, J. Kim, and J. Joo, "Single nanoparticle of organic p-type and n-type hybrid materials: nanoscale phase separation and photovoltaic effect," *Journal of Materials Chemistry*, vol. 22, no. 6, pp. 2485–2490, 2012.
- [41] B. L. Henke, E. M. Gullikson, and J. C. Davis, "X-ray transmission of a solid." [Online]. Available: [Http://henke.lbl.gov/optical_constants/filter2.html](http://henke.lbl.gov/optical_constants/filter2.html).
- [42] B. L. Henke, E. M. Gullikson, and J. C. Davis, "X-ray interactions: Photoabsorption, Scattering, Transmission, and Reflection at E=50-30,000 eV, Z=1-92," *Atomic Data and Nuclear Data Tables*, vol. 54, pp. 181–342, 1993.
- [43] B. S. Borbbly and L. Cser, "Temperature and Concentration Dependence of Properties of Sodium Dodecyl Sulfate Micelles Determined from Small-Angle Neutron Scattering Experiments," *Journal of Physical Chemistry*, no. 17, pp. 5138–5143, 1988.
- [44] F. C. Krebs, V. Senkovskyy, and A. Kiriya, "Preorganization of Nanostructured Inks for Roll-to-Roll-Coated Polymer Solar Cells," *IEEE Journal of Selected Topics in Quantum Electronics*, vol. 16, no. 6, pp. 1821–1826, 2010.

- [45] C. Meier, A. Gondorf, S. Lüttjohann, A. Lorke, and H. Wiggers, "Silicon nanoparticles : Absorption , emission , and the nature of the electronic bandgap," *Journal of Applied Physics*, vol. 101, no. 10, pp. 103112 –103119, 2007.
- [46] R. Søndergaard, S. Strobel, E. Bundgaard, K. Norrman, A. G. Hansen, E. Albert, G. Csaba, P. Lugli, M. Tornow, and F. C. Krebs, "Conjugated 12 nm long oligomers as molecular wires in nanoelectronics," *Journal of Materials Chemistry*, vol. 19, no. 23, pp. 3899-3908, 2009.
- [47] M. Hesse, H. Meier, and B. Zeeh, *Spectroscopic Methods in Organic Chemistry*, First. Stuttgart: Georg Thieme Verlag., 1997, ISBN: 0-86577-667-9.
- [48] C. Book, "Chemical book." [Online]. Available: http://www.chemicalbook.com/SpectrumEN_92-69-3_1HNMR.htm. [Accessed: 06-Sep-2013].

3. Processing

3.1. Introduction

For OSCs to achieve its full potential as renewable energy source, the processing method should not add extraordinary time to the energy payback time (EPBT). The method commonly seen as fulfilling this requirement is film-deposition by roll-to-roll (R2R) coating and printing since it uses solution based coating and printing with a high throughput. Technologies to avoid during processing is the vacuum deposition and glovebox, since both of these methods requires a large amount of energy as described in Chapter 1.[1] Other requirements that need to be taken into consideration for the “optimal” processing are the use of a flexible substrate, the coating process should be free of toxic solvents, and the prepared devices should not contain expensive or scarce materials such as ITO.

Presently most publications deals with small devices, typically 0.04 cm^2 , prepared by spin coating (Figure 3.1A) with a vacuum deposited back-electrode, on a rigid glass-substrate, with a patterned ITO electrode produced in an inert atmosphere. Spincoating is used for applying thin, uniform, and highly reproducible films on a flat substrate and can be used for several of the layers in OSC devices. There are two major advantages of spincoating, it is a simple process and only a small amount of material is needed, this makes it suitable for scientific testing of materials.[2] However, there are also a couple of disadvantages such as poor compatibility with R2R-coating, rendering device optimizations found by spin-coating more or less useless, and significant ink waste due to ejection of the applied solution.[2,3]



Figure 3.1: A) A photograph of spin coating on the fly in a glovebox, [3] B) An illustration of two OSC modules, where the module on the left is prepared by spin-coating, and a module prepared by R2R coating on the right.

For large-scale preparation of OSCs R2R techniques are preferable, due to their potentially very high throughput.[3,4] R2R coating and printing does in contrast to spin coating involve a flexible substrate in a continuous roll. Modules can be prepared by both techniques as illustrated in Figure 3.1B. The module on the left is prepared by spin-coating, having the potential of high performance, however, the fabrication time will usually be in hours to days.[4] On the right is shown a R2R prepared module, which although having lower performance have a preparation time in seconds when prepared in large volume. [4]

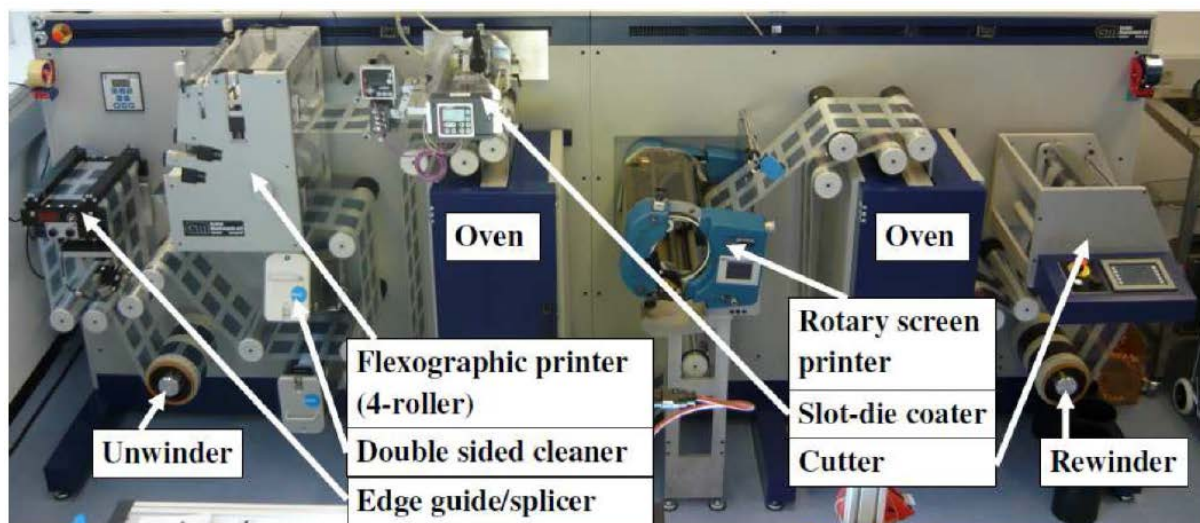


Figure 3.2: One of the roll-to-roll coating machines at DTU Energy Conversion.

An example of a R2R coater is shown in Figure 3.2. Beside the high-speed production of OSC, other demands such as solvent processing and high volume can also be fulfilled by this setup. Various coating methods can be utilized on the R2R setup including slot-die coating, flexographic printing, and rotary screen-printing. Furthermore, the R2R-coater is equipped with substrate cleaners, and other surface treatments, which can improve wetting properties of the inks.

In the following the coating and printing techniques that was used throughout this project will be briefly introduced.

3.1.1. Coating techniques

3.1.1.1. Spin coating

A spin-coater is simplified just of a spinning disc on which a substrate can be mounted (Figure 3.3). Spincoating operation involves application of an ink to a substrate followed by acceleration of the substrate to a chosen rotation speed.[3] An alternative deposition method is to apply the ink when the substrate is already spinning. The thickness of the applied film can be expressed by the empirical relationship presented in Equation 3.1. [3]

$$d = kw^\alpha \quad \text{(Equation 3.1)}$$

Where w is the angular velocity, k and α are empirical constants related to physical properties of the solvent, solute, and substrate. One of the physical properties with the largest influence on the dry thickness is the viscosity of the solution since a high viscosity ensures more ink to remain on the substrate during spinning.

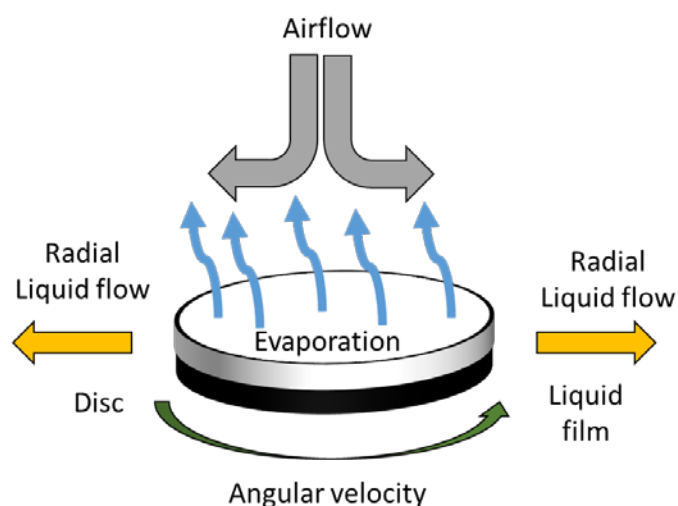


Figure 3.3: Schematic illustration of spin coating.[2]

3.1.1.2. Slot-die coating

Slot-die coating uses a slot-die head with a narrow gap to deposit the wet-film as illustrated in Figure 3.4. In contrast to spin coating, slot-die coating is a volumetric method with a continuous ink supply to the meniscus and has a minimum of ink waste. This also means that it is possible to control the wet thickness by controlling the pump-rate and the web-speed. A theoretic dry-thickness of the film can be calculated from Equation 3.2:

$$d = \frac{f}{S \times w} \times \frac{c}{\rho} \quad (\text{Equation 3.2})$$

Where d is the film thickness in cm, f is the flow rate in $\text{cm}^3 \text{min}^{-1}$, S is the web speed in cm min^{-1} , w is the width of the coating, c is the concentration of the ink g cm^{-3} , and ρ is the density of the dried ink materials in g cm^{-3} .

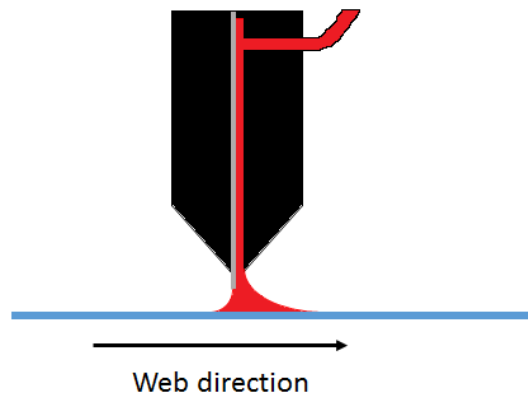


Figure 3.4: Schematic illustration of a slot-die coating-head with a meniscus guide.

Common coating defects when using slot-die coating includes picture-framing, dewetting and poisoning examples is shown in Figure 3.5.

- Dewetting occurs when the wetting properties of the ink on the substrate is too poor. The wetting properties can in general be evaluated through the contact angle between the substrate and the ink (Figure 3.5A) i.e. a low contact angle means that the wetting properties are good.
- Picture-framing describes a situation where ink accumulates at the edge of the coated stripe which results in an uneven film thickness (Figure 3.5B).
- Poisoning of the surface describes a situation where the ink initially wets the surface of the substrate after which it dewets leaving behind a thin film (Figure 3.5C).
- Poisoning of the meniscus occurs through up-concentration of an ink or surface component in the meniscus, thereby changing the wetting properties.

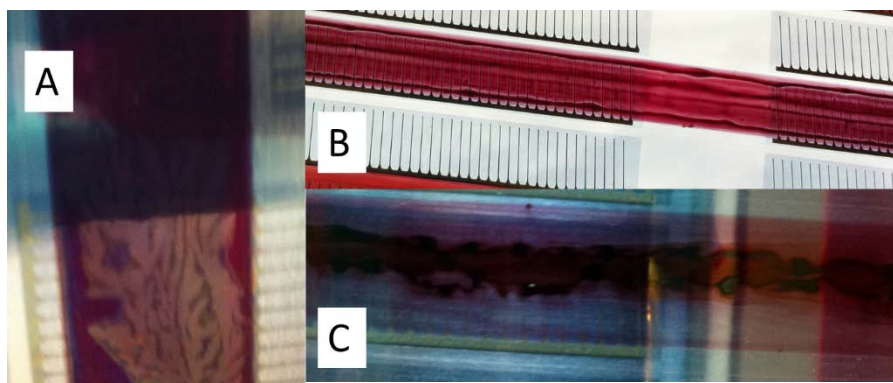


Figure 3.5: Pictures showing common coating defects, A) dewetting of PEDOT:PSS 4083 on active layer with an insufficient layer of compatibilizer, B) picture framing of the active layer, C) poisoning of the surface.

3.1.1.3. Flexographic printing

Flexographic printing is using direct contact to apply the ink; the ink is transferred to the substrate by a patterned roll made usually from rubber or photopolymer.[4] A typical R2R flexographic printing set up is comprised of four roller (Figure 3.6), a Fountain roller that re-inks an Anilox roller from which the ink is transferred to the printing plate cylinder. The ink is then applied to the substrate with the fourth roller (impression cylinder) functioning as a counter roller.[3]

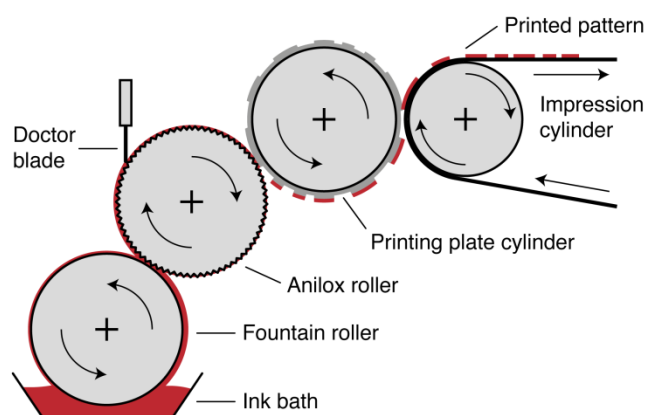


Figure 3.6: Schematic presentation of Flexographic printing. Figure prepared by Markus Hösel, DTU Energy Conversion.[5]

3.2. Mini roll-coater

An easier transition and better compatibility from laboratory scale testing to R2R manufacturing of OSCs was ensured by developing a mini roll-coater (MRC).[6] The MRC, seen in Figure 3.7, uses slot-die coating and flexographic printing for fabrication of OSCs, which are two of the ink deposition techniques used on the large R2R-coater. This should make the transition from laboratory scale to large-scale R2R fabrication easier.

The MRC consists of an aluminum wheel with a circumference of 1 meter on which the substrate is mounted. The coating-head and flexographic printing-roll are mounted in position 2 on Figure 3.7. The temperature of the aluminum wheel can be adjusted from room temperature to 150 °C in order to ensure an even and fast drying of the deposited solution. The wet thickness of the applied film is controlled by adjusting the rotation speed of the wheel between 0-2 m/min and by controlling the flow-rate of the solution, which is done by a syringe pump.

The coating head in Figure 3.7 consists of three parts of stainless steel. The front piece is designed with an inlet in the top of a groove with a depth of 50-60 μm to ensure a continuous flow throughout the entire width of the meniscus guide. The meniscus guide protrudes 0.5 mm and a width of 10 or 13 mm.

Even though the MRC buildup is simple and known coating/printing methods are used, extensive development had to be made to be able to prepare functional devices requiring experiments with coating temperature, rotation speed, and distance between the coating head and substrate. After months of further development, we finally were able to prepare devices with a reasonable PCE in day-to-day coatings.

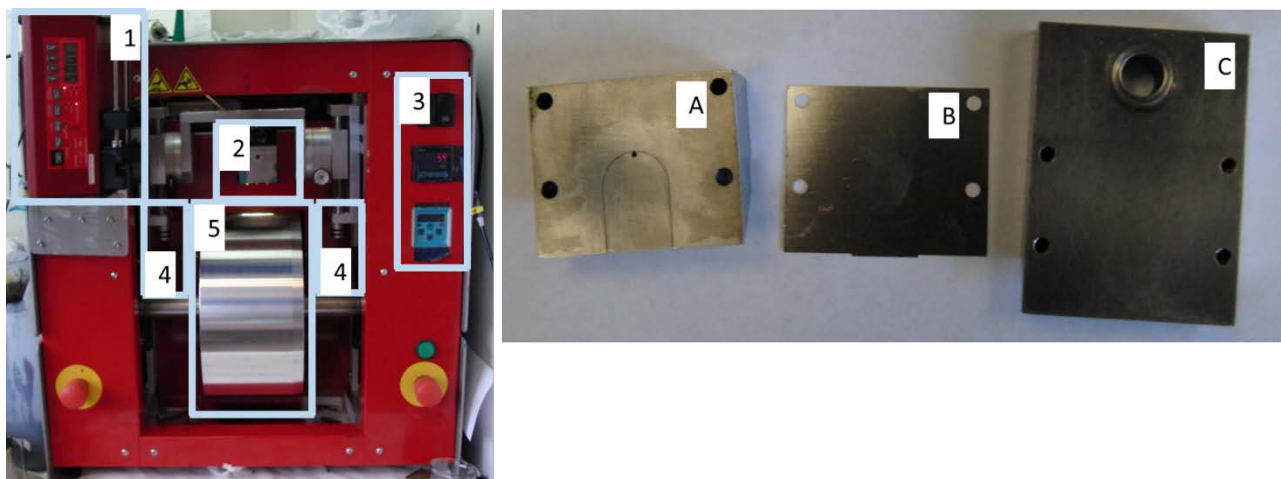


Figure 3.7: On the left: One of the mini roll-coaters (MRC) placed in a fumehood at DTU Energy Conversion, it consists of: 1) A syringe-pump, 2) coating-head mounting position, 3) temperature and rotation speed controls, 4) head height adjustment, 5) aluminium roll. On the right: Disassembled slot-die coating head, A) front piece with solution inlet and groove to ensure continuous flow, B) meniscus guide with a protrude of 0.5 mm, and C) back piece of the coating head.

3.2.1. Coating and printing parameters on the MRC

Slot-die coating of an active layer consisting of Polymer:PCBM dissolved in chloroform, chlorobenzene, or *o*-dichlorobenzene was performed with the equipment presented above (Figure 3.7). The dry thicknesses of the coated films were controlled by the concentration of the solution and the wet-thickness of the deposited film. Usually active layers were coated at 1 to 1.3 m min⁻¹ with a roll-temperature of 60-70 °C and a wet-thickness which resulted in a theoretical dry-thickness of 240 to 500 nm. For top-electrode either a PEDOT:PSS 5010 (specifications can be found in Table 3.1) or a three layer combination of PEDOT:PSS (PEDOT:PSS F010/PEDOT:PSS 4083/PEDOT:PSS F010) was used. The three layered PEDOT:PSS electrode was slot-die coated by first coating a thin PEDOT:PSS F010 layer (F010:IPA 1:4 with a wet-thickness of 8 μm) as a compatibilizer to enhance the wetting properties of PEDOT:PSS 4083 (4083:IPA 1:2 with a wet-thickness of 24 μm), which undergoes severe dewetting without the use of a compatibilizer. As a conductive electrode another layer of F010 (F010:IPA 2:1 with a wet-thickness of 40 μm) was coated on-top of PEDOT:PSS 4083. An optimal hole-

extraction is ensured by application of a silver-grid i.e. full, honeycomb, or shark pattern (Figure 3.8) was flexographically printed, at 60 °C with a roll-speed of 1.2 m min⁻¹.

Table 3.1: Specification of the different PEDOT:PSS used throughout this thesis.

<i>Abbreviate name</i>	<i>Full name</i>	<i>Produced by</i>	<i>Conductor</i>	<i>Neutralized</i>
<i>5010</i>	EL-P5010	Agfa	+	-
<i>F010</i>	CLEVIOS™ F010	Heraeus	+	-
<i>4083</i>	CLEVIOS™ P VP AL4083	Heraeus	-	-
<i>PH1000</i>	CLEVIOS™ PH1000	Heraeus	+	-
<i>HTL solar</i>	CLEVIOS™ HTL solar	Heraeus	-	-
<i>HTL solar N</i>	CLEVIOS™ HTL solar N	Heraeus	-	+
<i>HIL 3,3</i>	CLEVIOS™ HIL 3,3	Heraeus	-	-
<i>HIL 3,3 N</i>	CLEVIOS™ HIL 3,3 N	Heraeus	-	+

To finish the OSC, the substrate was taken off the roll and annealed in an oven for 10 minutes at 100-120 °C to remove residual solvents from the silver-paste. The separate cells were then cut out to obtain an area of 1 cm², which were encapsulated between two pieces of glass using an UV-curable adhesive from DELO. After encapsulation, an additional annealing step was conducted between 110 and 140 °C depending on the composition of the active layer. Usually three or four stripes were printed in each run on the MRC, making it possible to change processing parameters on only one meter of substrate. OSCs were prepared using as little as 10-15 mg of polymer and preparing 80-90 devices pr. stripe giving a total of 240-360 devices in one coating session.

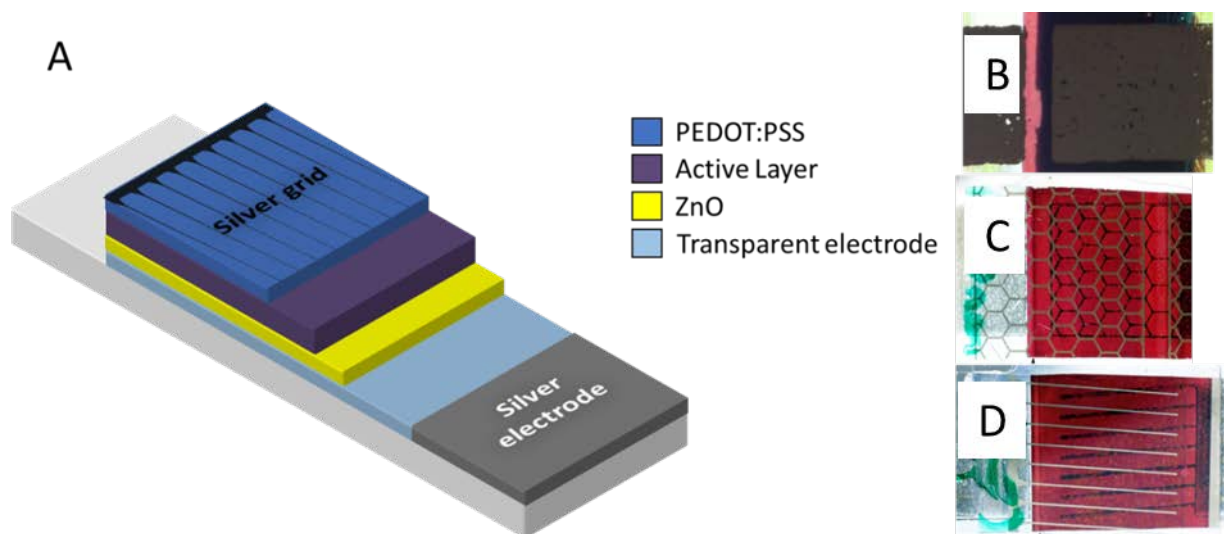


Figure 3.8: A) Schematic buildup of OSC as prepared on the MRC. B) Full-silver electrode, C) Honeycomb-silver electrode, and D) "Shark"-silver electrode.

3.2.2. OSC prepared on flexible substrate using MRC

The substrates used for the R2R coater needs to be flexible, so in order to ensure an easy transition from MRC to the R2R coater, a flexible substrate was also utilized on the MRC. The most used electrode material is at this moment still ITO because it has a high transmission and a relatively low sheet resistance. A couple of drawbacks with the use of ITO as electrode is its high embodied energy[1] and that it has a tendency to crack when bended which increases the sheet resistance.[7] Both of these drawbacks makes it difficult to bring OSCs to the next level since a high embodied energy will increase the EPBT and bending of the substrate will be difficult to avoid when preparing OSCs on the R2R coater. A new semi-transparent electrode also known as Flextrode[8] has therefore been invented. A schematic presentation of Flextrode is shown in Figure 3.9, it consist of a highly conductive PEDOT:PSS PH1000 with ZnO on top as the ETL, a silver grid is applied underneath the PEDOT:PSS in the improved version of Flextrode in order to decrease the sheet resistance.

Preparation of OSCs using MRC were in general performed on large scale produced Flextrode due to better meter-to-meter uniformity of the substrate than could be obtained when preparing Flextrode on the MRC.

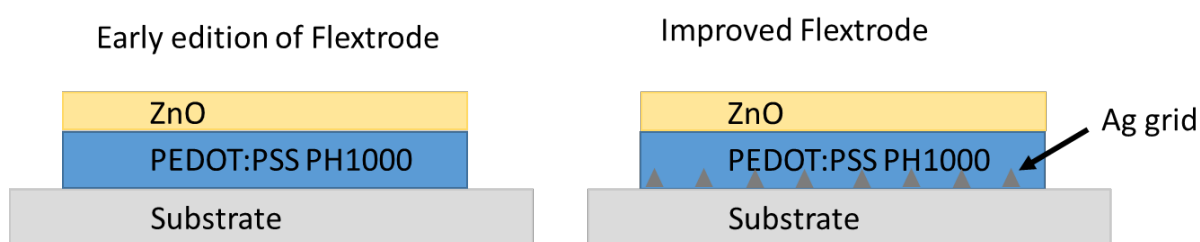


Figure 3.9: Schematic illustration of Flextrode both the early edition (on the left) and the improved Flextrode (on the right).

3.2.2.1. Testing and development of Flextrode

The aim of the work in this section was to do preliminary tests and development of Flextrode on a small scale using the MRC to prepare OSCs in order to reveal shortcomings of the earlier editions of Flextrode.

The early edition of Flextrode (Figure 3.9) consisting only of PEDOT:PSS PH1000 and ZnO was tested by preparing devices with a 480 nm thick P3HT:PCBM with a ratio of 1:1 (P3HT was purchased from Rieke) with a PEDOT:PSS 5010 as conductive top-layer. Photovoltaic characteristics (Table 3.2) of the same device under varying light intensity revealed that an extraction problem was present, which can be seen from the increasing FF (from 34 % to 41 %) by reducing the intensity from 1000 W m^{-2} to 250 W m^{-2} . The extraction problem is ascribed to the relatively high sheet resistance of 70-90 ohm/square for the early edition of Flextrode, which results in a larger series resistance.

Table 3.2: Photovoltaic characteristics of devices prepared on early edition of Flextrode tested under different light intensities.

<i>Light intensity</i> (W m^{-2})	V_{oc} (V)	J_{sc} (mA cm^{-2})	<i>FF</i> (%)	<i>PCE</i> (%)
1000	0.58	-6.5	34.2	1.31
500	0.57	-3.3	38.6	1.45
250	0.53	-1.5	40.6	1.35

The extraction problems can be overcome in two ways either by reducing the current or by increasing the conductivity of the electrode. Only an increase in conductivity of the electrode makes sense in practice since the current is directly scalable with the intensity of the sun which at AM1.5 is 1000 W m^{-2} . The application of a silver-grid in the bottom of Flextrode reduced the sheet resistance from 70-90 to 10 ohm/square.[8] Devices were prepared with similar parameters as presented above on the improved Flextrode with a front silver-grid (Figure 3.9). The photovoltaic performance was obtained at 1000 W m^{-2} and resulted in a FF of 42.4 % and a PCE of 1.5 %. It can therefore be concluded that the application of the silver-grid improved the extraction problems by enhancing the conductivity of Flextrode and thereby made it possible to prepare OSCs with a higher performance even though the silver-grid introduces shading.

3.2.2.2. Testing of three different substrates for Flextrode using MRC

In order to enhance the performance of the prepared OSCs even further it is necessary to investigate the other parameters than just the Flextrode stack. The PET substrate on which the OSCs are prepared can also have a large influence on the performance. A number of PET-substrates are commercially available, three of these (Melinex, Amcor, and Mitsubishi) were tested on the MRC to determine which one had the potential to prepare high efficient OSCs. Melinex is a pure PET foil where the two others are thin foils with different properties laminated together. This has an influence on the physical properties of the foils such as the transmission and barrier properties (limiting oxygen and water diffusion from the ambient surroundings to the active layer).

The transmission of the substrates were measured from 300 to 1000 nm to investigate the current potential for each substrate. Melinex had a transmission of approximately 87 % from 380 to 1000 nm whereas the transmission for Amcor and Mitsubishi was around 80 % and 75%, respectively (Figure 3.10A). When adding the Flextrode-stack (Ag/PEDOT:PSS PH1000/ZnO) on to the substrates the general transmission decreases, though most pronounced towards longer wavelengths, as in the case for Melinex it decreases from 75 % at 380 nm to around 55 % at 1000 nm. The lower transmission changes the theoretical current

density from the otherwise available 38.1 mA cm^{-2} under AM 1.5G conditions to 24.8 mA cm^{-2} from 300 to 1000 nm. In Figure 3.10B it is shown that the largest current contribution is between 480 and 700 nm when applying the transmission of Flextrode.

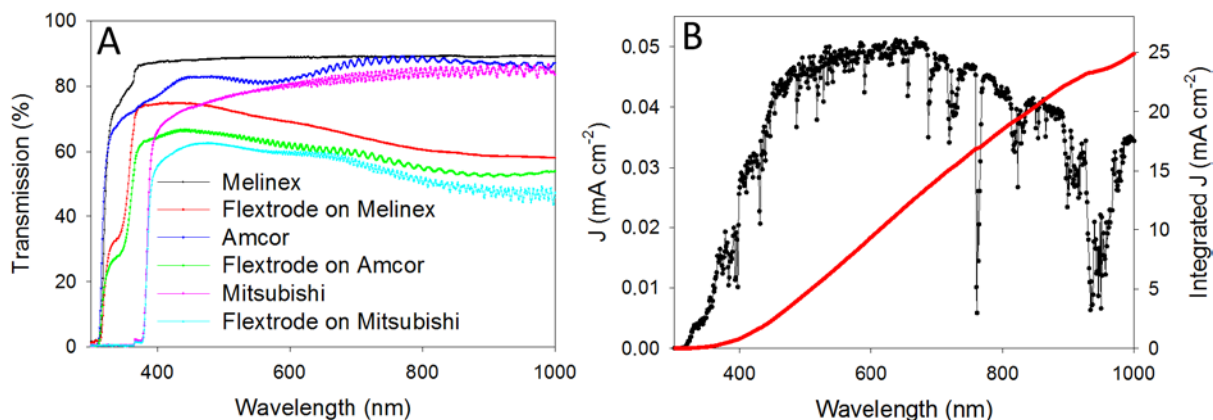


Figure 3.10: A) light-transmission of various PET substrates (Melinex, Amcor, and Mitsubishi) and their corresponding Flextrode transmission, B) Maximum current density achievable per nanometer on Flextrode with Melinex substrate (black circles) and the integrated current density (red line). The graph was prepared by multiplying the photon flux with the transmission for Flextrode on Melinex substrate.

Additional testing of these three substrates were conducted by preparing OSCs on each substrate-type with an active layer consisting of 480 nm thick P3HT:PCBM (P3HT and PCBM were purchased from Plextronic) with a 1:1 ratio coated from a 40 mg mL^{-1} solution in chlorobenzene with 10 % chloroform and 3 % chloronaphthalene. On top of the active layer the three layered PEDOT:PSS electrode (F010-4083-F010) was applied followed by a silver-grid. The resulting photovoltaic characteristics revealed similar V_{OC} and FF on each of the substrates. The J_{SC} is for Melinex with -9.31 mA cm^{-2} significantly higher than the J_{SC} obtained for Amcor and Mitsubishi, i.e. -7.73 mA cm^{-2} and -5.41 mA cm^{-2} , respectively, as shown in Figure 3.11 these J_{SC} are in agreement with the lower transmission of Amcor and Mitsubishi.

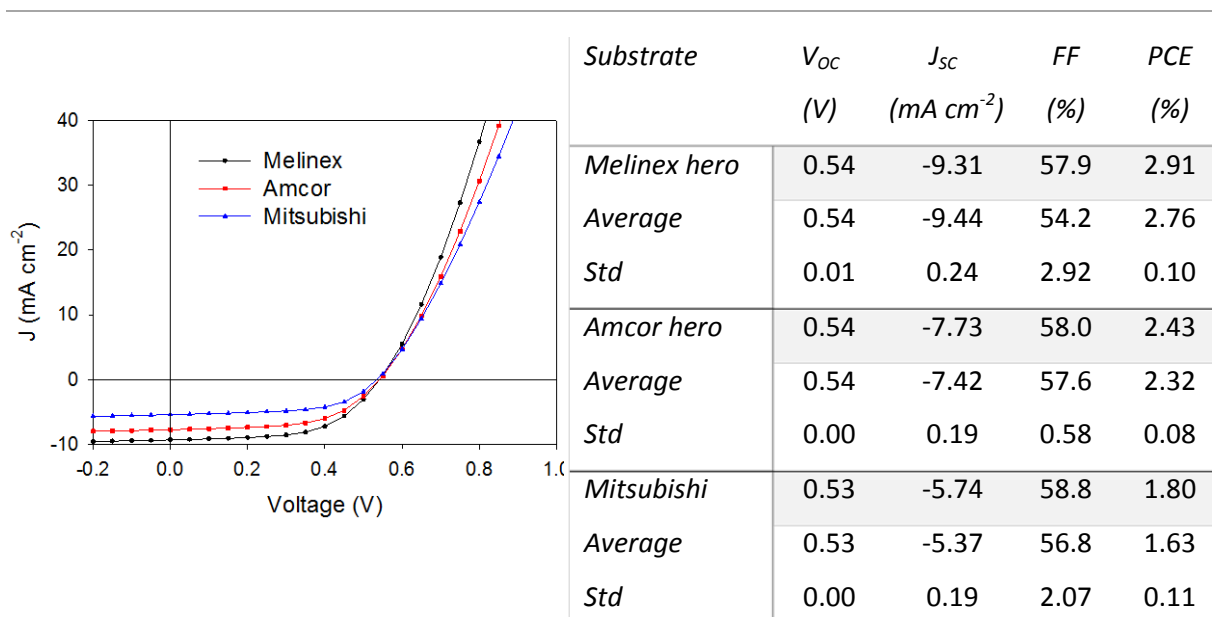


Figure 3.11: I-V characteristic and photovoltaic performance of P3HT:PCBM devices both as hero device and average of 8 devices printed on three different type PET-substrates, Melinex, Amcor, and Mitsubishi.

Another method to evaluate the performance of the devices is by IPCE-measurements, which was done on the hero device coated on each substrate. The IPCE measurements shows as expected the same tendencies as the transmission and PCE with Melinex peaking at 58 %, Amcor at 52 % and Mitsubishi at 42 % (Figure 3.12A). A Light Beam Induced Current image (LBIC) of the hero OSC printed on Melinex (Figure 3.12B) shows an uniform device performance without defects. Only the shading of the silver-lines resulted in non-performing areas. The device quality was reduced slightly on devices prepared on Amcor and Mitsubishi substrates, where a pattern of the top silver can be seen as non-performing area (Figure 3.12C and D) this is ascribed as a coating defect not a substrate parameter.

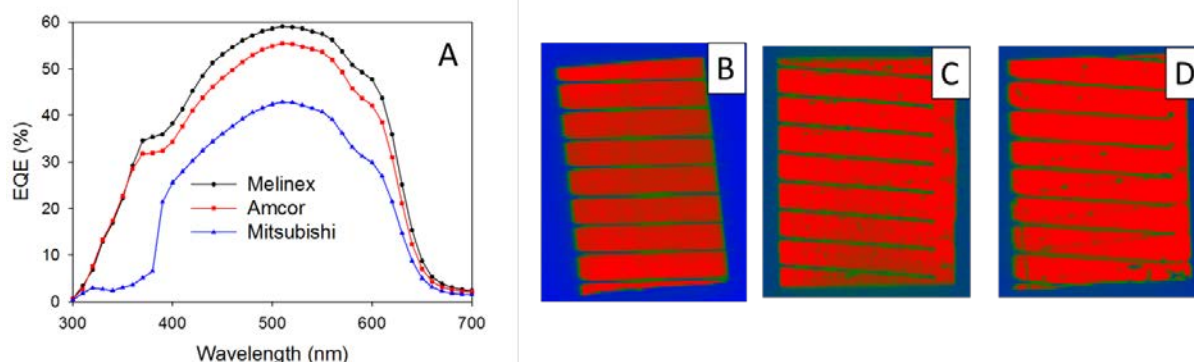


Figure 3.12: A) IPCE measurements of the device presented in Figure 3.11, B) LBIC-image of the device printed on Melinex, C) LBIC-image of the device printed on Amcor, D) LBIC-image of the device printed on Mitsubishi barrier foil.

The overall conclusion of the substrate test is that Melinex is the substrate with the potential to prepare high efficient OSCs primarily due to higher transmission than Amcor and Mitsubishi. A Drawback with Melinex is that it has no barrier properties in contrast to the two other substrates therefore making Melinex the less ideal choice for large scale production.

In order to evaluate the compatibility of PCEs obtained from OSCs prepared on the MRC and the R2R coater it makes sense to compare devices prepared with an active layer consisting of P3HT:PCBM since it is the most investigated active layer on R2R. The devices prepared with an active layer consisting of P3HT:PCBM on the MRC showed performances between 1.3 % and 2.9 %. The poor performing devices were prepared on early edition (April 2012) of Flextrode and is therefore not to be considered as state of the art performances for P3HT:PCBM devices prepared on the MRC. In opposition the devices with 2.9 % was prepared in June 2013 is therefore state of the art. A PCE of 2.9 % is higher than what is obtained when coating P3HT:PCBM on the large scale R2R-coater which in general give devices with a PCE around 1.8-2 % on Flextrode.[8-10] This difference is ascribed to the smaller area of the prepared devices and to the usage of the three layered PEDOT:PSS electrode for the devices prepared on MRC, which increases the current collection in comparison to device prepared with a single PEDOT:PSS 5010 layer. This increase in current, enhances the PCE from ~ 2 % to 2.9 %. Therefore, it can be claimed that the PCEs obtained on the MRC and the

R2R coater is if not the same then similar giving good compatibility between laboratory scale OSCs and large scale produced OSCs.

3.2.2.3. Polymer testing on the MRC

The efficiency of OSCs depends on several parameters, which all needs to be taken in to account not only device preparation but also the components combination in the active layer. In literature a number of new polymers having a broader absorption, and/or a better alignment of the LUMO-level of PCBM has been prepared. In order to determine which polymers are suited for roll coating a number of polymers some known from literature [11-14] were tested using the MRC (see Table 3.3 for details). However, not all of the polymers resulted in functional OSCs or they had a low performance. This could be due to several differences between device preparation by spincoating and on the MRC also the various drying steps at 60-70 °C and a subsequent drying step at 120 °C in an oven, could influence the morphology of active layer. Polymers giving functional devices with reasonable PCE are listed in Figure 3.13, all polymers were prepared in house by other members of the group.

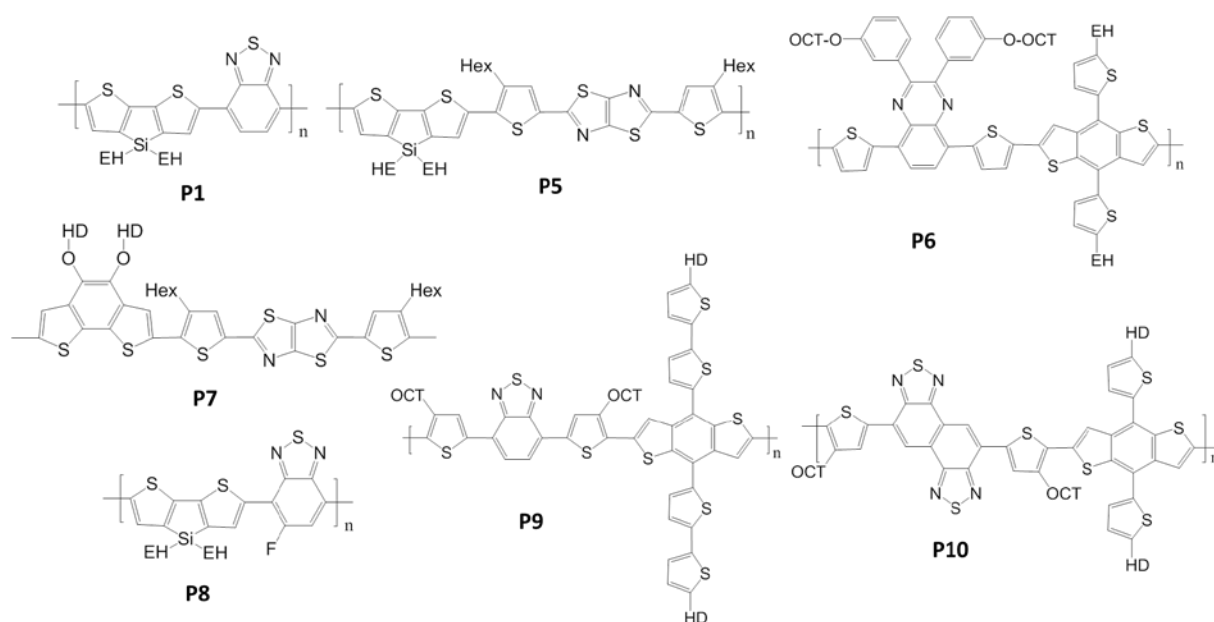


Figure 3.13: Schematic presentation of polymers succesfully tested on the MRC. HD=Hexyldecyl, EH=2-Ethylhexyl, Hex=Hexyl, OCT=Octyl.

OSCs prepared from these polymers had PCE values between 0.84 and 2.58 % (Table 3.3). As shown in entry 1 and 2 in Table 3.3, changing the coating solvent can have great influence on the performance, as it changed from 0.84 to 1.33 % when coating from chloroform instead of chlorobenzene. This increase is ascribed to a more favorable morphology for the active layer when coating from chloroform compared to chlorobenzene for this specific polymer(**P1**):PCBM combination. The FFs for the coated devices were generally low, with a couple of exceptions in entry 5 and 7 with a FF of 54 and 57 %. The low FF (37-47 %) causes a lowering of the overall performance for the other polymers. A possible explanation for a low FF is low charge carrier mobility in the film.[15] This could be solved by decreasing the layer thickness or by optimizing the polymer:PCBM ratio. However, a thinner film would decrease the absorption and since no reflective back-electrode is applied in these experiments, the current is likely to decrease and the possibility of creating electrical shorts between the top and bottom electrodes also increases.

A comparison between the IPCE measurements and the film absorption (Figure 3.14A and B) reveals that for most of the polymers the same trends are present in both measurements. As for **P1** which has its primary absorption in a range from 600 to 850 nm also have the primary current contribution in the same range. Other polymers (**P9** and **P6**) do not display the same consistency between the absorption spectrum of the film and the IPCE measurements, they both have their primary absorption around 700 nm but their peak IPCE is below 500 nm.

For the evaluation to be complete it is necessary to take the transmission of Flextrode into account since it affects the interval of the light spectrum where most photons are available. The polymers with the largest potential would therefore be polymers that have the main performance contribution in the same range as availability of photons is highest which is from approximately 480 to 700 nm (Figure 3.10B). This is the case for four out of the seven polymers, **P5**, **P6**, **P7**, and **P9**, where the last three polymers have the main contribution from 600 nm towards longer wavelength.

Table 3.3: Summary of I-V characteristics obtained from coating experiments of MRC on Flextrode with the polymers see in Figure 3.13. All Polymers were tested as donors in OSC together with PCBM the ratios, substrates, and solvents given in the table.

Active layer	Ratio (PX:PCBM)	Substrate	Solvent	V_{OC} (V)	J_{SC} ($mA\ cm^{-2}$)	FF (%)	PCE (%)	Literature PCE (%) ⁵
P1	2:3	Amcor ¹	CB	0.57	-3.38	43.4	0.84	5.10 ⁶ [11]
P1	2:3	Amcor ¹	CHCl ₃	0.56	-5.66	41.7	1.33	NA
P5	2:3	Amcor ¹	CB	0.68	-7,15	37.3	1.81	5.88 ⁶ [13]
P6	2:3	Melinex	CB	0.59	-9.52	41.2	2.30	5.00 ⁶ [14]
P7	1:2	Melinex	CB ²	0.83	-4.67	54.1	2.09	NA
P8	2:3	Amcor ¹	CB	0.63	-5,57	41.4	1.33	NA
P9	2:3	Melinex	<i>o</i> -DCB ³	0.65	-6.94	57.1	2.58	NA
P10	2:3	Amcor ¹	CB ⁴	0.69	-5.50	47.3	1.80	5.32 ⁷ [12]

¹UV-filter cut off at 380 nm

²Compatibilizer F010 changed to PFN

³PEDOT:PSS 5010 used as top

⁴2 % chloronaphthalene

⁵devices prepared by spin-coating with vacuum deposited back electrode

⁶[70]PCBM used as acceptor

⁷Sidechain variation

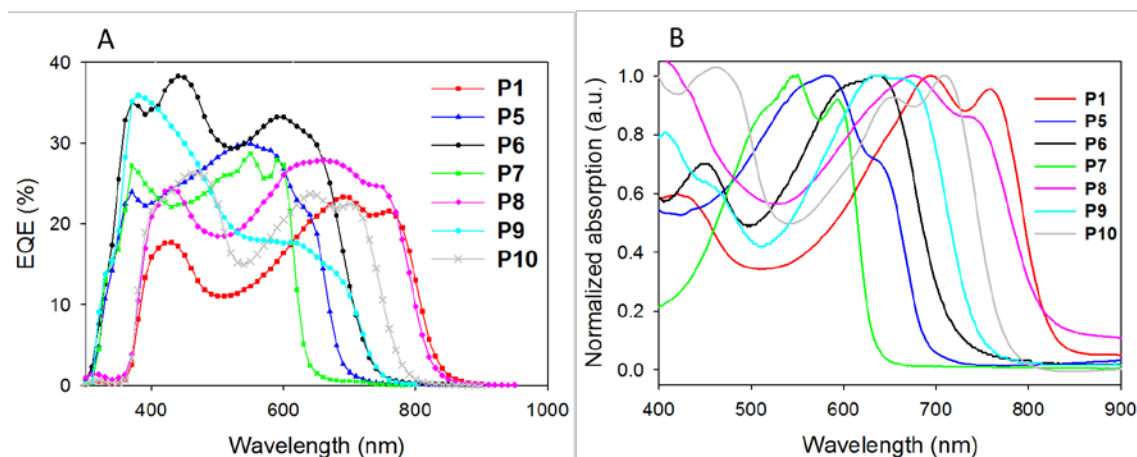


Figure 3.14: A) IPCE-measurement of devices presented in Table 3.3 and Figure 3.13. B) Absorption of films prepared of the polymer presented in Table 3.3 and Figure 3.13 spin-coated on a glass.

3.3. Small molecule OSCs

The materials and OSCs presented in this section were prepared in collaboration with students from the Chinese partners in the Danish-Chinese Center. My contribution to these experiments was the preparation of OSC by roll-coating on the MRC.

Small molecule OSCs have for the past years been an area of increasing interest due to easier material synthesis, molecule regularity, and less batch-to-batch variation.[16,17] Recently small molecule OSCs have made the transition from only being prepared by vacuum deposition to also being prepared from solution based inks by spin coating.[18,19] Very few attempts have been published where roll-coating methods have been used for the device preparation.[20,21] One of the difficulties when preparing OSCs with an inverted geometry, (which is used in the R2R coater) are dissolution of the active layer when coating subsequent layers. This dissolution problem was attempted to be counteracted through application of a more bulky star-shaped molecule (**SM-4**) and a cross-linkable molecule (**SM-3**) for the roll-coating experiments, structures are shown in Figure 3.15. Cross-linking of **SM-3** was performed either by UV-light or heating the active layer to 120 °C, thereby linking the entire active layer together rendering the film insoluble. OSCs from the two other small molecules **SM-1** and **SM-2** were fabricated in normal geometry using spin-coating and evaporation for fabrication to avoid dissolution of the formed active layer.

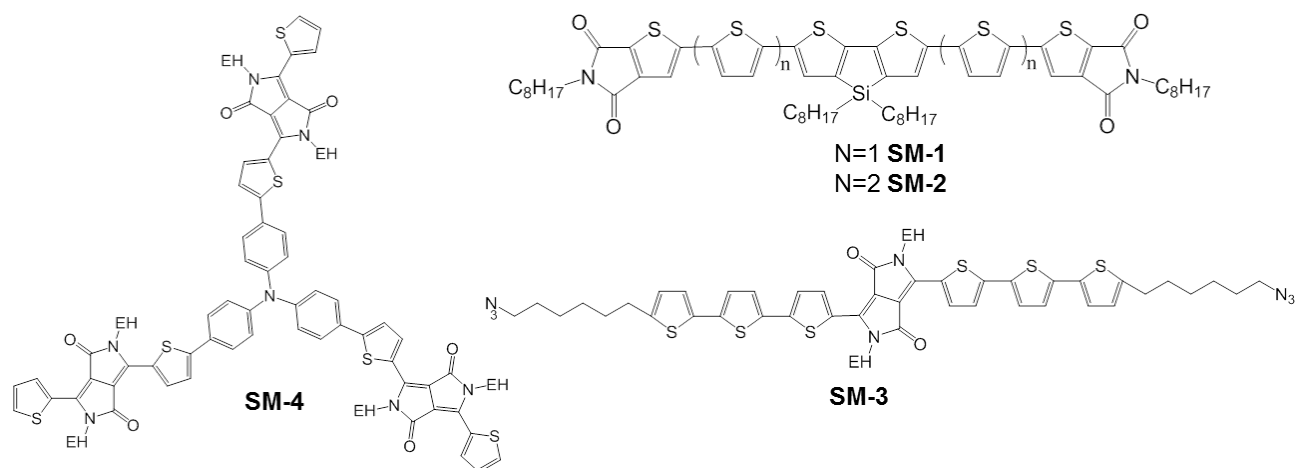


Figure 3.15: Schematic presentation of the small molecules used for fabricating OSC. EH=2-Ethylhexyl, OCT=octyl.

3.3.1. Device characterization

SM-1 and **SM-2** was synthesized and tested before the MRC was fully developed, therefore they were tested in devices prepared by spincoating. A normal geometry was applied in preparation of the OSCs with active layer thickness around 90 nm consisting of **SM-1** or **SM-2** in a 2:3 ratio with PCBM prepared with either a spin-coated layer PEDOT:PSS (4083) or evaporated MoO_x layer as HTL, as top-electrode aluminum was vacuum deposited. The performances of the prepared devices are listed in Table 3.4, which shows performances up to 1.2 % after annealing at 110 °C for **SM-1** using MoO_x for HTL and 1 % with PEDOT:PSS, and 0.75 % for **SM-2**, with very high V_{OC} from 0.88 to 0.97 V.

Table 3.4: Photovoltaic characteristics of OSCs prepared from SM-1 and SM-2 by spin-coating from a chlorobenzene solution with a thickness of 90-95 nm and vacuum deposited aluminum electrode.

<i>Active layer</i>	<i>Ratio</i>	<i>HTL</i>	<i>V_{oc}</i> (V)	<i>J_{sc}</i> (mA cm ⁻²)	<i>FF</i> (%)	<i>PCE</i> (%)
SM-1:PCBM ^a	2:3	4083	0.91	3.15	34.9	1.00
SM-1:PCBM ^a	2:3	MoO _x	0.97	2.60	47.6	1.20
SM-2:PCBM	2:3	4083	0.88	2.59	32.9	0.75

^aAnnealed at 110 °C for 3 min.

SM-3 was tested both as a donor and acceptor together with PCBM and P3HT, respectively. The prepared OSCs exhibits most potential when used as acceptor together with P3HT although the PCE achieved was only 0.067 %. This is twice the efficiency obtained for a **SM-3:PCBM** device which only reached 0.035% (Table 3.5). When cross-linking the active layer, the overall performance decreased. This effect was more pronounced when UV-irradiation was utilized for the cross-linking process than cross-linking by heating, which showed performances of 0.029 % and 0.06 %, respectively.

LBIC-images (Figure 3.16) of devices prepared with P3HT:**SM-3** showed effects from the printed silver on the obtained devices especially when the active layer have not been cross-linked. The areas under the silver electrode is less effected on image B and C compared to image A, indicating an increase in solvent resistance when the active layer is cross-linked.

Table 3.5: Photovoltaic characteristics of OSCs prepared from SM-3 with either PCBM or P3HT from a 40 mg/mL solution by roll-coating of all layers with the geometry (Ag/PH1000/ZnO/Active layer/PEDOT:PSS 5010/Ag). Cross-linking of the active layer was performed before coating 5010 on top.

Active layer	Ratio	Treatment	Solvent	V_{OC} (V)	J_{SC} ($mA\ cm^{-2}$)	FF (%)	PCE (%)
SM-3:PCBM	3:2	Non	DCM	0.53	0.24	27.4	0.035
SM-3:PCBM	3:2	Heat	DCM	0.62	0.075	25.3	0.012
SM-3:PCBM	3:2	UV	DCM	0.29	0.034	28.4	0.003
P3HT:SM-3	1:1	Non	CHCl ₃	0.53	0.34	37.6	0.067
P3HT:SM-3	1:1	Heat	CHCl ₃	0.61	0.25	39.1	0.060
P3HT:SM-3	1:1	UV	CHCl ₃	0.39	0.20	27.1	0.029

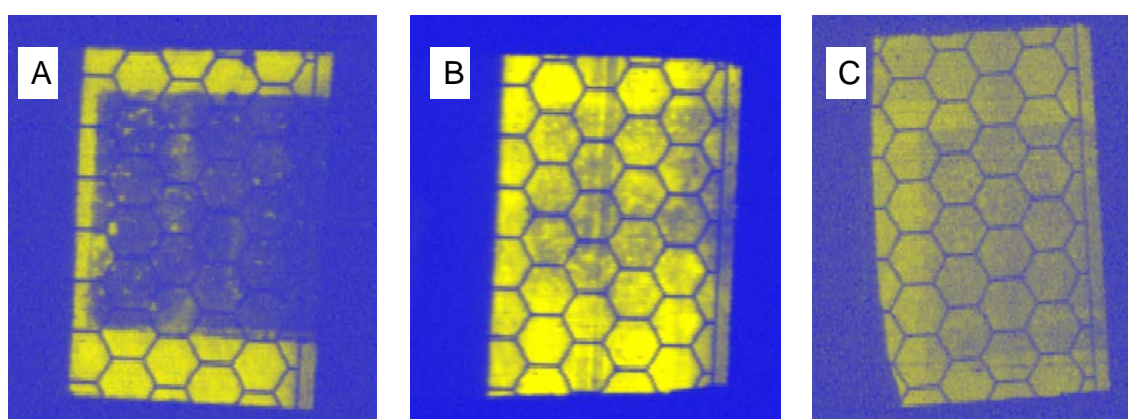


Figure 3.16: LBIC images of three P3HT:SM-3 OSC, A) No cross-linking, B) cross-linked by heat-treatment, C) cross-linked by UV-treatment.

Slot-die coating of **SM-4:PCBM** from high boiling solvents such as chlorobenzene or *o*-dichlorobenzene resulted in films of a poor quality due to picture-framing. The film quality could in theory be improved by enhancing the viscosity of the ink, by either increasing the concentration of the ink or by coating from a solvent with a lower boiling point. Even though devices were prepared with higher film quality by using higher concentrated inks and sol-

vents with lower boiling point, the performance of the obtained devices still had a low performance (Table 3.6). This is due to a lower J_{sc} which is ascribed to a less favorable morphology of the active layer when coating from low boiling point solvents.

Table 3.6: Fabrication details (solvent, ink concentration, and wet-thickness), and I-V characteristics of OSC prepared from SM-4:PCBM 1:1 ratio in the geometry (Ag/PH1000/ZnO/Active layer/PEDOT:PSS 5010 /Ag).

Active layer	Solvent	Conc. ($mg mL^{-1}$)	Wet-thickness (μm)	V_{oc} (V)	J_{sc} ($mA cm^{-2}$)	FF (%)	PCE (%)
SM-4	Toluene	30	19	0.72	0.27	33	0.065
SM-4	DCM	16	62	0.77	0.43	27	0.09
SM-4	CF	25	31	0.80	0.52	33	0.14
SM-4	CB	60	13	0.75	0.93	30	0.21
SM-4	CB	80	10	0.73	0.73	33	0.17
SM-4	CB/ <i>o</i> -DCB	80	6	0.64	0.83	31	0.17

From the three examples above where OSCs are prepared from small molecules, it can be seen that preparation of OSCs by slot-die coating on MRC revealed some of the known drawbacks regarding small molecules. The coated films had a tendency to picture-frame when coated from high boiling point solvents in cases where the small molecules were used as donor together with PCBM. This was solved by using more concentrated inks to be able to coat with a very low wet thickness or by changing to a low boiling point solvent such as dichloromethane or chloroform causing a rapid increase in viscosity after deposition. However, in the case of **SM-4** coating with low boiling point solvents resulted in OSCs with a lower performance than obtained for chlorobenzene, possibly due to a changed morphology. Coating from a low boiling point solvent would usually result in film with less phase separation between the two components.

Another problem encountered in the preparation of OSCs from small molecule was dissolution of the coated layer as seen for **SM-3** in Figure 3.16. Cross-linking of the active layer only diminished the dissolution problem, it did not solve them completely. It did, however, also have an undesirable effect on the PCE which decreased after the active layer was cross-linked.

3.4. Preparation of OSCs from aqueous inks

The basic idea behind the application of aqueous nanoparticle inks are threefold, as described in Section 2.2.1.1, to produce inks which have a pre-organized morphology, to reduce the use of organic solvent during fabrication of OSCs, and to lower the embodied energy in the OSCs. The aqueous inks consist of organic nanoparticles prepared from a blend of donor and acceptor materials, and therefore offers the possibility to have an internal morphology that can be controlled during the fabrication of the ink.

OSCs were prepared from the aqueous inks described in Section 2.2.1 on ITO/ZnO by coating at the large scale R2R coater or on Flextrode by the MRC.

3.4.1. Printed on an ITO substrate

Processing of aqueous inks on the large scale R2R coater proved to be a difficult task. Significant dewetting was observed (Figure 3.17A and B) when coating in an inverted geometry on an ITO-ZnO substrate. Investigating the surface of the ZnO stripe, revealed a thin layer of nanoparticles present on the entire ZnO stripe where the dewetting had occurred, as shown in Figure 3.17A. The coating had thus resulted in an initial wetting of the entire stripe, this phenomenon is known as “poisoning”. The problem was partially solved by addition of a nonionic fluorosurfactant (FSO-100) to the ink in a concentration of 5 mg mL^{-1} , which improved the wetting properties but not sufficiently to prepare a high quality film (Figure 15C).

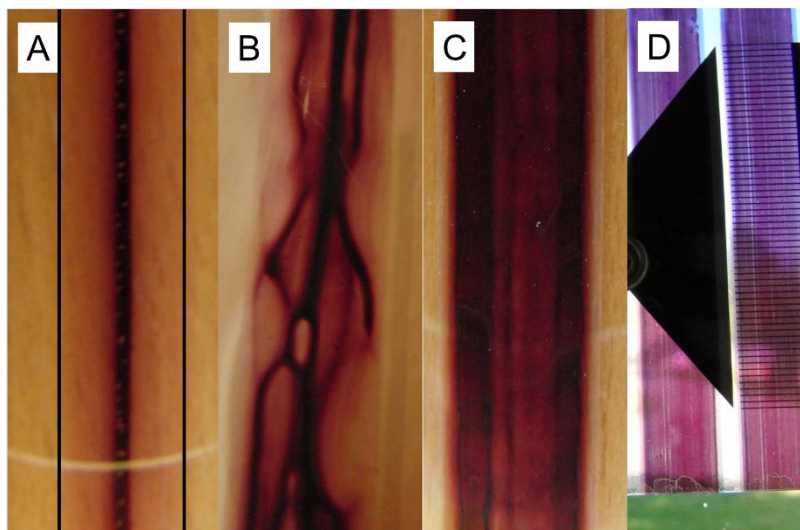


Figure 3.17: Learning curve when trying to coat water-based inks. A) Massive dewetting into a single stripe, B) severe dewetting into to several “waves”, C) covering film inhomogeneous in thickness, D) covering films with minor thickness variations.

For further improvement of the film quality, it was found necessary for the wet films to dry before the foil went over the first roller from the coating head into the oven. This condition was fulfilled by lowering the web-speed and applying a heat-gun onto the PET-substrate (Figure 3.18A), the resulting film can be seen in Figure 3.17D. As a consequence of the excessive heating the nanoparticles precipitated in the coating-head. This was solved by applying water-cooling to the coating-head and air-cooling of the tube as shown in Figure 3.18B. To finish up the OSCs a conductive electrode of PEDOT:PSS 5010 (5010:IPA 10:5 w/w) was used with screen-printed PV410 silver-paste.

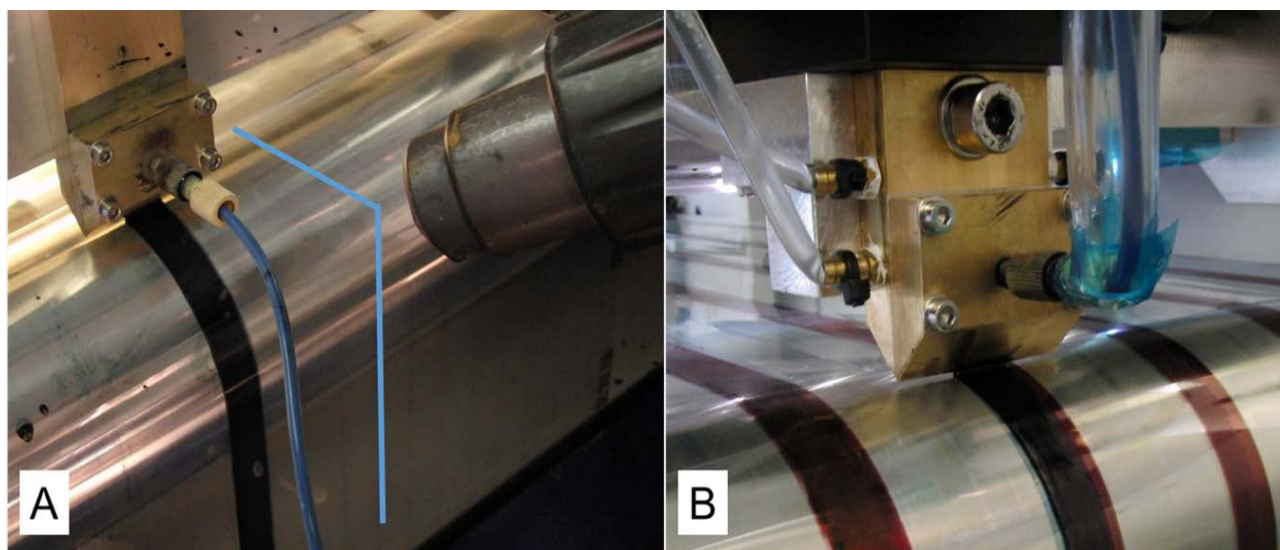


Figure 3.18: Improving methods for the coating with water-based inks. A) Applying heat-gun for faster drying of the film, B) cooling of the coating-head and tube to avoid precipitation of nanoparticles.

3.4.1.1. Device characterization

Using the coating parameters determined above OSCs were fabricated on an ITO substrate from aqueous inks prepared from four different polymers (**P1**, **P2**, **P3**, and P3HT structures and preparation parameters can be seen in Section 2.2.1). OSCs with performances from 0.07 and up to 0.55 % were obtained on an area of 4.2 cm² (Figure 3.19). The V_{OC} for the devices is approximately 0.1 V lower than what is generally obtained when coating from ordinary organic solvents for **P1**, and P3HT as seen in Table 3.3.

The J_{SC} values for the OSCs were quite low. This is ascribed to a non-optimal morphology of the active layer, since annealing of the nanoparticles at 140 °C have been reported to influence the efficiency negatively.[22]

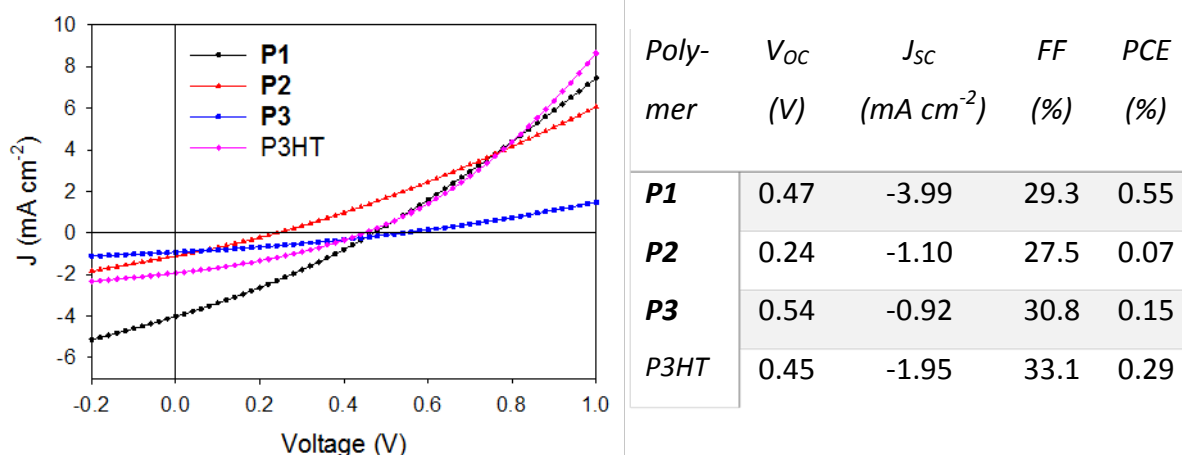


Figure 3.19: I-V characteristics and photovoltaic performance for the four different nanoparticle inks, which have been coated on ITO/ZnO substrate with PEDOT:PSS 5010 as top electrode.

3.4.2. Printed on Flextrode

Changing the substrate from ITO/ZnO to Flextrode and the coating procedure from R2R to MRC influenced the coatability of the aqueous inks. Thus, a new set of coating issues occurred that could not be solved by addition of FSO-100 or extensive heating of the substrate as in the previous experiments. It was observed that the first 10 cm of coating resulted in films of a decent quality after which dewetting started to occur. This phenomenon is known as “poisoning” of the meniscus, it appears as a consequence of a specie from either the ink or the substrate has been concentrated in the meniscus causing the wetting properties to change. Through additional experiments, it was found that addition of as little as 2 % ethylene glycol to the ink significantly improved the coatability of the ink to produce films with good quality. PEDOT:PSS F010 was used as top electrode instead of the previously used PEDOT:PSS 5010. OSCs prepared on Flextrode show similar performances to what was obtained when printing on ITO/ZnO as seen in Figure 3.19 and Figure 3.20. P3HT:PCBM based nanoparticles gave a performance of 0.29 % and 0.28 %, respectively.

The rather low V_{oc} for OSCs on Flextrode was suspected to be due to high surface roughness of the active layer. A possible way to reduce the surface roughness was to coat an organic solvent (CF, CB, or DCM) on top of the coated active layer, in order to dissolve the top

part of the active layer, thereby reducing the surface roughness. This treatment had, however, little influence on the V_{oc} obtained from the devices.

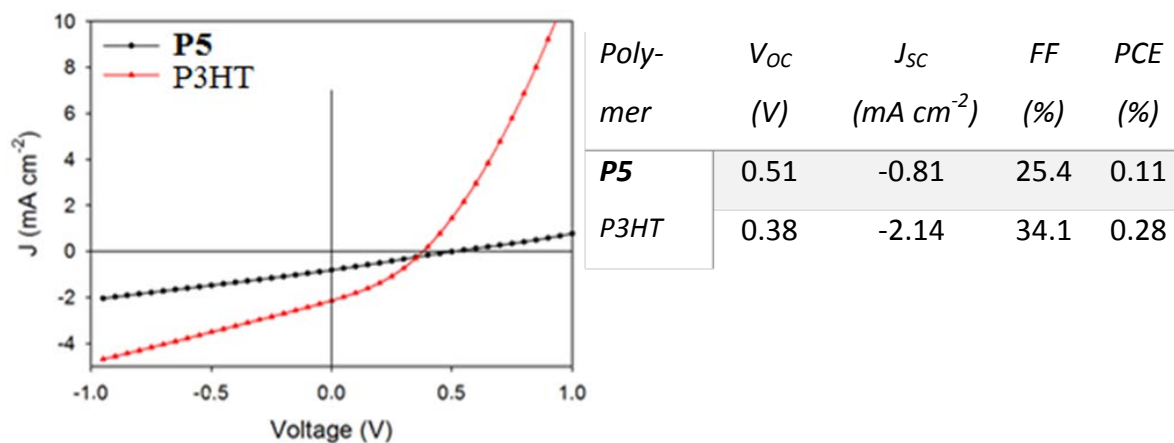


Figure 3.20: I-V characteristics for two different nanoparticle inks, which has been coated on Flex-trode with F010 PEDOT:PSS as top-electrode.

3.4.3. X-ray analysis of the morphology

The porosity of the coated nanoparticle ink was investigated by the X-ray method known as ptycography at the synchrotron in Switzerland. Samples were prepared by scraping off flakes of a coated film and placing them in a capillary, the sample was prepared from the P3HT:PCBM-nanoparticles presented in entry 7 in Table 2.2. The data-reconstruction obtained from the X-ray studies is shown in Figure 3.21, revealing that the coated films are porous. The green areas contain low density material (air+organic material) and the red areas contain higher density material (organic material). The X-ray experiments and data-analysis were conducted by Arvid Pihl Lauritzen Böttiger and Jens Wenzel Andreasen both from DTU Energy Conversion.

The porous film could be one of the reasons for the poor performance of the OSCs prepared from aqueous inks.

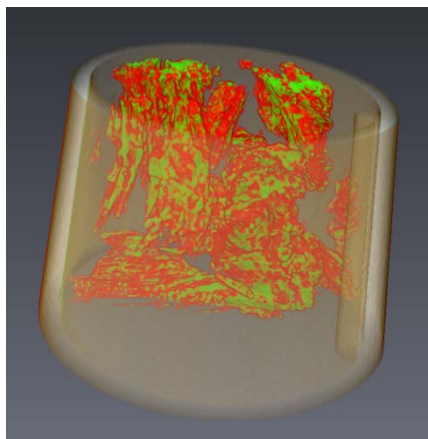


Figure 3.21: Film deposited from nanoparticle based ink (entry 7 Table 2.2), scraped off, placed in a capillary, and analyzed by ptychography on the synchrotron in Switzerland. The red colored areas are organic material whereas the green areas are vacancies. The x-ray sample preparation, measurement and data-treatment were conducted by Arvid Pihl Lauritzen Böttiger and Jens Wenzel Andreasen both from DTU Energy Conversion.

3.5. Summary

A laboratory scale approach (the MRC) for preparation of OSCs which allows the use of small amounts of material has been demonstrated. The MRC enables coating of complete OSCs by slot-die coating and flexographic printing under ambient conditions as is the case for the large-scale R2R coater. The MRC is capable of preparing OSCs with an active layer consisting of P3HT:PCBM with efficiencies up to 2.9 % when a three layered combination of PEDOT:PSS is applied as top electrode, when PEDOT:PSS 5010 is applied as top electrode PCEs around 2 % are generally obtained. This is just above the PCE (1.8 %) generally obtained for OSCs prepared on the R2R coater. This difference (2 % to 1.8 %) is ascribed to the smaller area of the prepared OSCs on the MRC. Thus, the PCE obtained for OSCs prepared on the MRC are similar to OSCs prepared by R2R.

Several other polymers were applied in the processing of OSCs on the MRC in the search for polymers with the potential to outperform P3HT on large scale production. OSCs prepared from these polymers gave PCEs between 0.8 and 2.5 %. It was further shown that a change in coating solvent can have a great influence on the PCE of the prepared OSC, as seen

for **P1**. The PCE increased from 0.84 % to 1.3 % by coating from chloroform instead of chlorobenzene. This is ascribed to an improvement in morphology of the active layer. In order to fully investigate which of the tested polymers have the potential for large scale OSC productions, IPCE measurements were conducted to determine which of the polymers had their main contribution where Flextrode has the highest transmission. Four of the seven polymers tested had a maximum contribution in the range from 480 nm to 700 nm, which is the range where the photon flux is greatest when Flextrode is applied as substrate.

Preparation of OSCs with an active layer consisting of small molecules were successfully by both spincoating and slot-die coating on the MRC. However, these experiments showed some of the weaknesses associated with wet processing of small molecules such as dissolution of the active layer during coating of subsequent layers and poorer film quality due to picture framing. The cross-linkable, **SM-3**, had little success in OSCs. It did, however, reveal that cross-linking of the active layer increased the solvent resistance and thereby counteracting dissolution. **SM-4** coated with PCBM as electron acceptor resulted generally in films of a poor quality due to picture-framing. It was attempted to solve this by coating highly concentrated inks and by changing to a low boiling point solvent. Both of these attempts improved the quality of the film, but the best performing OSC was still coated from chlorobenzene with a concentration of 60 mg mL⁻¹. OSCs prepared from **SM-1** with PCBM by spin coating resulted in a PCE of up to 1.2 % when prepared in normal geometry.

The aqueous inks prepared in Section 2.2 were coated by slot-die coating on either the R2R coater or the MRC, in both cases difficulties were observed. When coating on ITO substrates on the R2R coater significant dewetting problems occurred. They were solved by adding a known wetting agent (FSO-100) to the aqueous ink in a concentration of 5 mg mL⁻¹ and by increasing the temperature of the substrate directly after the coating head, in order to ensure a faster drying. The PCEs of OSCs, prepared in this manner, were between 0.07 and 0.55 % depending on the polymer. The relatively low performances are ascribed to shunting of the devices together with an unfavorable morphology after annealing at 140 °C. The substrate was changed from an ITO-based substrate to Flextrode, which gave new coating difficulties. These could not be solved by addition of FSO-100 or application of additional heat. Instead it was found that the addition of ethylene glycol to the ink enhanced the coatability,

thereby making it possible to prepare OSCs. OSCs were prepared from nanoparticles based on two polymers (P5 and P3HT) on the MRC with PCE of 0.1 and 0.28 %, respectively. The PCE of nanoparticles containing P3HT:PCBM is in good agreement with that obtained on ITO. These results show that it is possible to fabricate OSCs using aqueous inks although the PCEs were relatively low compared to PCEs obtained when coating from standard ink organic solutions.

3.6. References

- [1] N. Espinosa, M. Hösel, D. Angmo, and F. C. Krebs, "Solar cells with one-day energy payback for the factories of the future," *Energy & Environmental Science*, vol. 5, no. 1, pp. 5117–5132, 2012.
- [2] K. Norrman, A. Ghanbari-Siahkali, and N. B. Larsen, "6 Studies of spin-coated polymer films," *Annual Reports Section "C" (Physical Chemistry)*, vol. 101, pp. 174–201, 2005.
- [3] F. C. Krebs, "Fabrication and processing of polymer solar cells: A review of printing and coating techniques," *Solar Energy Materials and Solar Cells*, vol. 93, no. 4, pp. 394–412, 2009.
- [4] R. Søndergaard, M. Hösel, D. Angmo, T. T. Larsen-olsen, and F. C. Krebs, "Roll-to-roll fabrication of polymer solar cells As the performance in terms of power conversion efficiency and operational," *materials today*, vol. 15, no. 1, pp. 36–49, 2012.
- [5] R. R. Søndergaard, M. Hösel, and F. C. Krebs, "Roll-to-Roll fabrication of large area functional organic materials," *Journal of Polymer Science Part B: Polymer Physics*, vol. 51, no. 1, pp. 16–34, 2013.
- [6] H. F. Dam and F. C. Krebs, "Simple roll coater with variable coating and temperature control for printed polymer solar cells," *Solar Energy Materials and Solar Cells*, vol. 97, pp. 191–196, 2012.
- [7] K. Leppänen, B. Augustine, J. Saarela, R. Myllylä, and T. Fabritius, "Solar Energy Materials & Solar Cells Breaking mechanism of indium tin oxide and its effect on organic photovoltaic cells," *Solar Energy Materials and Solar Cells*, vol. 117, pp. 512–518, 2013.
- [8] M. Hösel, R. R. Søndergaard, M. Jørgensen, and F. C. Krebs, "Fast Inline Roll-to-Roll Printing for Indium-Tin-Oxide-Free Polymer Solar Cells Using Automatic Registration," *Energy Technology*, vol. 1, no. 1, pp. 102–107, 2013.

- [9] F. C. Krebs, M. Hösel, M. Corazza, B. Roth, M. V. Madsen, S. a. Gevorgyan, R. R. Søndergaard, D. Karg, and M. Jørgensen, "Freely available OPV-The fast way to progress," *Energy Technology*, vol. 1, no. 7, pp. 378–381, 2013.
- [10] J.-S. Yu, I. Kim, J.-S. Kim, J. Jo, T. T. Larsen-Olsen, R. R. Søndergaard, M. Hösel, D. Angmo, M. Jørgensen, and F. C. Krebs, "Silver front electrode grids for ITO-free all printed polymer solar cells with embedded and raised topographies, prepared by thermal imprint, flexographic and inkjet roll-to-roll processes," *Nanoscale*, vol. 4, no. 19, pp. 6032–6040, 2012.
- [11] J. Hou, H.-Y. Chen, S. Zhang, G. Li, and Y. Yang, "Synthesis, characterization, and photovoltaic properties of a low band gap polymer based on silole-containing polythiophenes and 2,1,3-benzothiadiazole.," *Journal of the American Chemical Society*, vol. 130, no. 48, pp. 16144–16145, 2008.
- [12] M. Wang, X. Hu, P. Liu, W. Li, X. Gong, F. Huang, and Y. Cao, "Donor Acceptor Conjugated Polymer Based on Naphtho[1,2-c:5,6-c']bis[1,2,5]thiadiazole for High-Performance Polymer Solar Cells," *Journal of American Chemical Society*, vol. 133, pp. 9638–9641, 2011.
- [13] Z.-G. Zhang, J. Min, S. Zhang, J. Zhang, M. Zhang, and Y. Li, "Alkyl chain engineering on a dithieno[3,2-b:2',3'-d]silole-alt-dithienylthiazolo[5,4-d]thiazole copolymer toward high performance bulk heterojunction solar cells," *Chemical communications (Cambridge, England)*, vol. 47, no. 33, pp. 9474–9476, 2011.
- [14] R. Duan, L. Ye, X. Guo, Y. Huang, P. Wang, S. Zhang, J. Zhang, L. Huo, and J. Hou, "Application of Two-Dimensional Conjugated Benzo[1,2- b :4,5- b ']dithiophene in Quinoxaline-Based Photovoltaic Polymers," *Macromolecules*, vol. 45, no. 7, pp. 3032–3038, 2012.
- [15] S. Günes, H. Neugebauer, and N. S. Sariciftci, "Conjugated polymer-based organic solar cells.," *Chemical reviews*, vol. 107, no. 4, pp. 1324–1338, 2007.
- [16] Y. Lin, Y. Li, and X. Zhan, "Small molecule semiconductors for high-efficiency organic photovoltaics.," *Chemical Society reviews*, vol. 41, no. 11, pp. 4245–4272, 2012.
- [17] X.-H. Zhu, J. Peng, Y. Cao, and J. Roncali, "Solution-processable single-material molecular emitters for organic light-emitting devices.," *Chemical Society reviews*, vol. 40, no. 7, pp. 3509–3524, 2011.
- [18] Y. Sun, G. C. Welch, W. L. Leong, C. J. Takacs, G. C. Bazan, and A. J. Heeger, "Solution-processed small-molecule solar cells with 6.7% efficiency," *Nature materials*, vol. 11, pp. 44–48, 2012.

- [19] Z. Li, G. He, X. Wan, Y. Liu, J. Zhou, G. Long, Y. Zuo, M. Zhang, and Y. Chen, "Solution Processable Rhodanine-Based Small Molecule Organic Photovoltaic Cells with a Power Conversion Efficiency of 6.1%," *Advanced Energy Materials*, vol. 2, no. 1, pp. 74–77, 2012.
- [20] M. T. Lloyd, J. E. Anthony, and G. G. Malliaras, "Photovoltaics from soluble small molecules Solution-processable small molecules have attractive features for," vol. 10, no. 11, pp. 34–41, 2007.
- [21] A. Mishra and P. Bäuerle, "Small molecule organic semiconductors on the move: promises for future solar energy technology.," *Angewandte Chemie (International ed. in English)*, vol. 51, no. 9, pp. 2020–2067, 2012.
- [22] S. Ulum, N. Holmes, D. Darwis, K. Burke, D. Kilcoyne, X. Zhou, W. Belcher, and P. Dastoor, "Determining the structural motif of P3HT:PCBM nanoparticulate organic photovoltaic devices," *Solar Energy Materials and Solar Cells*, vol. 110, pp. 43–48, 2013.

4. Tandem OSC processing

4.1. Introduction

Tandem OSCs were first described in 1986 by Tang.[1] In comparison to single junction OSCs tandem OSCs have two major advantages: 1) reduction of the thermalization and 2) better utilization of the solar irradiation spectrum.[2-5] Thermalization is due to the absorption of photons containing higher energy than the band gap of the absorber, leading to the formation of a “hot electron”. This hot electron will lose the excess energy while “relaxing” down to the LUMO of the absorber (Figure 4.1A).[2,3] The thermalization can be reduced by stacking polymers with different band gaps on top of each other having a high band gap (HBG) material absorbing the photons with the highest energy, while keeping an optimum alignment with the LUMO of the acceptor. Most polymers:PCBM blends have a film absorption spectrum as shown in Figure 4.1B with a strong absorption in a narrow wavelength range. The combination of two polymers such as **P1** and P3HT will therefore provide an optimal coverage of the solar irradiation spectrum from 400 to 850 nm.

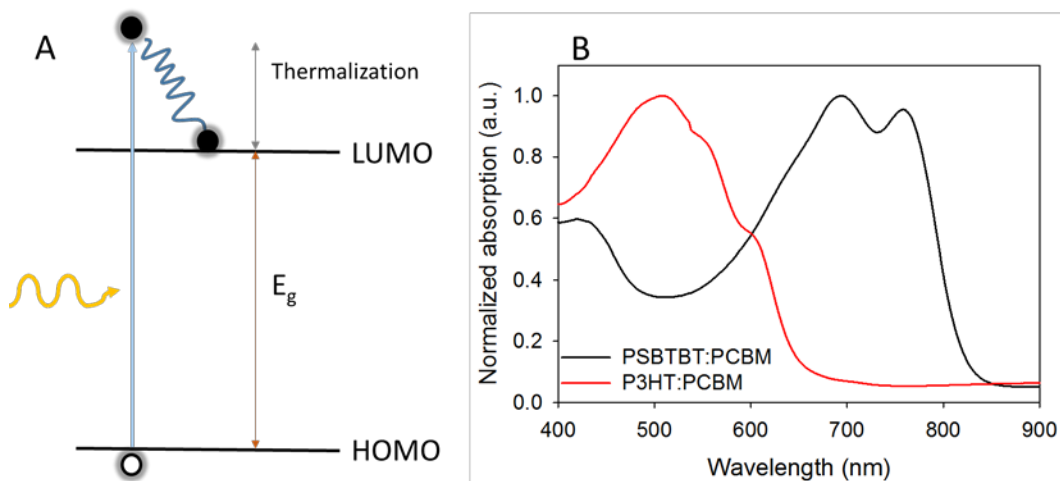


Figure 4.1: A) Illustration of the thermalization loss, when photons with a higher energy than the band gap is absorbed.[2,3] B) Normalized film absorption of two polymers with different band gaps in a blend with PCBM. P1 being a low bandgap polymer with E_g of 1.4 eV and P3HT with an E_g around 1.9 eV.

The different absorption spectra of the two polymers shown in Figure 4.1B, can be combined by stacking two sub-cells separated by an intermediate layer.[2] The intermediate layer consists of a HTL and an ETL material. At the interface between these materials recombination of holes and electrons, generated in the respective sub-cells, will occur.[6] A schematic illustration of tandem OSC in the two geometries is shown in Figure 4.2 where the two sub-cells consist of a HBG polymer in 1st sub-cell and the low band gap (LBG) polymer in 2nd sub-cell.

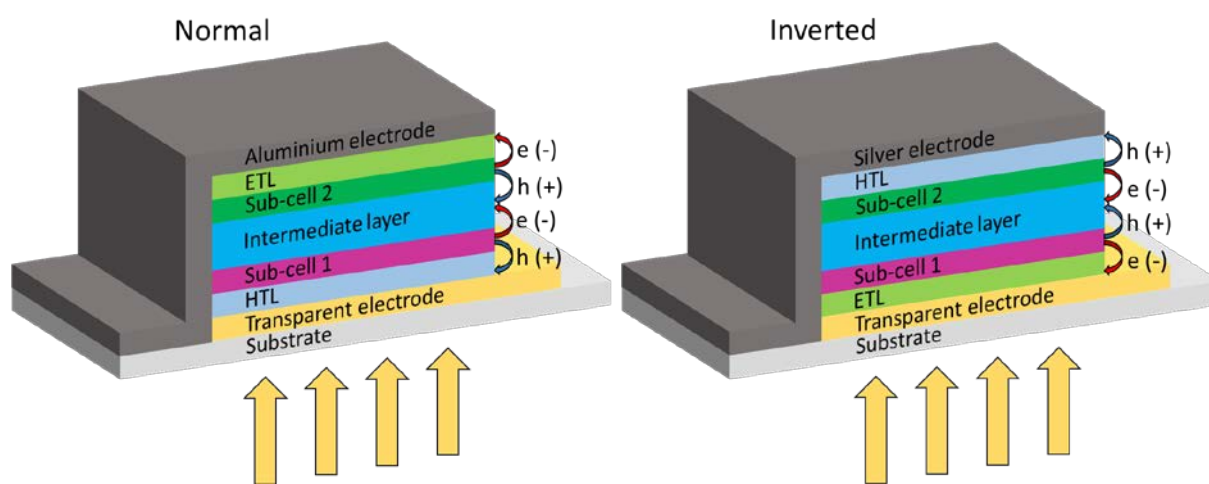


Figure 4.2. Schematic build-up of tandem OSC in the two general geometries; normal and inverted. The intermediate layer will consist of two materials, a HTL and an ETL material, having recombination of hole from one sub-cell and electrons from the other within when an inverted geometry is employed.

The V_{OC} of a tandem OSC, build up in series, will be the sum of the V_{OC} of both sub-cells as seen in Equation 4.1.[3]

$$V_{OC, \text{ tandem}} = V_{OC, 1^{\text{st}} \text{ sub-cell}} + V_{OC, 2^{\text{nd}} \text{ sub-cell}} \quad (\text{Equation 4.1})$$

Whereas the J_{SC} of the tandem OSC are determined by the sub-cell with the lowest J_{SC} as seen in Equation 4.2.[3]

$$J_{SC, \text{ tandem}} = \min[J_{SC, 1^{\text{st}} \text{ sub-cell}}, J_{SC, 2^{\text{nd}} \text{ sub-cell}}] \quad (\text{Equation 4.2})$$

Even though the first tandem OSC was prepared in 1986 issues within processing of tandem OSCs still occurs such as intermixing with the lower layer when depositing subsequent layers. The first solution to the intermixing was to use vacuum deposition as the primary method for parts of the intermediate layer and the 2nd sub-cell.[4] Later coating from orthogonal solvents was utilized to avoid dissolution of the previously deposited layers.[6] A more recent development has focused on wet processing of the entire stack by preparing a solvent resistant intermediate layer. This was first presented by Hau *et al.*[7] in 2010 and Larsen-Olsen *et al.*[8] in 2011. Both studies present inverted tandem devices prepared entirely by solution-processing via spincoating. They applied two different intermediate layers consisting of either PEDOT:PSS/ZnO or V₂O₅/ZnO and gave PCEs of 2.9 % and 1.4 %, respectively, using P3HT:fullerene blend in both sub-cells. Solution processing of tandem devices was taken to the next level by Ning *et al.*[9], who prepared inverted tandem OSCs by doctor-blading of the entire stack increasing the complexity of the preparation. They employed an intermediate layer of PEDOT:PSS and ZnO, and the as-prepared cells reached an efficiency of 4.85 % with sub-cells consisting of two different polymers. These results and intermediate layers are a timeline for the processing of tandem OSCs, the PCEs obtained are, however, not the highest achieved efficiencies. The highest efficiencies was introduced by Heliatek[10] and You *et al.*[11], who report 12 % and 10.6 %, respectively. Heliatek prepared a 1.1 cm² tandem device by vacuum deposition of small molecules whereas You *et al.* used spin coating of the entire stack except for the electrode to prepare a 0.1 cm² tandem device.

Tandem OSC will in general always consist of sub-cells with different polymers in order to present good coverage of the visible irradiation spectrum from 300 nm and upwards. The polymers, which was available for this study, are presented in Section 3.2.2.3 on Page 66. In order to obtain the best possible combination of polymers it is necessary to calculate the theoretical current within the absorption interval. The absorption interval was defined by recalling the IPCE data presented in Figure 3.14. Here, it is shown that two polymers (**P1** and **P8**) have a contribution up to 850 nm ($E_g \sim 1.45$ eV), therefore 1.45 eV is the lower limit of the band gap in this study. The maximum current density available harvesting light in the interval from 4 eV to 1.45 eV nm is 20.4 mA cm⁻² corrected for the transmission of Flextrode. This results in a maximum current of 10.2 mA cm⁻² for each of the two sub-cells. In Figure 4.3 the

approx. photon energies are marked, illustrating the band gaps for the HBG polymer and the LBG polymer in order to achieve a maximum theoretical current density. This is at approximately 2 eV and 1.45 eV nm for HBG and LBG, respectively.

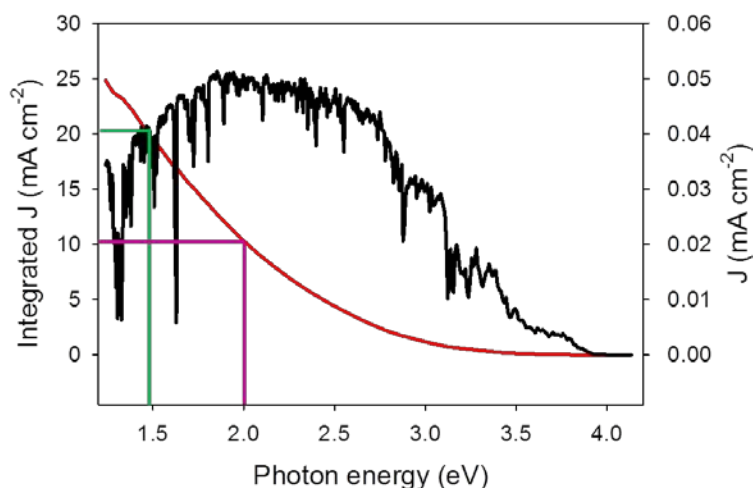


Figure 4.3: Maximum current density achievable per nanometer on Flextrode with Melinex substrate (black line) and the integrated current density (red line). Purple and green lines illustrate a theoretical material match for a tandem OSC with a max J_{sc} of 10 mA cm^{-2} when the material in the two sub-cells have band gaps of 2 eV and 1.46 eV.

These thoughts and arguments have been used to decide which polymers to apply as 1st and 2nd sub-cells later in this chapter. The chapter presents a tandem stack where all layers can be processed by slot-die coating or flexographic printing.

4.2. Tandem OSC prepared by wet-processing

Developing a layer stack for tandem OSC, where all layers are deposited either by slot-die coating or flexographic printing proved to be a difficult task since a multi layered stack leaves very little room for coating-errors. The tandem stack was started with Flextrode as the transparent electrode which caused an initial dissolubility challenge for the 1st sub-cell. As seen in Figure 4.4A dissolution of the 1st sub-cell occurred around the honeycomb silver-grid when pure chloroform was slot-die coated on top of the intermediate layer of a tandem stack having a 250 nm thick 1st sub-cell. This led us to analysis of the silver pattern by Dektak

Profilometer, the resulting height profile showed four silver spikes within a scan-length of 300 μm ; where the height of the spikes are between 300 and 600 nm (Figure 4.4B). The dissolution challenge was overcome by coating a thicker 1st sub-cell to embed a majority of the silver spikes in the 1st sub-cell; it was found that a 1st sub-cell with a theoretical thickness of 480 nm was sufficient.

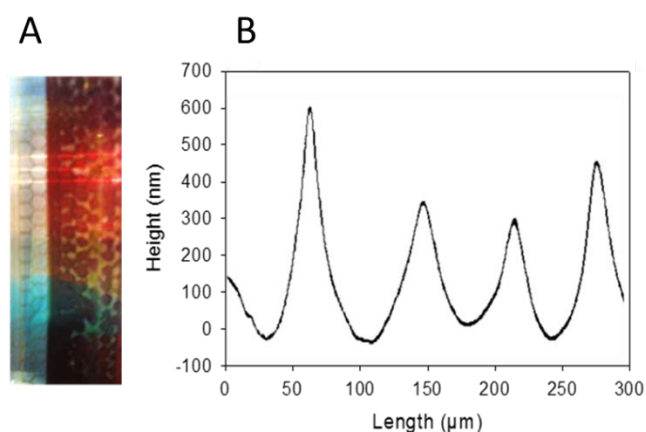


Figure 4.4: A) The first coated active layer (200-250 nm thin) dissolved around the silver grid when depositing chloroform on top of the intermediate layer. B) Height profile of the edge of a silver stripe on the Flextrode measured by a Dektak Profilometer. The height profile shows four silver spikes are present within a scan-length of 300 μm , varying from around 300 nm to 600 nm in height.

Preliminary stack development involved tandem OSC prepared with P3HT:PCBM in both sub-cells. P3HT is an easily accessible and well-known polymer widely used in R2R coating of OSCs and therefore almost guaranteed to prepare functional devices. The low transmission caused by the application of a thick (480 nm) 1st sub-cell gives problems, when preparing tandem cells with the same materials in both sub-cells. To overcome the low light intensity reaching the 2nd sub-cells a mirror set up was utilized allowing the devices to be illuminated from both sides with the same intensity. The mirror set up is buildup by placing two mirrors in a 90 degree angle and in between these the tandem OSC can be mounted at a 45 degree angle for two sided illumination (Figure 4.5). The mirror set up resulted in an irradiation intensity of 700 W m^{-2} from each side when placed under a solar simulator at 1000 W m^{-2} . The I-V curve of the first successfully prepared tandem device is shown in Figure 4.6.

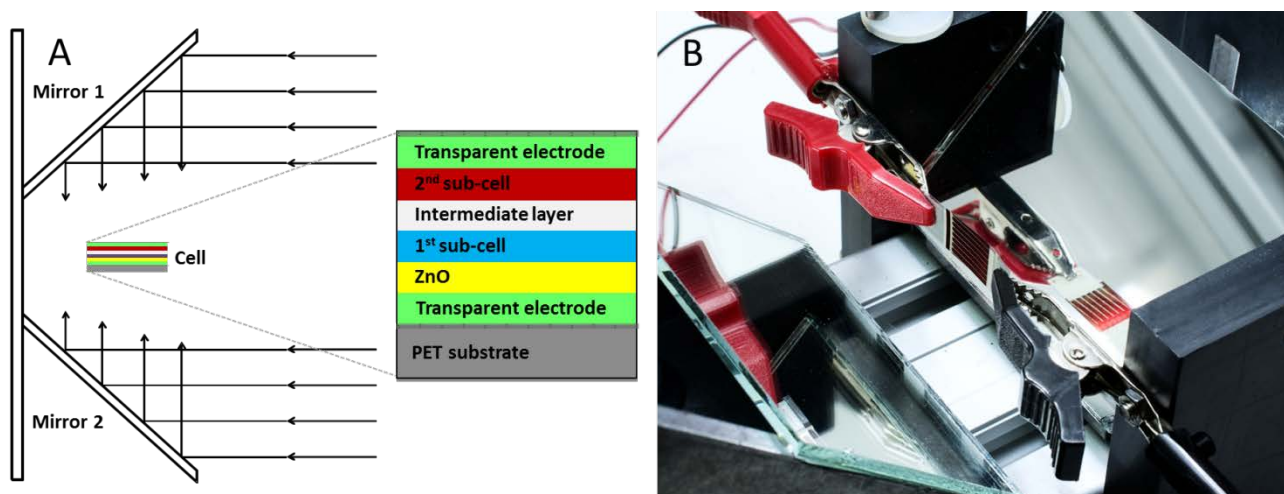


Figure 4.5: A) schematic build-up of the mirror set up used to characterize the prepared tandem OSC. B) Mirror set up for testing tandem with identical sub-cells, allowing the tandem OSC to be illuminated from both sides with an irradiation intensity of 700 W m^{-2} pr. side. Reproduced with permission from Elsevier.

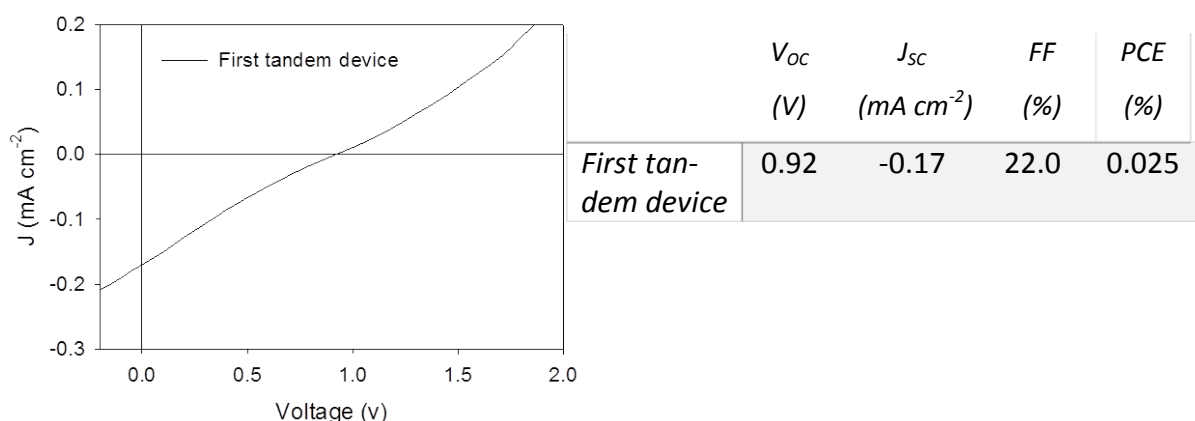


Figure 4.6: Photovoltaic characteristics of the first tandem fully wet processed and roll coated OSC prepared with P3HT:PCBM in both sub-cells.

4.2.1. Intermediate layer

The main issue encountered during fabrication of tandem OSC was the preparation of a solvent resistant intermediate layer. Recent literature presents solution based tandem devices prepared with intermediate layers consisting of $\text{V}_2\text{O}_5/\text{ZnO}$ [12] or PEDOT:PSS/ZnO[9] using spin-coating or doctor-blading as deposition methods. $\text{V}_2\text{O}_5/\text{ZnO}$ have previously been

used to prepare inverted tandem OSCs in our laboratory and were therefore obvious to use in the first attempts. The first round of tandem OSCs were prepared with intermediate layers consisting of inorganic oxides, V_2O_5 or MoO_x with ZnO with limited success. The problem of solvent resistance remained as shown in the microscopy image in Figure 4.7A. A large number of cracks were observed after coating of the 2nd sub-cell, this led to the conclusion that the intermediate layer lacked solvent resistance.

The other literature approach employed an intermediate layer of PEDOT:PSS/ZnO such as PEDOT:PSS 4083 or HIL 3,3 (for specifications see Table 3.1). These PEDOT:PSS materials are water-based making slot-die coating on top of P3HT:PCBM difficult due to significant dewetting. This was solved by coating a V_2O_5 layer as a compatibilizer which improved the wetting properties for PEDOT:PSS 4083 and HIL 3,3. V_2O_5 was chosen as compatibilizer because it is a HTL and have previously proven functional in inverted tandem devices.[8] Figure 4.7B shows a microscopy image acquired after deposition of the 2nd sub-cell, revealing a smooth crack-free surface. An intermediate layer consisting of V_2O_5 , PEDOT:PSS 4083, and ZnO therefore prevent intermixing between the sub-cells. Using PEDOT:PSS HIL 3,3 instead of PEDOT:PSS 4083 did not offer the same level of solvent resistance and was therefore not used in later experiments.

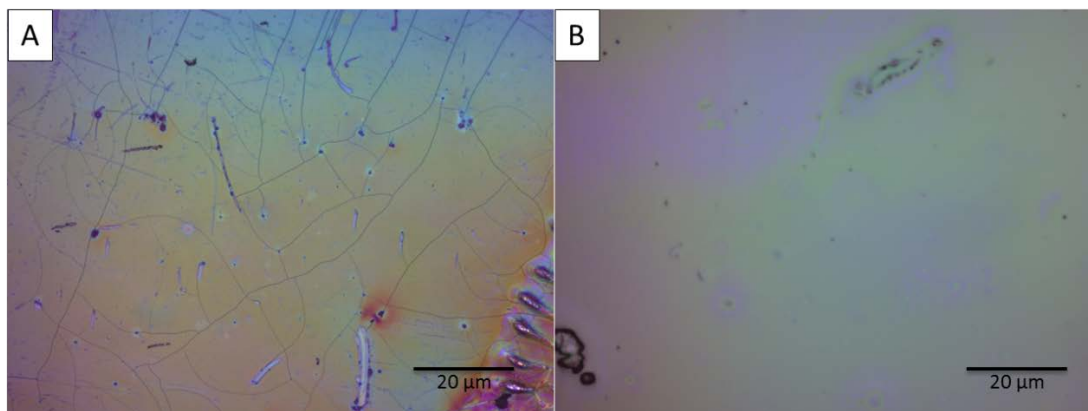


Figure 4.7: Variations of the intermediate layer to optimize solvent resistance. Microscopy images are shown after coating of the 2nd sub-cell. A) An intermediate layer consisting of MoO_x and ZnO with P3HT coating on top. The image shows significant crack formations. B) Intermediate layer with MoO_x, PEDOT:PSS 4083, and ZnO with P3HT coated on top. No cracks are seen in the layer when using a PEDOT:PSS 4083 layer as a HTL and solvent blocking layer. Reproduced with permission from Elsevier.

Optimization of the intermediate layer was conducted by varying the thickness on each of the three layers (V₂O₅, PEDOT:PSS 4083, and ZnO) on the tandem stack shown in Figure 4.8.

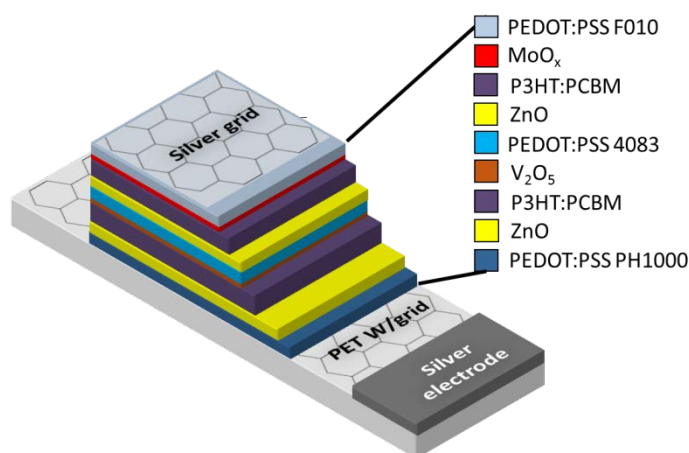


Figure 4.8: The tandem stack used for optimization of the intermediate layer consisting for V₂O₅, PEDOT:PSS 4083, and ZnO.

A variation in the thickness of the compatibilizing V₂O₅ layer was obtained by changing the ratio between vanadium triisopropoxide (VTIP) and isopropanol (IPA) (1:100, 1:1000, and 1:2000), while keeping the wet thickness constant at eight μm. The resulting photovoltaic

characteristics are shown in Table 4.1, with the 1:1000 ratio giving the best performing tandem OSC. The lower performance for the ratio 1:2000 is ascribed to a too thin V_2O_5 layer. When coating the subsequent PEDOT:PSS 4083 on this thickness dewetting occurred in spots thus allowing intermixing of the sub-cells.

Table 4.1. Thickness variation of the V_2O_5 compatibilizer layer. Layer thickness was controlled by coating a VTIP:IPA solution with different ratios (1:100, 1:1000, and 1:2000) while keeping a constant wet thickness at 8 μm . The remaining two intermediate layers were PEDOT:PSS 4083:IPA 1:2 coated with a wet thickness of 30.8 μm and ZnO coated with a wet thickness of 7.70 μm . Photovoltaic parameters V_{OC} , J_{SC} , FF, and PCE are presented from the obtained OSC.

Intermediate component	Ratio	Theoretical thickness (nm)	V_{OC} (V)	J_{SC} (mA cm^{-2})	FF (%)	PCE (%)
VTIP:IPA	1:100	30	0.88	-0.21	29.2	0.047
VTIP:IPA	1:1000	3	0.93	-2.41	29.5	0.60
VTIP:IPA	1:2000	1.5	0.85	-1.42	25.8	0.27

The influence of PEDOT:PSS 4083 thickness was studied by coating different wet thicknesses of a PEDOT:PSS 4083/IPA (1:2) while keeping the optimal V_2O_5 thickness (3 nm) found above. Wet thicknesses of 23.1 and 30.8 μm resulted in OSCs with the highest performances (Table 4.2). With the thinner wet thickness (15.4 μm) the intermediate layer started to lose solvent resistance due to an inhomogeneous film. Therefore, a wet thickness of 30.8 μm was used throughout the rest of the intermediate layer optimizations.

The influence of ZnO thickness was studied by coating two different wet thicknesses of the same ZnO solution. The two different wet thicknesses gave rise to very little if any difference in the performance of the obtained OSC (Table 4.3). A difference was observed during testing where the thinner ZnO needed much less light soaking to reach maximum efficiency. This is ascribed to a reduction in the UV-activation needed for the ZnO.[13,14]

Table 4.2: Thickness variation of the PEDOT:PSS 4083. Thicknesses were controlled by coating varying wet thicknesses (15.4, 23.1, 30.8, and 38.5 μm) while keeping a constant ratio between PEDOT:PSS 4083 and IPA (1:2). The remaining two intermediate layers were VTIP:IPA 1:1000 coated with a wet thickness of 8 μm and ZnO coated with a wet thickness of 7.70 μm . Photovoltaic parameter V_{OC} , J_{SC} , FF, and PCE are presented from the obtained OSC.

Intermediate component	Wet thickness (μm)	V_{OC} (V)	J_{SC} (mA cm^{-2})	FF (%)	PCE (%)
4083:IPA	15.4	0.87	-1.33	35.6	0.30
4083:IPA	23.1	0.93	-1.62	40.2	0.43
4083:IPA	30.8	0.84	-2.08	36.7	0.46
4083:IPA	38.5	0.76	-1.96	33.5	0.36

Table 4.3: Thickness variation of the ZnO ETL. The thickness was controlled by coating varying wet thicknesses (7.70 and 3.85 μm) while keeping a constant concentration (39 mg mL^{-1}). The remaining two intermediate layers were VTIP:IPA 1:1000 coated with a wet thickness of 8 μm and PEDOT:PSS 4083:IPA 1:2 coated with a wet thickness of 30.8 μm . Photovoltaic parameter V_{OC} , J_{SC} , FF, and PCE are presented from the obtained OSC.

Intermediate component	Concentration (mg mL^{-2})	Wet thickness (μm)	V_{OC} (V)	J_{SC} (mA cm^{-2})	FF (%)	PCE (%)
ZnO (acetone)	39	7.70	0.89	-2.16	39.4	0.65
ZnO (acetone)	39	3.85	0.97	-2.11	41.1	0.69

Optimizing the intermediate layer resulted in an overall performance increasing from 0.047 % in the first experiments to 0.69 %. These preliminary results have led to the development of a solvent resistant intermediate layer ($\text{V}_2\text{O}_5/\text{PEDOT:PSS 4083/ZnO}$) and optimizing it to a functional tandem. The tandem stack has until now only been applied on P3HT:PCBM, so to make sure it is also functional for other polymers, tandem OSCs were prepared containing P5:PCBM and P3HT:PCBM in four different sub-cell combinations. The photovoltaic characteristics are clearly divided into two groups regarding performance and J_{SC} (Figure 4.9). Using P5:PCBM as the 1st sub-cell resulted in an enhanced J_{SC} from around -2.5

mA cm^{-2} to around -4.30 mA cm^{-2} when compared to devices prepared with P3HT:PCBM. From this it can be concluded that the 1st sub-cell in the P3HT:PCBM tandem OSC is lowering the overall current since it is possible to obtain -4.27 mA cm^{-2} from a tandem OSC using P3HT:PCBM in the 2nd sub-cell.

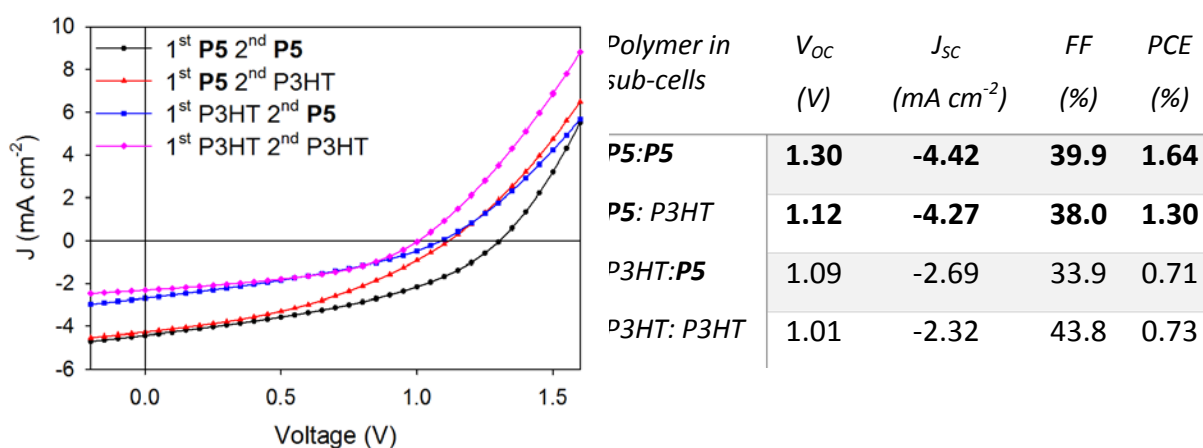


Figure 4.9: Photovoltaic characteristics of tandem OSC prepared with P5:PCBM and P3HT:PCBM in four different combinations of the sub-cells. The OSCs were tested using the mirror set up shown in Figure 4.5B.

To overcome the low performance for the 1st sub-cell, V_2O_5 was substituted with different HTLs or conducting layers (MoO_x , PEDOT:PSS HTL solar, and PEDOT:PSS F010). All three of these materials had the desired compatibilizing effect for the subsequent PEDOT:PSS 4083 layer although the adhesion between active layer and PEDOT:PSS HTL solar was too poor to prepare OSCs. Photovoltaic characteristics for the OSCs prepared with the other two compatibilizing layers were compared to the reference cell with V_2O_5 , the results are shown in Figure 4.10. It is clearly seen that PEDOT:PSS F010 outperforms both MoO_x and V_2O_5 , mostly due to an increase in the J_{sc} . It increases from -2.32 to -5.51 mA cm^{-2} when substituting V_2O_5 with PEDOT:PSS F010 whereas OSC prepared with MoO_x resulted in a J_{sc} of -2.68 mA cm^{-2} .

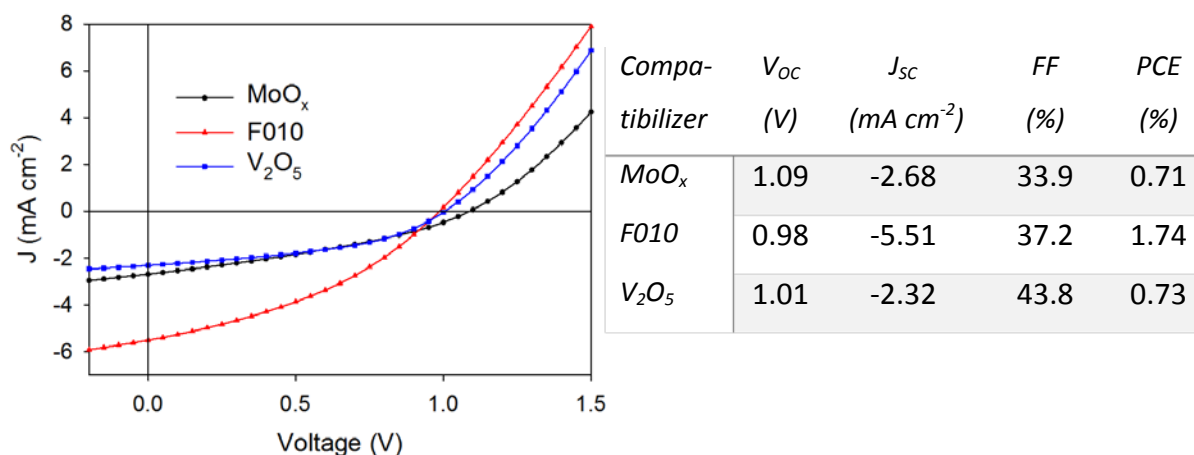


Figure 4.10: Photovoltaic characteristics for tandem OSCs prepared using different materials as the compatibilizer for the PEDOT:PSS 4083:IPA(1:2) layer. The OSCs were tested using the mirror set up shown in Figure 4.5B

The results obtained from the compatibilizer test revealed an increase of 138 % in terms of efficiency when changing the compatibilizer from V₂O₅ to PEDOT:PSS F10. This led to a reevaluation of the tandem layer stack from the 11 layered stack to a 12 layered stack. The new stack contains of silver, different PEDOT:PSS, ZnO and active layers as seen in Figure 4.11 with an intermediate layer offering good solvent resistance and efficient hole-electron recombination.

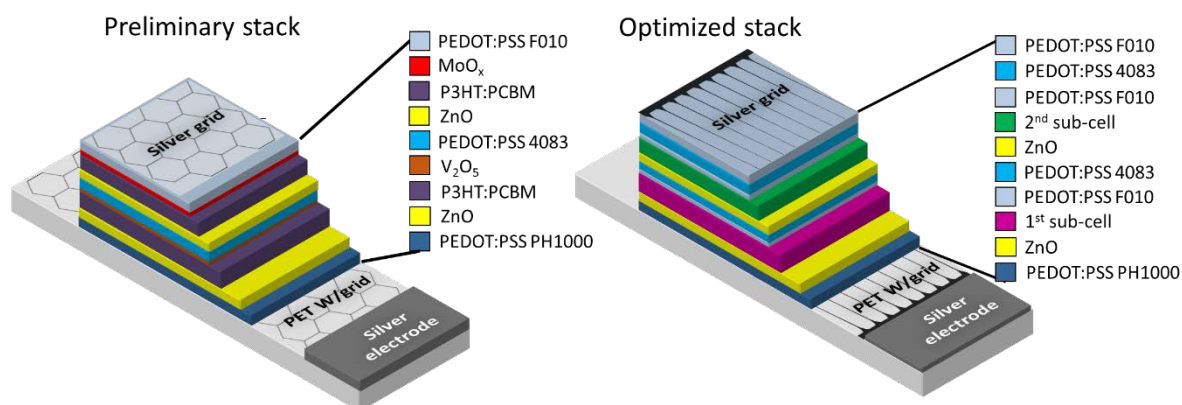


Figure 4.11: Schematic illustration of the initial tandem stack (on the left) and of the Improved stack (on the right) for preparing tandem OSC optimized to consist of 12 layers where only PEDOT:PSS, silver, ZnO and active layers are used.

Coating parameters for the improved tandem stack can be found in Table 4.4 with web speeds not under 1 m min^{-1} , wet thicknesses between 3.8 and $31 \mu\text{m}$, and every layer deposited with a relatively low roll temperature of $60 \text{ }^\circ\text{C}$.

Table 4.4: Coating parameters for the new optimized tandem stack with 12 coated or printed layers consisting of only PEDOT:PSS, ZnO, active layer, and silver.

<i>Layer</i>	<i>Material</i>	<i>Concentration</i>	<i>Temp.</i> ($^\circ\text{C}$)	<i>Web speed</i> (m min^{-1})	<i>Flow-rate</i> (ml min^{-1})	<i>T_{wet}</i> (μm)
<i>Substrate</i>	Flextrode					
<i>1st sub-cell</i>	P3HT:PCBM	20:20 mg ml^{-1}	60	1.0	0.20	15
<i>Compatibilizer</i>	F010:IPA	1:4 vol vol^{-1}	60	1.0	0.10	8
<i>HTL</i>	4083:IPA	1:2 vol vol^{-1}	60	1.0	0.30	23
<i>ETL</i>	ZnO	39 mg ml^{-1}	60	2.0	0.10	3.8
<i>2nd sub-cell</i>	P3HT:PCBM	20:20 mg ml^{-1}	60	1.0	0.08	6
<i>Compatibilizer</i>	F010:IPA	1:4 vol vol^{-1}	60	1.0	0.10	8
<i>HTL</i>	4083:IPA	1:2 vol vol^{-1}	60	1.0	0.30	23
<i>Conducting layer</i>	F010:IPA	1:1 vol vol^{-1}	60	1.0	0.40	31
<i>Top electrode</i>	Ag PV410		60	1.2		

4.2.2. Stability

The addition of layers to the tandem OSC stack in comparison to the single junction OSC stack can easily influence other parameters than just performance. Also stability has a tendency to change when incorporating new materials. The stability studies were performed according to ISOS-D-2 protocol[15] and by a bending test.

The ISOS-D-2 protocol[15] was employed to test the shelf life-time of the tandem OSCs under accelerated conditions in dark at $65 \text{ }^\circ\text{C}$. The life-time was evaluated for three tandem OSCs and three single junction OSCs, having active layers consisting of P3HT:PCBM, which all were tested under same conditions for more accurate comparison. The plots are given in

Figure 4.12, which shows similar degradation pattern and velocity as single junction OSCs containing the same layers.

A bending test was used to evaluate the response of the tandem OSC to mechanical strain. The weakest point in an OSC is generally the interfaces between the layers. Especially interfaces between the active layer and PEDOT:PSS have proven to have a poor adhesion when subjected to mechanical strain. Bending tests were performed on two tandem OSCs encapsulated in a flexible Amcor barrier foil without UV filter. It was conducted on a Mecmesin Multitest 5i tensile and compressive test bench with a bending radius of $10 \text{ mm} \pm 2 \text{ mm}$ as shown in Figure 4.13A and B. The performance of the OSC were tested after 0, 1, 10, 100, and 1000 bending operations normalized to the PCE measured at 0 bends. As shown in Figure 4.13C the performance is unaffected as function of the number of bending operations the OSCs were subjected to. During the bending test delamination of the barrier foil was observed on one of the samples. This is ascribed to insufficient hardening of the DELO adhesive for that cell.

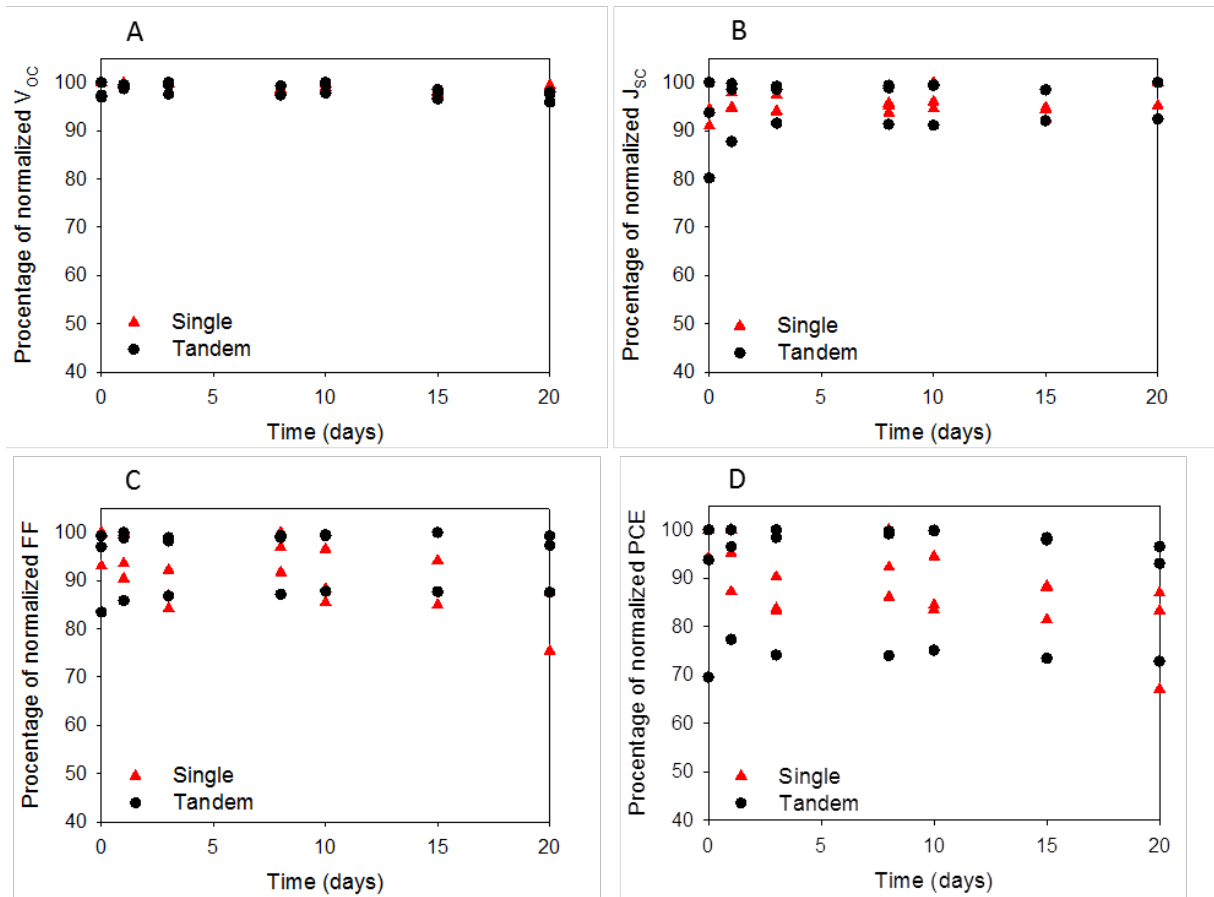


Figure 4.12: A short accelerated shelf life stability study of 20 days of duration according to ISOS-D-2 conditions was performed to find any increased degradation compared to single cell devices could be seen. No increased degradation was experienced for the tandem cells compared to the single cells, suggesting a stable intermediate layer. The figures are shown with normalized V_{OC} (A), J_{SC} (B), FF (C) and maximum power (D). Reproduced with permission from Elsevier.

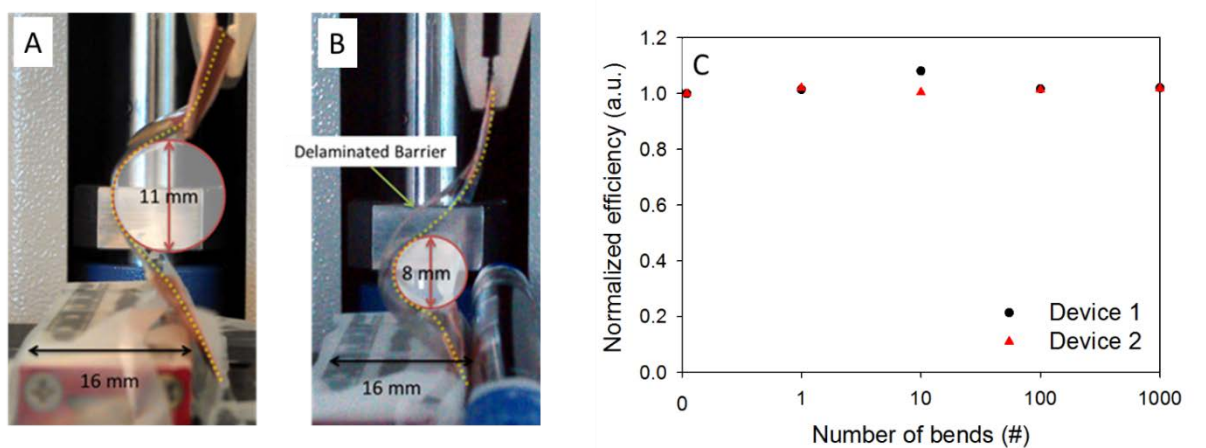


Figure 4.13: Results of bending test of Amcor barrier encapsulated cells. Two tandem OSCs were bended 1, 10, 100 and 1000 times and IV-curves were taken in between. C) Displays the normalized efficiency, showing the bending having little to none influence on the performance of the cells for a range of up to 1000 bends.

4.2.3. One side illuminated tandem OSC

As described above (section 4.1) the band gaps for the 1st and 2nd sub-cell should be at 2 eV and 1.45 eV, respectively, in order to prepare sub-cells with equal potential current. According to the absorption and IPCE data in Section 3.2.2.3 only 2-3 polymers (**P5**, **P7**, and P3HT) have the potential to meet these requirements for the HBG polymer. P3HT is commonly used to prepare tandem cells in literature[11,16]. The cells are, however, prepared on ITO based substrate and with indene-C₆₀ bisadduct (ICBA) as the acceptor reducing the loss during exciton dissociation significantly due to a better alignment of the LUMO-levels compared to PCBM. As a donor-acceptor mixture it has previously been proven to be unstable, so it will therefore not be taking into consideration.[17] **P5** has a band gap of approx. 1.75 thereby risking a lowering of the current for the tandem OSC due to a lower current of the 2nd sub-cell. **P7** is theoretically the most suitable of the three polymers to function as the HBG polymer with a band gap at approx. 2 eV nm and a V_{OC} of 0.8 V for a single junction OSC.

During the time spend developing the intermediate layer, the fabrication process of Flex-trode was improved. The dissolution problems of a thin 1st sub-cell when coating the subsequent sub-cell were improved, allowing tandem OSC with thinner 1st sub-cells to be prepared.

As described in Section 4.1 the performance of a tandem OSC depends on the performance of the individual sub-cells. This means that the performance of the single junction especially of the LBG polymers has to be improved from 1.33 %, which was described in Table 3.3, to achieve high performing tandem OSCs. This optimization was conducted by investigation of the polymer/PCBM ratio. Additional performance optimizing was conducted by addition of common additives (chloronaphthalene (CN) and diiodooctane (DIO)) with the concentration of 1, 2, and 3 % to the ink. For **P1** it was found that OSC prepared a ratio of 2:3 with PCBM obtained the highest efficiencies. The addition of DIO had a positive influence on the performance, top-performance was at the addition of only 1 % DIO as seen in Figure 4.14. Similar optimizations were done for **P8** and **P10**.

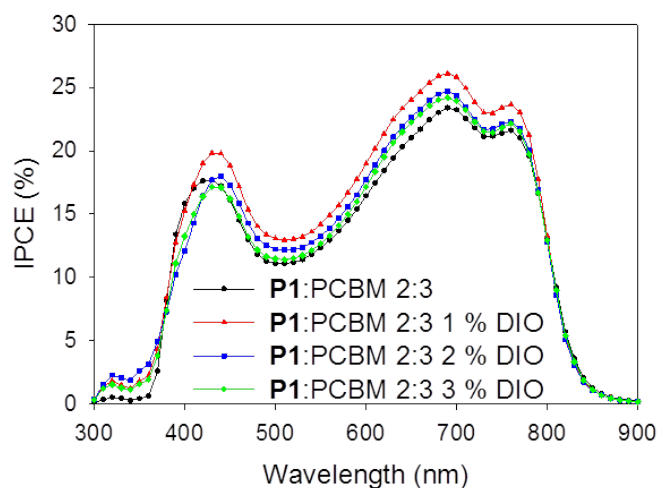


Figure 4.14: IPCE measurements of OSC prepared with an active layer consisting of P1:PCBM in a ratio of 2:3 with different volumes of DIO additive. The geometry of the OSC was (Ag/PH1000/ZnO/active layer/F010/4083/F010/Ag)

Tandem OSCs were prepared with **P5** and **P1** as sub-cells with active layer thicknesses of approx. 190 nm, calculated from the coated wet-thickness with densities similar to the those

obtained in a P3HT:PCBM film. The photovoltaic characteristics is shown in Figure 4.15, OSCs were prepared with **P5** both as 1st or 2nd sub-cell in attempt to compensate for the poor current density of the **P1** sub-cell. The performances were, however, when applying **P1** as 1st sub-cell only 1.71 % in comparison with 2.00 % when **P5** was applied as 1st sub-cell.

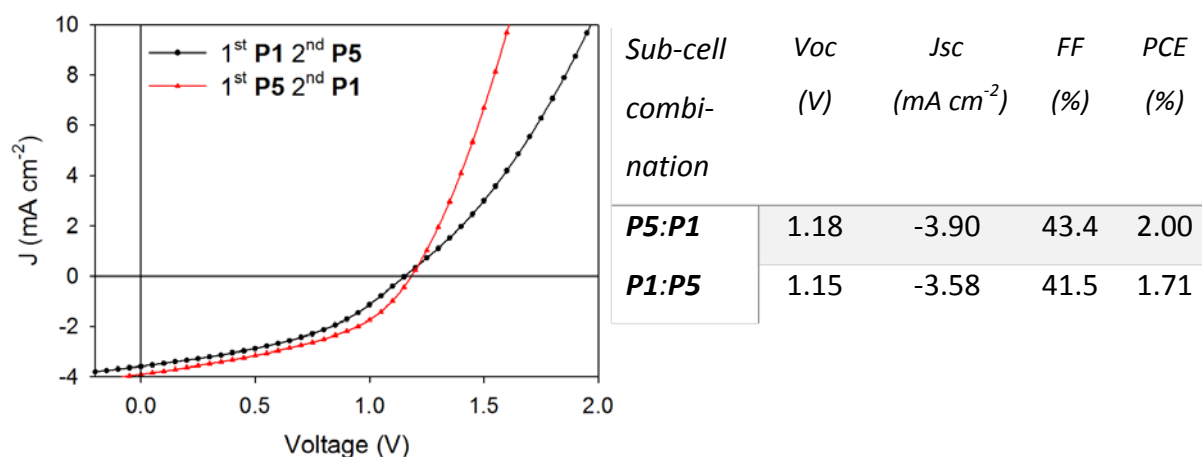


Figure 4.15: Photovoltaic characteristics of tandem OSC prepared with P5 as HBG polymer and P1 as LBG polymer. The OSC were prepared with HBG both as the first and second active layer. The cells were measured with one side illumination.

From the tandem OSC presented in Figure 4.15 to the ones presented in Figure 4.16, the present portion of **P1** had been consumed. During purification the polymer was divided into two portions, i.e. a low molecular weight fraction extracted with chloroform and a high molecular weight fraction extracted with chlorobenzene. Until this point it was the chlorobenzene fraction used to prepare OSCs but it will now change to the chloroform fraction. Single junction OSCs prepared with the chloroform fraction generally performed worse than OSCs prepared with the chlorobenzene fraction. The PCE went from 1.33 % to 0.9 % mainly due to a decrease in J_{sc} , which is ascribed to the lower molecular weight of the chloroform fraction. The HBG polymer **P7** was tested as 1st sub-cell together with **P1**, **P8**, and **P10** as LBG polymer. These combinations led to tandem devices with a performance from 0.95 % up to 1.45 % with a quite high V_{oc} of 1.22 V when combined with **P10**. This combination should though theoretically obtain a V_{oc} of around 1.5 V since V_{oc} for the single junctions are 0.82 V and 0.69 V, respectively. Another interesting observation is the poor opening of the diode in all

three cases. A similar behavior was observed when preparing single junction OSC with **P7:PCBM**.

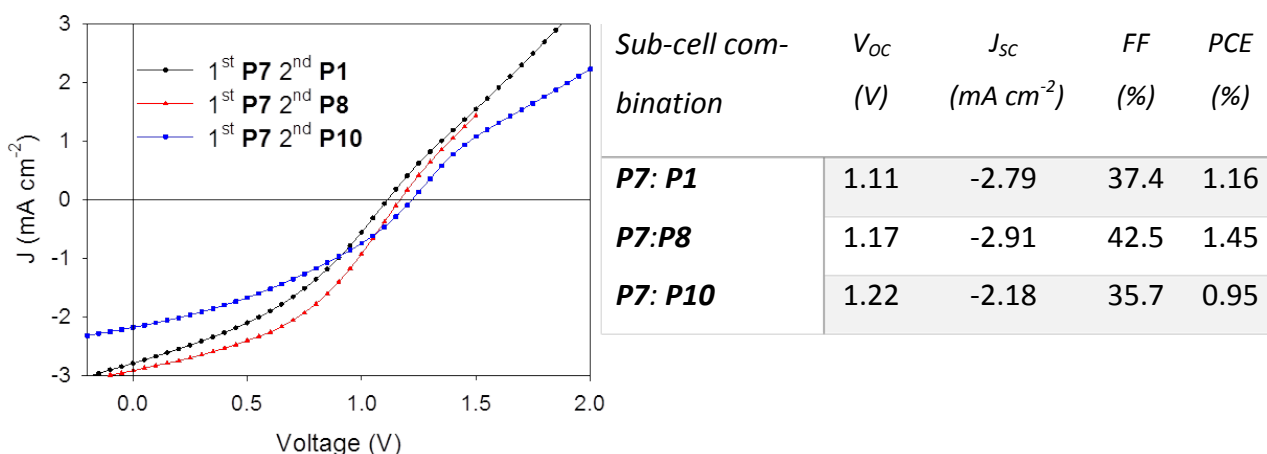


Figure 4.16: Photovoltaic characteristics of tandem OSC with P7 with three different LBG polymers; P1, P8, and P10. P1 used to prepare these tandem OSC was from the chloroform fraction. The cells were measured with one side illumination.

A few attempts to prepare modules have been conducted on the MRC by printing one layer at one stripe pr. circle meaning that an eight stripe module is 72 coatings, which all needs to be perfect (both in alignment and film quality) not to short the module or the stripe. Four- (Figure 4.17B) and eight-cell modules have been prepared although not obtaining fully functional modules. The four cell module had a V_{oc} of 2.9 V (Figure 4.17A) when using P3HT:PCBM as 1st sub-cell and **P1**:PCBM as 2nd sub-cell. The V_{oc} of an optimal functional tandem OSC module would be around 4.4 V with this material combination. Studying the LBIC image (Figure 4.17C) revealed all four cells in the module to be working but with large variety in intensity.

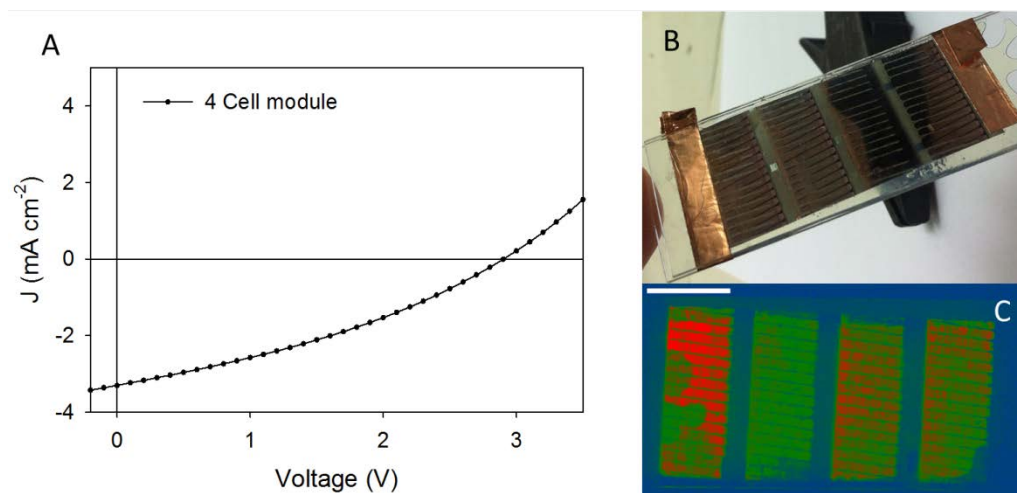


Figure 4.17: Characterization of the four cell module prepared with P3HT:PCBM in 1st sub-cell and P1 in 2nd subcell with an intermediate layer consisting of PEDOT:PSS F010 - PEDOT:PSS 4083 - ZnO. A) I-V characterization measured with one side illumination, B) photograph of the module, and C) LBIC image of the module.

The real issue in tandem processing is the ability to prepare all layers defect-free meter after meter, to make the preparation of modules of tandem OSC possible. For this to be technologically possible, the R2R coater set up needs to be utilized since the individual deposition of 72 layers promise to be an almost impossible task. The transfer from the MRC to the R2R coater revealed problems with the proposed tandem stack (Figure 4.11) during coating of the compatibilizing PEDOT:PSS F010 layer. It had a tendency to precipitate in the slot-die coating-head making deposition of uniform stripes impossible. In order to solve this problem a new investigation of materials with similar compatibilizing abilities as PEDOT:PSS F10 was carried out. The most promising was found to be poly[(9,9-bis(3'-(N,N-dimethylamino)propyl)-2,7-fluorene)-alt-2,7-(9,9-dioctylfluorene)] (PFN). PFN is normally used as an interface layer at the electron-collecting electrode.[18,19] I-V curves obtained from tandem OSCs prepared with PEDOT:PSS F010 or PFN as compatibilizers is shown in Figure 4.18. Both compatibilizers prepared OSCs with a performance around 1.45 %, but when using PFN the V_{oc} increased by 9 % to 1.28 V whereas both the J_{sc} and FF dropped slightly evening out the performance.

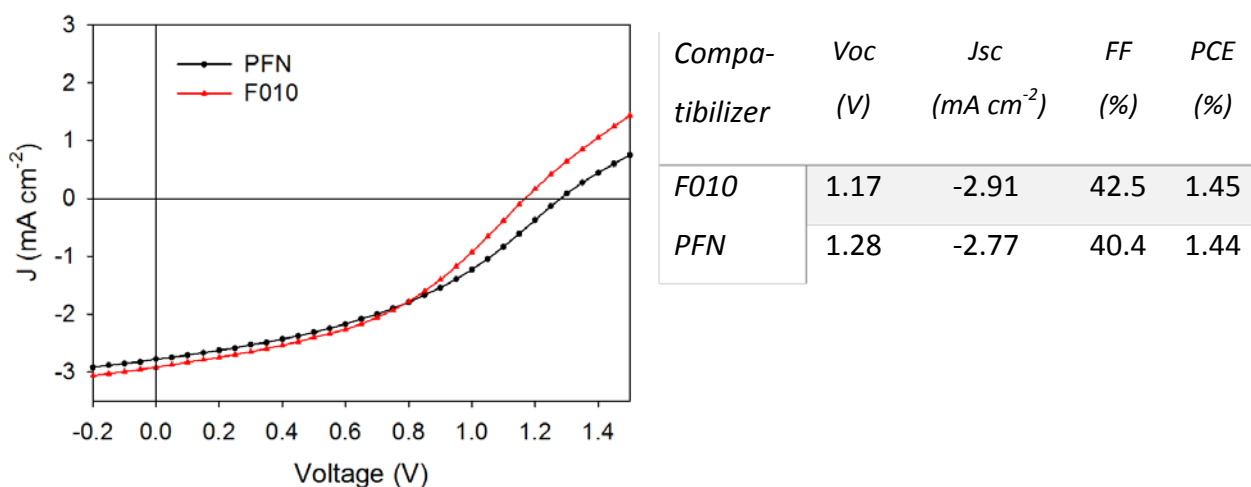


Figure 4.18: Photovoltaic characteristic of tandem OSC prepared with P7 as 1st sub-cell and P8 as 2nd sub-cell prepared with 2 different compatibilizing layers for the PEDOT:PSS 4083 layer. The cells were measured with one side illumination.

4.3. Summary

The first example of roll coated tandem OSCs on an ITO-free substrate were prepared by slot-die coating or flexographic printing of 11 or 12 layer in the optimized stack. The intermediate layer was optimized by utilizing a mirror setup for double sided illumination of tandem OSC with P3HT:PCBM in both sub-cells. The optimized tandem stack consisted of silver, PEDOT:PSS, ZnO, and active layers. After changing the compatibilizer between the active layer and the PEDOT:PSS 4083 layer from V₂O₅ to PEDOT:PSS F010 the performance increased from 0.73 % to 1.7 %.

Stability of the 12 layered tandem cells was tested both mechanically and with a shelf life-time protocol. The mechanical stability test was conducted as a bending test. The test showed a stable PCE up to at least 1000 bends. The shelf life-time was tested under accelerated conditions as described in the ISOS-D-2 protocol at 65 °C in dark. The tandem OSCs displayed similar degradation pattern and velocity as single junction OSCs containing the same layers.

The generally low performance of the prepared tandem OSCs is ascribed to the low performance of the LBG polymers. Only **P10** have a reasonable performance with 1.8 %, it has, however, a band gap of 1.55 eV giving it more overlap with the absorption spectrum for the HBG polymers. The two other LBG polymers (**P1** and **P8**) that were used to prepare tandem OSC have better absorption overlap with the HBG polymers. These had, however, only single junction performances around 1.3 % rendering it impossible to prepare tandem OSC with high efficiency. Even though, tandem OSC have been prepared with a performance of up to 2 % with all layer coated by slot-die coating or flexographic printing on a flexible ITO-free substrate using **P5** and **P1** as 1st and 2nd sub-cell, respectively.

The ultimate test of the tandem stack is the preparation of a tandem module in large R2R scale. Coating of the compatibilizing PEDOT:PSS F010 layer proved a difficult task on the R2R equipment due to precipitation of the suspension in the coating-head. This led to a reevaluation of the compatibilizer layer, changing F10 to a PFN layer resulted in tandem OSCs which achieved similar efficiencies as obtained using PEDOT:PSS F010.

4.4. References

- [1] C. W. Tang, "Two-layer organic photovoltaic cell," *Applied Physics Letters*, vol. 48, no. 2, p. 020183-020185, 1986.
- [2] T. Ameri, G. Dennler, C. Lungenschmied, and C. J. Brabec, "Organic tandem solar cells: A review," *Energy & Environmental Science*, vol. 2, no. 4, pp. 347–363, 2009.
- [3] T. Ameri, N. Li, and C. J. Brabec, "Highly efficient organic tandem solar cells: a follow up review," *Energy & Environmental Science*, vol. 6, pp. 2390–2413, 2013.
- [4] J. You, L. Dou, Z. Hong, G. Li, and Y. Yang, "Recent trends in polymer tandem solar cell research," *Progress in Polymer Science*, 2013, DIO:10.1016/j.progpolymsci.2013.04.005.
- [5] G. Dennler, H.-J. Prall, R. Koeppe, M. Egginger, R. Autengruber, and N. S. Sariciftci, "Enhanced spectral coverage in tandem organic solar cells," *Applied Physics Letters*, vol. 89, no. 7, p. 073502-073505, 2006.
- [6] S. Sista, Z. Hong, L.-M. Chen, and Y. Yang, "Tandem polymer photovoltaic cells—current status, challenges and future outlook," *Energy & Environmental Science*, vol. 4, no. 5, pp. 1606–1620, 2011.

- [7] S. K. Hau, H.-L. Yip, K.-S. Chen, J. Zou, and A. K.-Y. Jen, "Solution processed inverted tandem polymer solar cells with self-assembled monolayer modified interfacial layers," *Applied Physics Letters*, vol. 97, no. 25, p. 253307-253309, 2010.
- [8] T. T. Larsen-Olsen, E. Bundgaard, K. O. Sylvester-Hvid, and F. C. Krebs, "A solution process for inverted tandem solar cells," *Organic Electronics*, vol. 12, no. 2, pp. 364–371, 2011.
- [9] N. Li, T. Stubhan, D. Baran, J. Min, H. Wang, T. Ameri, and C. J. Brabec, "Design of the Solution-Processed Intermediate Layer by Engineering for Inverted Organic Multi junction Solar Cells," *Advanced Energy Materials*, vol. 3, no. 3, pp. 301–307, 2013.
- [10] Heliatak, "Heliatak consolidates its technology leadership by establishing a new world record for organic solar technology with a cell efficiency of 12%." [Online]. Available: www.Heliatak.com. [Accessed: 09-Sep-2013].
- [11] J. You, L. Dou, K. Yoshimura, T. Kato, K. Ohya, T. Moriarty, K. Emery, C.-C. Chen, J. Gao, G. Li, and Y. Yang, "A polymer tandem solar cell with 10.6% power conversion efficiency.," *Nature communications*, vol. 4, pp. 1446–1455, 2013.
- [12] T. T. Larsen-Olsen, E. Bundgaard, K. O. Sylvester-Hvid, and F. C. Krebs, "A solution process for inverted tandem solar cells," *Organic Electronics*, vol. 12, no. 2, pp. 364–371, 2011.
- [13] M. R. Lilliedal, A. J. Medford, M. V. Madsen, K. Norrman, and F. C. Krebs, "The effect of post-processing treatments on inflection points in current–voltage curves of roll-to-roll processed polymer photovoltaics," *Solar Energy Materials and Solar Cells*, vol. 94, no. 12, pp. 2018–2031, 2010.
- [14] F. C. Krebs, S. A. Gevorgyan, B. Gholamkhash, S. Holdcroft, C. Schlenker, M. E. Thompson, B. C. Thompson, D. Olson, D. S. Ginley, S. E. Shaheen, H. N. Alshareef, J. W. Murphy, W. J. Youngblood, N. C. Heston, J. R. Reynolds, S. Jia, D. Laird, S. M. Tuladhar, J. G. a. Dane, P. Atienzar, J. Nelson, J. M. Kroon, M. M. Wienk, R. a. J. Janssen, K. Tvingstedt, F. Zhang, M. Andersson, O. Inganäs, M. Lira-Cantu, R. de Bettignies, S. Guillerez, T. Aernouts, D. Cheyng, L. Lutsen, B. Zimmermann, U. Würfel, M. Niggemann, H.-F. Schleiermacher, P. Liska, M. Grätzel, P. Lianos, E. a. Katz, W. Lohwasser, and B. Jannon, "A round robin study of flexible large-area roll-to-roll processed polymer solar cell modules," *Solar Energy Materials and Solar Cells*, vol. 93, no. 11, pp. 1968–1977, 2009.
- [15] M. O. Reese, S. A. Gevorgyan, M. Jørgensen, E. Bundgaard, S. R. Kurtz, D. S. Ginley, D. C. Olson, M. T. Lloyd, P. Morvillo, E. a. Katz, A. Elschner, O. Haillant, T. R. Currier, V. Shrotriya, M. Hermenau, M. Riede, K. R. Kirov, G. Trimmel, T. Rath, O. Inganäs, F. Zhang, M. Andersson, K.

- Tvingstedt, M. Lira-Cantu, D. Laird, C. McGuinness, S. (Jimmy) Gowrisanker, M. Pannone, M. Xiao, J. Hauch, R. Steim, D. M. DeLongchamp, R. Rösch, H. Hoppe, N. Espinosa, A. Urbina, G. Yaman-Uzunoglu, J.-B. Bonekamp, A. J. J. M. van Breemen, C. Girotto, E. Voroshazi, and F. C. Krebs, "Consensus stability testing protocols for organic photovoltaic materials and devices," *Solar Energy Materials and Solar Cells*, vol. 95, no. 5, pp. 1253–1267, 2011.
- [16] L. Dou, J. You, J. Yang, C. Chen, Y. He, S. Murase, T. Moriarty, K. Emery, G. Li, and Y. Yang, "Tandem polymer solar cells featuring a spectrally matched low-bandgap polymer," *NATURE PHOTONICS*, vol. 6, pp. 180–185, 2012.
- [17] T. Tromholt, M. V. Madsen, J. E. Carlé, M. Helgesen, and F. C. Krebs, "Photochemical stability of conjugated polymers, electron acceptors and blends for polymer solar cells resolved in terms of film thickness and absorbance," *Journal of Materials Chemistry*, vol. 22, no. 15, p. 7592–7601, 2012.
- [18] J.-H. Kim, C. E. Song, H. U. Kim, A. C. Grimsdale, S.-J. Moon, W. S. Shin, S. K. Choi, and D.-H. Hwang, "High Open Circuit Voltage Solution-Processed Tandem Organic Photovoltaic Cells Employing a Bottom Cell Using a New Medium Band Gap Semiconducting Polymer," *Chemistry of Materials*, vol. 25, no. 13, pp. 2722–2732, 2013.
- [19] M. Kohlstädt, M. Grein, P. Reinecke, T. Kroyer, B. Zimmermann, and U. Würfel, "Inverted ITO- and PEDOT:PSS-free polymer solar cells with high power conversion efficiency," *Solar Energy Materials and Solar Cells*, vol. 117, pp. 98–102, 2013.

5. Summary and outlook

The focus in this thesis was threefold: morphology control by prearranged inks, improving the compatibility between laboratory scale OSC and R2R prepared OSC, and to prepare tandem solar cells in order to explore potentially better utilization of the solar irradiation spectrum.

Morphology control by prearranged inks was attempted by two methods. Firstly aqueous inks based on polymer and PCBM blends were investigated in order to characterize their potential to obtain an internal morphology. The particles were characterized to determine the distribution of the polymer and PCBM components inside the particles and the shape of the particles using X-ray and TEM. This showed spherical particles with a core-shell distribution of the two components inside the particles. The size control of the particles was obtained through variation of the preparation conditions, largest influence on the sizes was found to be through controlling the concentration of polymer and PCBM. It was possible to prepare OSCs with a PCE up to 0.55 % from these inks by slot-die coating after extensive ink formulation and coating optimization. Secondly, grafting of inorganic nanoparticles with organic oligomers were attempted, these showed little if any properties as materials for OSCs, due to a large loss of materials during purification, and OSC devices prepared together with PCBM only presented very low performances.

Further development of the aqueous nanoparticle inks can lead the way for OSC preparation with a prearranged morphology enabling the possibility of preparing an active layer with an optimal morphology. These inks can also prove to be an important method to reduce the use of organic solvent and thereby also the embodied energy. The performance of the prepared OSCs have not yet achieved a matching PCE compared to OSC prepared by solvent processing. There is, however, still a number of parameters, which needs to be optimized to fully assess the potential of these inks such as particle size vs performance and the optimal thickness of the active layer.

In order to make the transition from laboratory scale preparation to large scale OSC production easier, a new method for laboratory preparation of OSCs have been developed by

the invention of the mini roll coater (MRC). The MRC uses slot-die coating and flexographic printing to deposit the layers in an OSC, which are two of the methods available on the R2R coater. The MRC has throughout this thesis been used to prepare and optimize OSCs from a variety of polymers and for electrode optimizations.

A future use of the MRC can be very widely spread but the main areas are expected to be within testing and optimizing of new polymers as OSCs on a small scale before moving the production to larger scale. Beside the testing of new polymers, the MRC should also be applied for testing of new formulations (such as aqueous inks) or development of the general single junction stack.

Tandem OSCs were prepared by wet processing of up to 12 layers using slot-die coating and flexographic printing, 9 of these layers were deposited on the MRC. The tandem OSCs were prepared as two OSCs in series with an intermediate layer to separate each of the sub-cells. Performance of the tandem devices revealed the V_{OC} to be just below the sum of V_{OC} obtained from the two sub-cells. The overall performance of the prepared tandem OSC has not yet reach the state of single OSC, due to the 2nd sub-cell limiting the current.

A continuous development of the tandem stack to enable the preparation of tandem OSCs on the R2R-coater is needed. Besides the stack optimization it is also necessary to develop a low band gap material, which has a high current contribution after 650 nm. This will result in OSCs with a high PCE when prepared by slot-die coating, in order to increase the performance of tandem OSCs to a level, where tandem OSCs surpassed the performance obtained for single junction OSCs.

Appendix 1

The AFM images used to determine the size of the particles prepared in Table 2.5.

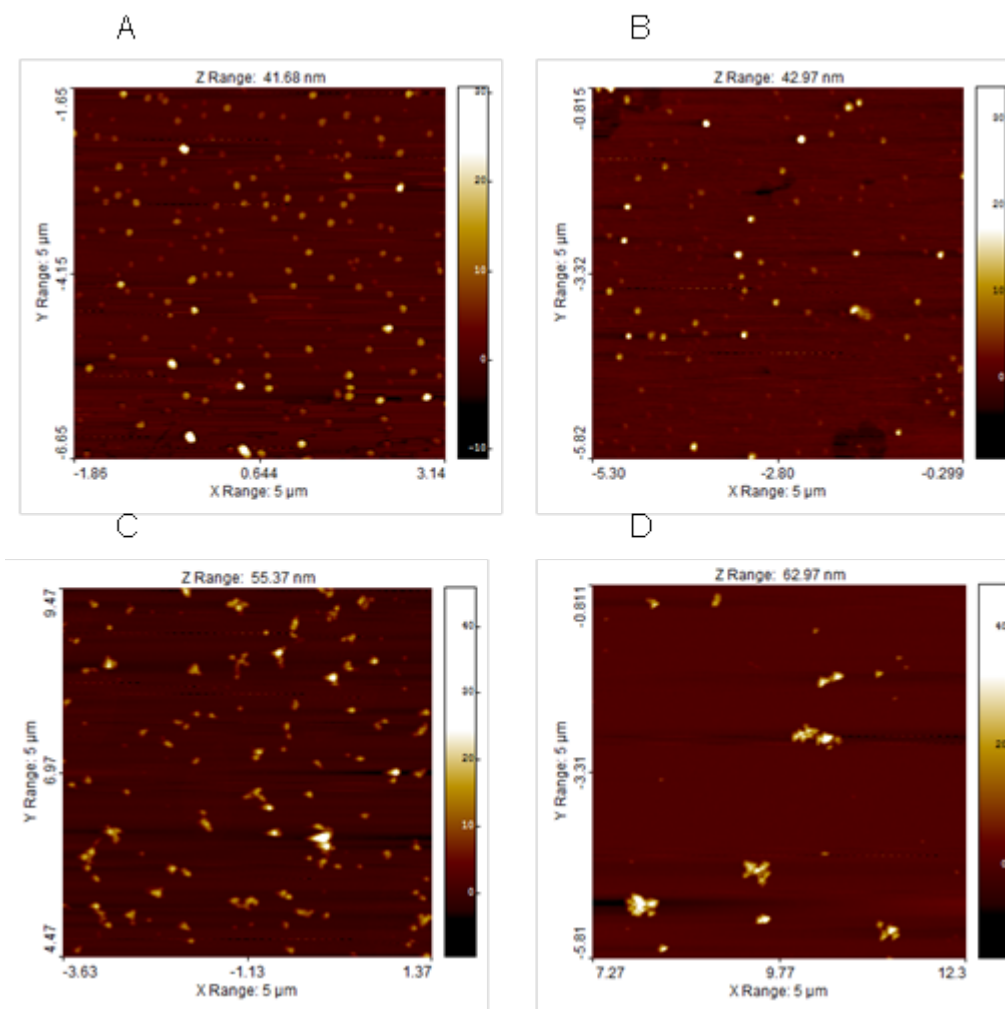


Figure A1: AFM-image used to calculate the size of the nanoparticles, The images were analyzed using the image processing software package SPIP 5.1.5 (Image Metrology A/S, Hørsholm, Denmark) for the height measurements, and the particle size determination.

Appendix 2

The published articles are attached without supporting information. The material is available free of charge via the Internet or by contacting the author.

List of Publications

A2.1

T. R. Andersen, T. T. Larsen-Olsen, B. Andreasen, A. P. L. Böttiger, J. E. Carlé, M. Helgesen, E. Bundgaard, K. Norrman, J. W. Andreasen, M. Jørgensen, and F. C. Krebs, *Aqueous processing of low-band-gap polymer solar cells using roll-to-roll methods*, ACS NANO, **2011**, 5, 4188-4196, DIO: 10.1021/nn200933r.

A2.2

T. T. Larsen-Olsen, T. R. Andersen, B. Andreasen, A. P. L. Böttiger, E. Bundgaard, K. Norrman, J. W. Andreasen, M. Jørgensen, and F. C. Krebs, *Roll-to-roll processed polymer tandem solar cells partially processed from water*, Solar Energy Materials and Solar Cells, **2012**, 97, 43-49, DIO: 10.1016/j.solmat.2011.08.025.

A2.3

T. T. Larsen-Olsen, B. Andreasen, T. R. Andersen, A. P. L. Böttiger, E. Bundgaard, K. Norrman, J. W. Andreasen, M. Jørgensen, and F. C. Krebs, *Simultaneous multilayer formation of the polymer solar cell stack using roll-to-roll double slot-die coating from water*, Solar Energy Materials and Solar Cells, **2012**, 22-27, DIO: 10.1016/j.solmat.2011.08.026.

A2.4

T. R. Andersen, Q. Yan, T. T. Larsen-Olsen, R. Søndergaard, Q. Li, B. Andreasen, K. Norrman, M. Jørgensen, W. Yue, D. Yu, F. C. Krebs, H. Chen, and E. Bundgaard, *A Nanoparticle Approach towards Morphology Controlled Organic Photovoltaics (OPV)*, Polymers, **2012**, 4, 1242-1258. DOI:10.3390/polym4021242

A2.5

L. Fu, H. Pan, T. T. Larsen-Olsen, T. R. Andersen, E. Bundgaard, F. C. Krebs, and H. Chen, *Synthesis and characterization of new electron-withdrawing moiety thieno [2, 3-c] pyrrole-4, 6-dione-based molecules for small molecule solar cells*, *Dyes and Pigments*, **2012**, 97, 141-147, DOI: 10.1016/j.dyepig.2012.12.009.

A2.6

L.-J. Zuo, X.-L. Hu, T. Ye, T. R. Andersen, H.-Y. Li, M.-M. Shi, M. Xu, J. Ling, Q. Zheng, J.-T. Xu, E. Bundgaard, F. C. Krebs, and H.-Z. Chen, *Effect of Solvent-Assisted Nanoscaled Organo-Gels on Morphology and Performance of Organic Solar Cells*, *The Journal of Physical Chemistry C*, **2012**, 116, 16893-16900, DIO: 10.1021/jp3049444

A2.7

T. R. Andersen, H. F. Dam, B. Andreasen, M. Hösel, M. V. Madsen, S. A. Gevorgyan, R. R. Søndergaard, M. Jørgensen, and F. C. Krebs, *A rational method for developing and testing stable flexible indium-and vacuum-free multilayer tandem polymer solar cells comprising up to twelve roll processed layers*, *Solar Energy Materials and Solar Cells*, **2013**, DOI: 10.1016/j.solmat.2013.07.006.

A2.8

J. E. Carlé, T. R. Andersen, M. Helgesen, E. Bundgaard, M. Jørgensen, and F. C. Krebs, *A laboratory scale approach to polymer solar cells using one coating/printing machine, flexible substrates, no ITO, no vacuum and no spincoating*, *Solar Energy Materials and Solar Cells*, **2013**, 108, 126-128, DOI: 10.1016/j.solmat.2012.09.008.

A2.9

M. Jørgensen, J. E. Carlé, R. R. Søndergaard, M. Lauritzen, N. A. Dagnæs-Hansen, S. L. Byskov, T. R. Andersen, T. T. Larsen-Olsen, A. P. L. Böttiger, B. Andreasen, L. Fu, L. Zuo, Y. Liu, E. Bundgaard, X. Zhan, H. Chen, and F. C. Krebs, *The state of organic solar cells—A meta analysis*, **2013**, DOI: 10.1016/j.solmat.2013.05.034.

Aqueous Processing of Low-Band-Gap Polymer Solar Cells Using Roll-to-Roll Methods

Thomas R. Andersen, Thue T. Larsen-Olsen, Birgitta Andreasen, Arvid P. L. Böttiger, Jon E. Carlé, Martin Helgesen, Eva Bundgaard, Kion Norrman, Jens W. Andreasen, Mikkel Jørgensen, and Frederik C. Krebs*

Solar Energy Programme, Risø National Laboratory for Sustainable Energy, Technical University of Denmark, Frederiksborgvej 399, DK-4000 Roskilde, Denmark

Aqueous processing of polymer solar cells presents the ultimate challenge in terms of environmental friendliness and has only been reported in a few instances. The approaches to solubilization of the conjugated and active material in water fall in three categories: solubilization through (1) ionic side chains such as sulfonic acid, carboxylic acid, or ammonium, (2) nanoparticle dispersions of hydrophobic polymers in water, or (3) nonionic alcohol and glycol side chains. The latter approach is the most recent and most successful in terms of performance where PCEs of up to 0.7% have been reached on indium tin oxide (ITO) substrates with aqueous processing of the four subsequent layers in the solar cell stack (including the printed metal back electrode).¹ The approach employing ionic side chains is perhaps conceptually the most appealing as it opens up for layer-by-layer assembly of the films or interface layers² but has so far not been employed successfully for the active layer itself. The nanoparticle dispersion approach developed by Landfester *et al.*^{3–7} is particularly appealing as it allows for control of the nanoparticle size and for processing using pure water as solvent for common hydrophobic conjugated polymers. In terms of development of the polymer and organic photovoltaic (OPV) technology, the latter point is of some significance since the large body of polymers available today has been developed for processing in organic solvents such as chlorobenzene, 1,2-dichlorobenzene, *etc.* One could envisage a complete redesign of the chemistry as described above¹ (method 3) but it will require a complete rediscovery of the solvent–material interaction and morphology relationships. While this may be necessary, in

ABSTRACT Aqueous nanoparticle dispersions of a series of three low-band-gap polymers poly[4,8-bis(2-ethylhexyloxy)benzo(1,2-b:4,5-b')dithiophene-alt-5,6-bis(octyloxy)-4,7-di(thiophen-2-yl)(2,1,3-benzothiadiazole)-5,5'-diyl] (P1), poly[(4,4'-bis(2-ethylhexyl)dithieno[3,2-b:2',3'-d]silole)-2,6-diyl-alt-(2,1,3-benzothiadiazole)-4,7-diyl] (P2), and poly[2,3-bis-(3-octyloxyphenyl)quinoxaline-5,8-diyl-alt-thiophene-2,5-diyl] (P3) were prepared using ultrasonic treatment of a chloroform solution of the polymer and [6,6]-phenyl-C₆₁-butyric acid methyl ester ([60]PCBM) mixed with an aqueous solution of sodium dodecylsulphate (SDS). The size of the nanoparticles was established using small-angle X-ray scattering (SAXS) of the aqueous dispersions and by both atomic force microscopy (AFM) and using both grazing incidence SAXS (GISAXS) and grazing incidence wide-angle X-ray scattering (GIWAXS) in the solid state as coated films. The aqueous dispersions were dialyzed to remove excess detergent and concentrated to a solid content of approximately 60 mg mL⁻¹. The formation of films for solar cells using the aqueous dispersion required the addition of the nonionic detergent FSO-100 at a concentration of 5 mg mL⁻¹. This enabled slot-die coating of high quality films with a dry thickness of 126 ± 19, 500 ± 25, and 612 ± 22 nm P1, P2, and P3, respectively for polymer solar cells. Large area inverted polymer solar cells were thus prepared based on the aqueous inks. The power conversion efficiency (PCE) reached for each of the materials was 0.07, 0.55, and 0.15% for P1, P2, and P3, respectively. The devices were prepared using coating and printing of all layers including the metal back electrodes. All steps were carried out using roll-to-roll (R2R) slot-die and screen printing methods on flexible substrates. All five layers were processed using environmentally friendly methods and solvents. Two of the layers were processed entirely from water (the electron transport layer and the active layer).

KEYWORDS: roll-to-roll coating polymer solar cells · organic solar cells · slot-die coating · aqueous inks · nanoparticle dispersions

the end it is of interest to simply adapt the large body of materials at hand to an aqueous process. It is also of critical importance to replace the organic solvents if one has the ambition to manufacture polymer solar cells on a gigawatt scale.

There are several concerns associated with the use of chlorinated and aromatic solvents on a very large scale. Concern for the people working at the manufacturing machine is crucial both in terms of toxicity and, in the case of aromatic solvents,

* Address correspondence to frkr@risoe.dtu.dk.

Received for review March 11, 2011 and accepted April 14, 2011.

Published online April 22, 2011
10.1021/nn200933r

© 2011 American Chemical Society

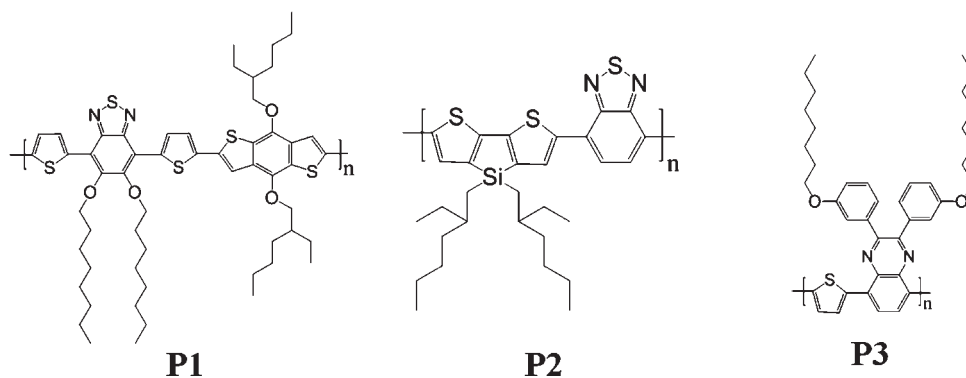


Figure 1. The structure for the three polymers used, P1, P2, and P3 (see text for the systematic names).

flammability. In the case of the chlorinated solvents the environmental concern is large, and it is unlikely that large scale manufacturing using such solvents is possible in a European setting. As an example, the current state of the art based on ProcessOne⁸ would involve approximately 16 million liters of chlorobenzene for the production of 1 GW_p of polymer solar cell. An additional concern is the cumulative energy needed for raw materials production, where a poor choice of processing method and processing materials can severely affect the energy payback time (EPBT) of the solar cell. Life cycle analysis has confirmed that water is the solvent that is most beneficial to use, requiring only a small electrical energy input for production.⁹ The cumulative thermal energy in materials production of chlorobenzene alone, as given in the example above, would be 880 TJ, adding 10 days to the EPBT. In contrast the use of water as the solvent would require only 17 TJ, adding only 4 h to the EPBT.

In terms of active materials the most successful approach so far has been the use of low-band-gap materials based on the donor–acceptor approach as shown in Figure 1. The UV–vis spectra of the three polymers **P1**, **P2**, and **P3** were recorded, and the optical band gaps were determined to be 1.8, 1.5, and 1.8 eV, respectively (Figure 2).

In this work we prepared aqueous nanoparticle dispersions of the known low-band-gap polymers poly[4,8-bis(2-ethylhexyloxy)benzo(1,2-b:4,5-b')dithiophene-alt-5,6-bis(octyloxy)-4,7-di(thiophen-2-yl)(2,1,3-benzothiadiazole)-5,5'-diyl] (**P1**),¹⁰ poly[(4,4'-bis(2-ethylhexyl)-dithieno[3,2-b:2',3'-d]silole)-2,6-diyl-alt-(2,1,3-benzothiadiazole)-4,7-diyl] (**P2**),¹¹ and poly[2,3-bis(3-octyloxyphenyl)-quinoxaline-5,8-diyl-alt-thiophene-2,5-diyl] (**P3**)¹² (Figure 1) in mixtures with [60]PCBM. We developed an aqueous R2R manufacturing process for flexible polymer solar cells through careful ink formulation and processing.

RESULTS AND DISCUSSION

Overview. The polymer solar cell has grown from a laboratory experiment to an emerging technology

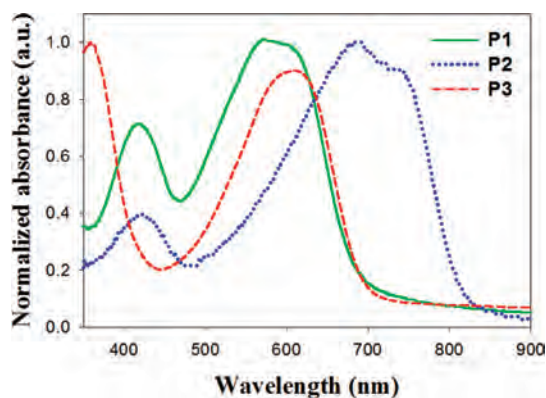


Figure 2. The UV–vis spectra of P1, P2, and P3. The optical band gap was determined to be 1.8, 1.5, and 1.8 eV for P1, P2, and P3, respectively.

with great potential to significantly contribute to future energy production. Currently, polymer solar cells can be prepared using industrial roll-to-roll methods⁸ and are sufficiently stable for demonstration products. They have for instance been employed as a low cost lighting solution for developing countries.¹³ While upscaling has been described successfully their current potential should be viewed critically^{14,15} and compared to existing thin film solar cell technologies such as CdTe and amorphous silicon. The polymer solar cell is currently the poorest performing PV technology (in existence) in terms of power conversion efficiency, while it has distinct advantages of high speed production, adaptability, and an abundance of raw materials. Recent work on the life cycle analysis from several groups⁹ have highlighted the potential of the technology and in one case, where the source of data was fully public, revealed EPBTs in the range of 1.35–2.02 years.⁹ As outlined in the introduction there is an urgent need for processes and processing materials that lower the embedded energy and the process energy, as this is a necessary method for lowering the EPBT. This should of course go in hand with an increase in efficiency. In this work where we aim at replacing the organic solvent for processing of the active area with water there is a direct gain at the site of manufacture but it should be emphasized that solvents and large amounts of

detergent are required for the manufacture of the nanoparticle dispersions. It is assumed that those can be recycled to fully benefit from the aqueous processing of hydrophobic materials that has already been developed. If this is not the case then there might not be any gain in the cumulative energy for raw materials production but there will still be a large gain in terms of human safety and lower emission of chlorinated or aromatic solvent into the environment because the preparation of the nanoparticle dispersions inherently allows for containment and reuse of solvents. A detailed life cycle analysis of the inks is thus warranted and until this has been carried out a complete comparison is not possible. At this point however the benefits of an aqueous ink are large enough to justify research in this direction.

Formation of Nanoparticle Dispersions. The generic method developed by Landfester *et al.* in a series of original research papers during the period from 1999 to 2004 was followed and found to be directly applicable with minor modifications.^{3–7} A significantly larger amount of SDS was found to be needed than reported previously for a given nanoparticle size. The correlation between the size of the nanoparticles and the amounts of solvent, water, and SDS seem to be depending on the properties of the individual polymers. We found that a 100 mM SDS solution and a solid content in the organic phase of $\sim 40 \text{ mg mL}^{-1}$ reproducibly gave nanoparticles with a size below 150 nm as established with SAXS measurements. We also found that the nanoparticles were conserved in the coated films (*vide supra*). The observed discrepancy in particle size as a function of SDS content could also be linked to the

method of particle size determination where light scattering was employed previously. The reported method for the removal of the excess detergent comprises dialysis and centrifugal dialysis. These methods however allow for the preparation of only small quantities of ink. In our case large volumes ($>100 \text{ mL}$) of inks with a high solid content was needed, and we initially attempted using a large basket centrifuge allowing for the continuous addition of water but finally settled on a Millipore filter system with a processing volume of 500 mL. Using this method, ink volumes of 100 mL with a solid content of 60 mg mL^{-1} could be prepared in a few hours. The inks were diluted 625 times corresponding to a final SDS concentration in the ink of 0.16 mM.

Particle Size and Crystalline Order. SAXS was employed on both the aqueous dispersions and on the solid films to determine particle sizes. AFM images of the films were analyzed to determine particle size distributions and gave similar results.

GIWAXS data showed poorly developed crystalline order of polymers **P2** and **P3**, with only weak first order reflections corresponding to lamellar spacings of 18.2 and 24.0 Å, respectively, and a broad peak at $\sim 1.34 \text{ \AA}^{-1}$ that we ascribe to packing of disordered side chains. **P1** showed very weak scattering, with no features that may be attributed to crystalline order of the polymer (the wide peak at high q values is the background signal from the glass substrate). All three films show a weak peak at $\sim 0.69 \text{ \AA}^{-1}$ that we ascribe to nanocrystalline [60]PCBM (Table 1 and Figures 3 and 4).

Inks and Roll-to-Roll Coating. The spin coating of thin films was possible, whereas large area films with the thickness/coverage required for making functional OPV devices was not possible. It was further found impossible to successfully coat these inks even with very fast web speeds and fast drying on a heated roller and a short distance (18 cm) between the coating head and the oven. Web speeds as high as 8 m min^{-1} were employed with a roller temperature of $80 \text{ }^\circ\text{C}$. By heating the foil just after coating, quick drying was possible (within seconds), but significant dewetting was still observed (see Supporting Information).

TABLE 1. The Average Particle Diameter in P1, P2, and P3 As Determined by SAXS and AFM. The Standard Deviation Is Given in the Brackets

polymer	SAXS (dispersions)	AFM (films)	GISAXS (films)
P1	130(38) nm	<i>a</i>	<i>a</i>
P2	32(10) nm	69(47) nm	32(22) nm
P3	87(21) nm	120(82) nm	107(72) nm

^a Not possible to establish due to aggregation in the sample.

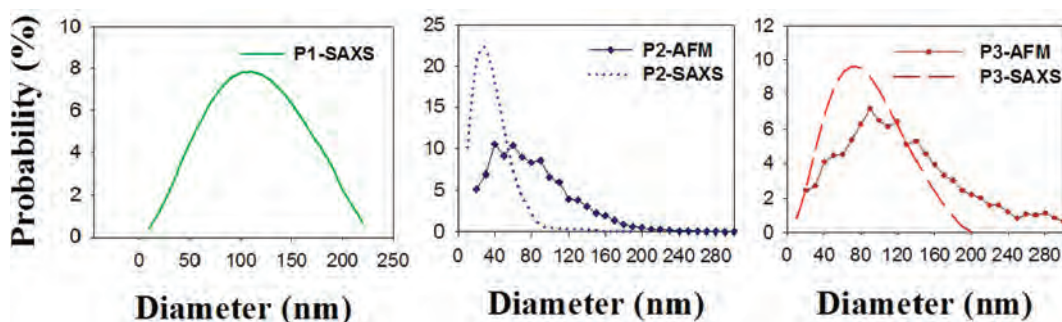


Figure 3. Size distributions of the particles P1 (left), P2 (middle), P3 (right) measured by AFM and SAXS. The SAXS measurements were performed with the particles in a water suspension, and the AFM was measured from spin-coated films. The distribution of P1 could not be determined by AFM due to aggregation of the particles.

Careful inspection of the wetting behavior revealed that the ink initially wets the surface and then dewets leaving a thin film (possibly comprising a single layer of nanoparticles). We ascribe this to the initial wetting and drying followed by lowering of the surface energy of the first layer and subsequent dewetting of the higher surface tension solution.

This phenomenon is quite well-known in the area of coating technology and is in essence a result of poisoning the otherwise wettable surface by the surface active properties of the ink itself. To solve this problem, the addition of a nonionic fluorosurfactant (FSO-100) was found to be necessary. The amount added was critical, and with too little material dewetting was still observed,

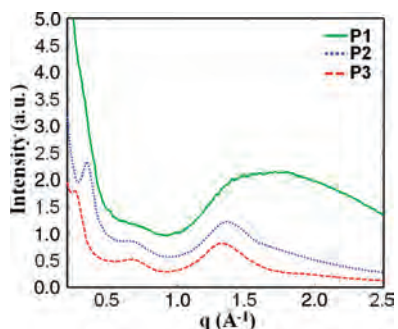


Figure 4. GIWAXS patterns of the three polymers, spin-coated on glass. No texture was observed, and the 2D patterns were thus azimuthally averaged as a function of q . The patterns are scaled for clarity.

whereas too much led to films with extremely poor adhesion. A concentration of 5 mg mL^{-1} was found to be the best compromise between coatability and adhesion. Films prepared in this manner passed the tape test.¹⁶ The age of the meniscus was found to be of critical importance for efficient wetting and good adhesion of the dried film. This phenomenon is well-known in the area of coating technology, where shear induced in the ink as a result of the coating process itself leads to depletion of surfactant at the surface of the ink. In the case of water based inks this implies that the surface tension of the ink in the region of coating increases to a level where dewetting occurs. In such cases the speed of the coating process must be decreased to a level where the surfactant has time to diffuse to the surface and maintain the lower surface tension. Web speeds of 1 m min^{-1} were found to present the best conditions even though web speeds as high as 1.6 m min^{-1} could also be employed. A web speed of 0.6 m min^{-1} was used in all experiments to fabricate the devices presented in this work. Examples of dewetting during coating can be seen in the Supporting Information, and correct wettings are shown in Figure 5. The thickness of the dry active layers of **P1**, **P2**, and **P3** were measured by AFM profilometry and were found to be 126 ± 19 , 500 ± 25 , and $612 \pm 22 \text{ nm}$, respectively.

The devices were completed by slot-die coating poly-(3,4-ethylenedioxythiophene) poly(styrenesulfonate) (PEDOT:PSS) on top of the active layer and interestingly

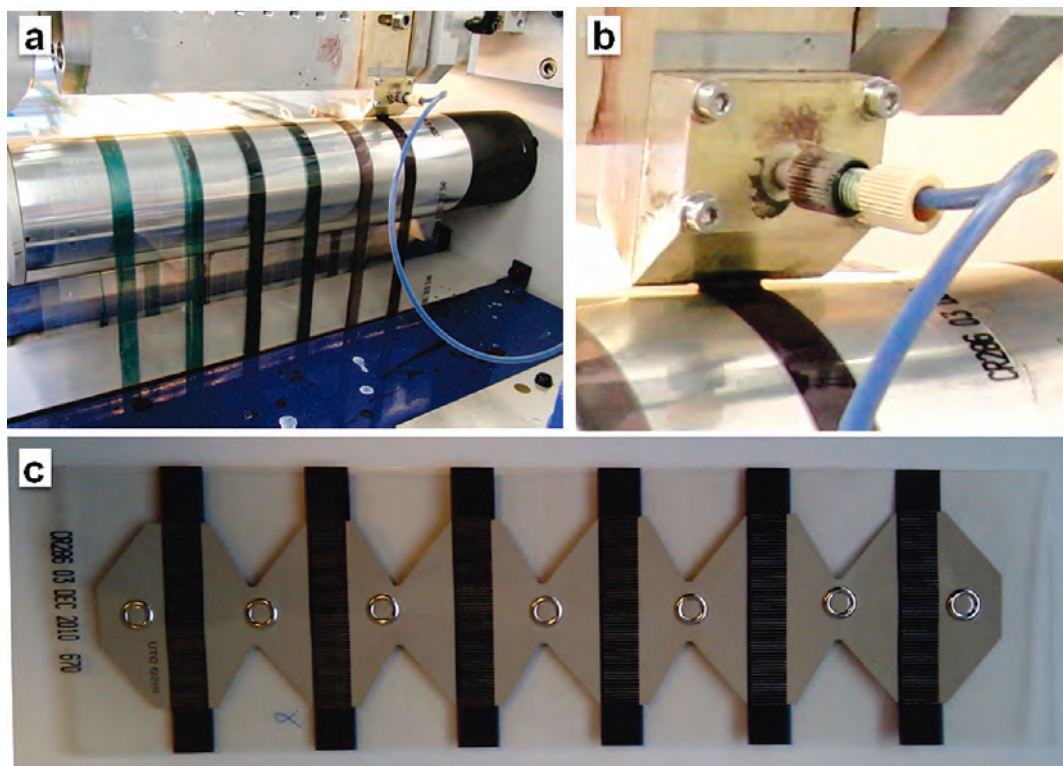


Figure 5. (a) Slot-die coating of the active layer using the aqueous nanoparticle dispersions and (b) an enlargement of the coating head, coating bead and wet film, and (c) showing a complete device with six individual solar cells.

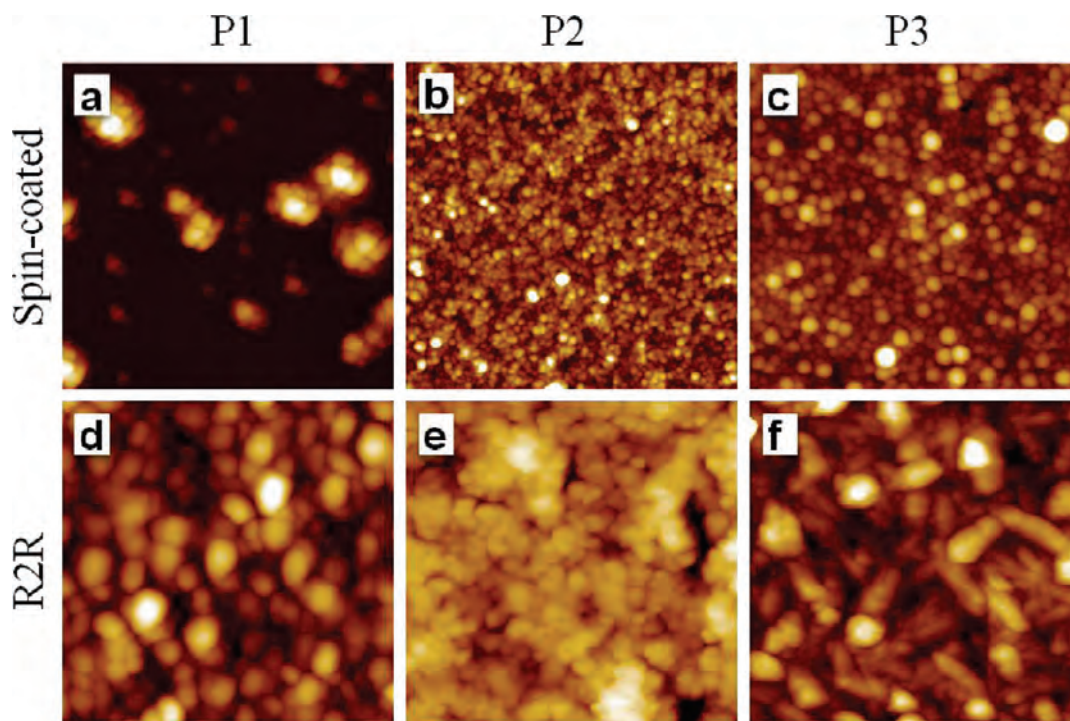


Figure 6. AFM topography images of spin-coated (a–c) and R2R (d–f) prepared samples of P1, P2, and P3. All the images were taken at $5 \times 5 \mu\text{m}^2$.

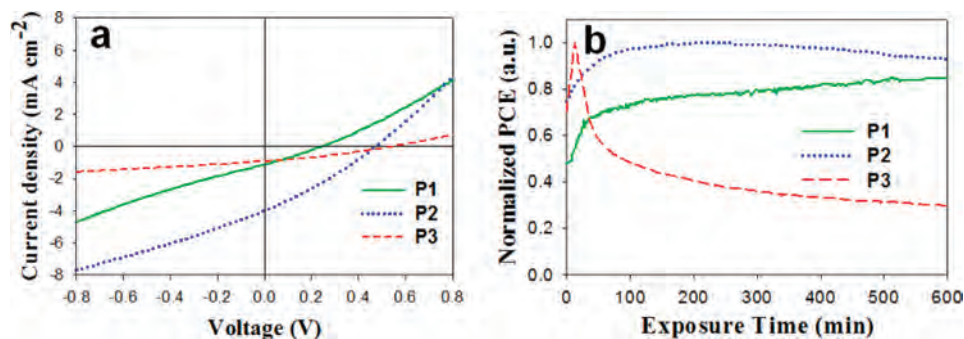


Figure 7. (a) *IV*-curves for the devices based on the three different polymers, at peak performance (AM1.5G , 1000 W m^{-2} , $85 \pm 5 \text{ }^\circ\text{C}$). (b) The development of the solar cell PCE during the initial 10 h of the exposure to 1 sun is shown for the three different polymers. Values are normalized to the corresponding peak value for each polymer (see Table 2).

no prewetting of the active layer with isopropyl alcohol was needed. We ascribe this to a fortuitous interaction between the fluorosurfactants in the PEDOT:PSS formulation and in the coated active layer. The devices were completed by screen printing a silver ink onto the PEDOT:PSS electrode. The devices were finally encapsulated using a simple barrier foil as described earlier and tested using an automated roll-to-roll IV-tester.^{8,14,15}

Morphology. The morphology differences between spin-coated and R2R prepared samples and between the different sample materials can clearly be observed in the AFM images in Figure 6. On the spin-coated samples the individual nanoparticle shapes can be observed (with exception of **P1**, which looks like agglomerates made up of smaller particles). In the R2R samples the nanoparticles can no longer be clearly

distinguished; instead it looks like the nanoparticles have merged in places. The different morphologies observed across the R2R samples could be caused by the “harsh” process conditions, where annealing at high temperatures is involved, and due to the different thermal properties of the polymers.

When the R2R coated samples in Figure 6 panels d, e, and f are compared, it looks like the particles are increasingly merged ($d < f < e$). This could be because these samples were prepared at slightly different conditions with the annealing time increasing ($d < f < e$). Each roll-to-roll experiment (a roll of foil) comprises six coated stripes as described earlier.¹⁵ The first coated stripe will thus pass the oven a total of eight times, whereas that last coated stripe will pass the oven a total of three times (including the two passages when

coating PEDOT:PSS and printing the silver back electrode).

Device Performance. The freshly prepared devices were put under a calibrated solar simulator (AM1.5G, 1000 W m^{-2}) and *I*/*V*-scans were recorded every 1 min, for up to 36 h (according to the ISOS-L-1 procedure²⁶ using a temperature of $85 \pm 5 \text{ }^\circ\text{C}$). For all devices an initial steady increase in PCE during exposure to sunlight was generally observed.

However the optimum period of light exposure was significantly different for the three photoactive polymers, as can be seen in Figure 7. The PCE increase was caused by improvement of both the short circuit current and open circuit voltage, while the fill-factor was relatively constant. This behavior is not unique for these cells prepared from water-dispersed nanoparticles, but is readily observed for other polymer solar cells, having the same layer structure but an active layer processed from organic solvents such as chlorobenzene.¹⁵ It is ascribed to a combination of effects such as photodoping of the zinc oxide layer by UV-light, accompanied by beneficial morphological changes in the active layer due to the relatively high temperature ($85 \pm 5 \text{ }^\circ\text{C}$).¹⁴

The devices prepared from the aqueous dispersions show poorer performance compared to earlier reported efficiencies for devices based on **P1**, **P2**, and **P3**, prepared using chlorobenzene as solvent (Figure 7).^{10–12} The source of this most likely shunts across the active layer. Because of the particle nature of the active layers (Figure 6), the film will be somewhat porous and thus susceptible to shunting by the subsequent processing of PEDOT:PSS. It is thus likely that the amount of shunts should be dependent on the layer thickness relative to the particle diameters. When the obtained PCEs for the different polymers are

compared, it is observed that thicker layers and smaller particle size seem to give a higher performance. Apart from these suspected microscopic shunts, there are some larger shunts for some devices due to incomplete coverage evident from optical inspection of the film and even more so from the light beam induced current (LBIC) scan shown in Figure 8 where (blue) dots within the (red/green) active area reveal such shunts. Furthermore, effects from the significant amount of fluorosurfactant present in the ink along with the residual SDS bound to the surface of the nanoparticles have not been determined. This does however show that it is possible to prepare devices from water with a non-negligible performance, and worth noting that a large part of the relatively low performance of these devices prepared from water could be due to coating technicalities that are bound to become less pronounced as further experience is gained.

Directions for Future Work. The possibility of achieving aqueous processing and operator safety and avoiding the emission of environmentally harmful solvents to the environment was demonstrated, and while this is a great step forward it was achieved at the expense of using a fluorinated surfactant. There is a well-documented concern over release of fluorinated surfactants to the environment where extremely harmful effects have been documented.¹⁷ In our case the surfactant is not released directly to the environment but will follow the solar cell until the end of its life cycle, where it should be properly disposed. The identification of existing environmentally friendly surface active materials or the development of new ones for coating should be researched actively to avoid the use of fluorinated detergents while maintaining the advantages of aqueous processing of OPV.

The relationship between the chemical disposition of the polymer materials and nanoparticle size in the final ink will have to be established along with the relationship between the size of the nanoparticles and the performance of the solar cell printed from them. Since this requires quite large quantities of conjugated polymer material, the type of materials that perform best should be identified followed by replacement of the fluorinated surfactant. Once the truly environmentally friendly ink with the best performance has been identified the ink can be finally optimized with respect to nanoparticle size, solid content, drying time, etc.

TABLE 2. The Photovoltaic Properties Obtained for the Devices When Processed from Water^a

polymer	V_{oc} (V)	J_{sc} (mA cm^{-2})	FF (%)	PCE (%)
P1	0.24	1.10	27.5	0.07
P2	0.47	3.99	29.3	0.55
P3	0.54	0.92	30.8	0.15

^aThe device geometry was PET/ITO/ZnO/polymer-[60]PCBM/PEDOT:PSS/Ag-(printed), and the active area of the devices was 4 cm^2 . The testing conditions were AM1.5G, 1000 W m^{-2} , $85 \pm 5 \text{ }^\circ\text{C}$.

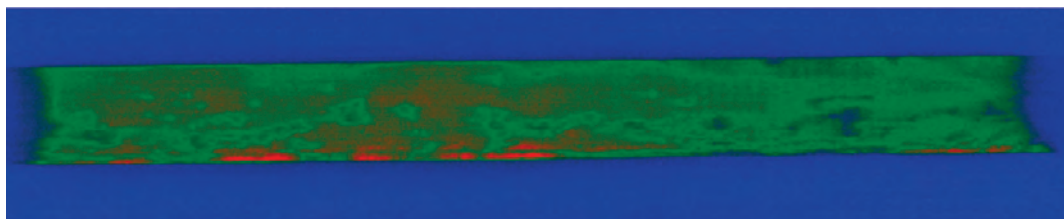


Figure 8. The LBIC image for a mapping of a P2 cell. The intensity scale is going from blue with no intensity over green to red with high intensity.

In our case **P2** proved to work best and further optimization using this class of materials should be pursued.

CONCLUSIONS

We have successfully prepared aqueous nanoparticle dispersions of three low-band-gap polymers and formulated inks for roll-to-roll processing into polymer solar cells on a flexible substrate which resulted in PCEs of 0.55, 0.15, and 0.07% for poly[(4,4'-bis(2-ethylhexyl)dithieno[3,2-b:2',3'-d]silole)-2,6-diyl-alt-(2,1,3-benzothiadiazole)-4,7-diyl], poly[2,3-bis-(3-octyloxyphenyl)-quinoxaline-5,8-diyl-alt-thiophene-2,5-diyl], and poly[4,8-bis(2-ethylhexyloxy)benzo(1,2-b:4,5-b')

dithiophene-alt-5,6-bis(octyloxy)-4,7-di(thiophen-2-yl)(2,1,3-benzothiadiazole)-5,5'-diyl], respectively. We analyzed the nanoparticles in aqueous dispersion using SAXS and in solid film using GISAXS, GIWAXS, and AFM. The ink formulation and roll-to-roll processing was found to be challenging, however a reproducible method giving homogeneous films that adhered well to the surface of the zinc oxide based electron transport layer was obtained. The relatively poor device performance is ascribed to shunting and non-optimum morphology. Further work should be directed at improving coating condition and ink formulation as this has been successful in the case of organic solvent systems.

METHODS

Materials. The polymers were prepared as described in the literature.^{10–12} They had values for M_n , M_w , and polydispersities of, respectively, 11.0 kDa, 28.7 kDa, and 2.6 for **P1**, 6.0 kDa, 10.9 kDa and 1.8 for **P2**, and 21.0 kDa, 89.0 kDa, and 4.2 for **P3**. [60]PCBM, SDS and chloroform were purchased in standard grade. An aqueous precursor solution for the zinc oxide was prepared as described in the literature.¹ PEDOT:PSS was based on EL-P 5010 from Agfa that was diluted with isopropyl alcohol to a viscosity of 200 mPa·s. The printable silver back electrode was PV410 from Dupont.

Nanoparticle Preparation. The typical recipe for small scale production, the polymer material (0.3 g) was together with [60]PCBM (0.3 g) dissolved in chloroform (15.5 mL) and mixed with an aqueous 100 mM SDS solution (50 mL) in a large beaker. The mixture was stirred vigorously for 1 h and then subjected to ultrasound (1 kW) for 5 min using an UIP 1000hd transducer from Hielscher ultrasound technology fitted with a booster head. The mixture was then stirred on a hot plate at 65 °C for 3 h until all the chloroform had evaporated. For small scale preparations, the aqueous dispersion was then dialyzed in dialysis tubing against 2×10 L pure water. In the final step the suspensions were concentrated to have a solid content of approximately 60 mg mL⁻¹.

For large scale preparations, the aqueous dispersion was dialyzed using a Millipore system with a capacity of 500 mL. The mixture was concentrated by dialysis from a volume of 500 mL to a volume of 100 mL with a forward pressure of 1.4 bar and a pressure gradient across the filter of 0.7 bar. Pure water (400 mL) was then added and the procedure was repeated 4 times corresponding to a dilution of the solution by a factor of 625. In the final step the suspensions were concentrated to have a solid content of 60 mg mL⁻¹.

X-ray Scattering. The SAXS and grazing incidence SAXS (GISAXS) experiments were performed at a laboratory setup using a rotating Cu-anode operating at 46 kV and 46 mA as X-ray source. The SAXS instrument was configured for a fully evacuated sample to detector distance of 4579 mm covering a q -range of $2.5 \times 10^{-3} < q < 0.12 \text{ \AA}^{-1}$, where the length of the scattering vector $q = 4\pi \sin(\theta)/\lambda$, with θ equal to half the scattering angle, and λ being the X-ray wavelength for Cu K α (1.5418 Å). The X-rays are monochromated and collimated by two-dimensional multilayer optics and detected by a 2D “Gabriel”-type gas-proportional delay line detector.¹⁸ The nanoparticle dispersions were measured in 1 mm borosilicate capillaries, sealed with epoxy glue for the SAXS experiments, and GISAXS of films spin-coated on glass were measured by orienting the substrate at an X-ray incidence angle of 0.5°. The 2D scattering images of the randomly oriented particles in dispersion were reduced to 1D cross sections by azimuthal

averaging, whereas the GISAXS scattering were reduced to 1D curves by taking projections through the Yoneda peak¹⁸ at constant q_z . The reduced 1D data were analyzed by using the Bayesian inverse Fourier transform (BIFT).¹⁹

GIWAXS of spin-coated films on glass were acquired by orienting the substrate surface just below the critical angle for total reflection with respect to the incoming X-ray beam (0.18°), maximizing scattering from the deposited film with respect to scattering from the substrate. In the wide scattering angle range ($>5^\circ$), the X-ray scattering is sensitive to crystalline structure. For the experiment we used a camera comprising an evacuated sample chamber with an X-ray photosensitive image plate as detector and a rotating Cu-anode operating at 50 kV/200 mA as X-ray source, focused and monochromatized (Cu K α , $\lambda = 1.5418 \text{ \AA}$) by a 1D multilayer.¹⁹ The samples were mounted 120 mm from the detector. The GIWAXS data were analyzed by reducing the acquired 2D data by azimuthal averaging of intensity as a function of scattering vector length, q , to determine the characteristic d -spacings of the polymers, using the software SimDiffraction.²⁰

Atomic Force Microscopy. AFM imaging was performed on an N8 NEOS (Bruker Nano GmbH, Herzogenrath, Germany) operating in an intermittent contact mode using PPP-NCLR cantilevers (NANOSENSORS, Neuchatel, Switzerland). Images were recorded at a scan speed of 0.8 lines min⁻¹. The images were analyzed using the image processing software package SPIP 5.1.5 (Image Metrology A/S, Hørsholm, Denmark).

The samples were first delaminated by ripping the plastic laminate off in a swift motion and thereafter placed on a glass slide using double sided tape.

It is well-known that AFM can at times overestimate particle sizes in the lateral plane and therefore the height z is often used as a measure for the diameter of spherical particles.^{21–23} However, since the particles in the samples at hand are closely packed the height measurements of individual particles would be too time-consuming and inaccurate.²⁴ Therefore the best estimate to determine the particle size was to employ the Particle & Pore Analysis module included in the SPIP 5.1.5 software. The size was analyzed on at least two different positions of the sample analyzing a minimum of 2000 particles on each sample.

The thicknesses of the dry films were measured by AFM profilometry, see Figure 9. The thickness was measured at a minimum of three different positions on each film, with each position consisting of at least three individual measurements.

Light Beam Induced Current (LBIC) Mapping. The LBIC experiments were carried out using a custom-made setup with 410 nm laser diode (5 mW output power, 100 μ m spot size ($\approx 65 \text{ W/cm}^2$), ThorLabs) mounted on a computer controlled XY-stage and focused to a spot size of $<100 \mu\text{m}$. The short circuit current from the device under study was measured using a computer

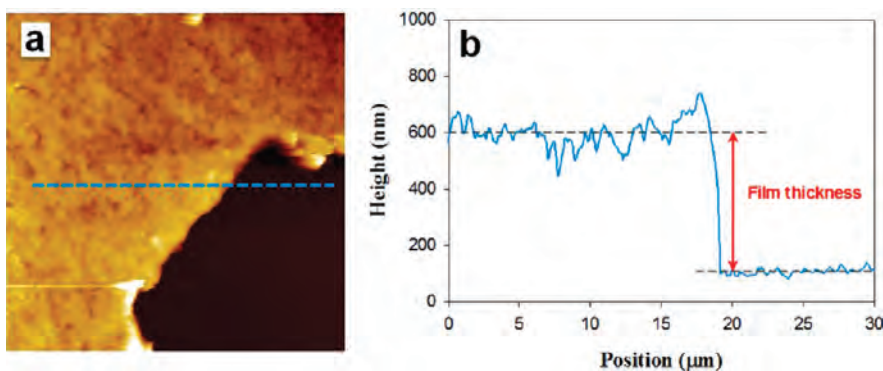


Figure 9. (a) $30 \times 30 \mu\text{m}^2$ AFM topography image indicating where the thickness was measured. (b) line profile extracted from the AFM image (dashed line).

controlled source measure unit (Keithley 2400), and mapped by raster scanning across the device. Further details are available elsewhere.²⁵

Ink Formulation. The nonionic fluorosurfactant (FSO-100) was added to the dialyzed aqueous suspension of the polymer/[60]PCBM nanoparticles. The concentration of fluorosurfactant was 5 mg mL^{-1} and the polymer/[60]PCBM concentration was 60 mg mL^{-1} . This solution was employed directly for slot-die coating.

Roll-to-Roll Coating. A PET substrate with an ITO pattern was prepared and cleaned as described earlier.^{13–15} The zinc oxide precursor solution was prepared as described earlier¹ and comprised $\text{Zn}(\text{OAc})_2 \cdot 2\text{H}_2\text{O}$ (100 mg mL^{-1}), $\text{Al}(\text{OH})(\text{OAc})_2$ (2 mg mL^{-1}), and FSO-100 (2 mg mL^{-1}) in water. This solution was microfiltered immediately prior to use ($0.45 \mu\text{m}$) and then slot-die coated at a speed of 2 m min^{-1} with a wet thickness of $4.9 \mu\text{m}$. After the initial drying of the precursor film it was converted into an insoluble film by passage through an oven at a temperature of $140 \text{ }^\circ\text{C}$ with a speed of 0.2 m min^{-1} (oven length = 4 m). This gave an insoluble doped zinc oxide film with a thickness of $25 \pm 5 \text{ nm}$. The aqueous polymer/[60]PCBM nanoparticle dispersion was then slot-die coated at a speed of 1 m min^{-1} with a wet thickness of 30.4 , 17.6 , and $20.8 \mu\text{m}$ for **P1**, **P2**, and **P3**, respectively. The coating speed and the time between application of the wet film and the drying were critical for successful formation of a homogeneous film without dewetting. The slot-die coating head had a temperature of $60 \text{ }^\circ\text{C}$, the coating roller had a temperature of $80 \text{ }^\circ\text{C}$, and the temperature of the foil was kept at $80 \text{ }^\circ\text{C}$ until it reached the oven at $140 \text{ }^\circ\text{C}$. The distance from the point of coating to the oven entry was 18 cm . PEDOT:PSS was then applied by slot-die coating at a speed of 0.2 m min^{-1} and dried at $140 \text{ }^\circ\text{C}$ (oven length = 2 m). It was found unnecessary to wet the film surface prior to coating the PEDOT:PSS and this might be due to the beneficial interaction between the fluorosurfactants in the active layer film and in the PEDOT:PSS. Finally the device was completed by roll-to-roll screen printing a silver grid electrode and drying at $140 \text{ }^\circ\text{C}$. The devices were encapsulated using roll-to-roll lamination of a simple food packaging barrier with a pressure sensitive adhesive onto both sides of the foil.^{13–15}

IV-Characterization. In each coated stripe that represents one set of experiments a total of 150 solar cells were prepared (900 cells for each roll). The devices were light soaked with continuous sweeping of the *IV*-curve until a constant performance was reached. Typically the performance dropped rapidly during the first 10 min of light soaking followed by a slow improvement in performance over 4–6 h where a stable level of performance was reached. The data reported is for the stable regime. The devices were initially tested using a roll-to-roll tester and the functional devices were the recovered for further testing using a calibrated solar simulator (AM1.5G , 1000 W m^{-2} , $85 \pm 5 \text{ }^\circ\text{C}$). The prolonged testing was made according to the ISOS-L-1 procedure.²⁶

Acknowledgment. This work was supported by the Danish National Research Foundation. We gratefully acknowledge the

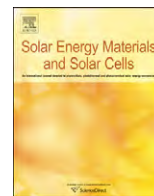
assistance of Steen Hansen with modifying the BIFT algorithm for use with polydisperse systems and Lasse Gorm Jensen for creating graphical illustrations.

Supporting Information Available: Details of the GISAXS analysis of solid films, with data and the description of the data reduction procedure; details of dewetting during coating. This material is available free of charge via the Internet at <http://pubs.acs.org>.

REFERENCES AND NOTES

- Søndergaard, R.; Helgesen, M.; Jørgensen, M.; Krebs, F. C. Fabrication of Polymer Solar Cells Using Aqueous Processing for All Layers Including the Metal Back Electrode. *Adv. Eng. Mater.* **2011**, *1*, 68–71.
- Rider, D. A.; Worfolk, B. J.; Harris, K. D.; Lalany, A.; Shahbazi, K.; Fleischauer, M. D.; Brett, M. J.; Buriak, J. M. Stable Inverted Polymer/Fullerene Solar Cells Using a Cationic Polythiophene Modified PEDOT:PSS Cathodic Interface. *Adv. Funct. Mater.* **2010**, *20*, 2404–2415.
- Landfester, K. The Generation of Nanoparticles in Miniemulsions. *Adv. Mater.* **2001**, *13*, 765–768.
- Kietzke, T.; Neher, D.; Landfester, K.; Montenegro, R.; Güntner, R.; Scherf, U. Novel Approaches to Polymer Blends Based on Polymer Nanoparticles. *Nat. Mater.* **2003**, *2*, 408–412.
- Piok, T.; Gamerith, S.; Gadermaier, C.; Plank, H.; Wenzl, F. P.; Patil, S.; Montenegro, R.; Kietzke, T.; Neher, D.; Scherf, U.; *et al.* Organic Light-Emitting Devices Prepared from Semiconducting Nanospheres. *Adv. Mater.* **2003**, *15*, 800–804.
- Kietzke, T.; Neher, D.; Kumke, M.; Montenegro, R.; Landfester, K.; Scherf, U. A Nanoparticle Approach to Control the Phase Separation in Polyfluorene Photovoltaic Devices. *Macromolecules* **2004**, *37*, 4882–4890.
- Antonietti, M.; Landfester, K. Polyreactions in Miniemulsions. *Prog. Polym. Sci.* **2002**, *27*, 689–757.
- Krebs, F. C.; Gevorgyan, S. A.; Alstrup, J. A Roll-to-Roll Process to Flexible Polymer Solar Cells: Model Studies, Manufacture, and Operational Stability Studies. *J. Mater. Chem.* **2009**, *19*, 5442–5442.
- Espinosa, N.; Garcia-Valverde, R.; Urbina, A.; Krebs, F. C. A Life Cycle Analysis of Polymer Solar Cell Modules Prepared Using Roll-to-Roll Methods Under Ambient Conditions. *Sol. Energy Mater. Sol. Cells* **2011**, *95*, 1293–1302.
- Bundgaard, E.; Hagemann, O.; Jørgensen, M.; Krebs, F. C. Low-Band-Gap Polymers for Roll-to-Roll Coated Organic Photovoltaics Design, Synthesis and Characterization. *Green* **2011**, *1*, 55–64.
- Hou, J.; Chen, H. Y.; Zhang, S.; Li, G.; Yang, Y. Synthesis, Characterization, and Photovoltaic Properties of a Low Band Gap Polymer Based on Silole-Containing Polythiophenes and 2,1,3-Benzothiadiazole. *J. Am. Chem. Soc.* **2008**, *130*, 16144–16145.
- Wang, E.; Hou, L.; Wang, Z.; Hellström, S.; Zhang, F.; Inganäs, O.; Andersson, M. R. An Easily Synthesized Blue

- Polymer for High-Performance Polymer Solar Cells. *Adv. Mater.* **2010**, *22*, 5240–5244.
13. Krebs, F. C.; Nielsen, T. D.; Fyenbo, J.; Wadstrøm, M.; Pedersen, M. S. Manufacture, Integration and Demonstration of Polymer Solar Cells in a Lamp for the “Lighting Africa” Initiative. *Energy Environ. Sci.* **2010**, *3*, 512–512.
 14. Krebs, F. C.; Tromholt, T.; Jørgensen, M. Upscaling of Polymer Solar Cell Fabrication Using Full Roll-to-Roll Processing. *Nanoscale* **2010**, *2*, 873–886.
 15. Alstrup, J.; Medford, A. J.; Jørgensen, M.; Krebs, F. C. Ultrafast and Parsimonious Materials Screening for Polymer Solar Cells Using Differentially Pumped Slot-Die Coating. *ACS Appl. Mater. Interfaces* **2010**, *2*, 2819–2827.
 16. ASTM INTERNATIONAL Standards Worldwide. Standard Test Methods for Measuring Adhesion by Tape Test. p. 8.
 17. Renner, R. Growing Concern over Perfluorinated Materials. *Environ. Sci. Technol.* **2001**, *35*, 154A–160A.
 18. Yoneda, Y. Anomalous Surface Reflection of X-Rays. *Phys. Rev.* **1963**, *131*, 2010–2013.
 19. Apitz, D.; Bertram, R.; Benter, N.; Hieringer, W.; Andreasen, J.; Nielsen, M.; Johansen, P.; Buse, K. Investigation of Chromophore-Chromophore Interaction by Electro-optic Measurements, Linear Dichroism, X-ray Scattering, and Density-Functional Calculations. *Phys. Rev. E* **2005**, *72*, 036610-1–036610-10.
 20. Breiby, D. W.; Bunk, O.; Andreasen, J. W.; Lemke, H. T.; Nielsen, M. M. Simulating X-ray Diffraction of Textured Films. *J. Appl. Crystallogr.* **2008**, *41*, 262–271.
 21. Villarrubia, J. Algorithm for Scanned Probe Microscope Image Simulation, Surface Reconstruction, and Tip Estimation. *J. Res. Natl. Inst. Stand. Technol.* **1997**, *102*, 425–454.
 22. Hoo, C. M.; Starostin, N.; West, P.; Mecartney, M. L. A Comparison of Atomic Force Microscopy (AFM) and Dynamic Light Scattering (DLS) Methods to Characterize Nanoparticle Size Distributions. *J. Nanopart. Res.* **2008**, *10*, 89–96.
 23. Boyd, R. D.; Cuenat, A. New Analysis Procedure for Fast and Reliable Size Measurement of Nanoparticles from Atomic Force Microscopy Images. *J. Nanopart. Res.* **2011**, *13*, 105–113.
 24. Dias, A.; Buono, V. T. L.; Vilela, J. M. C.; Andrade, M. S.; Lima, T. M. Particle Size and Morphology of Hydrothermally Processed MnZn Ferrites Observed by Atomic Force Microscopy. *J. Mater. Sci.: Mater. Med.* **1997**, *32*, 4715–4718.
 25. Krebs, F. C.; Søndergaard, R.; Jørgensen, M. Printed Metal Back Electrodes for R2R Fabricated Polymer Solar Cells Studied Using the LBIC Technique. *Sol. Energy Mater. Sol. Cells* **2011**, *95*, 1348–1353.
 26. Reese, M. O.; Gevorgyan, S. A.; Jørgensen, M.; Bundgaard, E.; Kurtz, S. R.; Ginley, D. S.; Olson, D. C.; Lloyd, M. T.; Morvillo, P.; Katz, E. A.; *et al.* Consensus Stability Testing Protocols for Organic Photovoltaic Materials and Devices. *Sol. Energy Mater. Sol. Cells* **2011**, *95*, 1253–1267.



Roll-to-roll processed polymer tandem solar cells partially processed from water

Thue T. Larsen-Olsen, Thomas R. Andersen, Birgitta Andreasen, Arvid P.L. Böttiger, Eva Bundgaard, Kion Norrman, Jens W. Andreasen, Mikkel Jørgensen, Frederik C. Krebs*

Risø National Laboratory for Sustainable Energy, Technical University of Denmark, Frederiksborgvej 399, DK-4000 Roskilde, Denmark

ARTICLE INFO

Available online 21 September 2011

Keywords:

Roll-to-roll processing
Tandem solar cells
Polymer solar cells
Printing and coating
Aqueous processing

ABSTRACT

Large area polymer tandem solar cells completely processed using roll-to-roll (R2R) coating and printing techniques are demonstrated. A stable tandem structure was achieved by the use of orthogonal ink solvents for the coating of all layers, including both active layers. Processing solvents included water, alcohols and chlorobenzene. Open-circuit voltages close to the expected sum of sub cell voltages were achieved, while the overall efficiency of the tandem cells was found to be limited by the low yielding back cell, which was processed from water based ink. Many of the challenges associated with upscaling the multilayer tandem cells were identified giving valuable information for future experiments and development.

© 2011 Elsevier B.V. All rights reserved.

1. Introduction

The ultimate efficiency of polymer solar cells is inherently limited by the narrow absorption bands of the chromophores that constitute the photoactive layer of the solar cells. One obvious route to circumvent this is to stack several junctions having complementary absorption bands, thus increasing the spectral overlap of the solar cell and the terrestrial solar spectrum. The benefits of the tandem architecture over single junction cells have been thoroughly studied and reviewed [1–4], and within reasonable assumptions it has been found that a tandem architecture can increase the ultimate efficiency of polymer solar cells with 20–50%, where the highest increase is seen in the case where the single junction cells perform under their ultimate potential [1,2].

The most advantageous approach to polymer solar cell fabrication, with respect to application as an energy technology, is to allow for fast processing of all layers relying on as few coating/printing methods as possible using roll-to-roll (R2R) processing. With regards to tandem polymer solar cells the most obvious device is an all solution processed monolithic tandem cell where the sub cells are connected in series rather than parallel. This naturally presents some challenges in multilayer coating where the typical number of layers required in a tandem cell is around 6–8. All these layers (some of them very thin) have to be coated on top of each other without having subsequent coating steps adversely affecting already coated layers. The traditional laboratory approach to building up the stack is thus not expected to be easily scalable

since it often employs vacuum deposition of many of the layers and a rational choice in the order of application. With the boundary condition that all layers have to be processed in air without vacuum, using only solution based printing and coating techniques, it becomes very challenging to realize functional tandem structures. So far only one report has documented vacuum free solution processing of all layers, including the printed metal back electrode [5], while large stacks by solution processing (and vacuum deposited back electrodes) have been reported [6]. Most tandem solar cell reports today employ one or more vacuum coating steps.

In this report we demonstrate R2R processing of tandem polymer solar cells on flexible substrates and show that there are many challenges associated not only with solution processing of entire tandem solar cell stacks, but also with the transfer from laboratory scale batch processing on rigid substrates to a full R2R only process on flexible films.

2. Experimental section

2.1. Materials

Poly-3-hexylthiophene (P3HT) was commercially available and had an M_n of ~20000 Da and an M_w ~40000 Da. Phenyl- C_{61} -butyric acid methyl ester (PC[60]BM) had a purity of 99%. Poly-[thiophene-2,5-diyl-*alt*-(2,3-bis(3-octyloxyphenyl)quinoxaline-5,8-diyl)] (TQ-1) was synthesized according to the method described in the literature [7] and had an M_n of ~29000 Da and an M_w ~89000 Da.

The ink used for the front bulk heterojunction (BHJ) active layer comprised PC[60]BM as the acceptor material (18 mg mL⁻¹) and

* Corresponding author. Tel.: +45 46 77 47 99.
E-mail address: frkr@risoe.dtu.dk (F.C. Krebs).

P3HT as the donor polymer (22 mg mL^{-1}) dissolved in chlorobenzene. For the back BHJ active layer an aqueous ink [8] comprising an aqueous dispersion of nanoparticles consisting of the low band gap polymer TQ-1 (Fig. 1) and PC[60]BM prepared as described earlier [8]. An aqueous precursor solution for the zinc oxide (ZnO) used as electron transporting layer (ETL) was prepared as described earlier [9] and comprised $\text{Zn}(\text{OAc})_2 \cdot 2\text{H}_2\text{O}$ (100 mg mL^{-1}), $\text{Al}(\text{OH})(\text{OAc})_2$ (2 mg mL^{-1}) and FSO-100 (2 mg mL^{-1}) in water. Vanadium(V)oxide (V_2O_5) employed as hole transporting layer (HTL) was prepared by diluting a base solution of vanadium(V)-oxoisopropoxide with isopropanol to a concentration of 25 mg mL^{-1} , following recommendations of earlier studies [10,11]. Poly(3,4-ethylenedioxythiophene) poly(styrenesulfonate) (PEDOT:PSS) was based on Orgacon EL-P 5010 from Agfa diluted 2:1 (w:w) with isopropanol. The printable silver back electrode was PV410 from Dupont. The substrate was a 130 micron PET substrate with a patterned ITO layer (nominally $60 \Omega \text{ square}^{-1}$).

2.2. Slot-die coating

The bottom electron contact was prepared directly on the PET/ITO substrate, prepared and cleaned as described earlier [12]. The zinc oxide precursor solution was microfiltered immediately prior

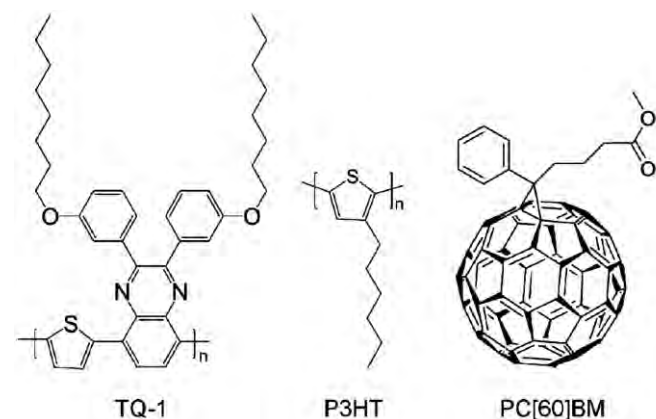


Fig. 1. Structure of poly-[thiophene-2,5-diyl-*alt*-(2,3-bis(3-octyloxyphenyl)quinoxaline-5,8-diyl)] (TQ-1), poly-3-hexylthiophene (P3HT), and phenyl- C_{61} -butyric acid methyl ester (PC[60]BM).

to use (filter pore size of $0.45 \mu\text{m}$) and then slot-die coated at a speed of 2 m min^{-1} with a wet thickness of $4.9 \mu\text{m}$. After the initial drying of the precursor film it was converted into an insoluble film by passage through an oven at a temperature of $140 \text{ }^\circ\text{C}$ with a speed of 0.2 m min^{-1} (oven length = 4 m). This gave an insoluble doped zinc oxide film with a thickness of $25 \pm 5 \text{ nm}$. The P3HT:PC[60]BM ink described above was microfiltered and slot die-coated with at a web speed of 1.6 m min^{-1} and a wet thickness of $11.2 \mu\text{m}$. The film was dried by passage through an oven (2 m) at $140 \text{ }^\circ\text{C}$. The recombination layer comprised a $\text{V}_2\text{O}_5/\text{ZnO}$ stack that was slot-die coated in two steps. The V_2O_5 layer was slot-die coated directly on top of the dried P3HT:PC[60]BM layer, with a web speed of 2 m min^{-1} and a wet thickness of $8 \mu\text{m}$. The film was dried by passage through an oven (2 m) at $140 \text{ }^\circ\text{C}$. The second zinc oxide layer was prepared exactly as the first (anode) layer, directly on the V_2O_5 layer. The back cell was prepared by slot-die coating an aqueous TQ-1:PC[60]BM nanoparticle dispersion (Fig. 2) at a web speed of 0.2 m min^{-1} and a wet thickness of $30 \mu\text{m}$. The wet film was dried at $140 \text{ }^\circ\text{C}$ (oven length = 2 m) as described earlier [8]. The back electrode was prepared by applying PEDOT:PSS by slot-die coating at a speed of 0.2 m min^{-1} with drying at $140 \text{ }^\circ\text{C}$ (oven length = 2 m). It was found unnecessary to wet the film surface prior to coating the PEDOT:PSS and this might be due to the beneficial interaction between the fluorosurfactants in the aqueous nanoparticle dispersion and in the PEDOT:PSS. Finally, the device was completed by R2R screen printing a silver grid electrode and drying at $140 \text{ }^\circ\text{C}$. The devices were encapsulated using R2R lamination of a simple food packaging barrier with a pressure sensitive adhesive onto both sides of the foil [12b].

2.3. TOF-SIMS depth profiling analysis

Time-of-flight secondary ion mass spectrometry (TOF-SIMS) was employed to perform a depth profiling analysis. The experiments were conducted using a TOF-SIMS IV (ION-TOF GmbH, Münster, Germany). 25-ns pulses of 25-keV Bi^+ (primary ions) were bunched to form ion packets with a nominal temporal extent of $< 0.9 \text{ ns}$ at a repetition rate of 10 kHz yielding a target current of 1 pA . These primary ion conditions were used to obtain depth profiles in both negative and positive ion mode. Depth profiling was performed using an analysis area of $100 \times 100 \mu\text{m}^2$

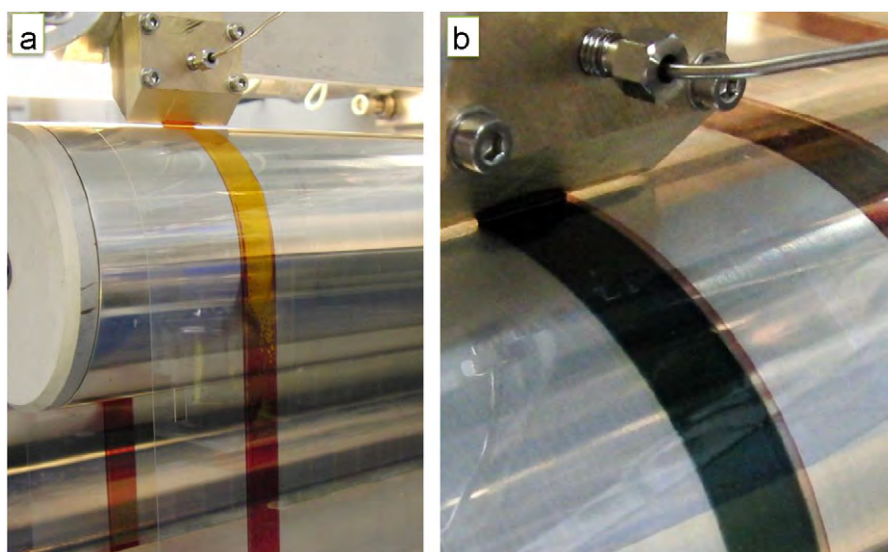


Fig. 2. Photographs of the actual R2R coating experiment in progress. (a) Coating of the front BHJ material (the drying process of the film is visible). (b) Coating of the back BHJ material.

and a sputter area of $300 \times 300 \mu\text{m}^2$. 30 nA of 3-keV Xe^+ were used as sputter ions. Electron bombardment (20 eV) was used to minimize charge build-up at the surface. Desorbed secondary ions were accelerated to 2 keV, mass analyzed in the flight tube, and post-accelerated to 10 keV before detection.

2.4. *J–V* characterization

The final devices were put under simulated sunlight at 1000 W m^{-2} , $85 \pm 5 \text{ }^\circ\text{C}$, $40 \pm 10\%$ relative humidity (rh) (AM1.5G). *J–V* curves were recorded by sweeping from -1 V to $+1 \text{ V}$ in steps of 20 mV and a rate of 0.1 V s^{-1} to ensure that no dynamic effects resulted in over/under estimation of J_{sc} and V_{oc} . The time evolution of the photovoltaic performance was recorded by continuously illuminating the device under the above conditions while recording complete IV data every one minute according to ISOS-L-1 [13].

3. Results and discussion

3.1. The tandem cell

This study describes the transfer of a laboratory scale tandem solar cell process on rigid glass substrates to a R2R process on flexible plastic substrates. The laboratory process was described previously [11] and was developed with an aim of being compatible with R2R processing. The tandem solar cell structure comprised a multilayer stack with the composition PET/ITO/ZnO/front-BHJ/ V_2O_5 /ZnO/back-BHJ/PEDOT:PSS/Ag, where PET is poly(ethylene terephthalate) (substrate), ITO is indium tin oxide (transparent front electrode), ZnO is the electron transport layer, front-BHJ is the front bulk heterojunction consisting of P3HT:PC[60]BM (active layer 1), V_2O_5 /ZnO is the recombination layer, back-BHJ consists of TQ-1:PC[60]BM (active layer 2), PEDOT:PSS is the hole transport layer, and Ag is the back electrode. Illustrative photographs of the coating process are shown in Fig. 2.

The first attempts resulted in very poorly performing devices typically showing open-circuit voltages around what is expected for single junction devices. Optical inspection of the completed devices revealed the possible origin of this malfunction to be cracks in the V_2O_5 part of the recombination layer (Fig. 3). It was found that these cracks form at some point during the processing of the V_2O_5 layer, possibly due to the heat treatment and/or bending of the substrate as it passes through the R2R equipment. As is also hinted in Fig. 3 these cracks persist after processing of the ZnO layer thus rendering the recombination layer penetrable to the solute of the back BHJ

as this is coated. This would most likely solubilize the front BHJ and thus seriously compromise the integrity of the serial connection of the two sub cells. This situation is schematically described in Fig. 4a. Such a short-circuiting of the recombination layer would make the two active layers effectively function as one poorly performing active layer, in turn, explaining the single junction-like low open-circuit voltage observed for these devices.

However, it was possible to work around this issue by utilizing an aqueous ink for the processing of the back BHJ using a method recently described by Andersen et al. [8]. This presented a unique opportunity for orthogonal processing since water cannot solubilize the front BHJ. From the photomicrographs shown in Fig. 4 it is evident that the back cell looks less affected by the cracks in the recombination layer when water based processing is employed (Fig. 4b compared to Fig. 4a).

3.2. TOF-SIMS depth profiling analysis

TOF-SIMS depth profiling analysis was employed in both negative and positive ion mode in order to document the layer stack order. The encapsulation film is too thick for a depth profiling analysis, so it was necessary to delaminate the tandem solar cell. TOF-SIMS mass spectra of the exposed surfaces revealed that delamination took place at the PEDOT:PSS/back BHJ interface.

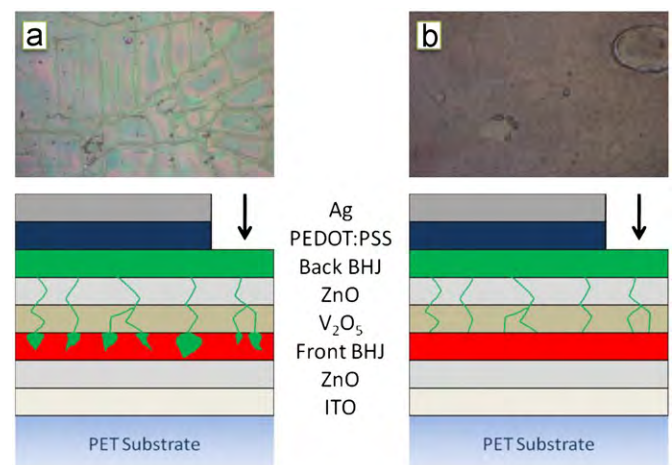


Fig. 4. Schematics of the tandem solar cell under study and photomicrographs ($230 \times 150 \mu\text{m}^2$) obtained at the indicated positions (black arrows), which illustrates the proposed consequence of the observed cracks in the recombination layer when using (a) a non-orthogonal solvent (chloroform) and (b) an orthogonal solvent (water), for the processing of the back BHJ.

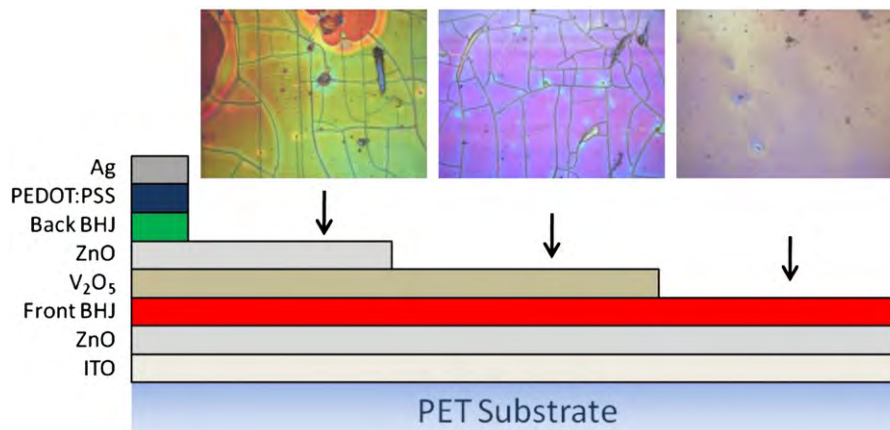


Fig. 3. Schematic of the tandem solar cell under study and photomicrographs ($260 \times 195 \mu\text{m}^2$) revealing cracks in the V_2O_5 layer, which persist through the ZnO layer.

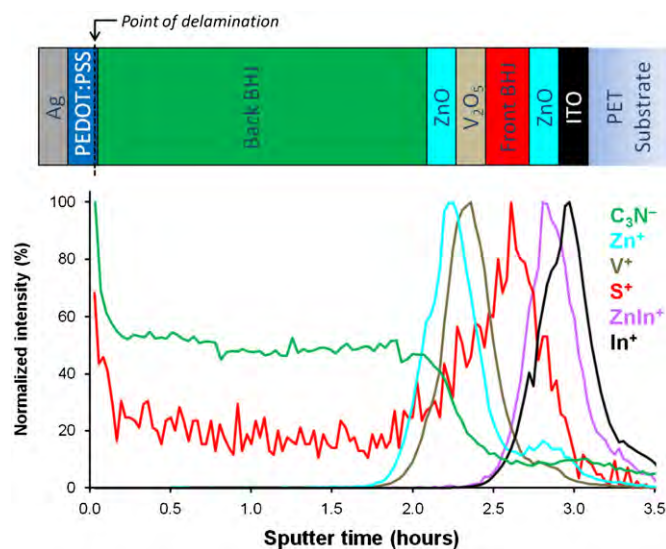


Fig. 5. TOF-SIMS depth profiles through the delaminated tandem solar cell. C_3N^- is a marker for the back BHJ obtained from a depth profile run in negative mode, Zn^+ is a marker for the ZnO , V^+ is a marker V_2O_5 , S^+ is a marker for both front and back BHJ, and $ZnIn^+$ (formed during the ionization step of the analysis) is a marker for the front ZnO and In^+ is a marker for ITO.

Fig. 5 shows the results of the depth profile analysis. Various factors complicated the analysis, such as interface roughness, which is well known phenomenon in R2R processing (e.g. compared to spin coating). Furthermore, depth profiling in soft materials is associated with an inferior depth resolution (under the given sputter conditions), compared to hard materials (e.g. metals). These conditions constitute a challenge especially when it comes to performing depth profiling on very thin layers such as the ZnO (~25 nm) and V_2O_5 (~15 nm) layers present in this device. However, as is evident from **Fig. 5** it was quite possible, in spite of the conditions, to document the multilayer stack composition in the tandem solar cell device. Residual PEDOT:PSS was present in the PEDOT:PSS/back BHJ interface after the delamination process presumably due to a small degree of interlayer mixing that resulted in presumably a matrix effect, which is observed as initially elevated signals from the back BHJ material (i.e. at the beginning of the sputter time window). During the ionization process the Zn^+ signal is discriminated due to the formation of the $ZnIn^+$ cluster ion caused by the close vicinity of the ITO (i.e. an ionization phenomenon). Finally, a significantly long sputter time window is observed for the back BHJ compared to the front BHJ, which suggests that the back BHJ is significantly thicker (assuming similar sputter rates) than the front BHJ consistent with an expected layer thickness of ~600 nm [8] for the back BHJ as compared to the thickness of the front BHJ ~200 nm.

3.3. Electrical characterization

J - V characteristics for the best performing tandem device are shown in **Fig. 6**, (blue triangles) together with representative J - V curves for both tandem and back cell reference devices with and without photo-annealing (800 min). The key photovoltaic parameters are summarized in **Table 1**, while the dynamic evolutions of the short circuit current (I_{sc}) and open-circuit voltage (V_{oc}) are shown in **Fig. 7**. By summing the V_{oc} values from the sub cell reference devices (**Table 1**) it is possible to estimate that the perfect tandem device would have an open-circuit voltage close to 1 V. As is clear from the presented data in **Table 1**, the actual tandem devices gave, at best, a V_{oc} around 0.9 V while V_{oc} values

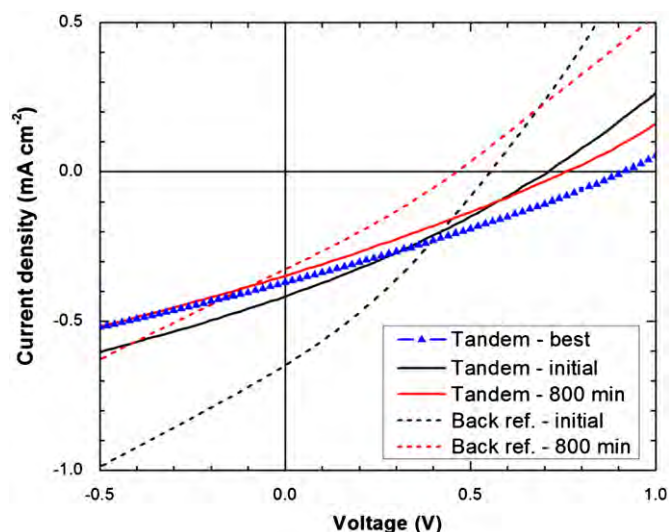


Fig. 6. J - V characteristics ($AM1.5G$ 1000 W m^{-2}) for the best performing tandem cells. Also shown is a more average cell, before (initial) and after (800 min) photo-annealing.

Table 1

Summary of the J - V characterization.

Cell	PCE (%)	J_{sc} (mA cm^{-2})	V_{oc} (V)	FF (%)
Tandem ^(a)				
(Initial)	0.09	-0.42	0.71	28.8
(800 min)	0.07	-0.35	0.76	27.5
(Best)	0.10	-0.37	0.91	28.2
Back cell ^(a)				
(Initial)	0.11	-0.65	0.55	30.2
(800 min)	0.04	-0.33	0.46	27.7
Front cell (Ref. [11])	1.32	-7.17	0.50	36.9

^a Cell active area of 4 cm^2 .

around 0.75 V were readily measured, hence between 0.1 and 0.25 V less than the expected ideal value.

Various loss mechanisms can influence the tandem voltage, of which most are related to the nature of the sub cell interconnection, i.e. the recombination layer. In this case it is highly probable that the before mentioned observed defects (**Fig. 3**) are likely to have a negative influence on V_{oc} if the mechanism schematically shown in **Fig. 4b** is considered, i.e. shunts across the recombination layer would lower the tandem V_{oc} . Furthermore, the results show that the front and back reference cells both exhibit a decreasing V_{oc} during the dynamic evolution J - V experiment as observed in **Fig. 7** and S7 (see e-component). For the tandem devices the trend is opposite, i.e. increasing V_{oc} over time. Both reference cells display saturation at around 0.45 V, which fits well with the peak value of the best tandem cell.

It appears that the sub cell interconnection improves over time, possibly due to burning of shunts across the recombination layer, originally formed as a consequence of the defects. With respect to the I_{sc} it is noticeable that the tandem device and the back cell reference device have rather similar I_{sc} values. This should be compared to the front cell I_{sc} , which is a factor of 10 to 20 times larger. Thus the tandem device is severely current limited by the poor performing back cell.

This significant current mismatch is likely to influence the current-voltage characteristics of the tandem cell. Hadipour et al. [14] found that the excess current will cause the surplus of free holes to pile up at the middle electrode (recombination layer), which will result in a lowering of the effective internal field in the

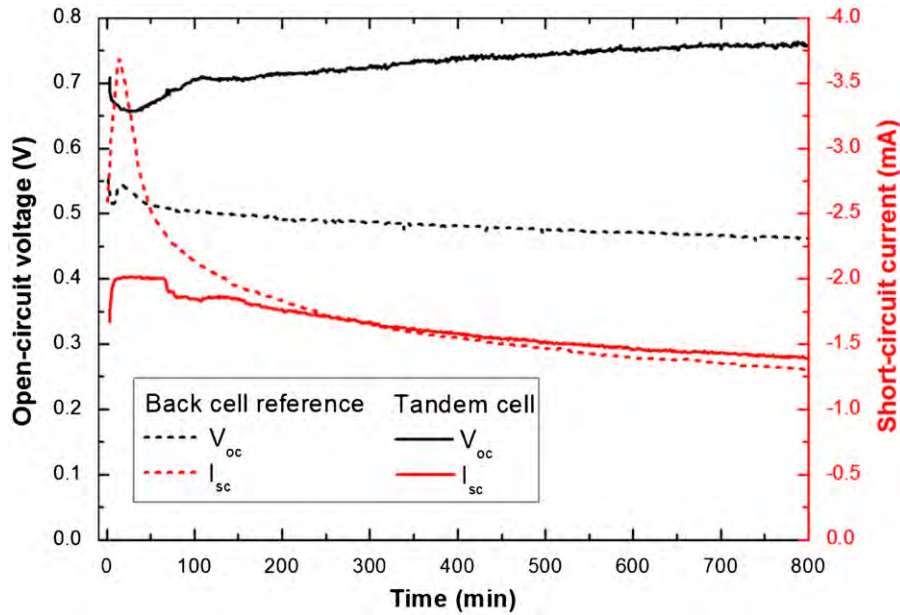


Fig. 7. Time evolution of the open-circuit voltage and short-circuit current during the 800 min of photo-annealing ($AM1.5G\ 1000\ W\ m^{-2}$) of the tandem cell, and a corresponding single junction reference cell mimicking the current-limiting back cell.

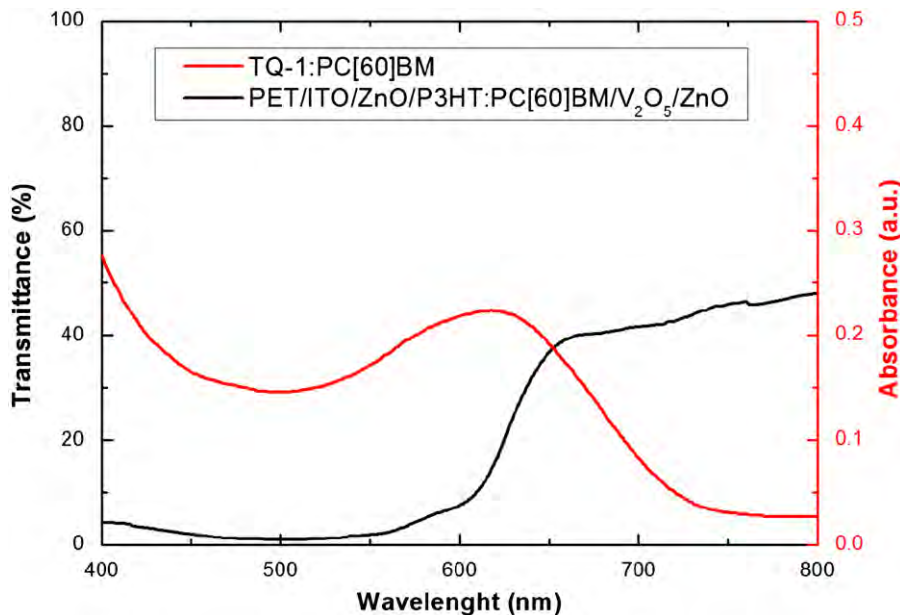


Fig. 8. Transmittance of the front cell and the recombination layer relative to the absorbance of the back cell active layer.

front sub cell, while for the back sub cell the opposite will be the case and the internal field will increase.

Hence the sub cell currents will equilibrate at some intermediate value, resulting in a higher I_{sc} value for the tandem device compared to the expected current of the limiting sub cell reference device. How the tandem current equilibrates is very much dependent on the slope of the $J-V$ curves of the sub cells around short-circuit as well as the degree of current mismatch, as recently pointed out by Braun et al. [15] for the case of an inorganic tandem cell. This can be easily understood, e.g. in the case of the current limiting sub cell; as the reverse biasing caused by the current mismatch will only result in a significant increase in current if the $J-V$ curve of the sub cell has a non zero slope in reverse bias, which is the case for the cells under study here. Furthermore, according to Fig. 8 the tandem back cell will suffer

from an obvious poor spectral matching with the front cell transmission spectrum, and thus receive a significantly lower photon flux than the reference cell. From this, a significant lowering of the back cell current would be expected. However, as the $J-V$ data shows that the I_{sc} of the tandem is not lower but rather comparable to that of the current limiting back cell reference device this would in fact imply a combination of the spectral mismatch and the increased quantum efficiency of the tandem back cell due to current mismatch (the effect described in Refs. [14 and 15]). To support this, we construct the ideal tandem curve from the two reference sub cells by summing voltages at equal currents, as described in Ref. [14]. We take into account the spectral mismatch by a mismatch factor S , which is simply multiplied with the current of the back cell reference. These can be seen in Fig. 9, for the case of $S=1$ and $S=0.5$, together with the

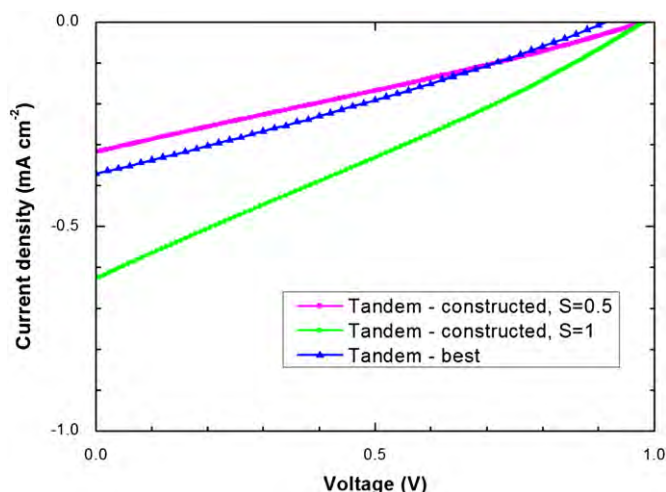


Fig. 9. Constructed tandem J - V characteristics with spectral mismatching ($S=0.5$) and without ($S=1$), compared with the best measured tandem device.

best tandem curve. As can be seen, it is likely that severe spectral mismatching is the cause of the low short-circuit current of the tandem cell, while the discrepancy between the model and the measurement can be explained by the somewhat crude model, such as negligence of V_{oc} dependence on light intensity [16], and the assumption of a perfect ohmic connection between the sub cells, e.g. a perfect recombination layer.

3.4. Future developments

The tandem approach within polymer photovoltaics has so far been utilized in an attempt to maximize efficiency, i.e. without constraints on materials and fabrication methods. The present work, however, demonstrates the fragility of the tandem device approach from a solution processing point of view, and in doing so, stresses the importance of having certain constraints in mind when assessing a given set of materials and processing methods. In this regard especially the recombination layer presents an all-determining weak-point of the tandem cell; a perfect recombination layer would be insoluble and solvent impenetrable, being either a pn-junction preferably a highly doped tunnel junction or alternatively having metal like characteristics. This has so far been achieved only for small area devices using rigid substrates [6,11,17–21]. Lee et al. [22] successfully demonstrated a small area tandem device on a flexible substrate but using vacuum deposition. However, as for upscaling of the fabrication, it is the view of the authors that a stable and highly reliable solution process for polymer tandem solar cells can only be ensured by a completely orthogonalized process in which none of the processing steps can seriously harm any of the previously processed layers. This has to do with the inherently rough nature of a high throughput R2R process, during which cracks and small coating imperfections would act as solvent paths leading to partial dissolution of underlying layers. The aqueous emulsion approach utilized in this work is one possible solution presenting both a stable and possibly environmentally friendly fabrication process. At the same time it allows for the use of the large amount of existing polymers. However, the success of this technique of course depends on whether significantly better device performance can be achieved. Another foreseeable solution would be a process where the layers by some in-line post process are rendered insoluble, for instance using thermal- or light-induced thermocleavage of the solubilizing groups as demonstrated earlier [5,23,24]. This would be very desirable as it ensures free choice of solvent for the subsequent layers, and also removes constraints

on the recombination layer in terms of materials and layer thicknesses, thus opening for a wider range of tweakable parameters.

4. Conclusions

We have successfully demonstrated large area flexible polymer tandem solar cells with all layers processed entirely from solution, and partially from water. The multilayer stack on flexible PET substrate comprised a cathode of ITO/ZnO, a recombination layer of V_2O_5 /ZnO, and a PEDOT:PSS/Ag (printed) anode. The two serially connected BHJs was comprised of a P3HT:PC[60]BM front cell processed from chlorobenzene and a back cell processed from an aqueous dispersion of poly[2,3-bis-(3-octyl oxyphenyl)-quinoxaline-5,8-diyl-alt-thiophene-2,5-diyl]:PC[60]BM nanoparticles. The composition and integrity of the multilayer stack was confirmed by TOF-SIMS depth profiling. The V_{oc} of the best tandem device was 0.9 V, while both the corresponding single junction reference devices had a V_{oc} around 0.5 V. This confirms a serial connection of the sub cells while the observed voltage losses are ascribed to visible defects in the recombination layer and a non-ohmic connection of the two sub cells.

Acknowledgment

This work was supported by the Danish National Research Foundation. We gratefully acknowledge Lasse Gorm Jensen for creating graphical illustrations and Jon E. Carlé and Martin Helgesen for preparing polymer materials.

Appendix A. Supplementary materials

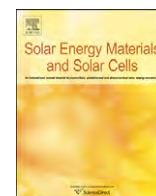
Supplementary data associated with this article can be found in the online version at doi:10.1016/j.solmat.2011.08.025.

Details of GIWAXS measurements and time evolution for the back reference cell.

References

- [1] T. Ameri, G. Dennler, C. Lungenschmied, C.J. Brabec, Organic tandem solar cells: a review, *Energy & Environmental Science* 2 (2009) 347–363.
- [2] G. Dennler, M.C. Scharber, T. Ameri, P. Denk, K. Forberich, C. Waldauf, C.J. Brabec, Design rules for donors in bulk-heterojunction tandem solar cells. Towards 15% energy-conversion efficiency, *Advanced Materials* 20 (2008) 579–583.
- [3] J.D. Kotlarski, P.W.M. Blom, Ultimate performance of polymer: fullerene bulk heterojunction tandem solar cells, *Applied Physics Letters* 98 (2011) 053301.
- [4] Y.M. Nam, J. Huh, W.H. Jo, A computational study on optimal design for organic tandem solar cells, *Solar Energy Materials and Solar Cells* 95 (2011) 1095–1101.
- [5] O. Hagemann, M. Bjerring, N.C. Nielsen, F.C. Krebs, All solution processed tandem polymer solar cells based on thermocleavable materials, *Solar Energy Materials and Solar Cells* 92 (2008) 1327–1335.
- [6] J. Gilot, M.M. Wienk, R.A.J. Janssen, Double and triple junction polymer solar cells processed from solution, *Applied Physics Letters* 90 (2007) 143512.
- [7] E. Wang, L. Hou, Z. Wang, S. Hellström, F. Zhang, O. Inganäs, M.R. Andersson, An easily synthesized blue polymer for high-performance polymer solar cells, *Advanced Materials* 22 (2010) 5240–5244.
- [8] T.R. Andersen, T.T. Larsen-Olsen, B. Andreasen, A.P.L. Böttiger, J.E. Carlé, M. Helgesen, E. Bundgaard, K. Norrman, J.W. Andreasen, M. Jørgensen, F.C. Krebs, Aqueous processing of low-band-gap polymer solar cells using roll-to-roll methods, *ACS Nano* 5 (2011) 4188–4196.
- [9] R. Søndergaard, M. Helgesen, M. Jørgensen, F.C. Krebs, Fabrication of polymer solar cells using aqueous processing for all layers including the metal back electrode, *Advanced Energy Materials* 1 (2011) 68–71.
- [10] N. Espinosa, H.F. Dam, D.M. Tanenbaum, J.W. Andreasen, M. Jørgensen, F.C. Krebs, Roll-to-roll processing of inverted polymer solar cells using hydrated vanadium(V)oxide as a PEDOT:PSS replacement, *Materials* 4 (2011) 169–182.

- [11] T.T. Larsen-Olsen, E. Bundgaard, K.O. Sylvester-Hvid, F.C. Krebs, A solution process for inverted tandem solar cells, *Organic Electronics* 12 (2011) 364–371.
- [12] a) F.C. Krebs, T. Tromholt, M. Jørgensen, Upscaling of polymer solar cell fabrication using full roll-to-roll processing, *Nanoscale* 2 (2010) 873–886; b) J. Alstrup, M. Jørgensen, A.J. Medford, F.C. Krebs, Ultra fast and parsimonious materials screening for polymer solar cells using differentially pumped slot-die coating, *ACS Applied Materials & Interfaces* 2 (2010) 2819–2827.
- [13] M.O. Reese, S.A. Gevorgyan, M. Jørgensen, E. Bundgaard, S.R. Kurtz, D.S. Ginley, D.C. Olson, M.T. Lloyd, P. Morvillo, E.A. Katz, A. Elschner, O. Haillant, T.R. Currier, V. Shrotriya, M. Hermenau, M. Riede, K.R. Kirov, G. Trimmel, T. Rath, O. Inganäs, F. Zhang, M. Andersson, K. Tvingstedt, M. Lira-Cantu, D. Laird, C. McGuinness, S. Gowrisanker, M. Pannone, M. Xiao, J. Hauch, R. Steim, D.M. DeLongchamp, R. Rösch, H. Hoppe, N. Espinosa, A. Urbina, G. Yaman-Uzunoglu, J.-B. Bonekamp, A.J.J.M. van Breemen, C. Girotto, E. Voroshazi, F.C. Krebs, Consensus stability testing protocols for organic photovoltaic materials and devices, *Solar Energy Materials and Solar Cells* 95 (2011) 1253–1267.
- [14] A. Hadipour, B. de Boer, P.W.M. Blom, Device operation of organic tandem solar cells, *Organic Electronics* 9 (2008) 617–624.
- [15] A. Braun, N. Szabo, K. Schwarzburg, T. Hannappel, E. Katz, J.M. Gordon, Current-limiting behavior in multijunction solar cells, *Applied Physics Letters* 98 (2011) 223506.
- [16] T. Tromholt, E. Katz, B. Hirsch, A. Vossier, F.C. Krebs, Effects of concentrated sunlight on organic photovoltaics, *Applied Physics Letters* 96 (2010) 073501.
- [17] A. Hadipour, B. de Boer, J. Wildeman, F.B. Kooistra, J.C. Hummelen, M.G.R. Turbiez, M.M. Wienk, R.A.J. Janssen, P.W.M. Blom, Solution-processed organic tandem solar cells, *Advanced Functional Materials* 16 (2006) 1897–1903.
- [18] J.Y. Kim, K. Lee, N.E. Coates, D. Moses, T.-Q. Nguyen, M. Dante, A.J. Heeger, Efficient tandem polymer solar cells fabricated by all-solution processing, *Science* 317 (2007) 222–225.
- [19] S. Sista, M.-H. Park, Z. Hong, Y. Wu, J. Hou, W.L. Kwan, G. Li, Y. Yang, Highly efficient tandem polymer photovoltaic cells, *Advanced materials* 22 (2010) 380–383.
- [20] D.J.D. Moet, P. de Bruyn, P.W.M. Blom, High work function transparent middle electrode for organic tandem solar cells, *Applied Physics Letters* 96 (2010) 153504.
- [21] C.-H. Chou, W.L. Kwan, Z. Hong, L.-M. Chen, Y. Yang, A. Metal-Oxide, Interconnection layer for polymer tandem solar cells with an inverted architecture, *Advanced Materials* 23 (2011) 1282–1286.
- [22] B.J. Lee, H.J. Kim, W. -ik Jeong, J.-J. Kim, A transparent conducting oxide as an efficient middle electrode for flexible organic tandem solar cells, *Solar Energy Materials and Solar Cells* 94 (2010) 542–546.
- [23] T. Tromholt, S.A. Gevorgyan, M. Jørgensen, F.C. Krebs, K.O. Sylvester-Hvid, Thermocleavable materials for polymer solar cells with high open circuit voltages – a comparative study, *ACS applied materials & interfaces* 1 (2009) 2768–2777.
- [24] F.C. Krebs, K. Norrman, Using light induced thermocleavage in a roll-to-roll process for polymer solar cells, *ACS applied materials & interfaces* 2 (2010) 877–887.



Simultaneous multilayer formation of the polymer solar cell stack using roll-to-roll double slot-die coating from water

Thue T. Larsen-Olsen, Birgitta Andreasen, Thomas R. Andersen, Arvid P.L. Böttiger, Eva Bundgaard, Kion Norrman, Jens W. Andreasen, Mikkel Jørgensen, Frederik C. Krebs*

Risø National Laboratory for Sustainable Energy, Technical University of Denmark, Frederiksborgvej 399, DK-4000 Roskilde, Denmark

ARTICLE INFO

Available online 23 September 2011

Keywords:

Double slot-die coating
Organic solar cells
Roll-to-roll coating polymer solar cells
Simultaneous multilayer formation
Slot-die coating

ABSTRACT

Double slot-die coating using aqueous inks was employed for the simultaneous coating of the active layer and the hole transport layer (HTL) in fully roll-to-roll (R2R) processed polymer solar cells. The double layer film was coated directly onto an electron transport layer (ETL) comprising doped zinc oxide that was processed by single slot-die coating from water. The active layer comprised poly-3-hexylthiophene:Phenyl-C₆₁-butyric acid methyl ester (P3HT:PCBM) as a dispersion of nanoparticles with a radius of 46 nm in water characterized using small-angle X-ray scattering (SAXS), transmission electron microscopy (TEM), and atomic force microscopy (AFM). The HTL was a dispersion of poly(3,4-ethylenedioxythiophene) poly(styrenesulfonate) (PEDOT:PSS) in water. The films were analyzed using time-of-flight secondary ion mass spectrometry (TOF-SIMS) as chemical probe and X-ray reflectometry as physical probe, confirming the identity of the layered structure. The devices were completed with a back electrode of either Cu tape or evaporated Ag. Under standard solar spectrum irradiation (AM1.5G), current–voltage characterization (*J*–*V*) yielded an open-circuit voltage (V_{oc}), short-circuit current (J_{sc}), fill factor (*FF*), and power conversion efficiency (*PCE*) of 0.24 V, 0.5 mA cm^{−2}, 25%, and 0.03%, respectively, for the best double slot-die coated cell. A single slot-die coated cell using the same aqueous inks and device architecture yielded a V_{oc} , J_{sc} , *FF*, and *PCE* of 0.45 V, 1.95 mA cm^{−2}, 33.1%, and 0.29%, respectively.

© 2011 Elsevier B.V. All rights reserved.

1. Introduction

Flexible polymer solar cells can be manufactured by roll-to-roll (R2R) processes, which are inherently faster than batch processing of solar cells [1]. The manufacture of polymer solar cells using R2R processing has been reported demonstrating high speed of manufacture even on a small scale [2–4]. Thus, polymer solar cell modules with the size of an A4 sheet of paper have total processing times in the range of one minute (45–90 s) [3]. This period of time is from the moment the fresh carrier substrate enters the process until the completed, encapsulated, and tested polymer solar cell module exits the process as a finished product. It is impossible to envisage such throughput speeds with any process that handles the solar cell as a discrete unit. The above example employed relatively simple R2R processing equipment and low web speeds in the range of 0.3–2 m min^{−1} processing one layer at a time by subsequent single passes through the machinery. In order to improve throughput speed there are a few

routes, which can be followed. One obvious route is to increase the processing speed, which puts significant requirements on the drying equipment. The faster the web speed, the larger and more complex the ovens and driers become. Another option is to make an inline printing and coating machine where the same web passes through several printing stations with each station representing each layer in the solar cell stack. This method has the advantage of minimizing handling damage of the web. The method does put some constraints on the chosen printing and coating methods as they all have to operate in the same window of web speed and the final web speed will be determined by the slowest process. A final route is the simultaneous formation of several layers of the solar cells stack. This method is in many ways ideal as it lowers the number of passages through the processing equipment thus lowering the handling damage, increases the processing speed significantly without increasing the web speed and thus does not necessarily require more complex drying technology. In addition, there are advantages in the context of life cycle analysis and the method provides a path to a reduction of the energy payback time (EPBT) by significantly reducing the direct process energy involved in the manufacture [5]. The approach also introduces a massive challenge in

* Corresponding author. Tel.: +45 46 77 47 99.

E-mail address: frkr@risoe.dtu.dk (F.C. Krebs).

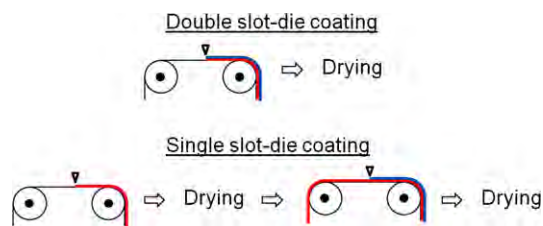


Fig. 1. Illustration of the double slot-die coating of the active layer (red) and the HTL (blue) in a R2R process, compared to the equivalent process using single slot-die coating. (For interpretation of the references to color in this figure legend, the reader is referred to the web version of this article).

the ink formulation for the layers that are coated simultaneously as the formation and drying of a wet multilayer film is highly complex. The successful application of the technique is however rewarding in terms of processing speed and simplicity, see Fig. 1.

In this work we demonstrate the simultaneous formation of two of the layers in the polymer solar cell stack by double slot-die coating of the active layer and the hole transporting layer (HTL) from aqueous dispersions. We describe the ink formulation and the required steps to efficiently design inks that give stable bilayer structures in the wet film and during drying.

2. Experimental

2.1. Materials

P3HT (Sepiolid P-200 from BASF) was employed as the donor polymer and technical grade PCBM was employed as the acceptor material (Solenne BV). An aqueous precursor solution for the ZnO was prepared as described earlier [6] and comprised $\text{Zn}(\text{OAc})_2 \cdot 2\text{H}_2\text{O}$ (100 mg mL^{-1}), $\text{Al}(\text{OH})(\text{OAc})_2$ (2 mg mL^{-1}), and the non-ionic fluorosurfactant (FSO-100) (2 mg mL^{-1}) in water. PEDOT:PSS was based on an aqueous dispersion (2:1 w/w) of Orgacon EL-P 5010 from Agfa that was used directly as received. The electrode material was either Cu tape or evaporated silver. The substrate was a $130 \mu\text{m}$ poly(ethylene terephthalate) (PET) substrate with a patterned ITO layer (nominally $60 \Omega \text{ square}^{-1}$) (acquired from IST).

2.2. Nanoparticle preparation and ink

P3HT (4 g, Sepiolid P200, BASF) and PCBM (4 g, 99%, Solenne B.V.) were dissolved in chloroform (268 g, Spectrophotometric grade, Sigma-Aldrich) and mixed with an aqueous 100 mM sodium dodecyl sulfate (SDS) solution (480 mL) (99%, Sigma-Aldrich) in a large beaker. The mixture was stirred vigorously for one hour and then subjected to ultrasound (0.9 kW) for 6.5 min using an UIP 1000 hd transducer from Hielscher ultrasound technology fitted with a booster head. The mixture was then stirred on a hot plate at 65°C for three hours until all the chloroform had evaporated. The aqueous dispersion was dialyzed to remove SDS using a Millipore system with a capacity of 500 mL. The mixture was concentrated by dialysis from a volume of 500 mL to a volume of 100 mL with a forward pressure of 1.4 bar and a pressure gradient across the filter of 0.7 bar. Pure water (400 mL) was then added and the procedure was repeated 4 times corresponding to a dilution of the solution by a factor of 625. In the final step the suspension were concentrated to have a solid content of 60 mg mL^{-1} . FSO-100 was added to the dialyzed aqueous suspension of the P3HT:PCBM nanoparticles. The concentration of fluorosurfactant was 5 mg mL^{-1} and the P3HT:PCBM concentration was 60 mg mL^{-1} . This solution was employed directly for slot-die coating.

2.3. TOF-SIMS

Depth profiling analysis was performed using a TOF-SIMS IV (ION-TOF GmbH, Münster, Germany). 25-ns pulses of 25-keV Bi^+ (primary ions) were bunched to form ion packets with a nominal temporal extent of $< 0.9 \text{ ns}$ at a repetition rate of 10 kHz yielding a target current of 1 pA. Depth profiling was performed using an analysis area of $100 \times 100 \mu\text{m}^2$ and a sputter area of $300 \times 300 \mu\text{m}^2$. 30 nA of 3-keV Xe^+ was used as sputter ions. Electron bombardment (20 eV) was used to minimize charge build-up at the surface. Desorbed secondary ions were accelerated to 2 keV, mass analyzed in the flight tube, and post-accelerated to 10 keV before detection.

2.4. SAXS

The X-ray source for the SAXS measurements was a Cu rotating anode (Rigaku H3R), collimated and monochromatized by 2D multilayer optics (K_α radiation, $\lambda = 1.5418 \text{ \AA}$). The anode was operated in fine focus mode at 46 kV/46 mA and the beam diameter was collimated by 3 pinholes to 1.0 mm diameter at the sample position. An $18 \times 18 \text{ cm}^2$ 2D position sensitive gas detector was used for collecting the scattering data, and a 4 mm beamstop was placed in front of the gas detector, situated 4579 mm from the sample.

2.5. Reflectometry

The reflectometry measurement was made on setup with a rotating Cu-anode (Rigaku RU-200) operated at 50 kV/200 mA as X-ray source, focused and monochromatized by a 1D multilayer optic (K_α radiation, $\lambda = 1.5418 \text{ \AA}$).

2.6. AFM

The P3HT:PCBM nanoparticle dispersion was spin-coated on a glass substrate. The AFM imaging was performed on an N8 Neos (Bruker Nano GmbH, Herzogenrath, Germany) operating in an intermittent contact mode using PPP-NCLR cantilevers (NANO-SENSORS, Neuchatel, Switzerland). The images were recorded at a scan speed of 0.8 lines s^{-1} .

2.7. Substrate preparation

A PET substrate with an ITO pattern was prepared and cleaned as described earlier [2]. The ZnO solution was microfiltered immediately prior to use (filter pore size of $0.45 \mu\text{m}$) and then slot-die coated at a speed of 2 m min^{-1} with a wet thickness of $4.9 \mu\text{m}$. After the initial drying of the precursor film it was converted into an insoluble film by passage through an oven at a temperature of 140°C with a speed of 0.2 m min^{-1} (oven length = 4 m). This gave an insoluble doped zinc oxide film with a thickness of $25 \pm 5 \text{ nm}$.

2.8. Double slot-die coating

The web was forwarded at a speed of 1 m min^{-1} when the aqueous P3HT:PCBM nanoparticle dispersion was pumped into the first chamber of a double slot-die coating head. The aqueous PEDOT:PSS dispersion was pumped into the second chamber of the double slot-die coating head. The double film was then slot-die coated at a nominal wet thickness of $23 \mu\text{m}$ for both the P3HT:PCBM film and the PEDOT:PSS dispersion. The slot-die coating head and the coating roller had temperatures of 60°C and 80°C , respectively. The temperature of the foil was kept at

80 °C until it reached the oven at 140 °C. The distance from the point of coating to the oven entry was 18 cm.

2.9. Device characterization

The devices were placed under simulated sunlight in a solar simulator with the following specifications: 1000 W m⁻², AM1.5G, 85 ± 2 °C, and 45 ± 5% relative humidity. The *J*-*V* curves were measured here were carried out at 85 °C by scanning both forwards and backwards in steps of 20 mV ensuring that no hysteresis was present. The scanning speed was 0.1 V s⁻¹.

3. Results and discussion

The simultaneous multilayer formation by roll coating methods has been achieved with only a few techniques such as curtain coating, slide coating, and slot-die coating [1]. The two former are only operational in the very high speed regime (typically > 4 m s⁻¹) and require relatively viscous solutions. In return, they offer the simultaneous formation of many layers. Slot-die coating has been explored for multilayer film formation with up to three layers (in triple slot-die coating) or in combination with the slide coating technique in slot-slide coating. In the context of polymer solar cells the simultaneous multilayer formation has not been reported so far.

There are many good reasons for double slot-die coating not having been employed for polymer solar cells. Firstly, the multilayer formation requires that the same solvent is used for the coated layers and that the layer coated first has the highest surface tension. Secondly, the drying has to be sufficiently fast to minimize diffusion of solutes between the layers. For a bilayer film with a total wet thickness of 100 μm, diffusion of solutes such as small molecules and ions are exceptionally fast unless the viscosity is high. In our case we employ water and the viscosity of the solutions are low (< 25 mPa s) implying that it would be difficult to prevent interlayer diffusion. The mean displacement for a molecule such as phenyl-C₆₁-butyric acid methyl ester (PCBM) is on the order of 30 μm s⁻¹ and with wet thicknesses on the order of ≪ 100 μm this would imply that drying should be completed on timescales much faster than a second to avoid complete interlayer mixing by diffusion. We estimated the diffusion lengths using the Einstein equation [7] where we have the diffusion constant and mean displacement, as follows:

$$D = \frac{k_B T}{6\pi\eta r}, \lambda_{1d} = \sqrt{2Dt}.$$

here k_B is boltzman's constant, T is absolute temperature, η is the viscosity (of the ink), r is the particle radius, and t is time. Eliminating D , we get the following mean displacement, during 1 s diffusion, for a C₆₀ molecule (taken to be similar to PCBM) at 80 °C:

$$\lambda_{C_{60}} = \sqrt{\frac{k_B}{3\pi} \times \frac{1 \text{ s} \times 353 \text{ K}}{1 \text{ mPa s} \times 0.5 \text{ nm}}} = 3.22 \times 10^{-5} \text{ m}.$$

For $r = 50 \text{ nm}$ particle

$$\lambda_{np} = \sqrt{\frac{k_B}{3\pi} \times \frac{1 \text{ s} \times 353 \text{ K}}{1 \text{ mPa s} \times 50 \text{ nm}}} = 3.22 \times 10^{-6} \text{ m}.$$

here we have assumed a constant viscosity of 1 mPa s, which should be considered a conservative estimate, as it is likely to be higher and will increase as the drying proceeds. In our case, the inks P3HT:PCBM, and poly(3,4-ethylenedioxythiophene):poly(styrenesulfonate) (P3HT:PCBM and PEDOT:PSS) are both aqueous dispersions of large aggregates with average sizes 50–100 times larger than the PCBM molecule, hence interlayer mixing due to

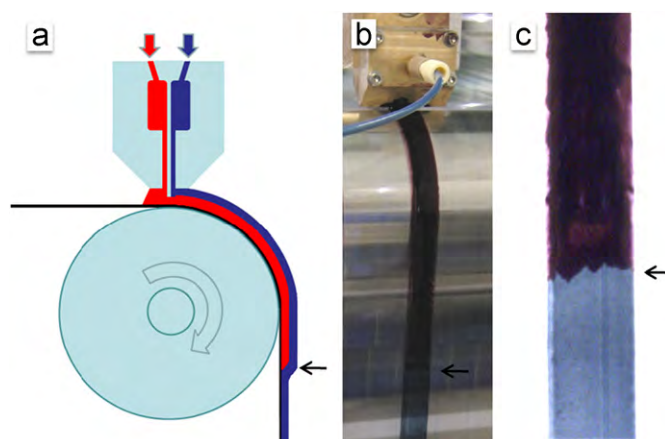


Fig. 2. Double slot-die coating experiment at an instance where the film changes appearance going from a single layer of PEDOT:PSS (blue) to a simultaneous coating of P3HT:PCBM (red) and PEDOT:PSS. The transition is marked by the arrows going from (a) a schematic of the experimental situation, to (b) a photograph of the experiment, and to (c) a close-up photograph of the same foil piece, taken after the coating experiment. (For interpretation of the references to color in this figure legend, the reader is referred to the web version of this article.)

diffusion of the particles between the two layers would be 1–2 orders of magnitude slower, thus enabling drying without detrimental interlayer mixing. At the same time a limited amount of interdiffusion should be advantageous as it gives a diffusive interface between the coated layers with much higher adhesion, possibly lowering device degradation due to layer delamination. Experience gained from the actual coating experiments suggests that the process is very parameter sensitive. However, a stable operation regime was found and a very illustrative example of the simultaneous bilayer formation from the coating experiment is shown in Fig. 2, where it was possible to turn on and off the flow of one of the inks, thus revealing a sharp transition from single- to bilayer.

3.1. Nanoparticle characterization

3.1.1. X-ray scattering

The aqueous ink was studied by small angle X-ray scattering (SAXS) in order to determine the size of the particles. The ink was placed in 1 mm capillaries and sealed with epoxy glue, and the data were analyzed using the Bayesian Indirect Fourier Transform [8]. The average particle radius was found to be 46 nm, see Fig. 3.

3.1.2. Microscopy

The drop-cast and spin-coated samples of the nanoparticles were imaged using transmission electron microscopy (TEM) (Fig. 3b) and atomic force microscopy (AFM) (Fig. 3c), respectively. The image documented that spherical nanoparticles had formed.

3.2. Bilayer characterization

3.2.1. Time-of-flight secondary ion mass spectrometry (TOF-SIMS) depth profiling analysis

The obvious concern when performing double slot-die coating is whether the expected bilayer is formed, or whether complete mixing of the layers had occurred. An experiment was designed to resolve this issue. A piece of double slot-die coated sample was submerged in a sodium hydroxide solution in order to facilitate delamination (Fig. 4b). After a while a discrete PEDOT:PSS film simply floated off the top of the surface leaving a P3HT:PCBM film

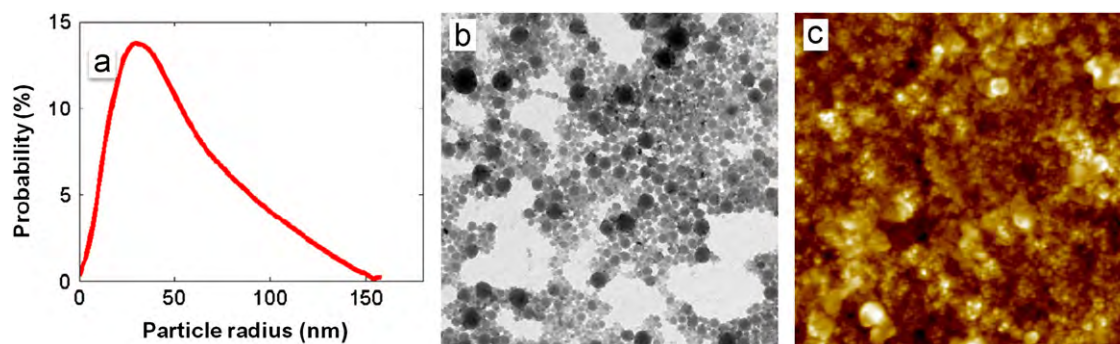


Fig. 3. (a) Volume weighted size distribution of the nanoparticles calculated from the SAXS measurement. (b) TEM image ($5 \times 5 \mu\text{m}^2$) of a drop-cast sample. (c) AFM image ($5 \times 5 \mu\text{m}^2$) of a spin-coated sample.

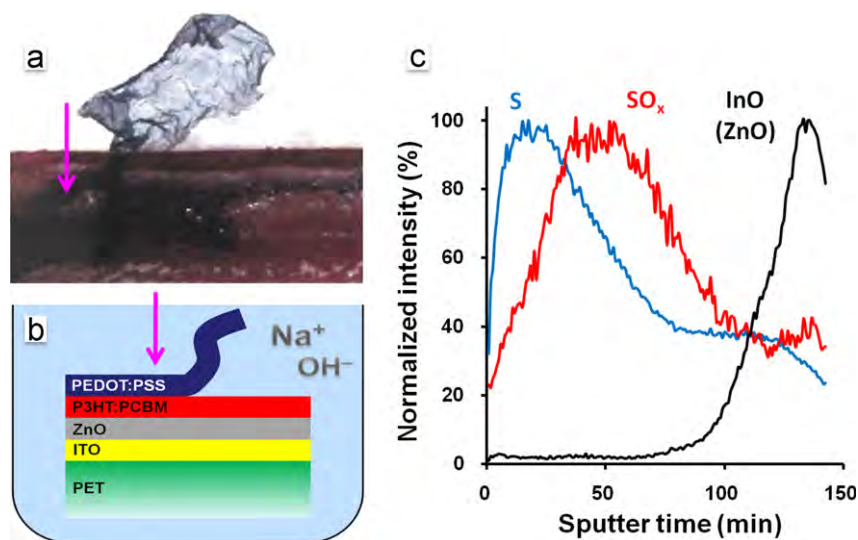


Fig. 4. (a) Photograph showing a $18 \times 7 \text{ mm}^2$ film section delaminated from the double slot-die coated film in NaOH (aq). (b) Schematic of the submerged sample showing the surface location (purple arrow) for the TOF-SIMS depth profiling analysis. (c) TOF-SIMS depth profiles in negative ion mode confirming that the double slot-die coated film has formed a bilayer. The ZnO layer was so thin that the resulting profile was too noisy, so it was left out for clarity. The noisy ZnO profile is superimposed (due to the thin nature of the film) on the InO⁻ profile.

on the substrate surface (Fig. 4a). This is clear visual evidence that the double slot-die coating experiment yields a discrete bilayer film. The observations were confirmed by chemical analysis using TOF-SIMS.

TOF-SIMS depth profiling was in addition employed to support the observation and to further document that a bilayer had indeed formed during the double slot-die coating process. Fig. 4a–b shows the surface location where the depth profiling analysis was carried out. Several factors complicate the depth profiling analysis: (i) the sputter depth resolution (under the conditions in question) in soft materials is very poor (compared to hard materials, e.g. metals), and (ii) depth profiles are typically based on unique mass spectral markers that consist of molecular fragment ions or atomic ions, but no unique mass spectral markers are formed under the given experimental conditions. However, due to the fact that equivalent mass spectral markers originating from different molecular environments will produce a different signal response, the different materials may still be uniquely resolved. It turns out that the signal intensities for the S⁻ and SO_x⁻ fragment ions (formed in both layers) are extremely dependent on their origin. S⁻ is intense in PEDOT:PSS and relatively weak in P3HT:PCBM whereas SO_x⁻ exhibits the opposite behavior. Fig. 4c shows the depth profiles using S⁻ and SO_x⁻ as mass spectral markers. In spite of the complicated experimental conditions it was still possible to confirm that a bilayer was formed during the double slot-die coating process. In addition, a

depth profile was acquired at a surface location where delamination had occurred that showed the presence of the expected one layer (see Fig. S1 in supporting information). Due to the aforementioned factors affecting the analysis it is not possible to conclude anything about the extent of interlayer mixing that was a consequence of the coating process. From the delamination experiment shown in Fig. 4 we however assume that the interface is discrete when viewed on the scale of the film thickness and probably resembles the roughness that an individual film of the P3HT:PCBM nanoparticles would.

3.2.2. Reflectometry

The coated films were studied with reflectometry in order to determine whether the two double slot-die coated liquids had mixed. Two samples were measured, a double slot-die coated PEDOT:PSS/P3HT:PCBM bilayer and a single slot-die coated PEDOT:PSS layer, both on a ZnO/ITO/PET substrate. The top layer of the two samples showed the critical angle for total reflection at the same position corresponding to the same electron density for the top layer in both preparations, see Fig. 5.

3.3. Device performance

The *J*–*V* characteristics of the freshly prepared solar cells are shown in Fig. 6 together with a reference device, also processed using the aqueous P3HT:PCBM nanoparticle ink as active layer

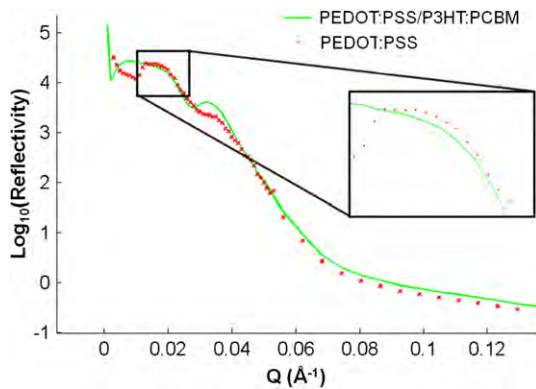


Fig. 5. Reflected intensity for two coated samples. One with PEDOT:PSS and one double slot-die coated PEDOT:PSS/P3HT:PCBM bilayer. The critical angle (θ_c) for total reflection is at 0.176° for both films corresponding to a scattering vector Q_c of 0.025 \AA^{-1} ($Q = 4 \pi \sin \theta / \lambda$, $\lambda = 1.5418 \text{ \AA}$).

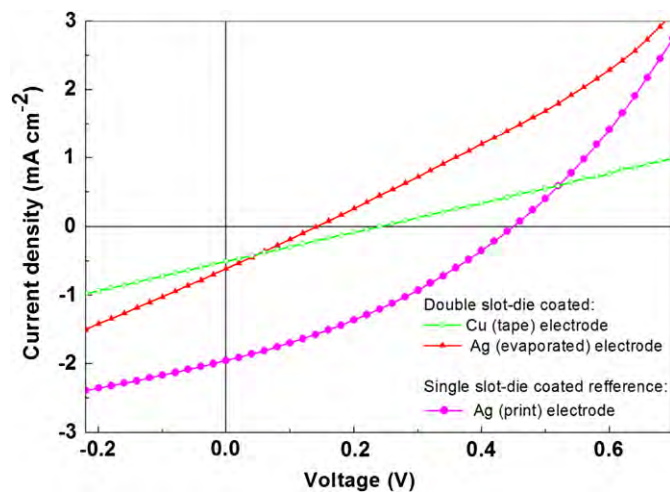


Fig. 6. J - V curves of the double slot-die coated devices shown in comparison with a device of similar layer structure processed by standard single slot-die coating.

Table 1
Summary of the J - V characterization.

Cell ID	PCE (%)	J_{sc} (mA cm^{-2})	V_{oc} (V)	FF (%)
Double slot-die (Cu tape)	0.03	0.5	0.24	25.0
(Ag evaporated)	0.02	0.61	0.14	25.6
Single slot-die	0.29	1.95	0.45	33.1

and PEDOT:PSS as HTL, but prepared by two sequential single slot-die coating steps (i.e. one layer at the time). The use of this nanoparticle ink constitutes a unique route for aqueous processing of large area low band gap polymer solar cells recently demonstrated by our group [9]. The extracted photovoltaic parameters are summarized in Table 1. As is evident the photovoltaic response is significantly lower for the double slot-die coated devices compared to the reference device with respect to all photovoltaic parameters. One notable feature is the linearity of the J - V curves within the active quadrant (FF of 25%), which suggests that the operation of the cells is dominated by the internal resistances in the devices, i.e. a low shunt resistance and a high series resistance. A low shunt resistance can be ascribed to two possible effects: (1) from the complex dynamic nature of the simultaneous bilayer formation, as it is likely that PEDOT:PSS forms percolation paths through the active layer during formation, which, in turn, will short the device. (2) It could also be

linked to the known photoinduced defects in ZnO as reported recently [10].

Furthermore, the devices having the evaporated Ag electrode display the lowest shunt resistances and consequently lowest V_{oc} , probably due to shunts being formed during evaporation, while the Cu-tape avoids shunts by preferentially contacting the top-most part of the bilayer film, suggesting a somewhat inhomogeneous film. However, the higher series resistance for the devices utilizing a Cu-tape electrode hints to a large contact resistance at the PEDOT:PSS/Cu interface.

We also constructed the reference (blank) devices comprising ITO/ZnO/P3HT:PCBM/Cu-tape, and ITO/ZnO/PEDOT:PSS/Cu-tape, where ITO is indium tin oxide. The corresponding J - V curves under standard illumination conditions revealed no photovoltaic response thus documenting the photovoltaic properties of double slot-die coated films. The relatively poor performance of the double slot-die coated devices possibly also has its roots in the large areas we explore (several cm^2) compared to relative film inhomogeneity for the double slot-die coated films. Also the shunts might be located at the edges as is evident from the photograph in Fig. 4a where the PEDOT:PSS has the possibility to overspill the undercoat of P3HT:PCBM and thus short circuit the device. By further tuning the coating conditions, surface tensions for the inks and substrate surface energies it should be possible to minimize these effects.

4. Conclusions

We have successfully demonstrated double slot-die coated polymer solar cells processed roll-to-roll, using two aqueous inks for the simultaneous formation of both the active layer (P3HT:PCBM) and hole transporting layer (PEDOT:PSS). The devices performed relatively poor compared to similar devices processed by single slot-die coating. This is ascribed to far from perfect layer separation due to the complex nature of the bilayer formation process; resulting in shunts and low current extraction efficiencies. This convincingly demonstrates a possible route for lowering the energy payback time of polymer solar cells, which is an important factor in a possible future scenario of large scale energy production.

Acknowledgements

This work was supported by the Danish National Research Foundation. We also thank Dr. T. Kasama at DTU Center for Electron Nanoscopy for TEM measurements.

Appendix A. Supporting information

Supplementary data associated with this article can be found in the online version at [doi:10.1016/j.solmat.2011.08.026](https://doi.org/10.1016/j.solmat.2011.08.026).

References

- [1] F.C. Krebs, Fabrication and processing of polymer solar cells. A review of printing and coating techniques, *Solar Energy Materials and Solar Cells* 93 (2009) 394–412.
- [2] F.C. Krebs, T. Tromholt, M. Jørgensen, Upscaling of polymer solar cell fabrication using full roll-to-roll processing, *Nanoscale* 2 (2010) 873–886.
- [3] F.C. Krebs, T.D. Nielsen, J. Fyenbo, M. Wadstrøm, M.S. Pedersen, Manufacture, integration and demonstration of polymer solar cells in a lamp for the Lighting Africa initiative, *Energy & Environmental Science* 3 (2010) 512–525.
- [4] F.C. Krebs, J. Fyenbo, M. Jørgensen, Product integration of compact roll-to-roll processed polymer solar cell modules: methods and manufacture using flexographic printing, slot-die coating and rotary screen printing, *Journal of Materials Chemistry* 20 (2010) 8994–9001.

- [5] N. Espinosa, R. García-Valverde, A. Urbina, F.C. Krebs, A life cycle analysis of polymer solar cell modules prepared using roll-to-roll methods under ambient conditions, *Solar Energy Materials and Solar Cells* 95 (2010) 1293–1302.
- [6] R. Søndergaard, M. Helgesen, M. Jørgensen, F.C. Krebs, Fabrication of polymer solar cells using aqueous processing for all layers including the metal back electrode, *Advanced Energy Materials* 1 (2011) 68–71.
- [7] A. Einstein, On the motion of small particles suspended in liquids at rest required by the molecular-kinetic theory of heat, *Annalen Der Physik* 17 (1905) 549–560.
- [8] S. Hansen, Bayesian estimation of hyperparameters for indirect Fourier transformation in small-angle scattering, *Journal of Applied Crystallography* 33 (2000) 1415–1421.
- [9] T.R. Andersen, T.T. Larsen-Olsen, B. Andreasen, A.P.L. Böttiger, J.E. Carle, M. Helgesen, E. Bundgaard, K. Norrman, J.W. Andreasen, M. Jørgensen, F.C. Krebs, Aqueous processing of low-band-gap polymer solar cells using roll-to-roll methods, *ACS Nano* 5 (2011) 4188–4196.
- [10] A. Manor, E.A. Katz, T. Tromholt, F.C. Krebs, Electrical and photo-induced degradation of ZnO layers in organic photovoltaics, *Advanced Energy Materials* (2011) 836–843.

Article

A Nanoparticle Approach towards Morphology Controlled Organic Photovoltaics (OPV)

Thomas R. Andersen ¹, Quanxiang Yan ^{2,3}, Thue T. Larsen-Olsen ¹, Roar Søndergaard ¹, Qi Li ², Birgitta Andreasen ¹, Kion Norrman ¹, Mikkel Jørgensen ¹, Wei Yue ³, Donghong Yu ³, Frederik C. Krebs ¹, Hongzheng Chen ² and Eva Bundgaard ^{1,*}

¹ Department of Energy Conversion and Storage, Technical University of Denmark, Frederiksborgvej 399, DK-4000 Roskilde, Denmark; E-Mails: tria@dtu.dk (T.R.A.); thols@dtu.dk (T.T.L.-O.); rosq@dtu.dk (R.S.); baan@dtu.dk (B.A.); kino@dtu.dk (K.N.); mijq@dtu.dk (M.J.); frkr@dtu.dk (F.C.K.)

² State Key Laboratory of Silicon Materials, MOE Key Laboratory of Macromolecule Synthesis and Functionalization and Department of Polymer Science and Engineering, Zhejiang University, Hangzhou 310027, China; E-Mails: yqx0116@163.com (Q.Y.); 11210440008@fudan.edu.cn (Q.L.); hzchen@zju.edu.cn (H.C.)

³ Department of Biotechnology, Chemistry, and Environmental Engineering, Aalborg University, Sohngaardsholmsvej 57, DK-9000 Aalborg, Denmark; E-Mails: wy@bio.aau.dk (W.Y.); yu@bio.aau.dk (D.Y.)

* Author to whom correspondence should be addressed; E-Mail: evbu@dtu.dk; Tel.: +45-4677-5498; Fax: +45-4677-4791.

Received: 16 April 2012; in revised form: 24 May 2012 / Accepted: 4 June 2012 /

Published: 11 June 2012

Abstract: Silicon nano-particles grafted with two different organic oligomers were prepared; the oligomers used were a phenylene-vinylene (PV) oligomer and a 3,3''-didodecylquaterthiophene. The graftings were performed by the use of two different functional groups, the PV oligomer was grafted by a hydroxyl-group in the form of a phenol and a lithium derivative was used to graft the 3,3''-didodecylquaterthiophene. The morphology and size of the grafted particles were analyzed by atomic force microscopy (AFM) and the extent of the grafting was analyzed by NMR. Organic photovoltaics with normal geometry (ITO/PEDOT:PSS/active layer/Al) were prepared using these materials as a donor and phenyl-C61-butyric acid methyl ester ([60]PCBM) as the acceptor and yielded a power conversion efficiency (PCE) of 0.27%, an open circuit voltage (V_{OC}) of

0.93 V, a short circuit current density (J_{SC}) of 0.89 mA/cm², and a fill factor (FF) of 32.5% for a lead device with an active area of 0.25 cm².

Keywords: organic photovoltaics; silicon nano-particles; morphology control

1. Introduction

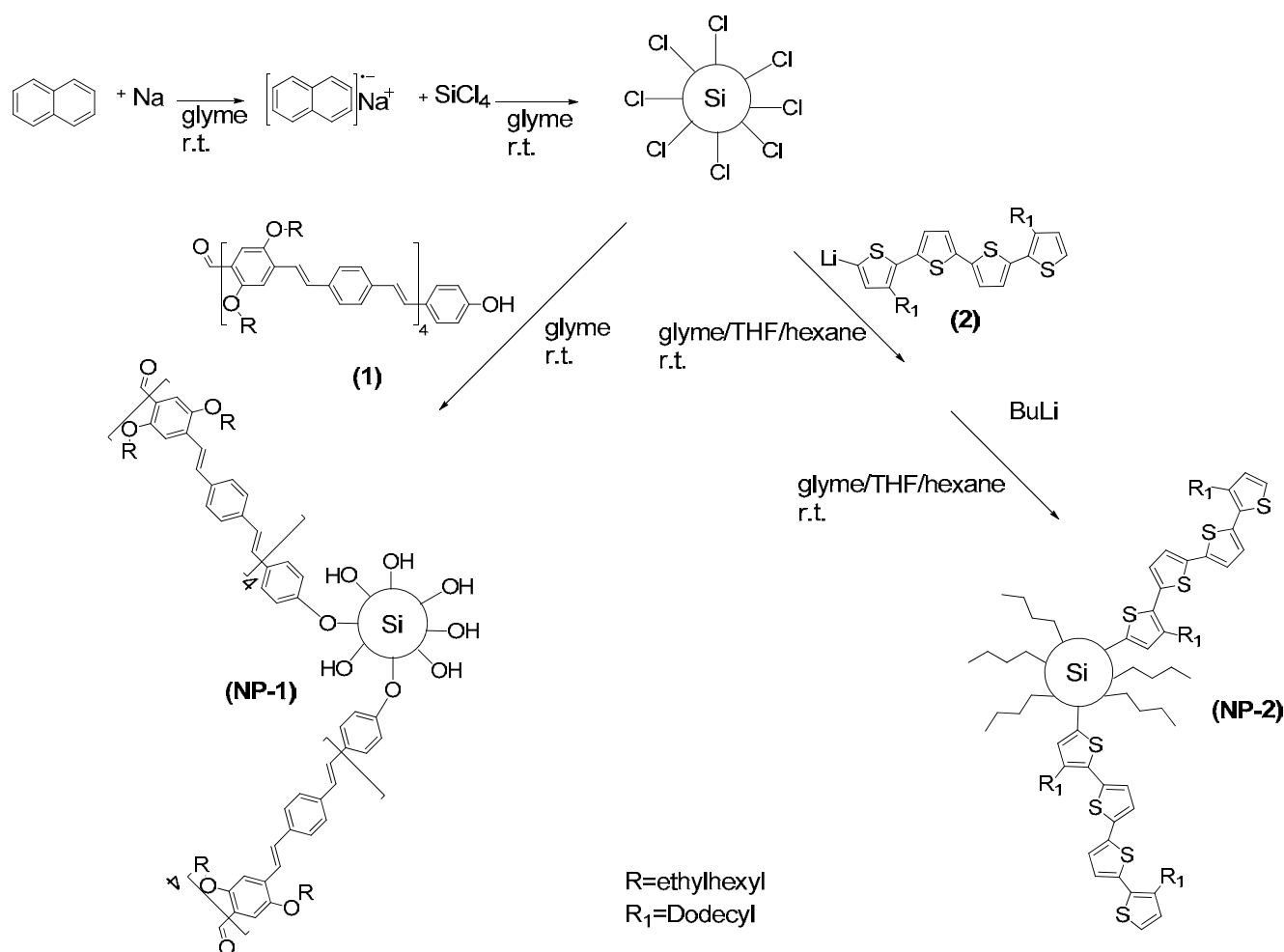
Organic photovoltaics (OPV) have in the past decade been the subject of increasing interest, primarily due to its potential as a low cost sustainable energy source [1–5]. The best performing OPV devices have been prepared with the bulk heterojunction (BHJ) architecture in the photoactive layer, which is a blend of a p-type (donor) and an n-type material (acceptor) [2]. It is well-known that the morphology of the photoactive layer in a BHJ has a large influence on the power conversion efficiency (PCE) [3–5]. This is mainly ascribed to: (1) the crystallinity of the organic materials, where a higher degree of crystallinity enhances the carrier transport through higher mobility and thus increases the efficiency [4,6], and (2) the phase separation between the donor and acceptor materials, which should form a continuous entangled network of the donor and acceptor with domain sizes similar to the exciton diffusion length of about 10 nm [4]. Thus, ensuring the optimal conditions for exciton disassociation is directly correlated with the short circuit current [2]. Morphology optimization is often attempted by self assembly; the two most widely used methods are thermal annealing and solvent annealing [4,5]. Thermal annealing is a post production heat-treatment of the active layer, which often promotes the semi-crystalline components in the active layer to form a more ordered packing or crystals if possible [4]. The technique of solvent annealing uses a solvent with a higher boiling point thereby decreasing the rate of evaporation, which allows larger domains to form [5]. This can lead to an improvement of the interpenetration between the donor and acceptor and usually also an increased order within the polymer domains [5]. Another method for this optimization is the use of additives such as 1,8-octanedithiol, 1,8-diiodooctane etc. This method is similar to solvent annealing since the additive has a higher boiling point than the main solvent and provides better solubility for one of the components. In the case of 1,8-octanedithiol, 1,8-diiodooctane and 1-chloronaphthalene the solubility of PCBM is larger than a donor-polymer such as poly(3-hexylthiophene) (P3HT) [4] and this results in the formation of large domains of PCBM. These methods are generally easy and of low cost and therefore often used. However, the morphologies obtained are often not stable for a long time [6,7]. They have a tendency to form larger domains causing the overall performance to drop especially after exposure to heat [6,7]. A couple of methods for overcoming the bulk diffusion have been presented. The first method is to cross link either the donor- or the acceptor-molecules within the bulk, thereby forming a rigid network which makes the diffusion more limited [8,9]. A drawback to this method is that the modifications within the active layer are carried out during or after fabrication of the device, thus risking residual products or initiators from the cross-linking to be contained within the film, which could potentially decrease the device life-time.

A radically different approach is to use preformed nano-particles as templates for the morphology, which is the focus of this paper. Instead of relying on a random self-assembly process as described above, this approach uses nano-particles of 15–20 nm, thus automatically ensuring an optimal

interpenetrating network of donor and acceptor. The approach was introduced by Kiriy *et al.* [10–12], where P3HT is polymerized from the surface of silica (SiO_2) nano-particles, thereby achieving polymer chains that are covalently grafted onto the surface of nano-particles. This eliminates diffusion and locks the morphology. A disadvantage to this method is the introduction of silica within the active layer which results in very limited contribution to the absorption of photons leading to thicker active layers to ensure the same absorption thereby risking a decrease in fill factor [13].

In this paper we report a pathway to overcome the lack of absorption from the nano-particle approach; we exchanged the silica with silicon nano-particles in our study. This should also ensure a stable morphology, but more importantly, increases the absorption since the absorption from silicon is much greater than for silica towards longer wavelengths. The absorption of the silicon nano-particles should theoretically be size dependent [14], *i.e.*, larger nano-particles result in longer wavelengths of the absorbing light. For the organic grafting agent two different organic molecules were used; a PV oligomer (**1**) presented by S ndergaard *et al.* [15], and 3,3''-didodecylquaterthiophene (**2**) (see Scheme 1). The latter was used to compare the nano-particles with current materials used in OPV devices.

Scheme 1. Preparation of the silicon nano-particles (NP) and the grafting of the nano-particles with compounds **1** and **2**.



2. Experimental Section

2.1. Preparation of Nano-Particles

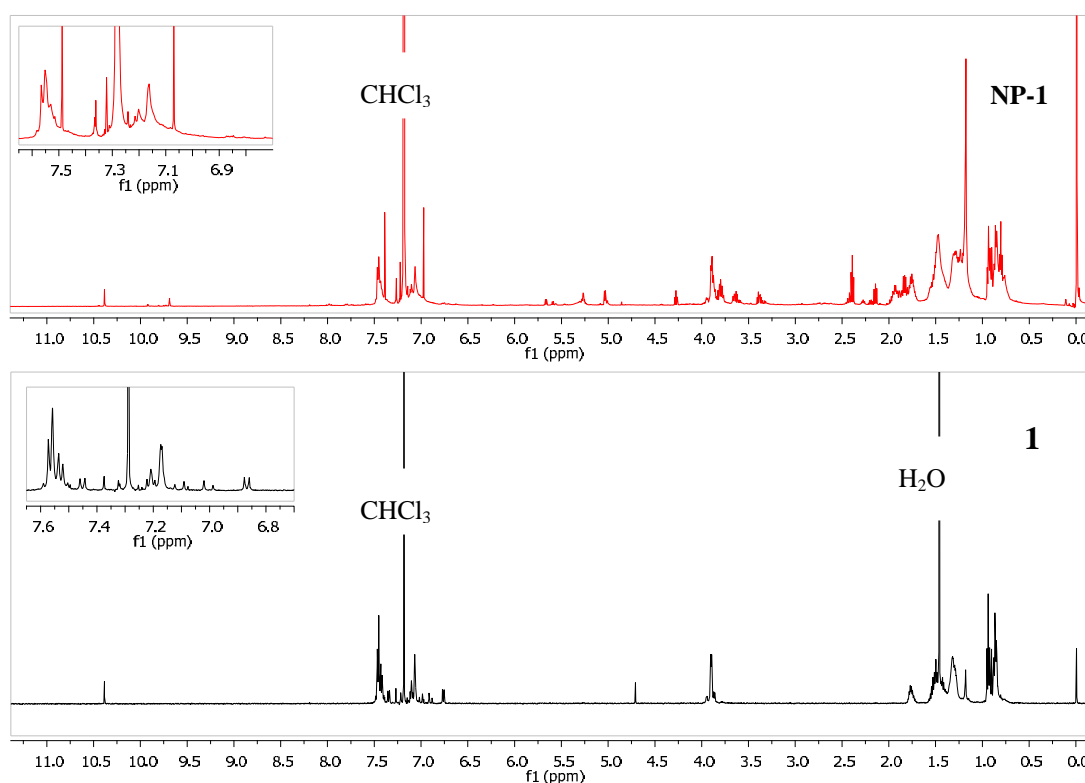
All chemicals for the preparation of the silicon nano-particles were purchased from Sigma-Aldrich, and were used as received except glyme which was dried over sodium prior to use. The PV oligomers were prepared as describe by Søndergaard *et al.* [15]. All reactions were carried out under an argon atmosphere.

The Si-nano particles used for **NP-1** and **NP-2** were prepared as described by Baldwin *et al.* [16] and Baldwin *et al.* [17], respectively.

NP-1: Sodium (0.1 g, 4.3 mmol) was added to a dry glyme solution (5 mL) and naphthalene (0.35 g, 2.7 mmol) and stirred for 3 hours after which a black yellowish solution of sodium naphthalide was obtained. This solution was added to SiCl₄ (99.9%, 0.08 mL, 0.7 mmol) in dry glyme solution (30 mL) and stirred for 30 min. after which the organic grafting agent (**1** (see Scheme 1), 100 mg, 0.05 mmol) was added and the reaction mixture was stirred for 2 hours. The solvent was removed under reduced pressure; the residue was dissolved in heptane and washed with water. During the washing a red solid phase was formed near the water/heptane interface which was filtered off and was verified by ¹H-NMR to be unreacted grafting agent. The organic phases were collected and the solvent was removed under reduced pressure, the residue was heated to 90 °C also in vacuum to remove residual naphthalene. The solid was extracted with chloroform and heptane, and when these were combined precipitation occurred. The suspension was filtered to give the functionalized nano-particles (**NP-1**) as a sticky red solid (108 mg).

¹H NMR spectra of compound **1** and **NP-1** are shown in Figure 1.

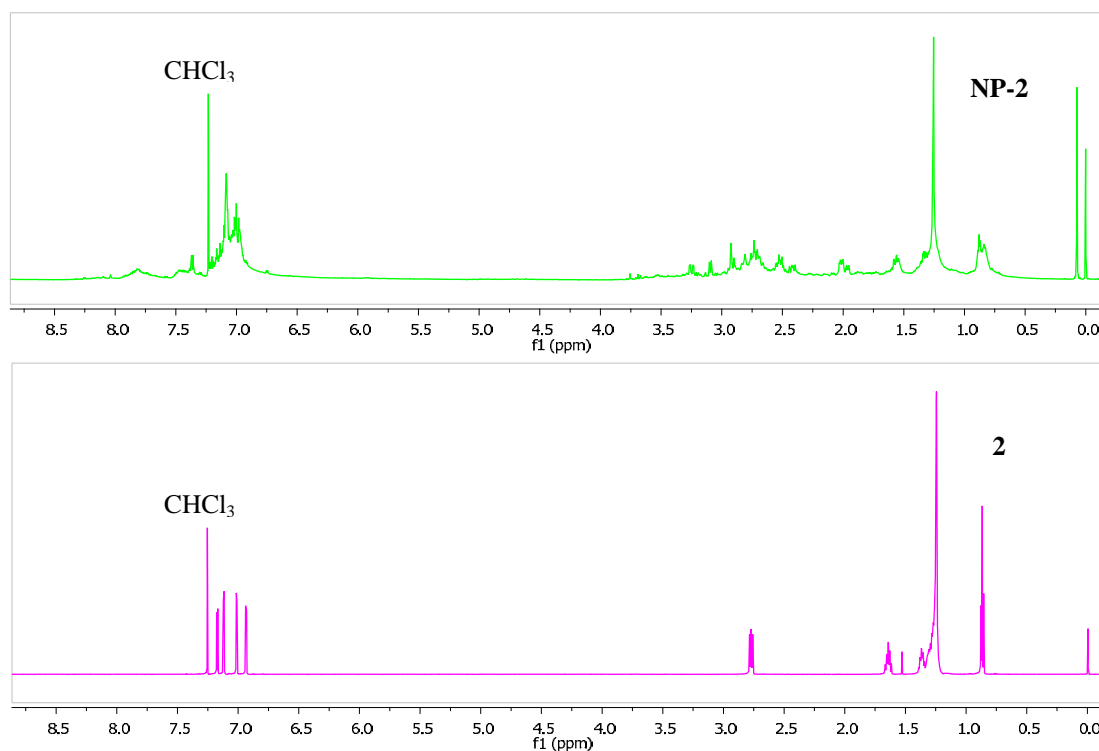
Figure 1. ¹H-NMR spectra of compound **1** and **NP-1** measured in CDCl₃.



NP-2: Sodium naphthalide was prepared from sodium (0.36 g, 15.7 mmol) and naphthalene (1.48 g, 11.5 mmol) in dry glyme (20 mL). After stirring over night SiCl₄ (0.52 g, 4.5 mol) was added drop-wise into the dry glyme solution of sodium naphthalide. The color of the suspension changed from dark yellow to deep brown. After stirring for 2 hours, 5-lithio-3,3''-didodecylquaterthiophene (80 mg 0.12 mmol) (prepared from 3,3''-didodecylquaterthiophene **2** and n-butyl lithium in 10 mL THF) was added. Excess of n-butyl lithium was added to the reaction-flask to passivate silicon nano-particles with butyl groups. After vigorously stirring overnight, the solvent was removed under reduced pressure and naphthalene was removed by continuously purging N₂ into the flask in a heating mantle under vacuum for 12 hours. The resulting yellow solid was extracted with hexane and washed three times with distilled water. The hexane layer was collected and solvent was removed in vacuum to give the functionalized nano-particles (**NP-2**) as a waxy yellow solid (67 mg).

¹H NMR spectra of compound **2** and **NP-2** are shown in Figure 2.

Figure 2. The ¹H-NMR-spectra of compound **2** and **NP-2** measured in CDCl₃.



2.2. UV-Vis Spectroscopy

The UV-Vis spectroscopy in solution was carried out on a Varian Cary50 Bio UV-Visible Spectrophotometer (Agilent Technologies, USA) and in film on a PharmaSpec UV-1700 (SHIMADZU, Japan).

2.3. Device Fabrication and Characterization

Photovoltaic devices were fabricated by spin coating PEDOT:PSS (Clevios PVP.AI 4083, Heraeus) (3000 rpm) on top of pre-cleaned, patterned indium tin oxide (ITO) on glass slides and then baked at 140 °C for 5 min. The active layer was deposited by spin coating a mixture of the functionalized

nano-particles (**NP-1** or **NP-2**) and [60]PCBM in chloroform (1:1, 20 mg/mL). The back electrode consisting of about 100 nm aluminum was deposited by vacuum evaporation. Some samples were annealed at 140 °C for 2 min. I-V measurements were carried out with a Keithley (2440) as a source meter under a solar simulator from Steuernagel (solar constant KHS 575) with 1000 W/m², AM1.5G. The active area of the devices was 0.25 cm² and the thickness of the active layer was determined by atomic force microscopy (AFM).

2.4. Atomic Force Microscopy

AFM imaging of the active layers was performed on an N8 NEOS (Bruker Nano GmbH, Herzogenrath, Germany) operating in an intermittent contact mode using PPP-NCLR cantilevers (NANOSENSORS, Neuchatel, Switzerland). Images were recorded at a scan speed of 1 line/sec. The images were analyzed using the image processing software package SPIP 5.1.5 (Image Metrology A/S, Hørsholm, Denmark) for the height measurements, and the particle size determination. AFM images of nanoparticles were performed in semi-contact mode on a NTEGRA life instrument (NT-MDT), with an Olympus AC240TS cantilever at a resonance frequency of 140 kHz. WSxM Program was used for image data processing [16], samples were prepared by drop-casting a dilute solution of nano-particles in chlorobenzene on to a substrate of Muscovite Mica (size: 9.5 mm Diameter, thickness: 0.15–0.21 mm, Electron Microscopy Science).

3. Results and Discussion

3.1. Fabrication of Nano-Particles

The grafting technique used to graft the organic oligomers onto the silicon nano-particles, has previously been reported [17–19]. The grafting reactions were carried out by nucleophilic substitution by organic materials containing a hydroxyl-group as a final step in the preparation of the nano-particles, but also by the use of lithiated-molecules.

The preparation of silicon nano-particles presented two major challenges. In previously published work [16,20] the nano-particles were washed with water as part of the purification, however, in this work an impurity was observed, which was evident from a peak around 7 ppm in the ¹H-NMR-spectrum (Figure S1 in Supporting Information). This can be overcome by employing sublimation as the primary method for removal of naphthalene. This approach was developed using silicon nano-particles with meta-cresol as the grafting agent. The ¹H-NMR spectra of these test reactions can be seen in the Supporting Information (Figure S1).

The second challenge that was discovered during the preparation of the nano-particles was the irreversible adsorption of nano-particles onto the glassware and aggregation of nano-particles when solvents were removed during purification, which unfortunately led to an unavoidable and significant loss of material.

The ¹H-NMR spectra of compound **1** and **NP-1** are given in Figure 1. Some of the key features in the spectrum of **NP-1** originating from compound **1** are very similar after grafting. In particular, this includes the peaks from 6.7 to 7.7 ppm due to protons in the aromatic moieties but also from 0.7 to 2 ppm that are due to protons in the aliphatic side chains. However, the signal from the phenol-group

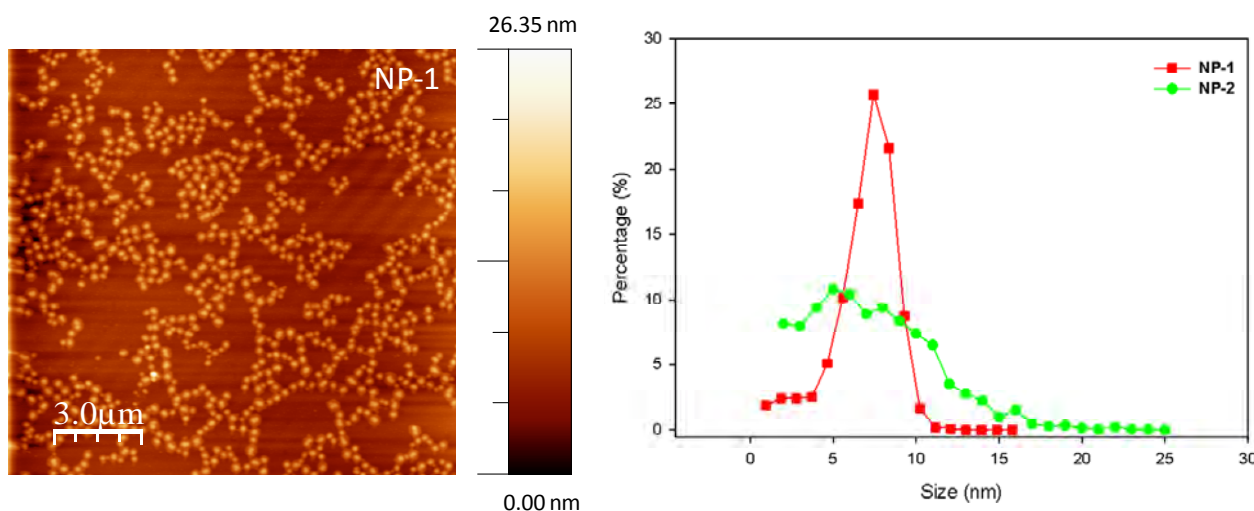
(4.85 ppm) has disappeared as expected; a small singlet at 4.95 ppm remains that could be the signal from compound **1** where the phenol has not reacted. However, this peak integrates only to 0.14 against the aldehyde-group, which leads us to the conclusion that at least 85% of compound **1** within the sample is grafted to the surface of the nano-particles. Besides these results the spectra between 6.7 ppm to 7.7 ppm are less defined which should be expected by the lower mobility induced by the grafting. These results correlate well with results already published by Ruckenstein *et al.* [21] where it is shown that grafting of silicon nano-particles with an organic agent results in very little, if any, shifts in the NMR-spectra for the organic grafting agent.

In contrast to **NP-1**, the ^1H -NMR spectrum of **NP-2** shows very broadened signals in the regions compared to the spectrum of **2** (see Figure 2). This broadening of the signals is probably an effect of the greatly diminished mobility of the quarterthiophene molecule after it has been grafted onto the nano-particle. It is not possible to find which ^1H signal has disappeared due to the grafting, partially because of the presence of an impurity giving rise to signals in the aromatic region. Signals in the aliphatic regions from both **2** and butyl groups, which were also grafted, are visible.

3.1.1. Morphology and Size Characterization

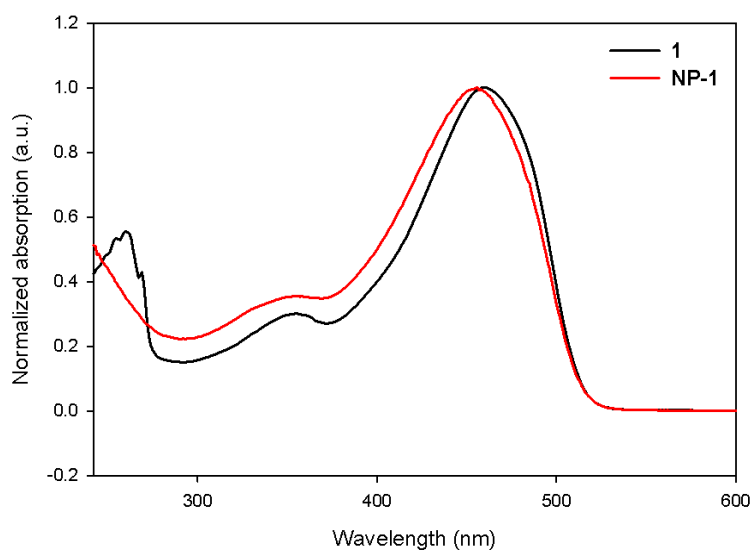
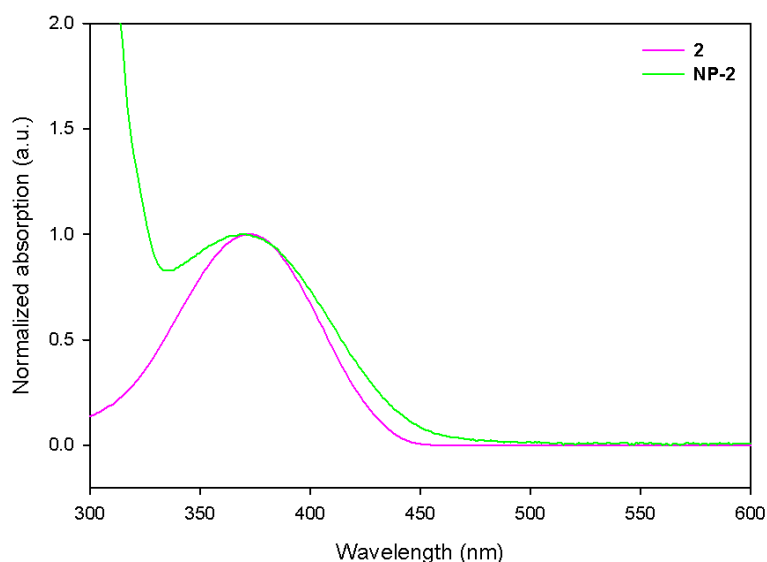
AFM was used to measure the size of the Si nano-particles. The AFM image of **NP-1** (see Figure 3) shows a monolayer of spherical particles which have a tendency to aggregate into clusters. The size distribution of the particles shows the main particle size to be 7.0 (± 1.8) nm for **NP-1** and 6.8 (± 3.8) nm for **NP-2**, which is about half the size of what is thought to be the optimal size, *i.e.*, 15–20 nm.

Figure 3. AFM image of **NP-1** coated on mica by drop casting from a diluted solution in chlorobenzene (**left**) and the size distribution of the particles determined by their height (**right**).



3.2. Optical Properties

The normalized absorption spectra for all materials are given in Figure 4 for compound **1** and **NP-1** and Figure 5 for compound **2** and **NP-2**, respectively.

Figure 4. Absorption spectra of compound **1** and **NP-1** in CHCl_3 .**Figure 5.** The absorption of compound **2** and **NP-2** in CH_2Cl_2 .

The absorption of **NP-1** in a chloroform solution is very similar to that of compound **1**. There is a slight difference in the maximum absorption where **NP-1** seems to have a small blue-shift (from 460 nm for **1** to 456 nm for **NP-1**). There is also a difference at low wavelengths, where the absorption from **1** decreases after peaking at 260 nm and the absorption from **NP-1** continues to increase. The variation is ascribed to the absorption of the Si-nano-particles.

The absorption spectra for compound **2** and **NP-2** have some similarities. As observed for **1** and **NP-1**, a very small blue-shift (from 373 to 370 nm) can also be observed for the max absorption in the range from 350–450 nm after grafting. There is, however, some difference in the spectra at the edge absorption, where **2** absorbs from 433 nm, **NP-2** absorbs from 443 nm. The major difference is the point at lower wavelengths (less than 340 nm) which is ascribed to absorption of the Si-nano particles (see Supporting Information Figure S2). The difference between **NP-1** and **NP-2** is ascribed to **NP-2** containing larger nano-particles, *i.e.*, up to above 15 nm, and **NP-1** only containing nano-particles up to 10 nm (see Figure 3).

3.3. Device Performance

OPV devices were prepared as described in the experimental section and measured under artificial sun (1000 W/m^2 , AM1.5G). The IV data are summarized in Figure 6 and Table 1.

The devices prepared with compound **1** and **NP-1** both show clear solar cell characteristics (Figure 6). When examining the devices carefully, it became clear that there was a large difference in absorption for **Device 1** and **Device 4**. This difference was investigated by the optical reflectance of the two devices, which was measured using the back electrode as a mirror.

Figure 6. I-V-curves for the two different device types, **Device 1** and **Device 4**.

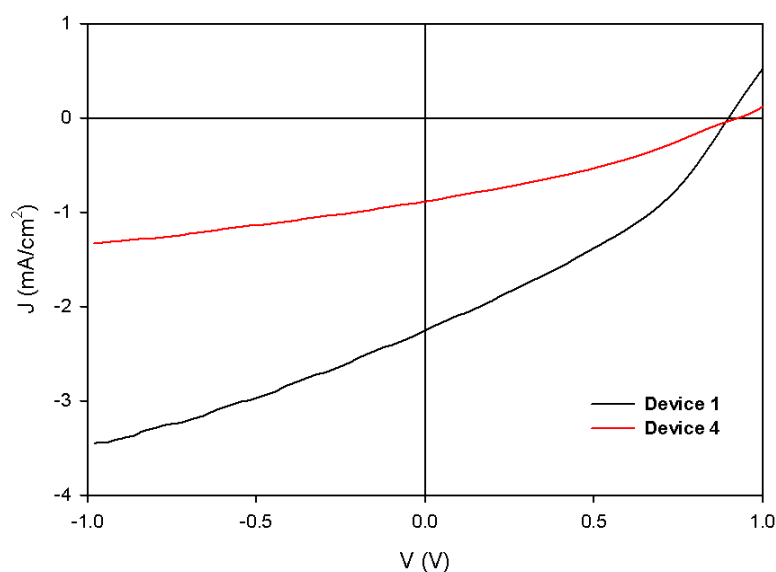


Table 1. A collection of the data obtained for all the devices, *i.e.*, thickness, absorption in the active layer, reflectance, device material, and photovoltaic properties: PCE, open circuit voltage (V_{OC}), short circuit current density (J_{SC}), and fill factor (FF) obtained for the devices with the geometry glass/ITO/PEDOT:PSS/donor-[60]PCBM (1:1 w/w, 20 mg/mL)/Al and an active area of the devices of 0.25 cm^2 . The testing conditions were AM1.5G (Xe-lamp, 1000 W/m^2 , $85 \pm 5 \text{ }^\circ\text{C}$). The thicknesses were determined by AFM as reported previously [22].

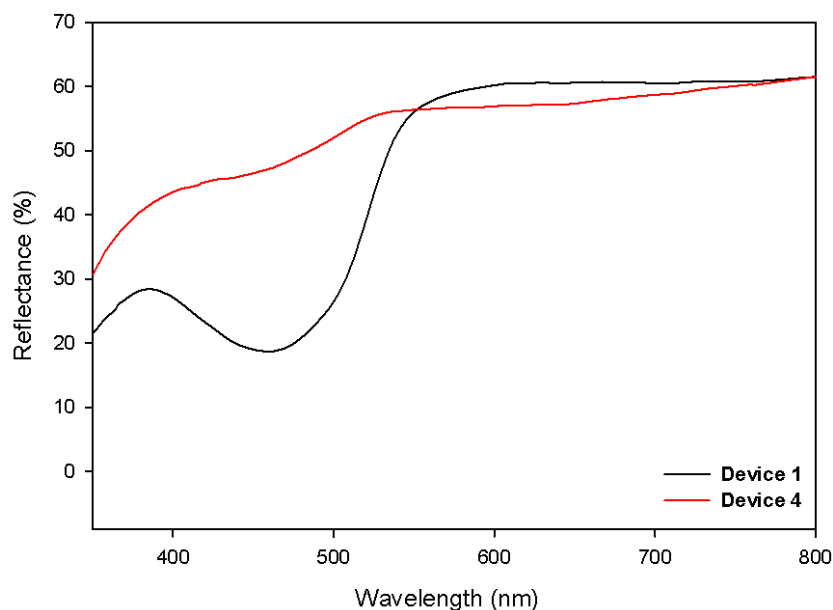
Device	Material	Thickness (nm)	Abs. ^a	Reflec. ^b (%)	J_{SC} (mA/cm^2)	V_{OC} (V)	FF (%)	PCE (%)
1	1	232	NA	40	2.26	0.90	35.0	0.71
2	1	146	0.451	NA	1.77	0.54	30.5	0.29
3	1	63	0.181	NA	2.15	0.05	25.5	0.03
4	NP-1	124	NA	10	0.89	0.93	32.5	0.27
5	NP-1	141	0.243	NA	0.44	0.76	28.0	0.09
6	NP-1	101	0.130	NA	0.70	0.41	29.8	0.09

^a Light absorption in the active layer given as the peak absorption in the range 400–530 nm;

^b Reflectance of the device given as the drop in reflectance for approx. 600 nm to 470 nm.

The reflectance (Figure 7) for **Device 1** drops from 60% to approximately 20% at the wavelength where **1** absorbs (400–530 nm), whereas the reflection for **Device 4** only drops from 55% to around 45%. This large difference in reflectance could be the main reason for the poorer J_{SC} for **Device 4** in comparison with **Device 1**. To further determine which influence the introduction of silicon nano-particles have on the OPV devices, another batch of devices were prepared with the aim of creating active layers with similar absorption in the range of 400–530 nm.

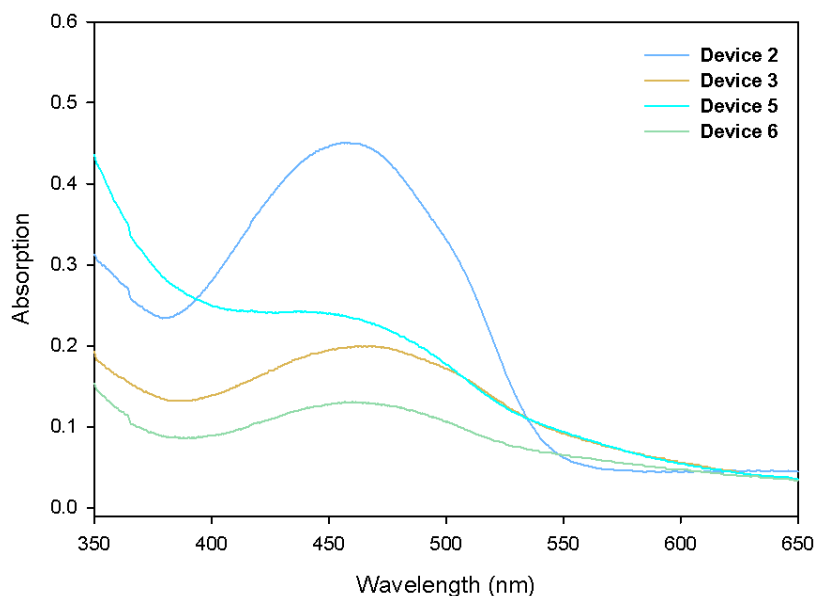
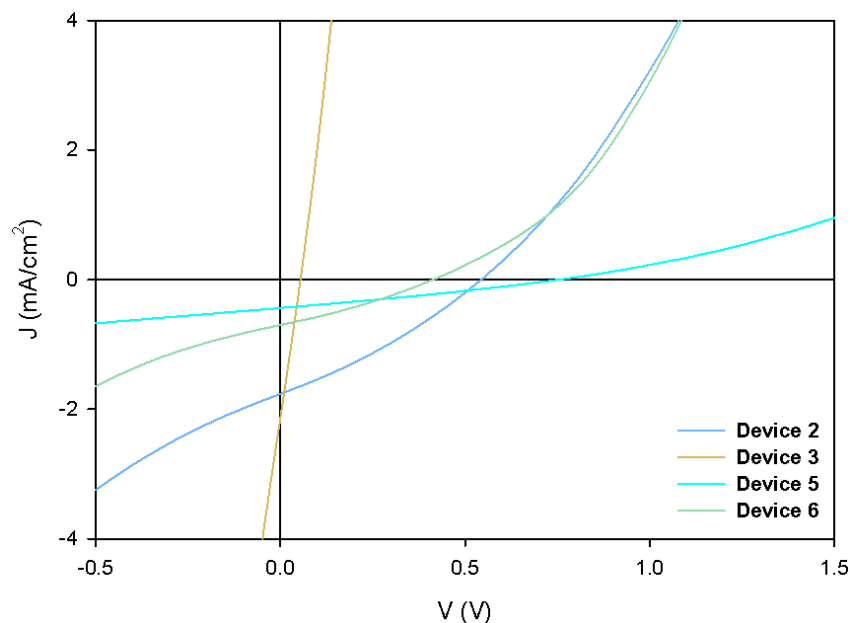
Figure 7. Reflection spectra of **Device 1** and **Device 4**.



The absorption curves of the active layers and the I-V curves for these devices can be found in Supporting Information. The data is summarized in Table 1.

For the absolute absorptions, as illustrated in Figure 8 and summarized in Table 1, it is seen that **Device 5**, **Device 6**, and **Device 3** to a large extent have comparable absolute absorptions and only a small difference is observed: **Device 6** < **Device 3** < **Device 5**. In addition to these observations the position of the peak absorption between 400 and 600 nm are as for the solution still very similar (Figure 8). The phenomena was reported by Senkovskyy *et al.* [10] who ascribe it to an effect of grafting on small nano-particles which leads to distant organic chains thereby allowing them to have a similar behavior as “free” molecules.

The I-V curves (shown in Figure 9 and summarized in Table 1) obtained from the device prepared with the absorptions from Figure 8, display a device prepared with **1** (**Device 2**) as the champion device, whereas **Device 5** and **Device 6** despite the difference in absorption have very similar performance. **Device 3** is very poorly performing; this is ascribed to shorts in the very thin active layer (63 nm).

Figure 8. The absorption for the active layers in **Devices 2, 3, 5, and 6.****Figure 9.** I-V curves for the **Devices 2, 3, 5, and 6.**

Another parameter for comparison between the fabricated devices is the thickness of the active layer. From Table 1 it can be found that **Device 2** based on **1** and **Device 5** based on **NP-1** have very similar thicknesses with 146 and 141 nm, respectively. Although the device thicknesses are very similar the rest of the device characteristics are very different; the absolute absorption for **Device 2** is almost twice the absorption of **Device 5** and the PCE of 0.29% is about three times as high as for **Device 5** which is mainly ascribed to a larger J_{SC} . This would perhaps be less pronounced if the silicon nano-particles had a size in the range of 15–20 nm, which could increase the maximum wavelength at which they absorb.

Previously it has been reported that Si nano-particles have a strong tendency to undergo oxidation when exposed to ambient air [23]. This oxidation would lead to undesirable properties or a least

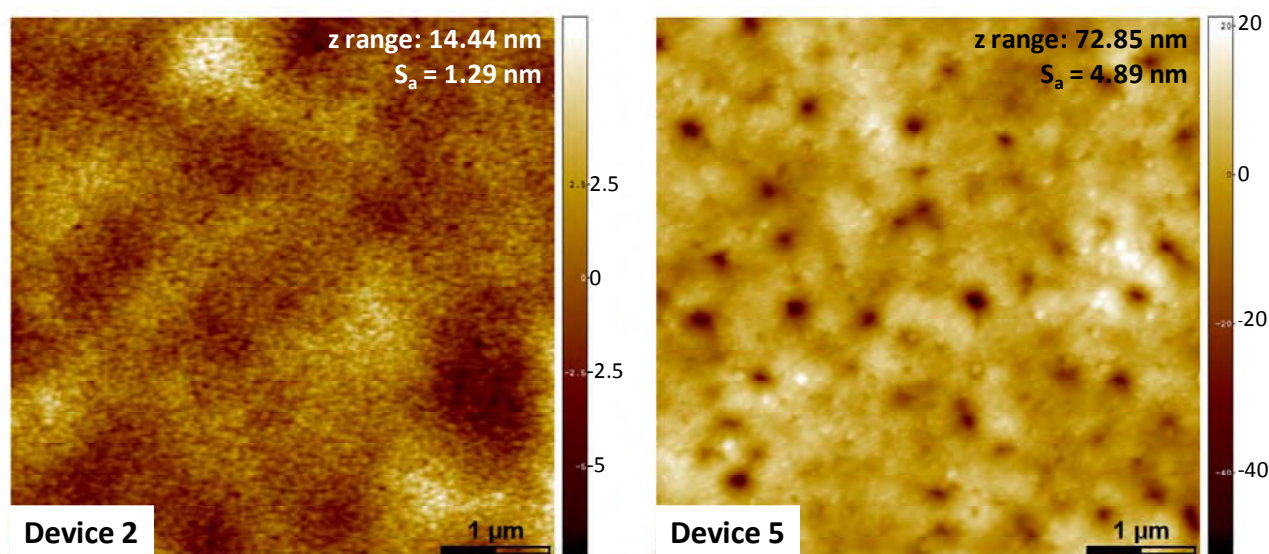
decrease the desired properties of the nano-particles. As an example, an insulating SiO₂ layer can be formed on the surface of the nano-particle [24]. Such an oxidation could be an additional explanation for the poorer performance of the devices containing Si nano-particles.

The I-V curves from the devices prepared with **2** or **NP-2** and [60]PCBM showed no or very little photovoltaic properties (see Supporting Information, Figure S3); the best performing device was **NP-2** annealed with a PCE of 0.001%.

3.3.1. Morphology of Active Layers

The AFM topography images of the active layers in **Device 2** and **Device 5** are shown in Figure 10. The images illustrate almost two different morphologies. **Device 2** seems to have a more homogeneous (smooth) surface with naturally occurring surface roughness containing no high peaks or pinholes. By comparison, the active layer in **Device 5** is covered with pinholes, which greatly affect the resulting surface morphology. The formation of pinholes could be one of the explanations as to why the devices containing **NP-1** perform poorly in comparison with the devices containing **1**.

Figure 10. AFM topography images of the active layers of **Device 2** and **Device 5** with their respective height difference (z range) and the calculated surface roughness (S_a). The imaging was conducted on the active layer of the fully assembled devices.



4. Conclusions

Silicon nano-particles grafted with two different organic conjugated oligomers were prepared and the nano-particles were investigated by AFM and NMR to verify the creation of nano-particles and the grafting of oligomers. AFM analysis showed nano-particles with sizes in the range of 5–10 nm for **NP-1** and in the range 4–15 nm for **NP-2**. NMR analysis showed a loss of the phenol-signal for **NP-1**, which shows successful grafting for **1**, for **NP-2** a significant broadening in the signal of the aromatic proton occurred which comes from the greater immobility after grafting. Photovoltaic devices were prepared with [60]PCBM. Devices containing nano-particles with compound **1** grafted on (**NP-1**)

yielded a power conversion efficiency of 0.27%, which is significantly lower than for the non grafted **1** (PCE 0.71%). However, reflection studies of the active layers showed an absorption in the active layer of the devices prepared with **NP-1**, which were much lower than for devices prepared with **1**. Another set of cells were prepared with similar absorption of **1** and **NP-1** in the active layer. Here the cells containing silicon nano-particles were still poorer performing. The devices prepared with 3,8-didodecylquaterthiophene (**2**) as the grafted oligomer and [60]PCBM showed very little photovoltaic properties after annealing whereas the devices prepared with **2** and [60]PCBM show no photovoltaic properties.

In this paper we have described a method to control the morphology of the active layer in an OPV device by grafting silicon nano-particles with different oligomers. There is, however, some drawbacks to this method, *i.e.*, it is very difficult to purify the grafted nano-particles and there is a great loss of material during this purification due to aggregation and adsorption to glassware. The devices prepared from the nano-particles showed a decrease in the photovoltaic performance compared to devices prepared with non-grafted oligomer. This drop in performance could be due to the formation of pinholes within the nano-particle film, even with relative thick films (141 nm). Furthermore, the drop in performance could be due to oxidation of the nano-particles surface, which could be overcome by carrying out the synthesis, fabrication, and measurements in a glove box.

Acknowledgments

This work was financially supported by the Danish National Research Foundation (DNRF) and the National Natural Science Foundation of China (NSFC) (Grants 50990063 and 51011130028). We would also like to gratefully acknowledge support from the DNRF and the NSFC for the Danish-Chinese Center for Organic based Photovoltaic Cells, within which this work was performed.

References

1. Helgesen, M.; Søndergaard, R.; Krebs, F.C. Advanced materials and processes for polymer solar cell devices. *J. Mater. Chem.* **2010**, *20*, 36–60.
2. Cai, W.; Gong, X.; Cao, Y. Polymer solar cells: Recent development and possible routes for improvement in the performance. *Sol. Energy Mater. Sol. Cells* **2010**, *94*, 114–127.
3. Dennler, G.; Scharber, M.C.; Brabec, C.J. Polymer-fullerene bulk-heterojunction solar cells. *Adv. Mater.* **2009**, *21*, 1323–1338.
4. Peet, J.; Senatore, M.L.; Heeger, A.J.; Bazan, G.C. The role of processing in the fabrication and optimization of plastic solar cells. *Adv. Mater.* **2009**, *21*, 1521–1527.
5. Yang, X.; Loos, J. Toward high-performance polymer solar cells: The importance of morphology control. *Macromolecules* **2007**, *40*, 1353–1362.
6. Bertho, S.; Janssen, G.; Cleij, T.J.; Conings, B.; Moons, W.; Gadisa, A.; D'Haen, J.; Goovaerts, E.; Lutsen, L.; Manca, J.; Vanderzande, D. Effect of temperature on the morphological and photovoltaic stability of bulk heterojunction polymer:fullerene solar cells. *Sol. Energy Mater. Sol. Cells* **2008**, *92*, 753–760.

7. Paci, B.; Generosi, A.; Albertini, V.R.; Generosi, R.; Perfetti, P.; de Bettignies, R.; Sentin, C. Time-resolved morphological study of bulk heterojunction films for efficient organic solar devices. *J. Phys. Chem. C* **2008**, *112*, 9931–9936.
8. Griffini, G.; Douglas, J.D.; Piliago, C.; Holcombe, T.W.; Turri, S.; Fréchet, J.M.J.; Mynar, J.L. Long-term thermal stability of high-efficiency polymer solar cells based on photocrosslinkable donor-acceptor conjugated polymers. *Adv. Mater.* **2011**, *23*, 1660–1664.
9. Drees, M.; Hoppe, H.; Winder, C.; Neugebauer, H.; Sariciftci, N.S.; Schwinger, W.; Schäffler, F.; Topf, C.; Scharber, M.C.; Zhu, Z.; Gaudiana, R. Stabilization of the nanomorphology of polymer–fullerene “bulk heterojunction” blends using a novel polymerizable fullerene derivative. *J. Mater. Chem.* **2005**, *15*, 5158–5163.
10. Senkovskyy, V.; Tkachov, R.; Beryozkina, T.; Komber, H.; Oertel, U.; Horecha, M.; Bocharova, V.; Stamm, M.; Gevorgyan, S.A.; Krebs, F.C.; Kiriy, A. “Hairy” poly(3-hexylthiophene) particles prepared via surface-initiated kumada catalyst-transfer polycondensation. *J. Am. Chem. Soc.* **2009**, *131*, 16445–16453.
11. Krebs, F.C.; Senkovskyy, V.; Kiriy, A. Preorganization of nanostructured inks for roll-to-roll coated polymer solar cells. *IEEE J. Sel. Topics Quant. Electron.* **2010**, *16*, 1821–1826.
12. Tkachov, R.; Senkovskyy, V.; Horecha, M.; Oertel, U.; Stamm, M.; Kiriy, A. Surface-initiated Kumada catalyst-transfer polycondensation of poly(9,9-dioctylfluorene) from organosilica particles: Chain-confinement promoted b-phase formation. *Chem. Commun.* **2010**, *46*, 1425–1427.
13. Gupta, D.; Mukhopadhyay, S.; Narayan, K.S. Fill factor in organic solar cells. *Sol. Energy Mater. Sol. Cells* **2010**, *94*, 1309–1313.
14. Meier, C.; Gondorf, A.; Lüttjohann, S.; Lorke, A.; Wiggers, H. Silicon nanoparticles: Absorption, emission, and the nature of the electronic bandgap. *J. Appl. Phys.* **2007**, *101*, 103–112.
15. Søndergaard, R.; Strobel, S.; Bundgaard, E.; Norrman, K.; Hansen, A.G.; Albert, E.; Csaba, G.; Lugli, P.; Tornow, M.; Krebs, F.C. Conjugated 12 nm long oligomers as molecular wires in nanoelectronics. *J. Mater. Chem.* **2009**, *19*, 3899–3908.
16. Horcas, I.; Fernandez, R.; Gomez-Rodriguez, J.M.; Colchero, J.; Gomez-Herrero, J.; Baro, A.M. WSXM: A software for scanning probe microscopy and a tool for nanotechnology. *Rev. Sci. Instrum.* **2007**, *78*, 013705:1–013705:8.
17. Baldwin, R.K.; Pettigrew, K.A.; Garno, J.C.; Power, P.P.; Liu, G.-y.; Kauzlarich, S.M. Room temperature solution synthesis of alkyl-capped tetrahedral shaped silicon nanocrystals. *J. Am. Chem. Soc.* **2002**, *124*, 1150–1151.
18. Baldwin, R.K.; Pettigrew, K.A.; Ratai, E.; Augustine, M.P.; Kauzlarich, S.M. Solution reduction synthesis of surface stabilized silicon nanoparticles. *Chem. Commun.* **2002**, 1822–1823.
19. Lee, J.-L.; Kung, M.C.; Trahey, L.; Missaghi, M.N.; Kung, H.H. Nanocomposites derived from phenol-functionalized Si nanoparticles for high performance lithium ion battery anodes. *Chem. Mater.* **2009**, *21*, 6–8.
20. Chen, L.; Pan, X.; Zheng, D.; Gao, Y.; Jiang, X.; Xu, M.; Chen, H. Hybrid solar cells based on P3HT and Si@MWCNT nanocomposite. *Nanotechnology* **2010**, *21*, 345201–345211.
21. Ruckenstein, E.; Li, Z.F. Surface modification and functionalization through the self-assembled monolayer and graft polymerization. *Adv. Colloid Interface Sci.* **2005**, *113*, 43–63.

22. Andersen, T.R.; Larsen-Olsen, T.T.; Andreasen, B.; Böttiger, A.P.L.; Carlé, J.E.; Helgesen, M.; Bundgaard, E.; Norrman, K.; Andreasen, J.W.; Jørgensen, M.; Krebs, F.C. Aqueous processing of low-band-gap polymer solar cells using roll-to-roll methods. *ACS Nano* **2011**, *5*, 4188–4196.
23. Nelles, J.; Sendor, D.; Ebbers, A.; Petrat, F.M.; Wiggers, H.; Schultz, C.; Simon, U. Functionalization of silicon nanoparticles via hydrosilylation with 1-alkenes. *Colloid Polym. Sci.* **2007**, *285*, 729–736.
24. Hirschman, K.D.; Tsybeskov, L.; Duttagupta, S.P.; Fauchet, P.M.; Silicon-based visible light-emitting devices integrated into microelectronic circuits. *Lett. Nat.* **1996**, *384*, 338–341.

Supporting Information

Synthesis

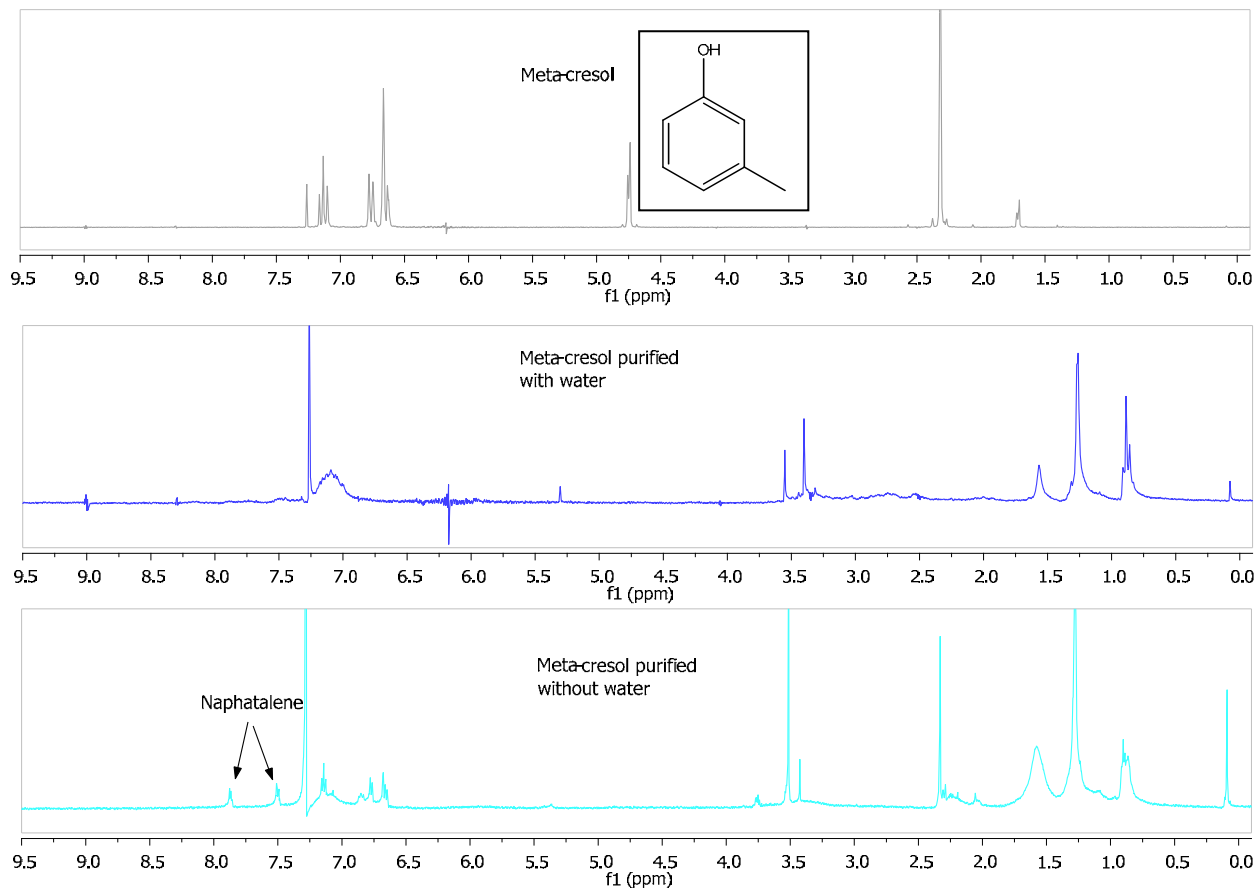
A small test was made where meta-cresol was grafted onto silicon nanoparticles to investigate the grafting and the following purification. The synthesis method was:

To a solution of naphthalene (0.35 g, 2.7 mmol) in dry glyme (5 mL) sodium (0.1 g, 4.3 mmol) was added and the mixture was stirred for 3 hours after which a black yellowish solution of sodium naphthalide was obtained. This solution was added to a solution of SiCl₄ (99.9%, 0.08 mL, 0.7 mmol) in dry glyme (30 mL) and stirred for 30 min. The organic grafting agent (0.19 mL, 1.78 mmol) was added and stirring continued for 2 hours.

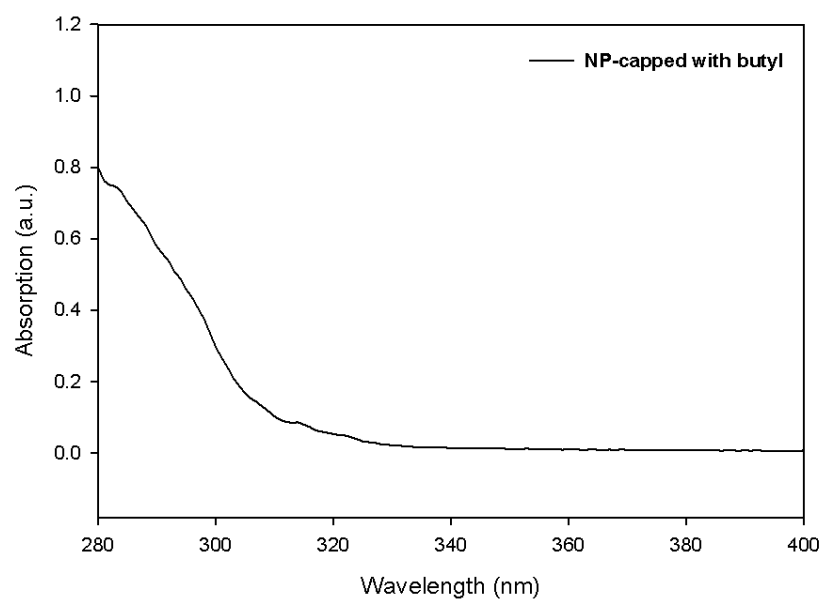
From this point on two different methods of purification was applied.

1. The solvent was removed under reduced pressure; the residue was dissolved in heptane and washed with water. The organic phases were collected and the solvent was removed under reduced pressure, the residue was heated to 90 °C to remove residual naphthalene and meta-cresol resulting in a yellowish solid.
2. The solvent was removed under reduced pressure. When all the solvent was removed the temperature was increased to 90 °C to remove residual naphthalene and meta-cresol resulting in a yellowish solid.

NMR Spectra

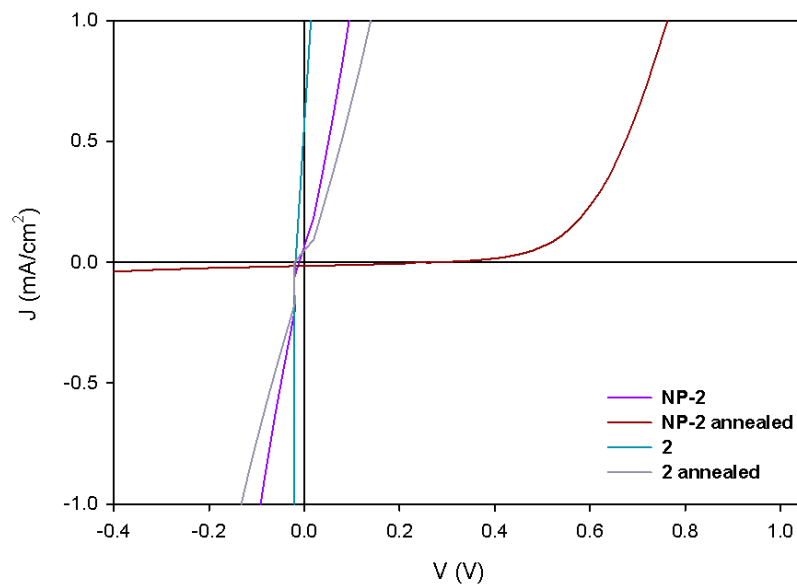
Figure S1. NMR-spectra of meta-cresol and the two different way of purification with and without water.

UV-Vis

Figure S2: Absorption spectra of Silicon nano-particles capped with butyl in hexane.

IV-Curves

Figure S3. I-V curves of unannealed and annealed devices prepared with **2** and **NP2** with [60]PCBM.



© 2012 by the authors; licensee MDPI, Basel, Switzerland. This article is an open access article distributed under the terms and conditions of the Creative Commons Attribution license (<http://creativecommons.org/licenses/by/3.0/>).



Synthesis and characterization of new electron-withdrawing moiety thieno[2,3-c]pyrrole-4,6-dione-based molecules for small molecule solar cells

Lei Fu^a, Hongbin Pan^a, Thue T. Larsen-Olsen^b, Thomas R. Andersen^b, Eva Bundgaard^b, Frederik C. Krebs^{b,**}, Hong-Zheng Chen^{a,*}

^a MOE Key Laboratory of Macromolecular Synthesis and Functionalization, State Key Lab of Silicon Materials, & Department of Polymer Science and Engineering, Zhejiang University, Hangzhou 310027, PR China

^b Department for Energy Conversion and Storage, Technical University of Denmark, DK-4000 Roskilde, Denmark

ARTICLE INFO

Article history:

Received 1 November 2012

Received in revised form

11 December 2012

Accepted 12 December 2012

Available online 19 December 2012

Keywords:

Conjugated small molecules

Thieno[2,3-c]pyrrole-4,6-dione

New electron-withdrawing moiety

Solution processability

Organic solar cells

Power conversion efficiency

ABSTRACT

New conjugated small molecules 5,5'-bis[5-Octyl-2-(2,2'-bithiophen-5-yl)-4H-thieno[2,3-c]pyrrole-4,6-dione]-3,3'-di-octylsilylene-2,2'-bithiophene **DTS(BTTPD)₂** and 5,5'-bis[5-Octyl-2-(2,5-thiophenyl)-4H-thieno[2,3-c]pyrrole-4,6-dione]-3,3'-di-octylsilylene-2,2'-bithiophene **DTS(TTPD)₂** of the acceptor- π -donor- π -acceptor type end-capped with thieno[2,3-c]pyrrole-4,6-dione (**TPD**) units for small molecule solar cells have been prepared through coupling of dithienosilole and **TPD** units bridged with thienylene and bithienylene. They are soluble in common organic solvents and show an interesting absorption. These small molecules have very similar optical band gaps (1.87 eV and 1.92 eV) and fairly close highest occupied molecular orbital energy levels (-5.52 to -5.55 eV). The best solar cells using **DTS(TTPD)₂** as an electron donor and [6,6]-phenyl-C61-butyric acid methyl ester (PC₆₁BM) as an electron acceptor demonstrated efficient performance with an obviously high open-circuit voltage (V_{OC}) of 0.97 V and a power conversion efficiency of 1.20% after annealing and using MoO₃ as electron-blocking layer. The solar cells based on **DTS(BTTPD)₂** and PC₆₁BM blend also exhibited a high V_{OC} of 0.97 V under optimized conditions.

© 2012 Elsevier Ltd. All rights reserved.

1. Introduction

Organic photovoltaic (OPV) cells have become a promising alternative technology for producing clean and renewable energy due to their unique advantages, such as low-cost, simple manufacturing process and light weight. Compared with silicon-based inorganic solar cells, OPVs possess huge commercial potential for large-scale flexible applications, for example, roll-to-roll printing [1–3]. Bulk heterojunction (BHJ) architecture based on the blends of electron donor and electron acceptor materials (such as [6,6]-phenyl-C61-butyric acid methyl ester (PCBM) and other fullerene derivative) has demonstrated its large potential for fabricating efficient OPV devices. The efficiencies are approaching 10% which have been reported by different methods, e.g. designing of novel materials, or optimizing the device structure and techniques [4–11]. Recently, the power conversion efficiency (PCE) of the push–pull (D–A) electron-

donating conjugated polymer has reached an efficiency of 8.3% by using conjugated polyelectrolyte as an n-type interface layer for devices based on the thieno[3,4-b] thiophene/benzodithiophene (TT–BDT) copolymer [6]. Although the efficiency of small molecule photovoltaics (PV) has remained below that of polymer PV because of the less ideal film quality and crystallization, solution-processed small molecule PV demonstrates some advantages over conjugated polymers, such as easy synthesis and purification, well-defined structures, no end group contaminants, high charge carrier mobility, and further the small molecules differ less from batch to batch [12–14]. Recently, a lot of improvements in the performance of small molecule PV have been reported with PCE above 5% [13,15,16]. Heeger et al. has reported efficient solution-processed small molecule PV based on 5,5'-bis[(4-(7-hexylthiophen-2-yl)thiophen-2-yl)-[1,2,5]thiadiazolo[3,4-c]pyridine]-3,3'-di-2-ethylhexylsilylene-2,2'-bithiophene, (**DTS(PTTh₂)₂**) with a PCE of 6.7% [13]. Another donor material based on **DERHD7H** was synthesized by Chen et al. with an OPV performance of 6.1% [17].

In this paper we synthesized a type of solution-processed small molecule donor materials based on new electron-withdrawing

* Corresponding author. Tel.: +86 571 87952557; fax: +86 571 87953733.

** Corresponding author. Tel.: +45 46774799; fax: +45 46774791.

E-mail addresses: frkr@dtu.dk (F.C. Krebs), hzchen@zju.edu.cn (H.-Z. Chen).

moiety thieno[2,3-c]pyrrole-4,6-dione (**TPD**): 5,5'-bis[5-Octyl-2-(2,2'-bithiophen-5-yl)-4H-thieno[2,3-c]pyrrole-4,6-dione]-3,3'-di-octylsilylene-2,2'-bithiophene, **DTS(BTTPD)₂** and 5,5'-bis[5-Octyl-2-(2,5-thiophenyl)-4H-thieno[2,3-c]pyrrole-4,6-dione]-3,3'-di-octylsilylene-2,2'-bithiophene **DTS(TTPD)₂** (shown in Scheme 1), and studied the PV devices with these small molecules. The molecular structures are based on acceptor- π -donor- π -acceptor (A- π -D- π -A) framework. The imide moiety from **TPD** is a simple and common electron-withdrawing substituent which can be easily modified to improve the solubility and efficiently lower the HOMO (Highest Occupied Molecular Orbital) of materials while maintaining or reducing band gap [18]; On account of only one relatively active position for substitution or coupling, **TPD** can end-cap the main conjugated chain of molecules, which is helpful to improve the stability of the small molecule material. The donor core dithienosilole (**DTS**) shows great electron-donating ability with a low-lying LUMO (Lowest Unoccupied Molecular Orbital), because the σ^* -orbital of the silicon carbon bond effectively interacts with the π^* -orbital of the butadiene fragment. Therefore, this new electron-withdrawing moiety was applied in our design of small molecule solar cells, the donor core **DTS** and acceptor moiety **TPD** are linked by bithienylene or thienylene as π -conjugated bridges, where holes of molecules may locate to make a good stability [19]. D- π -A molecular structure has emerged photo-induced intramolecular charge transfer properties and low band gap. This extended π -conjugated system makes a good planarity and efficient π - π interaction, which improve thin film forming quality [20,21].

2. Experimental

2.1. Materials and instrument

All reagents and solvents were purchased from Aldrich and used without further purification. Dichloromethane, tetrahydrofuran (THF) and toluene were dried with molecular sieves (3 Å) and used directly without filtration or distillation. 4,4'-Bis(*n*-octyl)-5,5'-bis(trimethyltin)-dithieno[3,2-b:2',3'-d]silole, 2-trimethylstannylthiophene, 5-trimethylstannyl-2,2'-bithiophene were prepared as the

reported methods [22,23]. NMR spectra were obtained on Bruker 500 MHz and 300 MHz spectrometers. Thermogravimetric analysis (TGA) and differential scanning calorimetry (DSC) were conducted on TA SDT 2960 Simultaneous DSC-TGA at the heating rate of 30 °C min⁻¹ under N₂. Absorption spectra were taken on a Varian CARY Bio spectrophotometer. Cyclic voltammetry (CV) was performed on a CHI600A electrochemical workstation with Pt disk coated by a film, Pt plate, and saturated calomel electrode (SCE) as the working electrode, counter electrode, and reference electrode, respectively, in a 0.1 mol/L tetrabutylammonium hexafluorophosphate (Bu₄NPF₆) acetonitrile solution. The film on the working electrode was formed by casting the solution of materials in chloroform (~1 mg/mL).

2.2. Synthesis

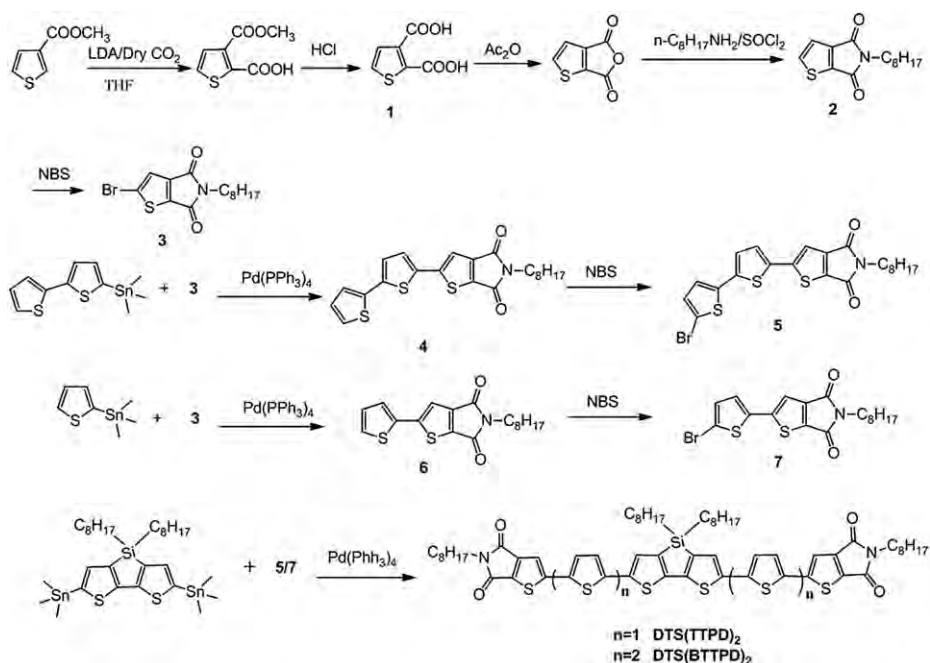
2.2.1. Thiophene-2,3-dicarboxylic acid (**1**)

Dry THF (10 ml) was cooled to -10 °C under argon followed by addition of 10 ml *n*-butyllithium (1.6 M in hexane). Then a solution of diisopropylamine (2.4 ml) and dry THF (7.6 ml) was added slowly and the reaction mixture was stirred for 30 min. The freshly prepared solution of lithium diisopropylamine (18.64 ml, 9.8 mmol) was added slowly to a cooled solution (-78 °C) of methyl thiophene-3-carboxylate (1.0 g, 7.01 mmol) in dry THF (20 ml). The reaction mixture was stirred for 1 h at -78 °C under argon followed by addition of excess dry ice. The formation of a white precipitate was immediately observed. The suspension was stirred for additional 30 min at -78 °C, and was afterward allowed to reach room temperature. The reaction was quenched with distilled water (5 ml), the organic phase was extracted by an aqueous phase of 10% NaOH (3*50 ml). Subsequently, HCl solution (6 M) was added and the formed precipitate was collected by filtration. Recrystallized from EtOH (50 ml) and H₂O (200 ml), dried under vacuum to give a light yellow powder of the title product (0.54 g, 41%).

¹H NMR (500 MHz, d-DMSO): δ 7.89 (d, *J* = 5.2 Hz, 1H), 7.71 (d, *J* = 5.2 Hz, 1H).

¹³C NMR (125 MHz, d-DMSO): δ 159.5, 158.7, 147.4, 145.4, 143.2, 123.3.

Mp 147 °C.



Scheme 1. Synthetic route toward **DTS(BTTPD)₂** and **DTS(TTPD)₂**.

2.2.2. 5-Octyl-4H-thieno[2,3-c]pyrrole-4,6-dione (2)

A solution of **1** (1.96 g, 11.38 mmol) in acetic anhydride (50 ml) was stirred at 140 °C overnight. The solvent was removed under reduced pressure and the crude product was used for the next step without any further purification. The brown solid was dissolved in toluene (50 ml), then 1.5 equiv of n-octylamine (2.82 ml, 17.07 mmol) was added and the mixture was refluxed for 24 h. The reaction mixture was cooled to room temperature and the solvent was removed under reduced pressure. The crude solid was dissolved in thionyl chloride (50 ml) and the mixture was refluxed for 4 h. After removal of the volatiles, the crude product was purified by column chromatography using dichloromethane as the eluent to afford the title product as dark yellow oil (2.28 g, 75%).

¹H NMR (500 MHz, CDCl₃): δ 7.76 (d, *J* = 4.7 Hz, 1H), 7.32 (d, *J* = 4.7 Hz, 1H), 3.64–3.58 (t, 2H), 1.71–1.61 (m, 2H), 1.40–1.20 (m, 10H), 0.96–0.83 (m, 3H).

¹³C NMR (125 MHz, CDCl₃): δ 163.8, 162.7, 144.6, 140.7, 137.2, 120.9, 39.2, 31.9, 30.7, 29.6, 26.7, 22.7, 19.9, 13.5.

2.2.3. 2-Bromo-5-octyl-4H-thieno[2,3-c]pyrrole-4,6-dione (3)

Compound **2** (1.14 g, 4.29 mmol) was dissolved in 40 ml of a 1:3 mixture of concentrated sulfuric acid and trifluoroacetic acid. NBS (0.92 g, 5.16 mmol) was added and the mixture was stirred at room temperature overnight. The dark brown solution was quenched with 100 ml of ice water, and extracted with dichloromethane. The organic phase was dried over anhydrous magnesium sulfate, filtered, and evaporated to afford the crude product as a brown oil. Purification by column chromatography using silica gel and petroleum ether/dichloromethane (1:2) as eluent gave **3** (1.05 g, 80%) as an off-white solid.

¹H NMR (500 MHz, CDCl₃): δ 7.29 (s, 1 H), 3.57 (t, 2 H), 1.6 (m, 2H), 1.33 (m, 10H), 0.92 (t, 3H).

¹³C NMR (125 MHz, CDCl₃): δ 162.9, 161.9, 143.8, 140.4, 125.3, 123.7, 39.2, 31.9, 30.2, 29.3, 29.0, 26.7, 22.7, 14.1.

Mp 61 °C.

2.2.4. 5-Octyl-2-(2,2'-bithiophen-5-yl)-4H-thieno[2,3-c]pyrrole-4,6-dione (4)

Compound **3** (0.67 g, 1.95 mmol) and 5-trimethylstannyl-2,2'-bithiophene (1.28 g, 3.90 mmol) were dissolved in toluene (20 ml). The solution was degassed with argon for 10 min, and Pd(PPh₃)₄ (112 mg, 5 mol% with respect to compound **3**) was added into the flask. The solution was degassed for 15 min. After which, the solution was heated to 110 °C under argon and stirred for 24 h. The solvent was removed under vacuum and the crude product was purified by flash chromatography on silica gel using a solution of hexane/CH₂Cl₂ (1:3) as the eluent, resulting in a yellow powder of **4** (0.56 g, 67%).

¹H NMR (500 MHz, CDCl₃): δ 7.33 (s, 1H), 7.31 (d, *J* = 1.1 Hz, 1H), 7.30 (d, *J* = 1.1 Hz, 1H), 7.27–7.25 (m, 2H), 7.15 (d, *J* = 3.9 Hz, 1H), 7.08 (dd, *J* = 5.1, 3.6 Hz, 2H), 3.64–3.60 (m, 3H), 1.66 (s, 4H), 1.40–1.22 (m, 28H), 0.94–0.85 (m, 11H).

¹³C NMR (125 MHz, CDCl₃): δ 163.9, 162.8, 149.8, 145.2, 139.4, 137.1, 136.1, 133.5, 130.7, 128.1, 128.0, 126.7, 125.5, 124.6, 38.6, 31.8, 31.6, 29.1, 28.6, 25.6, 22.6, 14.1.

Mp 156 °C.

2.2.5. 5-Octyl-2-(5-bromo-2,2'-bithiophen-5'-yl)-4H-thieno[2,3-c]pyrrole-4,6-dione (5)

Compound **4** (0.84 g, 1.95 mmol) was dissolved in 20 ml of a 1:1 mixture of dichloromethane and acetic acid solution. NBS (0.34 g, 1.95 mmol) was then added in darkness, and the reaction mixture was stirred at room temperature overnight. The yellow solution was quenched with 10 ml water, extracted with dichloromethane, washed with 10% aq. NaHCO₃ and water. The organic phase was dried over

anhydrous sodium sulfate and evaporated to afford **5** as a dark yellow solid (0.965 g, 99%), which was used without further purification.

¹H NMR (500 MHz, CDCl₃): δ 7.32 (s, 1H), 7.24 (d, *J* = 3.9 Hz, 1H), 7.09 (d, *J* = 3.8 Hz, 1H), 7.03 (d, *J* = 3.9 Hz, 1H), 6.99 (d, *J* = 3.9 Hz, 1H), 3.64–3.59 (t, 2H), 1.70–1.62 (m, 2H), 1.41–1.23 (m, 10H), 0.93–0.85 (m, 3H).

¹³C NMR (125 MHz, CDCl₃): δ 163.9, 162.7, 149.4, 145.2, 138.1, 137.7, 137.4, 133.9, 131.0, 126.8, 124.8, 124.5, 114.6, 112.7, 38.6, 31.8, 31.6, 29.1, 28.6, 25.6, 22.6, 14.1.

Mp 153 °C.

2.2.6. 5-Octyl-2-(5-bromothiophen-2-yl)-4H-thieno[2,3-c]pyrrole-4,6-dione (7)

Compound **7** was synthesized as the procedure of Compound **5**, resulting in a bright yellow powder.

¹H NMR (500 MHz, CDCl₃): δ 7.32 (s, 1H), 7.24 (d, *J* = 3.9 Hz, 1H), 7.09 (d, *J* = 3.8 Hz, 1H), 7.03 (d, *J* = 3.9 Hz, 1H), 6.99 (d, *J* = 3.9 Hz, 1H), 3.64–3.59 (t, 2H), 1.70–1.62 (m, 2H), 1.41–1.23 (m, 10H), 0.93–0.85 (m, 3H).

¹³C NMR (125 MHz, CDCl₃): δ 163.9, 162.7, 149.4, 145.2, 138.1, 137.7, 137.4, 133.9, 131.0, 126.8, 124.8, 124.5, 114.6, 112.7, 38.6, 31.8, 31.6, 29.1, 28.6, 25.6, 22.6, 14.1.

Mp 161 °C. Yield 61%.

2.2.7. 5,5'-bis[5-Octyl-2-(2,2'-bithiophen-5-yl)-4H-thieno[2,3-c]pyrrole-4,6-dione]-3,3'-di-octylsilylene-2,2'-bithiophene DTS(BTTPD)₂

Compound **5** (0.345 g, 0.68 mmol) and 4,4'-bis(n-octyl)-5,5'-bis(trimethyltin)-dithieno[3,2-b:2',3'-d]silole (0.22 g, 0.30 mmol) were dissolved in toluene (10 ml). The solution was degassed with argon for 10 min, and Pd(PPh₃)₄ (35 mg, 5 mol% with respect to dithienosilole (**DTS**)) was added into the flask. The solution was degassed again for 15 min. The solution was then heated to 110 °C under argon and stirred for 24 h. The solvent was removed under vacuum and the crude product was purified by flash chromatography on silica gel using dichloromethane as the eluent and the auto column (Combi-Flash Rf from TELEDYNE ISCO) using heptane/ethyl acetate (9:1) as eluent, leading to a dark red powder of the title product (210 mg, 42%).

¹H NMR (500 MHz, CDCl₃): δ 7.33 (s, 2H), 7.27 (d, *J* = 3.9 Hz, 2H), 7.18 (s, 2H), 7.17 (d, *J* = 3.8 Hz, 2H), 7.14 (d, *J* = 3.8 Hz, 2H), 7.11 (d, *J* = 3.8 Hz, 2H), 3.62 (t, *J* = 7.3 Hz, 4H), 1.67 (m, 4H), 1.44 (m, 4H), 1.38–1.17 (m, 12H), 1.01–0.94 (m, 6H), 0.89 (m, 6H).

¹³C NMR (125 MHz, CDCl₃): δ 163.92, 162.57, 149.97, 148.31, 145.11, 143.76, 139.15, 137.58, 136.75, 134.06, 133.25, 132.42, 131.07, 128.38, 126.51, 124.90, 124.08, 115.73, 48.44, 38.75, 33.06, 31.89, 31.73, 29.23, 29.15, 28.82, 26.83, 24.09, 22.70, 22.63, 14.07, 11.78.

Elem. Anal. Calcd. for C₆₈H₈₀N₂O₄S₈Si: C, 64.11; H, 6.33; N, 2.20. Found: C, 64.34; H, 6.21; N, 2.36.

Mp 263 °C.

2.2.8. 5,5'-bis[5-Octyl-2-(2,5-thiophenyl)-4H-thieno[2,3-c]pyrrole-4,6-dione]-3,3'-di-octylsilylene-2,2'-bithiophene DTS(TTPD)₂

Compound **5** was synthesized as the procedure of **DTS(BTTPD)**₂. ¹H NMR (300 MHz, CDCl₃): δ 7.29 (s, 2H), 7.24 (d, *J* = 3.9 Hz, 2H), 7.19 (s, 2H), 7.10 (d, *J* = 3.8 Hz, 2H), 3.64–3.55 (m, 4H), 1.64 (m, 4H), 1.51–1.04 (m, 12H), 0.91 (m, 12H).

¹³C NMR (75 MHz, CDCl₃): δ 164.22, 163.05, 150.13, 148.66, 145.52, 144.11, 139.64, 137.57, 137.41–136.92, 133.37, 127.80–127.36, 127.36–126.78, 124.63–123.84, 116.73–116.01, 39.00–38.70, 33.43–33.23, 32.04, 29.94, 29.40, 29.05, 27.05, 24.35, 22.86, 14.33, 12.21–11.71.

Elem. Anal. Calcd. for C₆₀H₇₆N₂O₄S₆Si: C, 64.94; H, 6.90; N, 2.52. Found: C, 65.08; H, 6.76; N, 2.78.

Mp 257 °C. Yield 35%.

2.3. Device fabrication

ITO/PEDOT:PSS/Donor molecule:PC₆₁BM/Al devices: the pre-fabricated glass substrates coated with a patterned ITO were first ultrasonically cleaned with water and 2-propanol. A filtered aqueous solution of poly(3,4-ethylenedioxythiophene): poly(styrenesulfonate) (PEDOT:PSS) (from Heraeus 4083) was spin-coated on top of the ITO at 3000 rpm. The substrates were further heated at 150 °C for 10 min before the active layer was spin-coated on top of the PEDOT:PSS layer. The aluminum electrode was applied by thermal evaporation at a pressure below 10⁻⁶ mBar.

ITO/MoO₃/Donor molecule:PC₆₁BM/Al devices: the pre-fabricated glass substrates coated with a patterned ITO were first ultrasonically cleaned with water and 2-propanol. MoO₃ was deposited on the substrates with the thickness of 10 nm in vacuum. Then the active layer was spin-coated on the MoO₃ layer. The aluminum electrode was applied by thermal evaporation at a pressure below 10⁻⁶ mBar.

The system was brought to atmospheric pressure and the devices were analyzed immediately after under AM1.5 100 mW/cm² sun in air using a Keithley 2400 source meter.

3. Results and discussion

3.1. Synthesis and characterization

The molecular structures are based on acceptor- π -donor- π -acceptor (A- π -D- π -A) framework. **DTS(BTTPD)₂** and **DTS(TTPD)₂** were synthesized through two steps of Stille coupling (Scheme 1). The donor core **DTS** shows great electron-donating ability, while the imide moiety from **TPD** is a simple and common electron-withdrawing substituent. Thieno[3,4-c]pyrrole-4,6-dione has been copolymerized with a lot of electron-donating units (such as benzodithiophene, dithienosilole and dithienopyrrole) showing low-lying HOMO energy level and high efficiency [7,24,25]. **TPD** shows a similar structure as thieno[3,4-c]pyrrole-4,6-dione coming with similar feature: an electron-withdrawing moiety, thus it can tune optoelectronic and morphologic properties [26]. Compound **2** was obtained by amidation of thiophene-2,3-dicarboxylic acid by three successive steps which is similar with 5-octylthieno[3,4-c]pyrrole-4,6-dione reported in literature [27]. Bromination of **TPD** in concentrated sulfuric acid and trifluoroacetic acid provided Compound **3** in 82% yield, which was firstly coupled with 5-trimethylstannyl-2,2'-bithiophene. The **DTS** moiety was obtained by cyclization between dichlorodioctylsilane and 5,5'-bis(trimethylsilyl)-2,2'-bithiophene treated with *n*-BuLi. The target molecule was obtained by another step of Stille coupling between **DTS** and Compound **5** or **6**. **DTS(BTTPD)₂** and **DTS(TTPD)₂** are soluble in common organic solvents, such as dichloromethane, chloroform, tetrahydrofuran, and toluene. The thermal properties of **DTS(BTTPD)₂** were investigated by thermogravimetric analysis (TGA) (Fig. 1). The materials exhibit good thermal stability, with the onsets decomposition temperature (*T_d*) at 258 °C and 315 °C under N₂ protection for **DTS(BTTPD)₂** and **DTS(TTPD)₂**, respectively.

3.2. Optical property

The UV-vis absorption spectra of these two materials in dilute chloroform solution and as film are shown in Fig. 2. Both **DTS(BTTPD)₂** and **DTS(TTPD)₂** exhibit broad and strong absorption bands in the visible region. **DTS(TTPD)₂** shows a maximum absorption peak (λ_{\max}) at 501 nm in chloroform solution while λ_{\max} of the solid film located at 521 nm. **DTS(BTTPD)₂** shows almost the same maximum absorption peak (λ_{\max}) at 500 nm

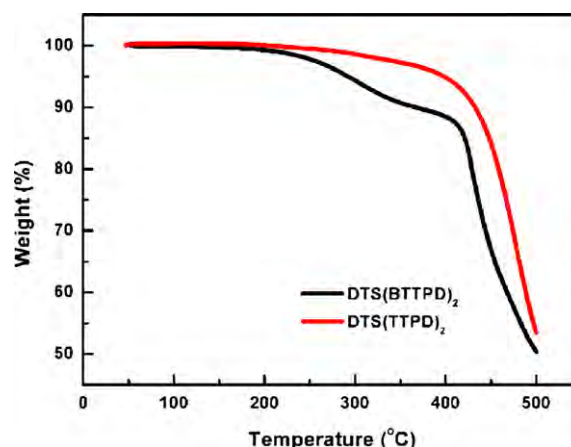


Fig. 1. TGA curves of **DTS(BTTPD)₂** and **DTS(TTPD)₂** (heating rate of 30 °C min⁻¹ under N₂).

as the **DTS(TTPD)₂** in chloroform solution. Compared to the solution, the absorption peaks of the fresh thin films are broadened and exhibit significant red-shift by 20 nm and 30 nm for **DTS(BTTPD)₂** and **DTS(TTPD)₂**, respectively, indicating good intermolecular interaction and that π - π stacking occurred in the solid state.

Interestingly, when the thin film of **DTS(BTTPD)₂** was placed for 2 min at the room temperature, the absorption maxima hypochromatic shifted to 511 nm, suggesting that H-aggregates might be formed in the solid state. Meanwhile, a sub shoulder peak appeared beside the maximum peak and another shoulder located at even longer wavelength, manifesting a vibronic progress due to a rigid coplanarization of the conjugated systems enforced by the crystal packing [28,29].

The absorption band-edges (λ_{onset}) of **DTS(BTTPD)₂** and **DTS(TTPD)₂** extended to 660 nm and 645 nm, and the optical band gap ($E_{\text{g}}^{\text{opt}}$) were calculated as 1.87 eV and 1.92 eV for **DTS(BTTPD)₂** and **DTS(TTPD)₂**, respectively. Because the delocalization of π -bridge bithienylene is slightly stronger than that of thienylene, the optical band gap of **DTS(BTTPD)₂** is lower than that of **DTS(TTPD)₂**. The relatively larger $E_{\text{g}}^{\text{opt}}$ of two molecules probably originated from TPD moiety, whose structure allowed relatively less tendency to adopt quinoid forms of TPD moiety through π -electron delocalization.

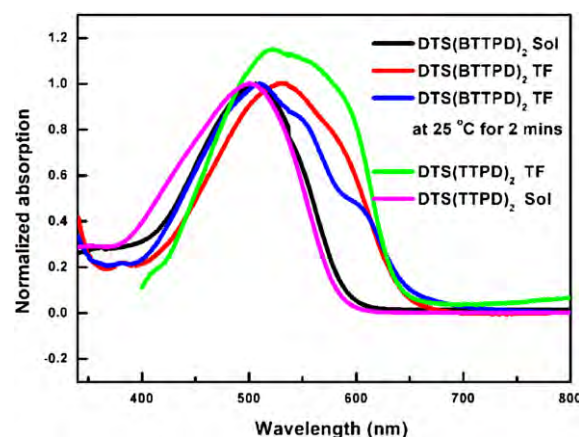


Fig. 2. UV-vis absorption spectra of **DTS(BTTPD)₂** and **DTS(TTPD)₂** in CHCl₃ solutions (Sol) and the thin films (TF).

3.3. Electrochemical property

The electrochemical properties of **DTS(BTTPD)₂** and **DTS(TTPD)₂** were investigated by cyclic voltammetry (CV). The CV curve was recorded versus the potential of SCE, which was calibrated by the ferrocene-ferrocenium (Fc/Fc⁺) redox couple (4.8 eV below the vacuum level). As shown in Fig. 3, the onset potential of oxidation wave (E_{ox}) of **DTS(BTTPD)₂** is 1.12 eV, which is similar as that of **DTS(TTPD)₂** (1.15 eV). The onset potential of reduction waves (E_{red}) are -0.83 eV and -0.96 eV for **DTS(BTTPD)₂** and **DTS(TTPD)₂**, respectively. From the empirical formulas $E_{HOMO} = -(E_{ox} + 4.4)$ eV and $E_{LUMO} = -(E_{red} + 4.4)$ eV, the HOMO and LUMO energy levels of **DTS(BTTPD)₂** can be calculated as -5.52 eV and -3.57 eV, respectively, while the HOMO and LUMO energy levels of **DTS(TTPD)₂** are -5.55 eV and -3.44 eV. Therefore, these two molecules possess similar electrochemical properties, which indicated that the different π -bridge units of thiophene and bithiophene can not strongly influence the bond length alternation (BLA) [1] due to the relatively neutral electron-withdrawing ability of thiophene and bithiophene. Compared with the HOMO and LUMO energy levels for PC₆₁BM, these compounds are suitable to be used as the photovoltaic donor materials.

3.4. Photovoltaic property

In order to investigate the photovoltaic property of **DTS(BTTPD)₂** and **DTS(TTPD)₂**, the bulk heterojunction solar cells were fabricated by using the two molecules as donor materials, and PC₆₁BM as the acceptor material. Tables 1 and 2 show the OPV performance of **DTS(BTTPD)₂** and **DTS(TTPD)₂** solar cells under the illumination of AM 1.5G solar irradiance (100 mW/cm²). The corresponding photovoltaic data, short-circuit current density (J_{sc}), open-circuit voltage (V_{oc}), fill-factor (FF) and power conversion efficiency (PCE) for the devices based on the two molecules and PC₆₁BM blends (2:3 by weight) with different spin-coating speeds are summarized in Table 1. It is found that the best PCE of both molecules was obtained with a spin-coating speed of 1500 rpm with the thickness about 90 nm, which indicated that controlling the thickness of the active layer is helpful to further study the OPV property of the two molecules.

Taking the above results as reference, the devices were fabricated with a spin-coating speed of 1500 rpm. The OPV performances of molecules blended with PC₆₁BM in different ratios are summarized in Table 2. It is found that most of the J_{sc} is improved as the content of PC₆₁BM increasing. As shown in Fig. 4, the best PCE of

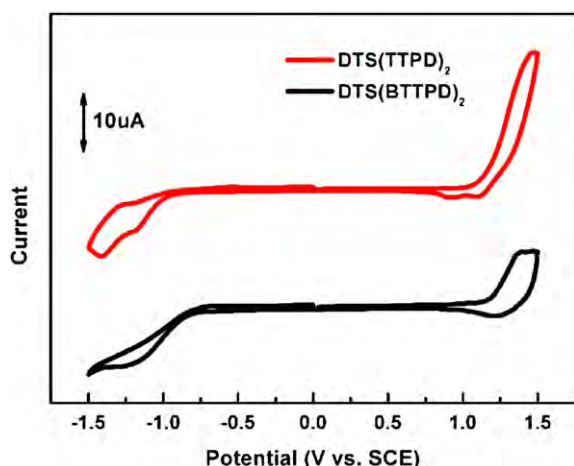


Fig. 3. CV traces of **DTS(BTTPD)₂** and **DTS(TTPD)₂**.

Table 1

Photovoltaic parameters for devices based on **DTS(TTPD)₂:PC₆₁BM** (2:3, w/w) and **DTS(BTTPD)₂:PC₆₁BM** (2:3, w/w) blends.

Molecule	Spinning speed (rpm)	Thickness (nm)	V_{oc} (V)	J_{sc} (mA/cm ²)	FF (%)	PCE (%)
DTS(TTPD)₂	1100	125	0.87	2.47	30.17	0.63
	1300	100	0.89	2.36	32.85	0.69
	1500	95	0.89	2.56	33.36	0.76
	1700	90	0.88	2.29	35.23	0.71
DTS(BTTPD)₂	300	160	0.85	1.66	27.64	0.39
	400	150	0.84	1.93	29.61	0.48
	800	135	0.84	1.73	29.98	0.43
	1500	90	0.88	2.59	32.90	0.75

DTS(BTTPD)₂ with the weight ratio of 2:3 is found to be 0.75% with a V_{oc} of 0.88 V, J_{sc} of 2.59 mA/cm² and FF of 32.90%.

From Table 2, we also observe that annealing can improve the performance of **DTS(TTPD)₂** efficiently. The best PCE of **DTS(TTPD)₂** with the weight ratio of 2:3 is found to be 1.00% with a V_{oc} of 0.91 V, J_{sc} of 3.15 mA/cm² and FF of 34.88% by annealing shown in Fig. 5. Compared to **DTS(TTPD)₂**, **DTS(BTTPD)₂** with larger molecular structure should have exhibited better film forming quality [30], however, the absorption of its thin film showed some transformation which was bad for photovoltaic performance with the lower V_{oc} of **DTS(BTTPD)₂** than **DTS(TTPD)₂**. Moreover, annealing at 110 °C for 3 min resulted in a sharp decrease in the efficiency of the devices from **DTS(BTTPD)₂**, which is corresponding with the phenomenon of UV-vis. There is some aggregation or transformation between the conjugated systems of **DTS(BTTPD)₂** enforced by the crystal packing when annealing which is bad for morphology. It is impressive that the V_{oc} of the two PVs made from the molecules is large enough owing to the electronegative carbonyl groups from the end-capped imide acceptor [22]. Especially the V_{oc} of **DTS(TTPD)₂** reached to 0.99 V, which is much larger than that of the reports [13,16] of small-molecule based on dithienosilole. However, the performance of these two molecules is much poorer than the reports of small-molecule based on dithienosilole, which is due to much lower J_{sc} and FF.

In order to improve the performance, we optimized the device structure further, replacing PEDOT:PSS layer with MoO₃. From Fig. 5, it is observed that both V_{oc} and FF increased (V_{oc} from 0.91 V to 0.97 V, FF from 34.88 % to 47.58 %) with MoO₃ instead of PEDOT:PSS. PEDOT/PSS is an inefficient electron-blocking layer,

Table 2

Photovoltaic parameters for normal geometry devices based on **DTS(TTPD)₂:PC₆₁BM** and **DTS(BTTPD)₂:PC₆₁BM** blends with spin-coating speed of 1500 rpm.

Molecule	Donor:PC ₆₁ BM (weight ratios)	V_{oc} (V)	J_{sc} (mA/cm ²)	FF (%)	PCE (%)
DTS(TTPD)₂	1:2	0.98	1.86	27.98	0.51
	2:3	0.99	2.28	31.01	0.70
	1:1	0.99	2.30	32.94	0.75
	2:1	0.93	2.00	30.64	0.57
	1:2 ^a	0.91	1.58	29.91	0.43
	2:3 ^a	0.91	3.15	34.88	1.00
	2:3 ^b	0.97	2.60	47.58	1.20
	1:1 ^a	0.90	2.54	33.68	0.77
DTS(BTTPD)₂	2:1 ^a	0.90	2.41	36.42	0.79
	2:3	0.88	2.59	32.90	0.75
	1:1	0.84	1.73	29.98	0.43
	3:2	0.84	1.08	28.19	0.25
	2:3 ^a	0.67	1.20	27.11	0.22
	1:1 ^a	0.71	1.59	28.48	0.32
	3:2 ^a	0.67	1.23	27.06	0.22

^a Annealed at 110 °C for 3 min.

^b ITO/MoO₃/Donor molecule:PC₆₁BM/Al structure and annealed at 110 °C for 3 min.

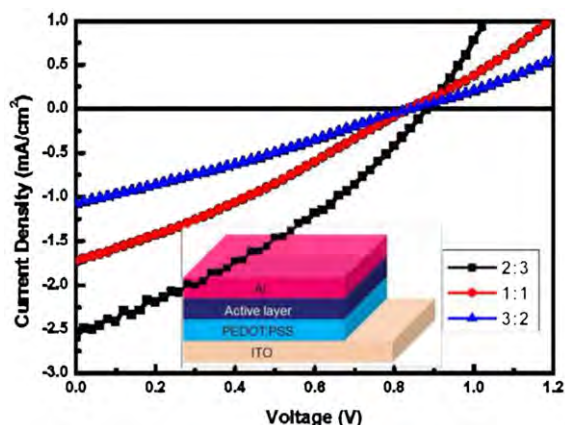


Fig. 4. J–V curves obtained from normal geometry devices with different $\text{DTS(BTTPD)}_2:\text{PC}_{61}\text{BM}$ blends without annealing.

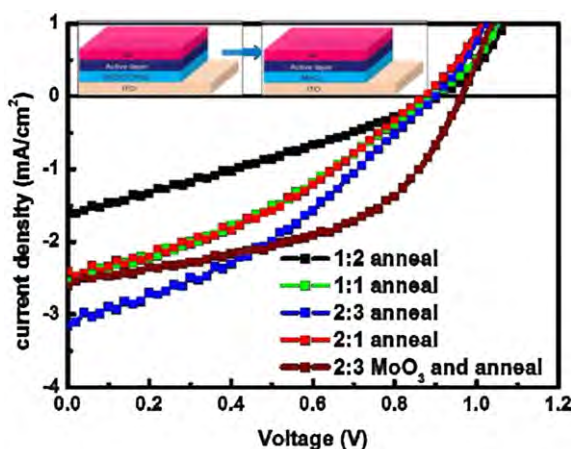


Fig. 5. J–V curves obtained from normal geometry devices with different $\text{DTS(TTPD)}_2:\text{PC}_{61}\text{BM}$ blends annealed at $110\text{ }^\circ\text{C}$ for 3 min.

reducing device current efficiency due to electron leakage to the anode. Compared to PEDOT/PSS, MoO_3 shows a better hole transporting property, which also serves as efficient electron-blocking layer because the conduction band of MoO_3 is much higher than the LUMO energy levels of the donor and acceptor in the active layer [31,32]. Therefore, the efficient electron-blocking of the MoO_3 can enhance V_{OC} and FF efficiently, resulting in a higher PCE of 1.20%.

We also synthesized another molecule without thiophene or bithiophene as π -bridge for a comparison. This molecule even can not show a solid state when spin-coating, indicating the awful film forming quality. Thiophene and bithiophene were applied in our molecular design as π -bridge, which improved the film forming quality and planarity efficiently. In the case of this design, thiophene tuned the photovoltaic performance efficiently, while bithiophene possessing a similar ability, however the poor aggregation or transformation between the conjugated systems caused a lower efficiency.

4. Conclusion

In summary, we designed, synthesized and characterized two novel small molecules DTS(TTPD)_2 or DTS(BTTPD)_2 based on a A– π –D– π –A framework end-capped with thieno[2,3-c] pyrrole-4,6-

dione (TPD) unit. These small molecules had very similar optical band gaps (1.87 eV and 1.92 eV) and fairly close HOMO energy levels (-5.52 to -5.55 eV). The best solar cells using DTS(TTPD)_2 as a donor and PC_{61}BM as an acceptor demonstrated efficient performance with an obviously high V_{OC} of 0.97 V and a PCE of 1.20% by annealing. The PV based on DTS(BTTPD)_2 and PC_{61}BM exhibited a high V_{OC} of 0.97 V under optimized conditions, however the device efficiency was relatively low (0.75%) with a low J_{SC} due to some aggregation or transformation between the conjugated systems. As a consequence of our synthetic design we could achieve the low HOMO energy levels of these two small molecules, which is very close to the proposed ideal HOMO of -5.4 eV [33] resulting in a notably high V_{OC} . Therefore, some stronger acceptor unit is required to combine with **DTS** and **TPD** as π -bridge to bathochromically tune the absorption band for better matching the solar spectrum, and also the morphology optimization. The performance of these two small molecules is suggesting that the structure based on **DTS** and **TPD** can become a potential material for small molecule solar cells.

Acknowledgments

This work was supported by the Danish National Research Foundation and the National Natural Science Foundation of China (Grant No. 51011130028) for the *Danish-Chinese Center for Organic based Photovoltaic Cells*, within which this work was performed. The work was also partly supported by the National Natural Science Foundation of China (Nos. 50990063).

References

- [1] Cheng YJ, Yang SH, Hsu CS. Synthesis of conjugated polymers for organic solar cell applications. *Chem Rev* 2009;109(11):5868–923.
- [2] Thompson BC, Frechet JM. Polymer-fullerene composite solar cells. *Angew Chem Int Ed Engl* 2008;47(1):58–77.
- [3] Krebs FC, Gevorgyan SA, Alstrup J. A roll-to-roll process to flexible polymer solar cells: model studies, manufacture and operational stability studies. *J Mater Chem* 2009;19(30):5442.
- [4] Zhou HX, Yang LQ, Stuart AC, Price SC, Liu SB, You W. Development of fluorinated benzothiadiazole as a structural unit for a polymer solar cell of 7% efficiency. *Angew Chem Int Ed Engl* 2011;50(13):2995–8.
- [5] Liang YY, Xu Z, Xia JB, Tsai ST, Wu Y, Li G, et al. For the bright future-bulk heterojunction polymer solar cells with power conversion efficiency of 7.4%. *Adv Mater* 2010;22(20):135–8.
- [6] He ZC, Zhong CM, Huang X, Wong WY, Wu HB, Chen LW, et al. Simultaneous enhancement of open-circuit voltage, short-circuit current density, and fill factor in polymer solar cells. *Adv Mater* 2011;23(40):4636–43.
- [7] Chu TY, Lu JP, Beaupre S, Zhang YG, Pouliot JR, Wakim S, et al. Bulk heterojunction solar cells using thieno[3,4-c]pyrrole-4,6-dione and dithieno[3,2-b:2',3'-d]silole copolymer with a power conversion efficiency of 7.3%. *J Am Chem Soc* 2011;133(12):4250–3.
- [8] Chen HY, Hou JH, Zhang SQ, Liang YY, Yang GW, Yang Y, et al. Polymer solar cells with enhanced open-circuit voltage and efficiency. *Nat Photon* 2009;3:639–53.
- [9] Dou LT, You JB, Yang J, Chen CC, He YJ, Murase S, et al. Tandem polymer solar cells featuring a spectrally matched low-band gap polymer. *Nat Photon* 2012;6(3):180–6.
- [10] Huang Y, Guo X, Liu F, Huo LJ, Li YF, Hou JH, et al. Improving the ordering and photovoltaic properties by extending π -conjugated area of electron-donating units in polymers with D–A structure. *Adv Mater* 2012;24(25):3383–9.
- [11] Huo LJ, Zhang SQ, Guo X, Xu F, Li YF, Hou JH. Replacing alkoxy groups with alkylthienyl groups: a feasible approach to improve the properties of photovoltaic polymers. *Angew Chem Int Ed Engl* 2011;50(41):9697–702.
- [12] Gupta A, Ali A, Bilic A, Gao M, Hegedus K, Singh B, et al. Absorption enhancement of oligothiophene dyes through the use of a cyanopyridone acceptor group in solution-processed organic solar cells. *Chem Commun* 2012;48(13):1889–91.
- [13] Sun Y, Welch GC, Leong WL, Takacs CJ, Bazan GC, Heeger AJ. Solution-processed small-molecule solar cells with 6.7% efficiency. *Nat Mater* 2012;11(1):44–8.
- [14] Lin YZ, Li YF, Zhan XW. Small molecule semiconductors for high-efficiency organic photovoltaics. *Chem Soc Rev* 2012;41:4245–72.
- [15] Liu YS, Wan XJ, Wang F, Zhou JY, Long GK, Tian JG, et al. High-performance solar cells using a solution-processed small molecule containing benzodithiophene unit. *Adv Mater* 2011;23(45):5387–91.

Appendix 2.5

- [16] Zhou JY, Wan XJ, Liu YS, Long GK, Wang F, Li Z, et al. A planar small molecule with dithienosilole core for high efficiency solution-processed organic photovoltaic cells. *Chem Mater* 2011;23(21):4666–8.
- [17] Li Z, He GR, Wan XJ, Liu YS, Zhou JY, Long GK, et al. Solution processable rhodanine-based small molecule organic photovoltaic cells with a power conversion efficiency of 6.1%. *Adv Energy Mater* 2012;2(1):74–7.
- [18] Shi MM, Fu L, Hu XL, Zuo LJ, Deng D, Chen J, et al. Design and synthesis of carbonyl group modified conjugated polymers for photovoltaic application. *Polym Bull* 2011;68(7):1867–77.
- [19] Qu SY, Wang B, Guo FL, Li J, Wenj Wu, Hua JL, et al. New diketopyrrolopyrrole (DPP) sensitizer containing a furan moiety for efficient and stable dye-sensitized solar cells. *Dye Pigment* 2012;92:1384–93.
- [20] Zhang J, Yu JT, He C, Deng D, Zhang ZG, Zhang MJ, et al. Solution-processable star-shaped photovoltaic organic molecules based on triphenylamine and benzothiadiazole with longer pi-bridge. *Org Electron* 2012;13(1):166–72.
- [21] Zeng SH, Yin LX, Jiang XY, Lia YQ, Li KC. D–A–D low band gap molecule containing triphenylamine and benzoxadiazole/benzothiadiazole units: synthesis and photophysical properties. *Dye Pigment* 2012;95:229–35.
- [22] Liao L, Dai LM, Smith A, Durstock M, Lu JP, Ding JF, et al. Photovoltaic-active dithienosilole-containing polymers. *Macromolecules* 2007;40:9406–7.
- [23] Huang JH, Teng CM, Hsiao YS, Yen FW, Chen P, Chang FC, et al. Nanoscale correlation between exciton dissociation and carrier transport in silole-containing cyclopentadithiophene-based bulk heterojunction films. *J Phys Chem C* 2011;115(5):2398–405.
- [24] Zhang Y, Zou JY, Yip HL, Sun Y, Davies JA, Chen KS, et al. Conjugated polymers based on C, Si and N-bridged dithiophene and thienopyrroledione units: synthesis, field-effect transistors and bulk heterojunction polymer solar cells. *J Mater Chem* 2011;21(11):3895.
- [25] Hu XL, Shi MM, Zuo LJ, Nan YX, Liu Y, Fu L, et al. Synthesis, characterization, and photovoltaic property of a low band gap polymer alternating dithienopyrrole and thienopyrroledione units. *Polymer* 2011;52(12):2559–64.
- [26] Melucci M, Zambianchi M, Favaretto L, Gazzano M, Zanelli A, Monari M, et al. Thienopyrrolyl dione end-capped oligothiophene ambipolar semiconductors for thin film- and light emitting transistors. *Chem Commun* 2011;47(43):11840–2.
- [27] Hong YR, Wong HK, Moh LC, Tan HS, Chen ZK. Polymer solar cells based on copolymers of dithieno[3,2-b:2',3'-d]silole and thienopyrroledione. *Chem Commun* 2011;47(17):4920–2.
- [28] Zhang Y, Hau SK, Yip HL, Sun Y, Acton O, Jen AKY. Efficient polymer solar cells based on the copolymers of benzodithiophene and thienopyrroledione. *Chem Mater* 2010;22(9):2696–8.
- [29] Uhrich C, Schueppel R, Petrich A, Pfeiffer M, Leo K, Brier E, et al. Organic thin-film photovoltaic cells based on oligothiophenes with reduced bandgap. *Adv Funct Mater* 2007;17(15):2991–9.
- [30] Shi MM, Hao F, Zuo LJ, Chen Y, Nan YX, Chen HZ. Effect of substituents on the aggregate structure and photovoltaic property of violanthrone derivatives. *Dye Pigment* 2007;17(15):2991–9.
- [31] Giroto C, Voroshazi E, Cheyons D, Heremans P, Rand BP. Solution-processed MoO₃ thin films as a hole-injection layer for organic solar cells. *ACS Appl Mater Interfaces* 2011;3(9):3244–7.
- [32] Garcia A, Welch GC, Ratcliff EL, Ginley DS, Bazan GC, Olson DC. Improvement of interfacial contacts for new small-molecule bulk-heterojunction organic photovoltaics. *Adv Mater* 2012;24(39):5368–73.
- [33] Scharber MC, Mühlbacher D, Koppe M, Denk P, Waldauf C, Heeger AJ, et al. Design rules for donors in bulk-heterojunction solar cells – towards 10% energy-conversion efficiency. *Adv Mater* 2006;18(6):789–94.

Effect of Solvent-Assisted Nanoscaled Organo-Gels on Morphology and Performance of Organic Solar Cells

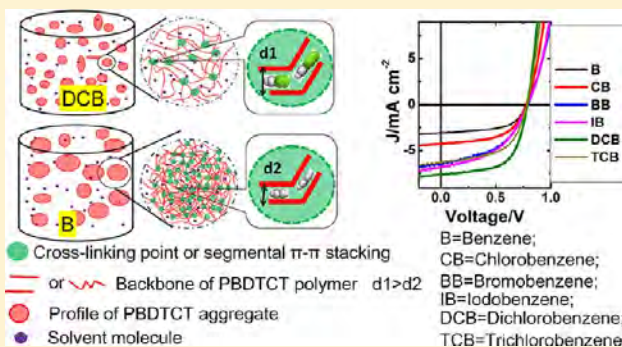
Li-Jian Zuo,[†] Xiao-Lian Hu,[†] Tao Ye,[†] Thomas R. Andersen,[‡] Han-Ying Li,[†] Min-Min Shi,^{*,†} Mingsheng Xu,[†] Jun Ling,[†] Qiang Zheng,[†] Jun-Ting Xu,[†] Eva Bundgaard,[‡] Frederik C. Krebs,[‡] and Hong-Zheng Chen^{*,†}

[†]State Key Laboratory of Silicon Materials, MOE Key Laboratory of Macromolecular Synthesis and Functionalization and Department of Polymer Science and Engineering, Zhejiang University, Hangzhou 310027, People's Republic of China

[‡]Department for Energy Conversion and Storage, Technical University of Denmark, Frederiksborgvej 399, DK-4000 Roskilde, Denmark

S Supporting Information

ABSTRACT: This paper reports how the morphology of a polymer–fullerene derivative blend is tuned via the different aggregate states of the polymer in solutions. Based on a copolymer with benzodithiophene and thiophene-3-carboxylate as alternating units (PBDTCT), we explored the polymer aggregation (i.e., organo-gels) behavior as a function of steric hindrance of aromatic solvents imposed by substituents. We showed that the size of organo-gels decreased as the substituents of solvents got larger. Also, the phase separation and domain size of the subsequent spin-coated films increased monotonically with that of the organo-gels in solution. Through this knowledge, we eventually achieve controlled morphology and optimized organic solar cells (OSCs) performance. Our results present a significant step forward for understanding the self-assembly behavior of conjugated polymers, control of their morphology and optimization of OSC performance.



INTRODUCTION

The self-assembly behavior of conjugated polymers, including the formation of gels or microgels in solution have been intensively studied with a fundamental view^{1–8} to construct highly efficient organic electronic devices such as organic light-emitting devices (OLEDs),^{9,10} organic field-effect transistors (OFETs),^{11–13} organic solar cells (OSCs),^{14–18} and so forth. For example, Nguyen et al. demonstrated that controlled aggregation could increase the efficiency of OLED, because it could increase the carrier mobility due to overlapping of the π orbitals of adjacent chains.^{9,10} Newbloom et al. identified that the formation of aggregation or colloidal network of regioregular poly(3-hexylthiophene) (rr-P3HT) would help to construct a mesoscale crystalline network and high-performance OFETs.¹³ Also, the structures and self-assembly mechanisms for these aggregates or gels have been partly understood.^{1–5,8} Chen et al. found that the conjugated polymers of poly(2,3-diphenyl-5-decyl-1,4-phenylenevinylene) and poly[9,9-bis(2-ethylhexyl)fluorene-2,7-diyl] would form transient loose aggregates or microgels due to the segmental association by strong π – π interaction.^{2,3} Furthermore, these conjugated polymer aggregates were dynamically stable, while the aggregation behaviors were greatly dependent on the degree of solvation,^{1,2,10} concentration,^{1,3,10} the steric hindrance

of the polymers,¹ the temperature,^{1,2,19} and so forth. Instead of the intuitive understanding that the aggregation of conjugated polymers in solution is driven by the π – π interaction between the polymer segments, further studies by Rahman et al. proved the existence of liquid crystal-like segmental alignment structures and the formation of strong polymer–solvent interaction.^{3,5} They suggested that the π – π interaction between the polymer segments and solvent molecules stabilized the aggregate domain,^{4,5} through the formation of a polymer–solvent complex that was induced by π – π interaction of solvent molecules and polymer segments.^{3,4} In the context of previous studies, we hypothesize that the steric hindrance of aromatic solvent molecules, which similar to the steric hindrance of polymers, also interrupts the polymer–solvents π – π interaction, should influence the aggregation behavior of polymer aggregates in solution as well.

For the past decade, OSCs have become a subject of intense study due to a variety of advantages including the availability of a large number of chemical structures, ease of fabrication, mechanical flexibility, and potentially low cost for renewable

Received: May 22, 2012

Revised: July 19, 2012

Published: July 24, 2012



energy production.^{20,21} The performance of OSCs shows critical dependence on the morphology of the active layer. A basic requirement for the highly efficient OSC is an optimized morphology featuring nanoscale phase separation of donor (D) and acceptor (A) and a bicontinuous pathway for charge transport that is induced by the spontaneous phase separation or self-assembly of the active layer during the process of solidification or annealing.²² The relation between morphology and device performance is also well-established.²³ For highly efficient OSCs, a group of processing factors influencing the morphology of the active layer was intensively studied, that is, annealing,^{22,24,25} additives,^{26–28} solvation,^{29–31} and interface engineering.³² The discovery of polymer gels in the solution of rr-P3HT, which is the most popular donor polymer employed in OSCs, triggered the general interest to control active layer morphology by constructing polymer aggregation.^{8,14–18,33–35} Also, the self-assembled nanogels or integrated gels would facilitate the phase separation between donor and acceptors. These preaggregation methods have proved an effective way to obtain the nanoscale interpenetrating network and high performance OSCs as well.^{19,35} In these studies, the degree of polymer aggregation due to the molecular self-assembly, which is controlled by the aging time or the solvation, was the most important factor. However, the knowledge about the aggregation state of conjugated polymers in solution is limited, and few have correlated the aggregation state with active layer morphology and device performance.

In this work, we systematically study the aggregation behavior of a copolymer with benzodithiophene and thiophene-3-carboxylate as alternating units (PBDTCT, molecular structure in Figure 1(a), donor, ref 36) in solution by changing the steric hindrance of aromatic solvents. The dynamically stable aggregation behavior of PBDTCT in these solvents shows large differences in solution due to the formation of different polymer–solvent complex species. The spin-coated film morphology also exhibits large dissimilarities after mixing these aggregates in solution with [6,6]-phenyl-C₆₁-butyric acid methyl ester (PCBM, acceptor). By comparing the aggregate states in solutions and the morphology in solid films, an aggregate assisted and D/A ratio independent phase separation behavior was observed: the size of the phase-separation domains increase monotonously with the size of the aggregates in solutions. With these findings, we achieve concisely controlled morphology and optimized device performance.

EXPERIMENTAL SECTION

Materials. PBDTCT ($M_w = 17.6$ K, $M_n = 12.2$ K, PDI = 1.4) was synthesized in our lab according to the reported procedure.³⁶ PCBM was purchased from Lumi. Tech. Corp. Other reagents and solvents, unless specified, were purchased from Sigma–Aldrich, Acros, and TCI Chemical Co. and used as received.

Equipment. UV–vis absorption spectra of the solutions of PBDTCT in different solvents (3 mg/mL) were recorded on a Varian CARY100 Bio spectrophotometer with a short optical path (1 mm) cuvette, in order not to exceed the upper limit in terms of absorbance (~ 4). Photoluminescence (PL) spectra were measured on a Hitachi F-4500 fluorescence spectrophotometer. Dynamic light scattering (DLS) measurements were performed on a Brookhaven BI-200SM equipment with an ALV/LSE-503 Multiple- τ digital detector. The instrument makes use of a 632 nm laser light, which is beyond the

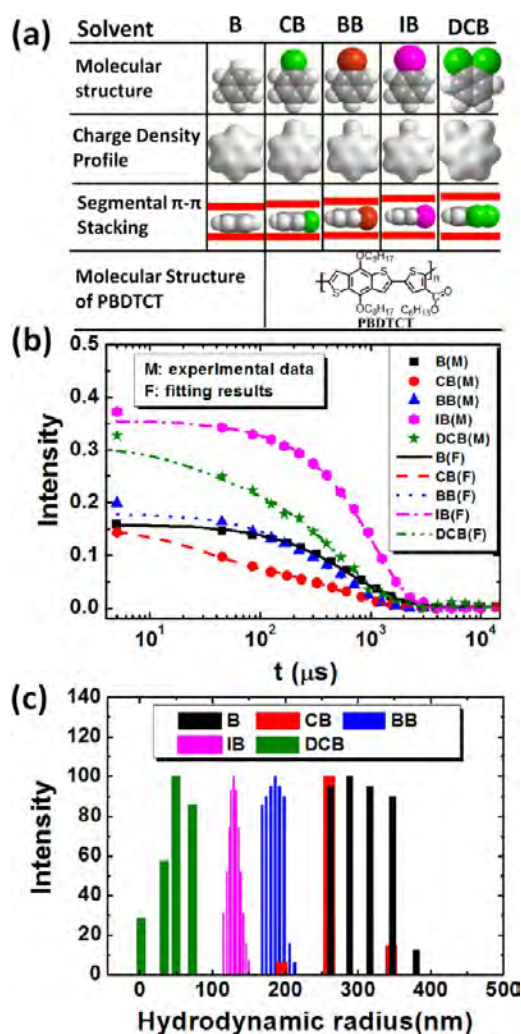


Figure 1. (a) Molecular structures for PBDTCT and the processing solvents; (b) normalized intensity correlation functions and the fitting curves by Contins function for PBDTCT solutions in different solvents collected at $\theta = 90^\circ$ and at 20°C ; (c) the radius distributions of PBDTCT aggregates in different solvents.

absorption range of PBDTCT in any solvent. The instrument is capable of distinguishing particles as small as 1 nm at relatively high particle concentrations and the upper limitation of the instrument is $10\ \mu\text{m}$. The scattered light is collect at 90° compared to the incident light at 20°C . The concentration of PBDTCT is around 3 mg/mL, which is in the semidilute region. The highest concentration of conjugated polymer allowed for DLS measurement is 1 wt % (around 10 mg/mL).¹ Thus, in our case, the multiple scattering effect should be avoided. Surface morphologies of films were imaged on a Veeco MultiMode atomic force microscope (AFM) operated in tapping mode under ambient condition. The samples for AFM measurements were prepared on cleaned ITO/glass substrates coated with a PEDOT/PSS film according to the device fabrication procedure. The film thickness was calibrated on an Ambios XP-2 profilometer.

Device Fabrication. OSCs were prepared on commercial glass slides coated with patterned ITO. The thickness and the sheet resistance of the ITO are 150 nm and $8.5\ \Omega/\text{square}$ (measured by the four probe method), respectively. The active area of each device was $0.09\ \text{cm}^2$ with an aspect ratio of 1:1. The substrates were sonicated sequentially in detergent, DI

water, acetone, and isopropanol. Immediately prior to device fabrication, the substrates were treated in a UV–ozone oven for 15 min. First, a poly(3,4-ethylenedioxythiophene)/poly(styrene sulfonate) (PEDOT/PSS, HC Starck, Clevious P VP AI 4083) thin film (~ 40 nm thick) was spin-coated through the $0.45\ \mu\text{m}$ filter and then baked at $140\ ^\circ\text{C}$ for 15 min in ambient air. Second, the active layer was spin-coated on top of the cooled PEDOT/PSS layer in a glovebox, with different spinning speed to confine the active layer thickness to around 110 nm (± 20 nm) as determined by an Ambios XP-2 profilometer. The PBDTCT/PCBM solution with a weight ratio of 1:1, and a total concentration of 20 mg/mL in different solvents (benzene, chlorobenzene, bromobenzene, iodobenzene, dichlorobenzene, and trichlorobenzene) was stirred overnight at $50\ ^\circ\text{C}$. Finally, 6 nm Cs_2CO_3 and 80 nm Al layers were deposited successively on the top of the active layer in a vacuum of 4×10^{-4} Pa to complete the device fabrication.

Device Characterization. Current density–voltage (J – V) characteristics of devices were recorded on a Keithley 2400 source meter, under AM 1.5G irradiation of $100\ \text{mW}/\text{cm}^2$ from a Xe lamp. The incident light intensity was determined by a calibrated silicon photodiode, and the quoted performance was not corrected for spectra mismatch. All device fabrication and characterization were conducted under ambient atmosphere, and the whole measuring process was completed within 5 min for each device.

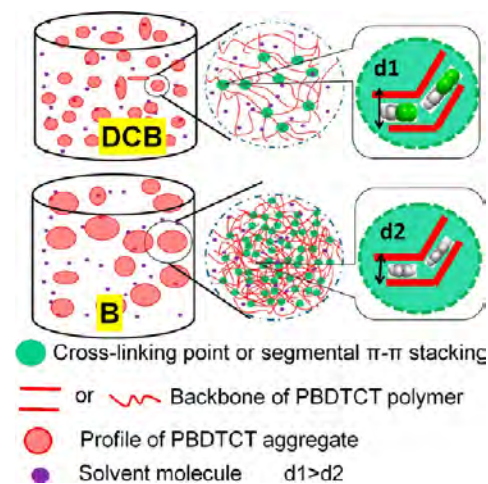
RESULTS AND DISCUSSION

Solvents Steric Hindrance Dependent Aggregation Behavior. DLS is widely used to study the polymer aggregation behavior in solution.¹ In this work, this technique is employed to directly observe the aggregation behaviors of PBDTCT solutions in different solvents (benzene, chlorobenzene, bromobenzene, iodobenzene, and dichlorobenzene). As revealed by Chen et al.,^{2–5} the aggregates in solution were stabilized by the polymer–solvent complex formation through π – π induction of solvent molecules and polymer segments. The binding strength of the polymer–solvent complexes, which is dependent on the π – π stacking distance between solvent molecule and conjugated polymer segment, is one of the most important factors influencing the conjugated polymer aggregation behavior in solution. The effect of steric hindrance of substituents on conjugated polymer has already been proven critical for polymer aggregation due to its interruption of the π – π interaction.^{1,2} Meanwhile, the aggregation behavior of conjugated polymers differ greatly in the aromatic solvents and the nonaromatic solvents.^{1,10} Thus, the effect of the solvent steric hindrance due to the substituents attached to the aromatic solvents might also influence the aggregation behavior. To our knowledge, this interesting topic has not been addressed systematically.

To explore this effect, we choose benzene, chlorobenzene, bromobenzene, iodobenzene, and *o*-dichlorobenzene as processing solvents. For short, we use the symbol B to stand for benzene, CB for chlorobenzene, BB for bromobenzene, IB for iodobenzene, DCB for dichlorobenzene, TCB for 1,2,4-trichlorobenzene, MB for toluene, and CF for chloroform. To obtain dynamically stable solutions, the solutions were stirred for 24 h at $50\ ^\circ\text{C}$ and then cooled down to room temperature. As shown in Figure 1(a), the steric hindrance of the solvents increases from B to DCB. Figure 1(b, c) displays the normalized intensity correlation functions (collected at $\theta = 90^\circ$), and the hydrodynamic radii (R_h) or the size distributions

of PBDTCT aggregates in different solvents, respectively. It is found that the radii of the aggregates show a trend of stepwise decrease from B to DCB (from 320 nm in B to 50 nm in DCB). Thus, a clear and dramatic dependence of polymer aggregation on the steric hindrance of solvents is observed. Another possible effect of the solvents on polymer aggregation could be due to the different dipole moments or the solubility parameters. However, we propose that this is not the dominant effect because the dipole moments of CB, BB, and IB are nearly identical and the solubility parameters do not show much difference between BB and DCB (see the Supporting Information, Table S1). We argue that the solvent steric hindrance effect on the aggregation behavior shares the similar mechanism with respect to that of the steric hindrance of polymers, where larger steric hindrance would interrupt the π – π interaction.^{1,2} To better illustrate this phenomenon, a schematic diagram is shown in Scheme 1. When the steric

Scheme 1. Aggregate Structures and Segmental π – π Stacking of PBDTCT with the Solvents Varying from B (Bottom) to DCB (Top)



hindrance of the processing solvents becomes larger, the distance for π – π interaction of the polymer–solvent complex becomes larger, too. Accordingly, the binding strength of the polymer–solvent complex becomes weaker, leading to better dispersion or smaller aggregation size for the polymer in solution.

Optical Properties. It is known that the aggregation of conjugated polymers would induce the changes in the optical spectra, for example, absorption or photoluminescence (PL). Figure 2 shows the UV–vis absorption spectra and PL spectra of PBDTCT in eight different solvents. As disclosed in Figure 2(a), the absorption peak and absorption edge of PBDTCT solutions exhibit stepwise red-shifts in sequence from TCB to B or with the decreasing of the steric hindrance of the substituent on the aromatic solvent. The details of the absorption changes with solvents are summarized in Table 1. The changes in the optical spectra are attributed to the aggregation because our density functional theory (DFT) calculation (shown in the Supporting Information, Figure S1) excluded the possibility of the absorption or photoluminescence change due to conjugated backbone chain torsion.

With the volume of the solvents decreasing from TCB to B, the absorption peak shows red-shift or the shoulder peak becomes more pronounced (Figure 2(a)). The distinction of

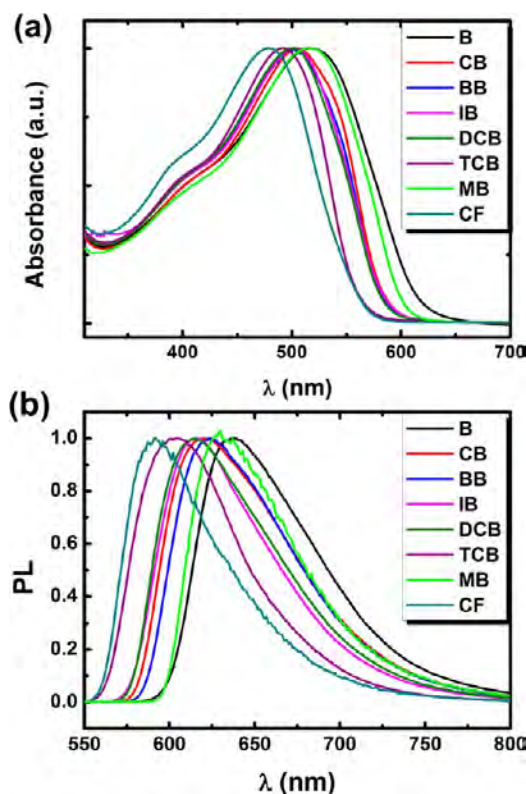


Figure 2. (a) Normalized UV-vis absorption spectra and (b) PL spectra of PBDTCT in eight different solvents (3 mg/mL for PBDTCT). The excited wavelength for PL spectra is 500 nm.

Table 1. Optical Data of PBDTCT Solutions in Different Solvents

solvent	absorption			hydrodynamic radius (nm)
	edge (nm)	λ_{\max} (nm)	PL peak (nm)	
B	618	516	639	320
CB	586	505	621	262
BB	585	501	621	176
IB	584	502	616	131
DCB	582	500	615	50
TCB	558	486	598	–
MB	607	515	629	–
CF	557	478	582	–

the absorption shift of PBDTCT in different solvents indicates the degree of aggregation is rather variable when different processing solvents are used. This is in accordance with the DLS results. With the steric hindrance of solvent decreasing, the polymer-solvent π - π interacting complex species became strong due to the shortened π - π stacking distance. This strengthened π - π interaction would certainly induce heavier aggregation, which was observed in the DLS results, and thus leading to stronger red-shift in the absorption spectra. Further, we use TCB, MB, and CF to confirm this argument. As shown in Figure 2, both UV-visible absorptions of PBDTCT in TCB and CF were strongly blue-shifted compared to those in other solvents, suggesting the aggregation of PBDTCT in solvents TCB and CF were the weakest. This is because, in solvent CF, polymer-solvent π - π interaction is regarded as the weakest due to the lack of conjugation or π orbital in CF molecules. In TCB, the formation of a polymer-solvent species was inhibited

due to the weak polymer-solvent π - π interaction induced by the large steric hindrance of the TCB molecules. Furthermore, the absorption peak of PBDTCT in TCB shows a slight red-shift compared with that in CF, which suggests some aggregation of PBDTCT in TCB. On the other hand, the absorption of PBDTCT in MB presents a larger red-shift compared with that in CF, indicating stronger aggregation. As the methyl substituent is smaller than the chlorine substituent, the absorption of PBDTCT in MB lies between those of B and CB. The PL spectra of PBDTCT in different solvents, shown in Figure 2(b), also follow the same trend as those of the absorption spectra. These results reconfirm the formation of different aggregation states of PBDTCT in different solvents and the argument that aromatic solvent steric hindrance would certainly influence the intensity of aggregation.

The absorption spectra of PBDTCT/PCBM in different solutions were also studied (see Supporting Information, Figure S2), which present a simple superposition for PBDTCT and PCBM in different solvents. The absorption peaks and shoulders of PBDTCT exhibit no difference between the PBDTCT pristine solutions and the PBDTCT/PCBM composite solutions. These results might indicate that PCBM molecules have little influence on the aggregation behavior of PBDTCT in solutions. Also, we found the absorption of PCBM were identical in any solvents. It should be noted that the absorption features (e.g., peak or edge wavelength) were less dependent on the concentration, where we diluted the solution by a factor of 10 but no changes in the spectra were observed (see the Supporting Information, Figure S3). The absorption of PBDTCT aggregate solutions shows little change after one week (see the Supporting Information, Figure S4), proving good stability of these aggregates.

Direct Observation of Aggregates in Solution and Their Transfer to Thin Solid Film. Evidence for the aggregates of conjugated polymers in solution being maintained upon solid film formation during the spin-coating process has been demonstrated.^{1,4,37} As shown by Rahman et al., the solvents trapped inside the alignment of conjugated polymer segments show much slower decay speed than the bulk free solvents during annealing.³ This phenomenon suggests the aggregation equilibrium requires a much longer time (~ 200 min)³ to achieve a new configuration. However, the time of film solidification during spin-coating (less than 1 min for MB and CF) is much shorter than the dynamic process of the aggregate evolution, which allows the aggregates to deposit into the thin film. Figure 3 shows the morphology images of PBDTCT films cast from MB and CF. As indicated in Figure 2(a), the aggregation of PBDTCT in MB was strong due to the polymer-solvent interaction, while PBDTCT in CF exhibited little aggregation due to the lack of polymer-solvent π - π interaction. As shown in Figure 3, the topology of PBDTCT film cast from MB solution shows distinct PBDTCT particle domains, which results in a much rougher surface than the corresponding films processed from CF. The phase image of PBDTCT film cast from MB shows distinct domains as well. However, PBDTCT film from CF presents a more homogeneous morphology, smaller domain size, and more ambiguous phase separation, estimated from the phase images. This observation coincides with the PBDTCT aggregation state in solutions. This direct observation indicates that the aggregates in solution are strong enough to survive the solidification process and are thus transferred to the thin film.

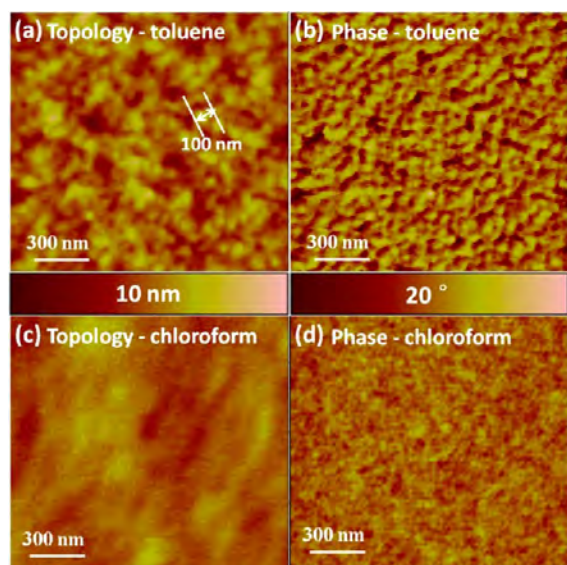


Figure 3. Morphology of pristine PBDTCT film cast from toluene and chloroform: (a) topology and (b) phase images from toluene; (c) topology and (d) phase images from chloroform.

Less Ratio Dependent Phase-Separation Process. In OSCs, the D/A ratio dependent morphology and device performance is widely reported.^{38–40} In this process, the interactions among donor, acceptor, and solvents, for example, solubility of D and A in solution and miscibility between D and A, play a major role to determine the morphology of the active layer.⁴¹ Here, we observed however a ratio independent phase-separation behavior. As shown in Figure 4, the active layer

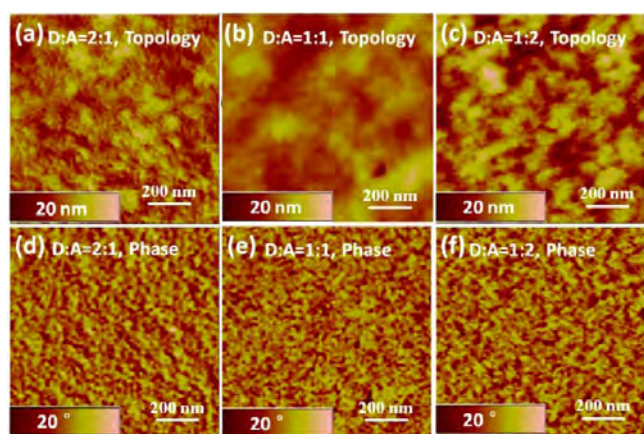


Figure 4. Morphology of composite PBDTCT/PCBM film with different ratios cast from dichlorobenzene: (a–c) topology images with the ratios of 2:1, 1:1, and 1:2, respectively; (d–f) phase images with the ratios of 2:1, 1:1, and 1:2, respectively.

morphology processed from different D/A ratios (2:1, 1:1, 1:2) using DCB as the processing solvent shows negligible changes in the phase images, especially the size of the phase separation domains. Thus, it is mainly the status of the aggregates in solution, which were strong enough to survive the spin-coating process as mentioned above, that control the whole phase-separation process in our case.

Aggregation-Induced Phase Separation. Though PBDTCT/PCBM composite film shows less ratio dependent behavior, it is solvent related. As can be seen from Figure 5, the

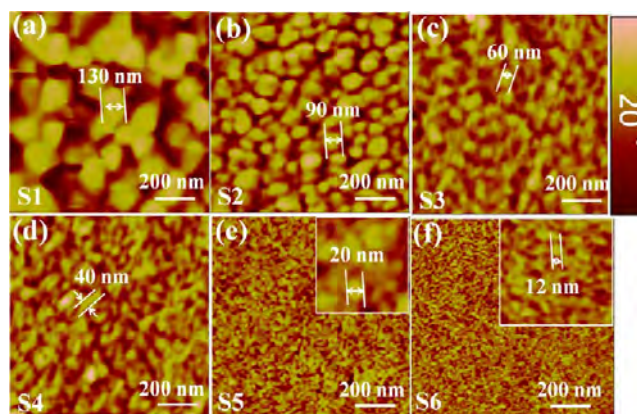


Figure 5. AFM phase images of PBDTCT/PCBM (1:1, w/w) films prepared from solutions in different solvents: (a) B; (b) CB; (c) BB; (d) IB; (e) DCB; and (f) TCB.

morphology or the phase-separated domain size of PBDTCT/PCBM film shows a monotonous decreasing trend from solvent B to TCB. This trend correlates well with the diameter of aggregates in different solvents and also the size of the steric hindrance of substituent groups attached to the benzene ring. Thus, in our case, aggregation of the polymer plays a dominant role in determining the morphology of the active layer used subsequently for solar cells.

It is interesting to observe that the phase-separated domains in films shown in Figure 5 have a smaller size compared with the corresponding aggregates in solutions presented in Figure 1(c). One possible explanation is that the aggregates of PBDTCT in solutions underwent shrinkage and survived during spin-coating procedure, due to the strong segmental π – π interactions among aggregates and long relaxation time for the aggregates to achieve new configuration. As discussed and observed above, the aggregates are composed of both polymers and solvents. Therefore, the aggregates will shrink to smaller domains after the evaporation of solvents. Thus, the scale of phase separation in composite films would depend on the diameter of aggregates in solution and the amount of PBDTCT polymer in the aggregates. At the same time, the shape of phase-separated domains is also influenced because of the irregular shrinking and collapse of these aggregates and the spatial hindrance effect of the surrounding PCBM component, which depends on the strength of the cross-linking points in solutions. Also, during the spin-coating process, the shearing force and the irregular collapse during the evaporation process would destroy and rebuild some of the polymer segments–solvent molecules π – π interaction, resulting in different domain structure. In B, the size of PBDTCT aggregates is the largest, and the strength of the cross-linking points are the strongest; thus, aggregates would undergo less shape shrinking or irregular collapse during the solidification process. As a result, the film prepared from B shows the largest domain size. The strong forces of cross-linking points of aggregates in B retain the spherical shape of the PBDTCT-rich phases. In contrast, in the other solvents, both the diameter of aggregates and the binding strength of the aggregates become weaker and weaker, leading to smaller and more irregular phase separation in films.

Photovoltaic Behaviors. J – V characteristics of PBDTCT/PCBM-based OSCs are illustrated in Figure 6, and the device parameters are summarized in Table 2. When the solvents

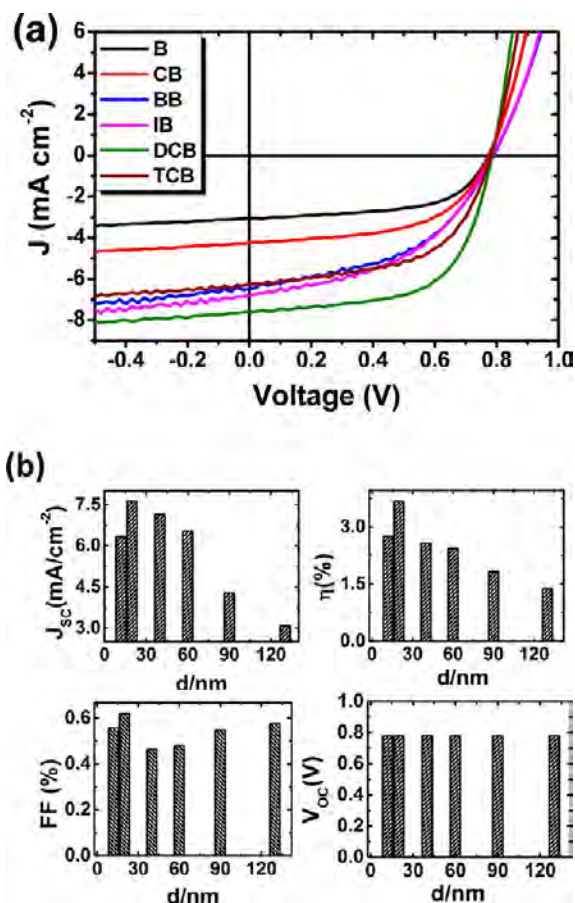


Figure 6. (a) J - V characteristics of ITO/PEDOT-PSS/PBDTCT-PCBM/ Cs_2CO_3 /Al devices with the active layer prepared from different solvents; (b) variations of device parameters (J_{SC} , η , FF, and V_{OC}) with the phase-separated domain size, d .

Table 2. Solvent Dependent PBDTCT-Based PSC Performance

solvent	device parameter			
	J_{SC} ($\text{mA}\cdot\text{cm}^{-2}$)	V_{OC} (V)	η (%)	FF (%)
B	3.08	0.78	1.38	57.7
CB	4.28	0.78	1.83	54.6
BB	6.53	0.78	2.44	47.8
IB	7.14	0.78	2.58	46.3
DCB	7.62	0.78	3.68	62.8
TCB	6.33	0.78	2.75	55.7

varied from B to DCB, the short-circuit current density (J_{SC}) increases monotonously from 3.08 to 7.62 $\text{mA}\cdot\text{cm}^{-2}$ and drops with TCB as the processing solvent. The fill factor (FF) first decreases gradually from B to IB, with the maximum of 0.628 using DCB as the processing solvent. The open-circuit voltage (V_{OC}) in all devices is almost identical (0.78 V). Finally, the best performance is achieved with DCB as the solvent, giving a power conversion efficiency (PCE, η) of 3.68%.

In OSCs, the device parameters are very morphology dependent, which has been intensively studied and reviewed.^{23,42-44} In our case, the correlation between device parameters and morphology is shown in Figure 6(b). With the size of phase-separated domains varying from 130 to 20 nm, J_{SC} increases stepwise and V_{OC} stays identical. It is reported that J_{SC} is determined by the exciton generation, exciton dissociation,

and charge collection processes. In organic semiconductors, the exciton diffusion length is limited to 10–20 nm. Thus, the exciton generated far beyond this length would be quenched instead of dissociated into free carriers at the donor/acceptor interface. Smaller domain sizes will result in more efficient exciton dissociation or charge generation in the bulk. Also, for efficient charge collection, the smooth pathways for both of electrons and holes should be guaranteed. Ordered and large phase-separated domains would benefit this process. In our case, the optimized active layer morphology featured 20 nm phase-separation domain size and nanofiber-like structure when processed from DCB, thus presenting a balance between efficient exciton dissociation and charge collection and leading to the highest J_{SC} and optimized PCE up to 3.68%. This is confirmed by the PL spectra of PBDTCT/PCBM composite film: with the increasing of phase-separation domain size, the PL intensity increased (see the Supporting Information, Figure S5). In the case of the TCB, although a more finely phase-separation morphology is obtained, the number of “dead zones” increased as well, which would induce local space charge zones and increase the bulk recombination of free carriers. Further, the change in J_{SC} is well-confirmed by the EQE spectra (see the Supporting Information, Figure S6). On the other hand, V_{OC} is dominated by the energy level difference of the HOMO of donor and the LUMO of acceptor, with little dependence on the change of built-in potential and leakage current. Therefore, little change on V_{OC} was observed due to the morphology variation.

The change of FF is more complex, which is related to the bulk charge transportation and recombination processes. As shown in Figure 6(b), a slow decreasing trend with phase-separated domain size from 130 to 40 nm was observed; then, FF comes to a maximum at 20 nm domain size and finally dropped with phase-separation domain size around 12 nm. The evolution of FF is attributed to the interplay of two factors, charge or geminate pair recombination and charge collection, which are determined by the size and the shape of the domain. With the phase-separation domain around 130 nm, which is nearly equal to the active layer thickness, it is much easier to form percolated pathways for the transportation of the generated charges, which provides relatively larger FF. When the size of the phase-separated domain becomes smaller, percolated charge-transporting channels are less readily formed, resulting in the observed decrease of FF with CB, BB, and IB as solvents. As in the case of DCB as the solvent, the size of phase-separated domains is small, but the domain shape also changes from spherical to fiberlike. Thus, charges would be transported rapidly to electrodes through the percolated one-dimensional pathways constructed by the connection of fiberlike domains, thereby giving the highest FF among all devices. When using TCB, the size of the phase-separated domain becomes even smaller, and the number of “dead zones” increases, which causes more charge recombination, and a decrease in the charge collection efficiency or FF is observed.

CONCLUSION

In summary, we found the steric hindrance of aromatic solvents greatly influences the aggregation of conjugated polymers in solution. With these controlled aggregates, the effect of solvent-assisted nanoscaled organo-gels on the morphology and performance of organic solar cells was investigated. The polymer aggregates were found to determine the morphologies of blended donor (PBDTCT) and acceptor (PCBM) films.

When the aggregates in solution became larger, the phase-separated domain size in the film became larger as well and less distorted. These results provide guidance to tune the morphology and optimize the photovoltaic properties of OSCs based on PBDTCT/PCBM composite films. We demonstrated the best performance with a power conversion efficiency of 3.68% when prepared from dichlorobenzene solutions (DCB) mainly due to the optimized phase-separated domain in the active layer. As such, this work provides, from a viewpoint of polymer physics, how the processing procedure of polymer thin films affects greatly the performance of OSC as well as implication in OSC optimization.

■ ASSOCIATED CONTENT

Supporting Information

Table of electric dipole moments and solubility parameters for the used solvents, details of the density functional theory calculation, and figures of the molecular structure of PBDTCT, dimer and trimer distortion angles, UV-vis spectra of PBDTCT/PCBM in different solutions, PBDTCT in toluene at different concentrations, PBDTCT in chloroform immediately and after one week, photoluminescence spectra of PBDTCT/PCBM from different solvents, and EQE spectra for devices processed from different solvents. This material is available free of charge via the Internet at <http://pubs.acs.org>.

■ AUTHOR INFORMATION

Corresponding Author

*E-mail: (M.-M. S.) minminshi@zju.edu.cn; (H.-Z. C.) hzchen@zju.edu.cn.

Notes

The authors declare no competing financial interest.

■ ACKNOWLEDGMENTS

This work was supported by the National Natural Science Foundation of China (nos. 50990063, 51073135). We also gratefully acknowledge support from the Danish National Research Foundation and the National Natural Science Foundation of China (grant no. 5101130028) for the Danish-Chinese Center for Organic based Photovoltaic Cells, within which this work was performed. The work was also partly supported by National High Technology Research and Development Program of China (863 Program) (no. 2011AA050520) and the Developing Program of Zhejiang Province Key Scientific and Technical Innovation Team (no. 2009RS0004).

■ REFERENCES

- (1) Li, Y. C.; Chen, C. Y.; Chang, Y. X.; Chuang, P. Y.; Chen, J. H.; Chen, H. L.; Hsu, C. S.; Ivanov, V. A.; Khalatur, P. G.; Chen, S. A. *Langmuir* **2009**, *25*, 4668–4677.
- (2) Li, Y. C.; Chen, K. B.; Chen, H. L.; Hsu, C. S.; Tsao, C. S.; Chen, J. H.; Chen, S. A. *Langmuir* **2006**, *22*, 11009–11015.
- (3) Rahman, M. H.; Liao, S. C.; Chen, H. L.; Chen, J. H.; Ivanov, V. A.; Chu, P. P. J.; Chen, S. A. *Langmuir* **2009**, *25*, 1667–1674.
- (4) Lee, C. K.; Hua, C. C.; Chen, S. A. *Macromolecules* **2010**, *44*, 320–324.
- (5) Rahman, M. H.; Chen, C. Y.; Liao, S. C.; Chen, H. L.; Tsao, C. S.; Chen, J. H.; Liao, J. L.; Ivanov, V. A.; Chen, S. A. *Macromolecules* **2007**, *40*, 6572–6578.
- (6) Babu, S. S.; Prasanthkumar, S.; Ajayaghosh, A. *Angew. Chem., Int. Ed.* **2012**, *51*, 1766–1776.
- (7) Nguyen, T. Q.; Doan, V.; Schwartz, B. J. *J. Chem. Phys.* **1999**, *110*, 4068–4078.

- (8) Huang, Y.; Cheng, H.; Han, C. C. *Macromolecules* **2011**, *44*, 5020–5026.
- (9) Nguyen, T. Q.; Kwong, R. C.; Thompson, M. E.; Schwartz, B. J. *Appl. Phys. Lett.* **2000**, *76*, 2454–2456.
- (10) Fakis, M.; Anastopoulos, D.; Giannetas, V.; Persephonis, P. J. *Phys. Chem. B* **2006**, *110*, 24897–24902.
- (11) Mas-Torrent, M.; Rovira, C. *Chem. Soc. Rev.* **2008**, *37*, 827–838.
- (12) Hong, J. P.; Um, M. C.; Nam, S. R.; Hong, J. I.; Lee, S. *Chem. Commun.* **2009**, 310–312.
- (13) Newbloom, G. M.; Kim, F. S.; Jenekhe, S. A.; Pozzo, D. C. *Macromolecules* **2011**, *44*, 3801–3809.
- (14) Huang, W. Y.; Huang, P. T.; Han, Y. K.; Lee, C. C.; Hsieh, T. L.; Chang, M. Y. *Macromolecules* **2008**, *41*, 7485–7489.
- (15) Kim, B. G.; Jeong, E. J.; Park, H. J.; Bilby, D.; Guo, L. J.; Kim, J. *ACS Appl. Mater. Interface* **2011**, *3*, 674–680.
- (16) Koppe, M.; Brabec, C. J.; Heiml, S.; Schausberger, A.; Duffy, W.; Heeney, M.; McCulloch, I. *Macromolecules* **2009**, *42*, 4661–4666.
- (17) Richards, J. J.; Weigandt, K. M.; Pozzo, D. C. *J. Colloid Interface Sci.* **2011**, *364*, 341–350.
- (18) Ren, S.; Chang, L. Y.; Lim, S. K.; Zhao, J.; Smith, M.; Zhao, N.; Bulović, V.; Bawendi, M.; Gradečak, S. *Nano Lett.* **2011**, *11*, 3998–4002.
- (19) Sun, S.; Salim, T.; Wong, L. H.; Foo, Y. L.; Boey, F.; Lam, Y. M. *J. Mater. Chem.* **2011**, *21*, 377–386.
- (20) Zhao, G. J.; He, Y. J.; Li, Y. F. *Adv. Mater.* **2011**, *22*, 4355–4358.
- (21) Chang, C. Y.; Cheng, Y. J.; Hung, S. H.; Wu, J. S.; Kao, W. S.; Lee, C. H.; Hsu, C. S. *Adv. Mater.* **2012**, *24*, 549–553.
- (22) Campoy-Quiles, M.; Ferenczi, T.; Agostinelli, T.; Etchegoin, P. G.; Kim, Y.; Anthopoulos, T. D.; Stavrinou, P. N.; Bradley, D. D. C.; Nelson, J. *Nat. Mater.* **2008**, *7*, 158–164.
- (23) Chen, D.; Nakahara, A.; Wei, D.; Nordlund, D.; Russell, T. P. *Nano Lett.* **2011**, *11*, 561–567.
- (24) Ma, W. L.; Yang, C. Y.; Gong, X.; Lee, K.; Heeger, A. J. *Adv. Funct. Mater.* **2005**, *15*, 1617–1622.
- (25) Kim, H.; Shin, M.; Kim, Y. *J. Phys. Chem. C* **2009**, *113*, 1620–1623.
- (26) Fan, H. J.; Shang, H. X.; Li, Y. F.; Zhan, X. W. *Appl. Phys. Lett.* **2010**, *97*, 133302.
- (27) Chen, H. Y.; Yang, H.; Yang, G.; Sista, S.; Zadoyan, R.; Li, G.; Yang, Y. *J. Phys. Chem. C* **2009**, *113*, 7946–7953.
- (28) Peet, J.; Kim, J. Y.; Coates, N. E.; Ma, W. L.; Moses, D.; Heeger, A. J.; Bazan, G. C. *Nat. Mater.* **2007**, *6*, 497–500.
- (29) Chan, S. H.; Hsiao, Y. S.; Hung, L. I.; Hwang, G. W.; Chen, H. L.; Ting, C.; Chen, C. P. *Macromolecules* **2010**, *43*, 3399–3405.
- (30) Shaheen, S. E.; Brabec, C. J.; Sariciftci, N. S.; Padinger, F.; Fromherz, T.; Hummelen, J. C. *Appl. Phys. Lett.* **2001**, *78*, 841–843.
- (31) Park, C. D.; Fleetham, T. A.; Li, J.; Vogt, B. D. *Org. Electron.* **2011**, *12*, 1465–1470.
- (32) Sun, Y.; Chien, S. C.; Yip, H. L.; Chen, K. S.; Zhang, Y.; Davies, J. A.; Chen, F. C.; Lin, B.; Jen, A. K. Y. *J. Mater. Chem.* **2012**, *22*, 5587–5595.
- (33) Xin, H.; Ren, G.; Kim, F. S.; Jenekhe, S. A. *Chem. Mater.* **2008**, *20*, 6199–6207.
- (34) Kim, J. H.; Park, J. H.; Lee, J. H.; Kim, J. S.; Sim, M.; Shim, C.; Cho, K. *J. Mater. Chem.* **2010**, *20*, 7398–7405.
- (35) Li, L.; Lu, G.; Yang, X. *J. Mater. Chem.* **2008**, *18*, 1984–1990.
- (36) Hu, X. L.; Shi, M. M.; Chen, J. A.; Zuo, L. J.; Fu, L.; Liu, Y. J.; Chen, H. Z. *Macromol. Rapid Commun.* **2011**, *32*, 506–511.
- (37) Nguyen, T. Q.; Martini, I. B.; Liu, J.; Schwartz, B. J. *J. Phys. Chem. B* **1999**, *104*, 237–255.
- (38) Mihailetchi, V. D.; Koster, L. J. A.; Blom, P. W. M.; Melzer, C.; de Boer, B.; van Duren, J. K. J.; Janssen, R. A. J. *Adv. Funct. Mater.* **2005**, *15*, 795–801.
- (39) Müller, C.; Ferenczi, T. A. M.; Campoy-Quiles, M.; Frost, J. M.; Bradley, D. D. C.; Smith, P.; Stingelin-Stutzmann, N.; Nelson, J. *Adv. Mater.* **2008**, *20*, 3510–3515.
- (40) Sanyal, M.; Schmidt-Hansberg, B.; Klein, M. F. G.; Munuera, C.; Vorobiev, A.; Colsmann, A.; Scharfer, P.; Lemmer, U.; Schabel, W.; Dosch, H.; Barrena, E. *Macromolecules* **2011**, *44*, 3795–3800.

(41) Collins, B. A.; Gann, E.; Guignard, L.; He, X.; McNeill, C. R.; Ade, H. *J. Phys. Chem. Lett.* **2010**, *1*, 3160–3166.

(42) Maturová, K.; van Bavel, S. S.; Wienk, M. M.; Janssen, R. A. J.; Kemerink, M. *Nano Lett.* **2009**, *9*, 3032–3037.

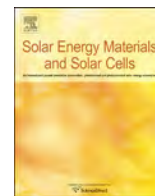
(43) Xin, H.; Reid, O. G.; Ren, G.; Kim, F. S.; Ginger, D. S.; Jenekhe, S. A. *ACS Nano* **2010**, *4*, 1861–1872.

(44) Meng, L.; Shang, Y.; Li, Q.; Li, Y.; Zhan, X.; Shuai, Z.; Kimber, R. G. E.; Walker, A. B. *J. Phys. Chem. B* **2010**, *114*, 36–41.



Contents lists available at ScienceDirect

Solar Energy Materials & Solar Cells

journal homepage: www.elsevier.com/locate/solmat

A rational method for developing and testing stable flexible indium- and vacuum-free multilayer tandem polymer solar cells comprising up to twelve roll processed layers

Thomas R. Andersen, Henrik F. Dam, Birgitta Andreasen, Markus Hösel, Morten V. Madsen, Suren A. Gevorgyan, Roar R. Søndergaard, Mikkel Jørgensen, Frederik C. Krebs*

Department of Energy Conversion and Storage, Technical University of Denmark, Frederiksborgvej 399, DK-4000 Roskilde, Denmark

ARTICLE INFO

Keywords:

Tandem polymer solar cells
ITO free
Vacuum free
Flexible
Roll printed
Stability

ABSTRACT

We demonstrate a method for the preparation of multijunction polymer solar cells without the use of vacuum evaporation methods or indium tin oxide (ITO). The entire layer stack is prepared by printing or coating of each layer. The number of layers typically employed in complete devices exceeds ten and to efficiently identify layers and interfaces that are not robust we developed a double sided illumination method and demonstrate how layer thicknesses can be optimized with respect to the roll processing in the aim of achieving functional tandem devices. The devices were prepared directly on barrier foil and were later encapsulated. In this study the same active material comprising poly-3-hexylthiophene (P3HT) and phenyl-C₆₁-butyric acid methyl ester ([60]PCBM) was employed using nanoparticle based zinc oxide for electron selectivity and several different PEDOT:PSS formulations for hole selectivity, electrode- and recombination layer formation. A novel slanted comb silver grid electrode structure was employed to enable efficient double sided illumination and minimize shunts. The operational stability of the tandem devices evaluated under ISOS-D-2 conditions demonstrated less variation in stability between devices than similar single junctions prepared in the same manner for reference. We demonstrate lifetime studies for 480 h without any sign of degradation and estimate that the tandem or multijunction polymer solar cells are as stable as single junctions.

© 2013 Elsevier B.V. All rights reserved.

1. Introduction

The polymer tandem solar cell has been reviewed several times [1,2] and until now it has mostly been reported with a very small active area on rigid glass substrates using indium tin oxide (ITO) as the semitransparent front electrode and vacuum evaporated back metal back electrodes. In many cases the recombination layer has also been vacuum processed and thus only the two active layers have been solution processed. In some cases the recombination layer has been solution processed [1,2] but in the majority of cases most processing has been carried out in a glovebox and using vacuum deposition for many of the layers. The polymer tandem solar cell prepared without the use of semitransparent indium-tin-oxide electrodes and vacuum steps using only ambient conditions for roll-to-roll printing and coating on flexible substrates undoubtedly represents the ultimate challenge and the pinnacle of complexity within the field of printed and organic electronics [3]. It is also likely that all these requirements will be necessary before

tandem polymer solar cells can become useful outside academic reports. The motivation for preparing the polymer tandem solar cell is clearly the desire to reach the highest achievable performance and the tandem approach or multi-junction approach to photovoltaics in general is the undisputed route to the highest performance in terms of power conversion efficiency. The tandem solar cell also presents the drawback of being more complicated with a significantly smaller room for error and the effort is only justified provided that the process is robust and the extra effort required for its making is returned as a higher efficiency at lower process intensity and a lower embodied energy. The increased complexity is quite possibly also the reason why tandem polymer solar cells initially did not attract so much attention compared to single junctions as shown in Fig. 1 where it is clear that the number of tandem solar cell publications did not increase significantly beyond 10 articles per year until 2010 [3]. In spite of this much lower number of publications by two orders of magnitude the tandem solar cell is rapidly approaching the best reported single junctions.

Printing and coating of polymer solar cells [4] has already been demonstrated to be a fast and viable approach to the manufacture of polymer solar cells while there has been a significant gap

* Corresponding author. Tel.: +45 46 77 47 99.
E-mail address: frkr@dtu.dk (F.C. Krebs).

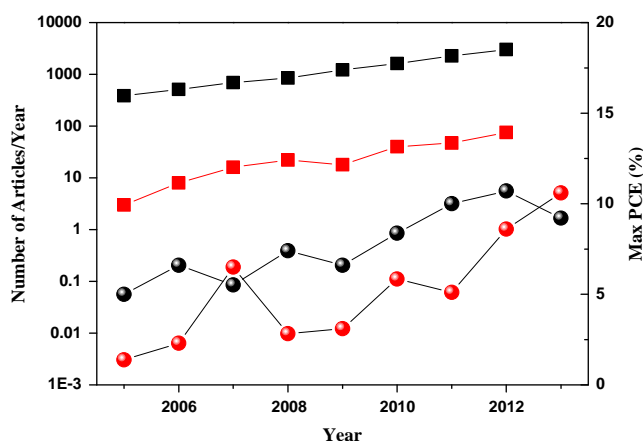


Fig. 1. The number of scientific reports on OPV as a function of time (black squares, left y-axis) as compared to the number of tandem solar cell reports (red squares, left y-axis) shown on a logarithmic scale. The maximum reported PCE (%) for each year for single junction cells (black spheres) and tandem cells (red spheres). (For interpretation of the references to color in this figure legend, the reader is referred to the web version of this article.)

between the reported record efficiencies for small laboratory cells and the well corroborated performance of large area polymer solar cell modules. In addition to this, early printed polymer solar cells still employed indium–tin-oxide as the semitransparent front electrode while several life cycle analysis studies showed that an alternative to indium based electrodes is mandatory for rational use of polymer solar cells including tandem polymer solar cells [5–8]. It was also established that vacuum processing steps require very high polymer solar cell performance to be justified and that printed or coated (vacuum free) polymer solar cells can reach much shorter energy payback times even with a lower performance [9]. While the justification for avoiding both vacuum and indium is compelling it has taken an enormous effort to find convincing alternatives due to the enormous complexity of printing and coating thin 2-dimensionally patterned multilayer films. Traditional processing has limited the number of wet coating steps and has employed vacuum processing wherever possible and this has elegantly avoided the unforgiving challenge of interfacing many thin layers without shunting. Recently a very efficient low cost flexible semitransparent electrode was developed which is in fact so cheap to process that it is freely available to academics [10]. This electrode and processing philosophy serves as the foundation in this work and is explored for processing of tandem polymer solar cells. The largest challenge for the tandem solar cell is how the thicknesses of the individual layers critically influence the overall device performance and imposes firm requirements on the processing conditions as subsequently processed layers must not adversely affect or change previously processed layers. This can to a certain extent be solved through vacuum processing of some layers such as the electrodes and oxide layers. The industrially relevant processes are however expected to employ only printing and coating which does represent a very challenging task and the successful development of functional tandem devices following that approach does require a novel protocol that enables fine tuning of the individual junctions and the interlayers such that a functional device is guaranteed during development even if the given device does not represent the optimal choice. There are two points that must be rationally addressed to achieve this, the first point is that one must be able to address the individual junctions optically such that their individual performance can be established and optimized and the second point is the optimization of the processing conditions for the secondly processed junction such that the performance of the first junction is not adversely affected.

We have in the past successfully prepared tandem solar cells through use of thermocleavable materials [11] whereby the active layers and the interlayers are insolubilized after processing thus enabling solution processing of subsequent layers without affecting underlying layers. The performance was however relatively poor for this approach and required temperature stable glass substrates. In a second embodiment full roll-to-roll processing was employed in all layers on flexible ITO substrates by use of water based emulsions for the back junction [12]. The performance was also found to be poor in this case as the devices had a large active area.

In this work we present our approach to optimize fully printed and coated flexible tandem polymer solar cells and we successfully demonstrate how this method allows for establishing the process windows for new materials combinations in multilayer tandem polymer solar cells. The use of organic solvent based inks was deemed necessary and an optimization of the intermediate layer towards a higher degree of solvent resistance was achieved. For testing of the device performance, and in particular the efficiency of the intermediate layers, a specialized illumination geometry was developed where the device is illuminated from both sides thus enabling controlling the incident light intensity on each junction.

2. Experimental

Solar cells were manufactured on a barrier material substrate (Amcor) with a silver grid/conductive PEDOT:PSS/ZnO electrode. This ITO-free semitransparent electron accepting front electrode known as Flextrode has been previously described [10] and can be obtained freely at www.plasticphotovoltaics.org. Cells were prepared directly on the Flextrode and consisted of a fully slot-die coated layer stack. The final metal back electrode was printed using the flexo technique. The machinery employed has been described [13,14]. ZnO was employed as an electron transport layer, P3HT:PCBM as the active layer, the intermediate recombination layer with a compatibilizing layer comprising PEDOT:PSS and ZnO.

2.1. Materials

Poly-3-hexylthiophene (P3HT from Plextronics) had a M_n of 40,000 Da. Phenyl- C_{61} -butyric acid methyl ester ([60]PCBM, from Solenne) had a purity of 99%. The P3HT:[60]PCBM ink used was 20:20 mg mL⁻¹ ink dissolved in chlorobenzene with 10% chloroform and 3% chloronaphthalene, for 100 nm thick active layer a 10:10 mg mL⁻¹ solution was used for coating. Electron transport layers (ETL) were coated using a stabilized ZnO nanoparticle solution in acetone (49 mg/mL). Several hole transport layers (HTL) were employed in the process of optimizing the method. V₂O₅ was employed where stated as a HTL and compatibilizer layer between the first active layer and the poly(3,4-ethylenedioxythiophene):poly(styrenesulfonate) (PEDOT:PSS) layer and comprised of a vanadium(V)oxiiso-propoxide:isopropanol (IPA) (1:100; 1:1000; 1:2000) solution. Several PEDOT:PSS HTL formulations were used; Clevious P VP Al 4083 or Clevious F-010. In the case of AL 4083 PEDOT:PSS it was mixed in a ratio of 1:2 with IPA and 2% ethyl glycol. PEDOT:PSS (Clevious F-010) was diluted 7:3 with IPA to enhance wetting properties. A MoO_x precursor solution in isopropanol was employed as a second HTL and/or compatibilizer where stated from a neutralized IPA solution. The printable silver back electrode used was PV410 from Dupont. The substrate used was Flextrode with a honeycomb (as described in Ref. [10]) or line silver pattern as developed in this work (see Fig. 2). The cells were encapsulated between two 18 × 18 mm² glass slides with

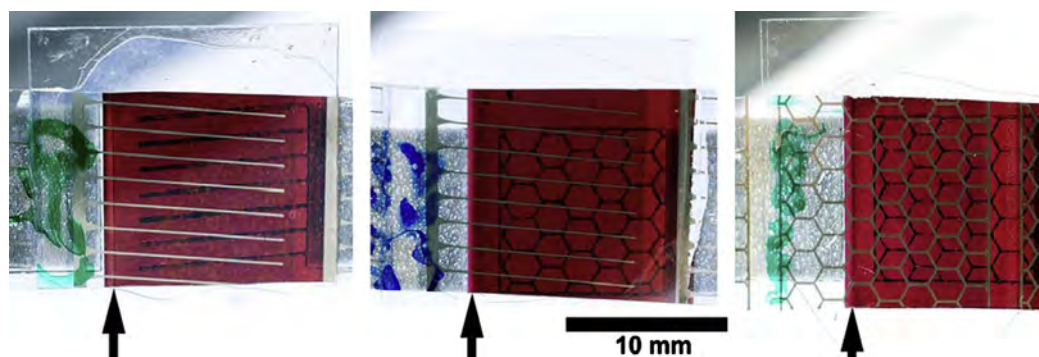


Fig. 2. Photographs of encapsulated tandem solar cells with our slanted grid design. In this left case each finger from front (light lines) and back-electrode (dark lines) has only one direct overlap. In the middle photograph the slanted front electrode has multiple overlaps with the printed honeycomb back electrode. The right photograph displays a tandem cell comprising two honeycomb electrodes. The arrows indicate the edge from the active layer of each subcell.

a UV curable epoxy resin (DELO LP655) adhesive and cured for 2 min under the solar simulator (1000 W m^{-2} , AM1.5G).

2.2. Printing and coating

The silver grids (bottom and top layers) were printed using flexographic printing whereas the remaining 9 layers all were fabricated by slot-die coating on lab scale roll-coater [13]. Flex-trode comprising a large scale roll-to-roll processed silver grid, PEDOT:PSS (Heraeus Clevious PH1000) and ZnO on barrier material was used as substrate in all the experiments. The parameters presented are used as standard parameters with variations for the optimization of the individual layers. The first coated active layer had a thickness of 450–500 nm with a width of 13 mm and was coated with a web-speed of 1 m min^{-1} at $60 \text{ }^\circ\text{C}$. The intermediate layer was coated in 3 steps; V_2O_5 -layers were coated with a web speed of 2 m min^{-1} at $30 \text{ }^\circ\text{C}$ and a wet-thickness of $11.5 \text{ }\mu\text{m}$, the HTL PEDOT:PSS coating had a wet-thickness of $31 \text{ }\mu\text{m}$ with a web speed of 1 m min^{-1} at $60 \text{ }^\circ\text{C}$, and the last layer in the intermediate layer, ZnO, was coated at $60 \text{ }^\circ\text{C}$ with a web speed of 2 m min^{-1} and a wet-thickness of $7.7 \text{ }\mu\text{m}$. To minimize the risk of solvent penetration through the intermediate layer the second active layer was coated at $80 \text{ }^\circ\text{C}$ for faster evaporation. The thickness of this layer was approximately 200 nm coated with a web speed of 1 m min^{-1} . The top electrode also consisted of 3 layers; a MoO_x HTL coated with a web speed of 2 m min^{-1} at $70 \text{ }^\circ\text{C}$ and a wet thickness of $5 \text{ }\mu\text{m}$. On top of the MoO_x , a conducting F010 PEDOT:PSS from a 7:3 solution with IPA was employed, coated with a web speed of 1 m min^{-1} at $70 \text{ }^\circ\text{C}$ and a wet thickness $23 \text{ }\mu\text{m}$. The top silver grid was printed as previously reported [14]. In this study two versions of the Flex-trode design was used. The already reported honeycomb pattern was used in the initial cells and as a reference, while we focused on the improved Flex-trode with slanted grid lines ($+5^\circ$) reported here. In combination with a slanted back electrode comb structure (-5°) we achieve a maximum of two direct overlaps (worst case) from each front and back electrode finger that minimizes the risk of silver-silver shorts. Since both sides of the solar cell present the same slanted comb structure and the same shadow loss this is optimal for double sided illumination and comparison of the two individual junctions. The design is also independent from the web-directional registration. Photographs of fully printed and coated tandem cells are shown in Fig. 2

2.3. External quantum efficiency

Quantum efficiency (QE) measurements of the tandem devices were performed. The approach of QE measurements for tandem devices is significantly more complex than that for the single

junction devices. Tandem devices require measuring each subcell individually within the device and therefore, the process includes a set of additional steps (see e.g. Gilot et al. [15] or ASTM standard E2236-10 [16]). In particular, in order to measure the QE of one subcell in a multijunction device one has to saturate all the other subcells not being measured, which is done via a bias light. To do so, a light with spectrum in the absorption range of the subcells not being measured is used to bias these assuring that the tested sample is the one limiting the current within the multijunction. Additionally, a bias voltage is applied to the tandem device equal to the sum of V_{oc} 's of the subcells not being measured to cancel out the potential of all the junctions not being measured. This assures that the tested sample is at a state of short circuit when QE is measured. In our studies however the QE testing was significantly simplified by the property of double side illumination. Since only double junction devices were in question, it was possible to saturate the bottom subcell by illuminating it from the bottom using simple white light. Most of the light would be absorbed by the bottom subcell due to the thick film assuring that the top cell is the limiting one. This was proved by absorption measurements, which showed that most of the light was absorbed by the first subcell facing the illumination and thus, the second subcell limited the current. The QE was measured using an IPCE setup, which was calibrated with a photodiode with a calibration against NIST standard 1755. The tandem device was placed in the IPCE system such that the bottom subcell faced the bias light and the top subcell faced the testing monochromatic beam. Bias voltage was applied to the sample with the magnitude equal to the V_{oc} of the subcell not being measured. After measuring the QE of the front junction, the sample was flipped and the back junction was measured in the same fashion.

2.4. Stability measurements

To study the stability, the devices were encapsulated using a glass and a UV curable adhesive. ISOS-D-2 testing procedure [17] was used to make a quick assessment of the stability of the completed devices. For that purpose the samples were placed in the dark in an oven with the temperature set to $65 \text{ }^\circ\text{C}$ and a low relative humidity level. During the storage the solar cells were periodically (once every few days) removed from the oven and tested for photovoltaic performance using a class A solar simulator.

2.5. Bending test

A bending test was completed on flexible tandem cells encapsulated with Amcor barrier foil. The test was carried out to establish the resilience of the tandem devices towards bending. The test was completed on a Mecmesin Multitest 2.5-i tensile and

compressive test bench, which was set in compression mode for 0, 1, 10, 100, 1000 times. The resulting bending radius was 10 ± 2 mm.

3. Results and discussion

3.1. Solvent resistance tests for the intermediate layer

One of the first obstacles of using printed electrodes is the inherent roughness of many of the coating methods. In the Flextrode substrate the general surface roughness is low, however distinct spikes are present in the flexographically printed silver grid in the range of 300–600 nm after printing of both PEDOT:PSS PH1000 and ZnO as seen in Fig. 3A. Fig. 3B displays a thin (200–250 nm) first coated active layer with the intermediate layer on top. A solubility test with chloroform on top of the intermediate layer selectively dissolves the active layer around the silver grid lines in the Flextrode. This led to a necessity for thick active layers to avoid dissolution and shunting of the first coated cell and intermediate layer in the tandem cell.

Since thick layers are necessary from a processing standpoint, tandem solar cells fabricated this way suffers from poor performance. This is the case since one active layer absorbs the main fraction of light, as seen in Fig. 4. This issue must of course be solved for tandem solar cells to be functional in a reasonable way.

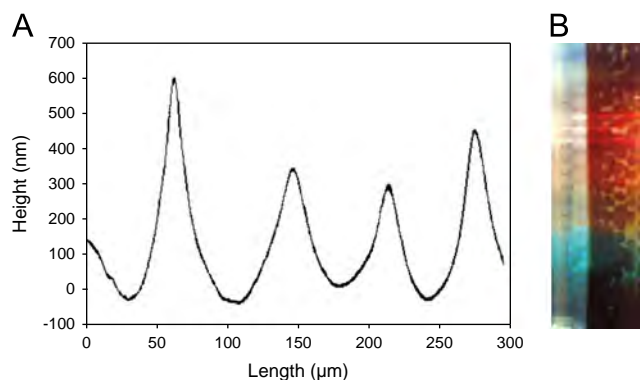


Fig. 3. (A) Height profile of the edge of a silver stripe on the Flextrode measured by a Dektak Profilometer. The height profile shows that four silver spikes are present within a scan-length of 300 μm , varying from around 300 to 600 nm in height. (B) The first coated active layer (thin 200–250 nm) dissolved around the silver grid when depositing chloroform on top of the intermediate layer.

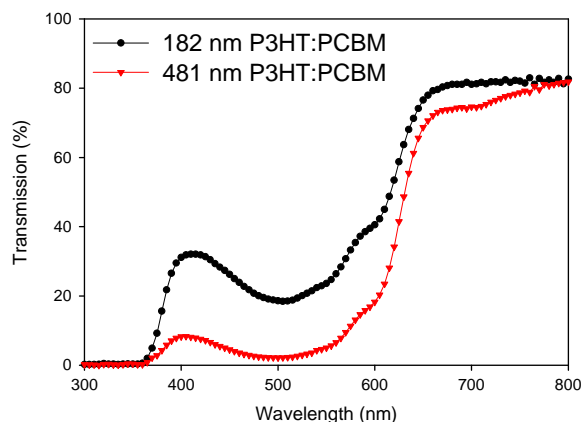


Fig. 4. Transmission through a P3HT:PCBM layer printed on Flextrode directly printed on barrier foil. The absorption of the P3HT film shows that less than 40% of the incoming light remains after a 182 nm layer while less than 10% is left after passage through a 481 nm layer (when integrating the transmission from 350–800 nm). This confirms the almost complete optical separation of the two subcells when using the same polymer in both layers.

Further, for tandem solar cells it is critically important that the materials absorb different parts of the spectrum since otherwise the tandem cell would not be an improvement over a standard cell. However before tandem solar cells can be developed to fulfill all operational requirements, useful information can be extracted from thick layered tandem cells during the development phase, especially when the aim is to be able to process functional multilayer stacks.

3.2. The double sided illumination method

The preparation of homo tandem cells with the same active layer material in both sub cells is the most rational way of testing losses incurred by intermediate layers and poor transport in the tandem cell. In order to do tests on these types of tandem solar cells illumination from both sides was found to be very useful and enabling the identification of failure in each discrete sub cell. This is of course only possible when both electrodes are somewhat transparent or ideally equally transparent.

For this study a mirror setup was constructed which allows double sided illumination under a standard solar simulator. The setup consists of two mirrors mounted 45 degrees to normal. When the cell is placed between the mirrors, light reflects from each mirror ensuring equal illumination from both sides.

3.3. Oxide based recombination layers

From previous publications reporting partially solution processed tandem devices, a stack as shown in Fig. 5 was used with the intermediate layer consisting of a vanadium-oxide layer and ZnO [18] or PEDOT:PSS 4083 and (Al)ZnO [19]. Firstly an intermediate layer comprising vanadium oxide and ZnO was attempted with limited success. Improvements, in single junction cells, have been shown by the use of molybdenum-oxide as a hole selective material [20] and has therefore been used as an alternative to vanadium-oxide. Trials with molybdenum-oxide was carried out with similar results and the main issue being cracks in the intermediate layer (shown in Fig. 6) leading to mixing of the first and second coated active layers. This resulted in poorly performing single junction cells following a device geometry as outlined in Fig. 7.

The same intermediate layer as presented in [19] were tried but dewetting occurred when attempting to slot-die coat the 4083 PEDOT:PSS layer on top the active layer, therefore the V_2O_5 -layer was coated as a compatibilizer, which has been shown to work in the tandem stack by [18]. Using a PEDOT:PSS 4083 layer in the intermediate stack solved the issue seen with cracks forming as shown in Fig. 6B.

Optimization of the intermediate layer was conducted by variation of the thicknesses of all three components (p-type oxide, PEDOT:PSS, n-type oxide). Firstly, we varied the thickness of the V_2O_5 layer by varying the VTIP:IPA concentration and keeping the wet-thickness constant. The results for this thickness variation can be seen in Supplementary information Fig. S2A, the VTIP:IPA 1:1000 out-performed both the thicker and thinner V_2O_5 with a PCE of 0.83% where the largest enhancement is seen for the short circuit current with an increase from respectively -0.28 and -1.40 to -2.40 mA/cm^2 . The lower performance for 1:2000 VTIP:IPA solution could be found in the loss of the ability to work as a compatibilizer, when coating the following 4083 PEDOT:PSS layer, as coating defects were observed. V_2O_5 films with different thicknesses can be seen in Fig. S2B and S2C. Fig. S2B is a V_2O_5 layer with a theoretical thickness of 60 nm, showing a film with discrete pinholes. The V_2O_5 layer seen in Fig. S2C has a theoretical solid thickness of 3 nm, the film is however not fully covering and displays discrete crystals and island formation.

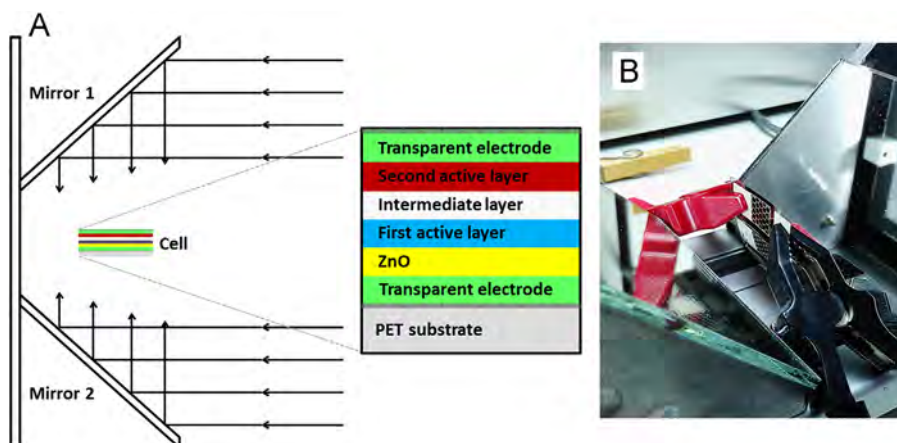


Fig. 5. (A) Illustration of the geometry used for illuminating the tandem solar cells when testing. The intensity received by the cell was effectively 1.4 suns with an equal distribution from both sides. The exploded view of the cell shows the stack of a standard tandem cell but with both top and bottom electrodes being transparent. (B) Image of the mirror test setup with a fully printed ITO-free flexible tandem solar cell in the center (red box). (For interpretation of the references to color in this figure legend, the reader is referred to the web version of this article.)

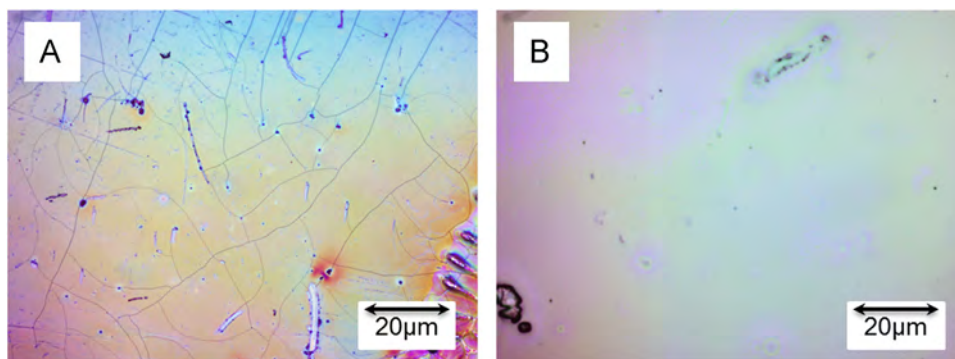


Fig. 6. Cracks in different intermediate layers. (A) Intermediate layer with only MoO_x and ZnO. (B) An intermediate layer containing MoO_x , PEDOT:PSS P VP AL4083 and ZnO.

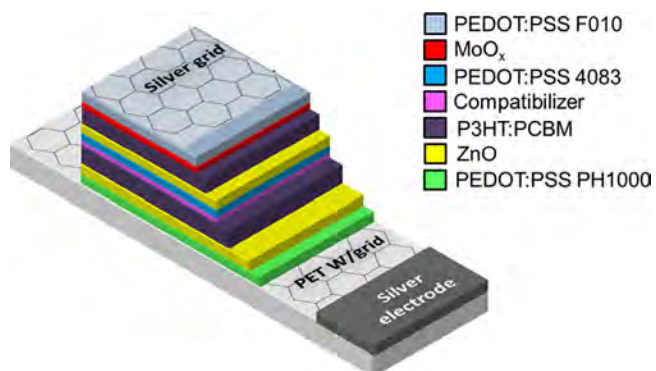


Fig. 7. The material stack first shown to work in a fully printed and roll coated flexible tandem stack on a honeycomb grid electrode. An intermediate layer consisting of a metal-oxide hole selector, PEDOT:PSS hole conductor and zinc-oxide electron selector was used.

IV-curves for devices prepared with a variation in the thickness of the intermediate 4083 PEDOT:PSS layer can be seen in Fig. 8A. They show a tradeoff between current and voltage. Thicker PEDOT:PSS layers yield devices with a higher current but lower voltage than those with a thinner 4083 PEDOT:PSS layer. The thinnest 4083 PEDOT:PSS however lost solvent resistance. Devices with different PEDOT:PSS thicknesses in the intermediate layer were coated from the same 1:2 (4083:IPA) solution by variation of the wet-thickness. The last layer in the intermediate layer is ZnO, Fig. 8B shows the *IV*-characterization for devices fabricated with

two different thicknesses of the ZnO layer. The current appears to be unchanged by the thickness variation whereas there is a small difference in voltage the latter can however be explained by the need for less light soaking when activating the ZnO in the thinner layer. Once we had defined the process conditions and interlayers we found that a device geometry as illustrated in Fig. 7 was robust. It comprised a total of 11 printed and coated layers applied to a flexible barrier substrate.

3.4. EQE measurements of each junction

After examining the *IV*-curves obtained from the optimization of the intermediate layers it is seen that the currents are still very low. To investigate the reason for these low currents, EQE measurements were recorded on the fabricated devices for both the 1st and 2nd active layer. The EQE data obtained can be seen in Fig. 9, the data for the 1st active layer show a large peak which tops at 530 nm with an EQE of around 23%. The EQE data for the 2nd active layer however displays a drop in EQE from 420 to 500 nm. This drop in EQE correlates well with the absorption peak for P3HT, therefore the drop could be caused by strong absorption in the top part of the 2nd active layer, making the distance from the dissociated electrons to the electrode long, giving larger possibility for recombination.

To avoid this drop in EQE in the 2nd active layer a variation of the layer thickness was conducted. Devices with a 2nd active layer estimated thickness of 100 nm, 200 nm, and 300 nm were coated. From the *I-V* curves presented in Fig. 10A it can be seen that a thickness of 200 nm outperforms both 100 nm and 300 nm.

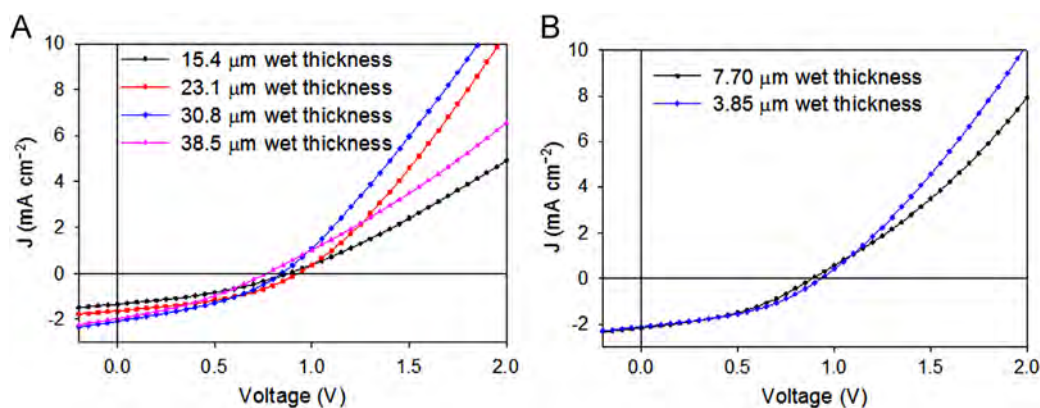


Fig. 8. (A) I - V curves for devices prepared with different thickness of PEDOT:PSS in the intermediate layer. (B) I - V curves from characterization of devices prepared with different thicknesses of the ZnO layer in the intermediate layer by varying the wet thickness in the coating but keeping the concentration constant.

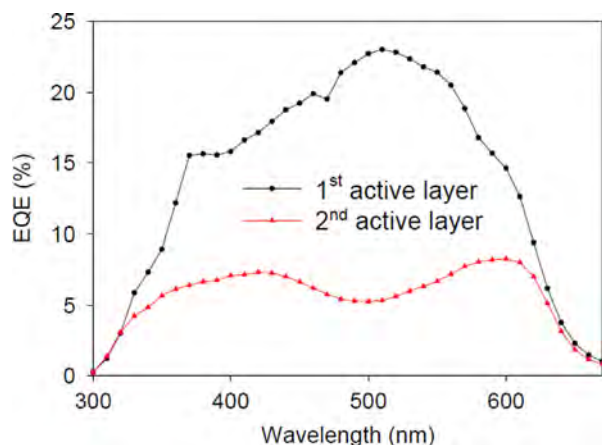


Fig. 9. EQE measurements of the 1st and 2nd active layer in a tandem device.

For the 100 nm thickness coating defects started to occur more frequently, leading to shorting through the active layer.

EQE measurements of device with a 2nd active layer thickness of 200 nm and 480 nm (previously shown) can be seen in Fig. 10B. The previously observed drop in EQE where P3HT absorbs the most has been effectively removed by reducing the layer thickness. As expected there is a minor peak in the EQE around 340 nm, which is due to the illumination through the top electrode and thereby the light doesn't get absorbed in the ZnO layer as it would when illuminating from ZnO.

3.5. The revised 12-layer tandem stack

Homo-junction tandem solar cells based on P3HT:PCBM were studied and achieved a maximum voltage of 1.00 V with a quite significant fill factor at 44% for initial devices with an active area of 1 cm². The current of -2.66 mA cm^{-2} , was however still very low, compared to a single junction P3HT:PCBM device at 700 W/m² illumination intensity. This was attributed to the thickness of V₂O₅, which was found to significantly influence the current that could be extracted from the device, as can be seen in Fig. S2. However, a minimum thickness was required to ensure wetting for the following 4083 PEDOT:PSS layer. This led to the investigation of whether MoO_x or F010 PEDOT:PSS could provide the same layer coating performance without the restriction in current. I - V -curves for the tandem devices are shown in Fig. S3, which clearly shows that the tandem cells with the best overall performance are prepared with F010 PEDOT:PSS as compatibilizer for AL P 4083 (Fig. 11). Devices obtained have similar V_{OC} as devices with V₂O₅ but the currents are much higher, with a J_{SC} of -5.11 mA cm^{-2} , where

devices containing V₂O₅ only have a J_{SC} of approx. -2.7 mA cm^{-2} . A reference single junction solar cell using the same electrodes, overall active layer thickness and active area is also shown. As expected the single junction perform better than the homo tandem junction and the deficit in performance is indicative of the losses incurred by the recombination layer and tandem stack processing. This loss of around 30% thus has to be counteracted by a wide bandgap/low band gap polymer couple for tandem devices that are more efficient than their individual single junction counterparts following the strategy and device geometry employed here.

This led to a simplified stack comprising silver, PEDOT:PSS, ZnO and P3HT:PCBM as shown in Fig. 12, with the intermediate layer stack offering good solvent resistance and an efficient recombination between holes from the 1st coated subcell and electrons from the 2nd coated subcell.

The specific coating parameters for the optimized tandem device with a stack as Fig. 11 can be seen in Table 1. It is noteworthy that all coating temperatures has been conducted at 60 °C, all speeds were 1 m per min. or faster, which for the small roll coater, where these experiments were conducted, is one minute or less per layer, and that the annealing step after coating of the first layer was found to be unnecessary.

3.6. Stability of 12-layer all printed flexible tandem solar cells according to ISOS-D-2

The best performing tandem cell structure, presented in Fig. 12, was chosen to evaluate the lifetime properties of the tandem devices. The stabilities of those were compared to the single devices (active layer thickness is around 480 nm) by performing testing of both types under the same conditions. Three samples of each structure were used for the studies. The efficiency for the single junction devices varied between 1.7 and 2.4%, while for the tandem devices between 0.8 and 1.3%, mainly due to the lower photocurrent of the latter, when measuring with the double illumination setup. For the stability measurement the light intensity were approx. 570 W m⁻² pr. side. The comparison of the stability curves of the normalized PV parameters for the single and tandem devices are shown in Fig. 13. The results revealed a similar stability performance during the period of 20 days, which confirms that the additional layers in the tandem structure did not affect the stability for the devices with the studied configurations.

3.7. Stability of devices to bending

The devices were tested for their stability towards bending. It is well known that ITO does not support bending and device performance is normally significantly reduced or destroyed after

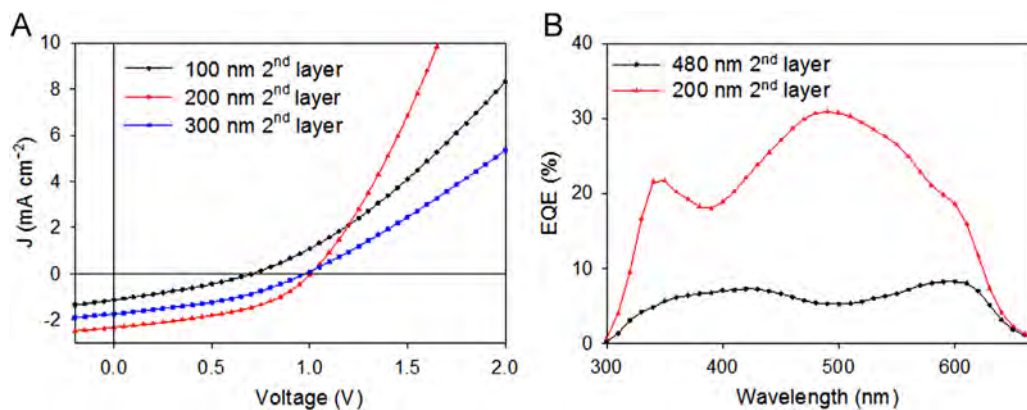


Fig. 10. (A) I - V curves from experiments with variation of the thickness of the 2nd active layer. The thicknesses given of the second cell are estimated from the concentration, wet thickness, and film density. (B) EQE measurements of the 2nd active layer of tandem cell prepared with two different thicknesses of the 2nd active layer.

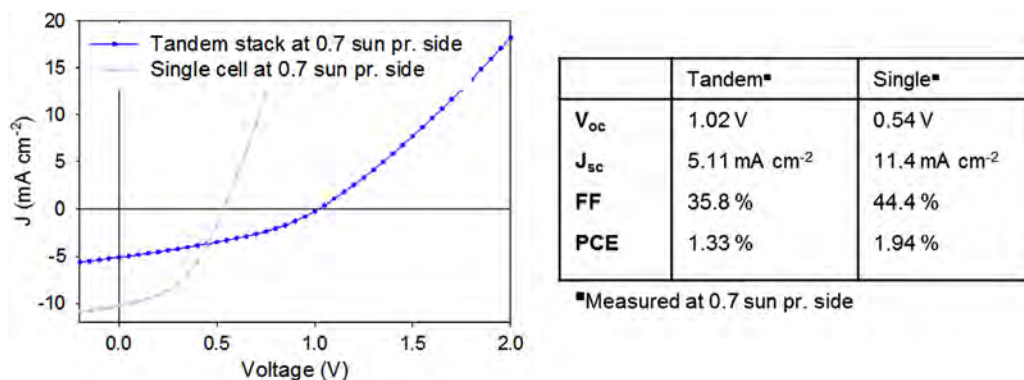


Fig. 11. I - V curves for a cell based on the revised stack comprising F010-ALP4083-ZnO as the intermediate layer and a single junction cell with same active layer thickness as the combined active layer thickness of the tandem cell. The performance given in the curve and table are all shown for a measurement performed with a light intensity of 1.4 suns (700 Wm⁻² pr. side).

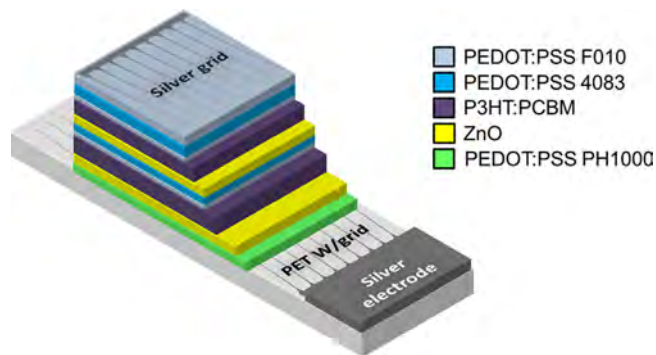


Fig. 12. The final stack, optimized by use of the mirror system, here shown with the slant type electrode.

Table 1

The coating parameters used for the developed coating stack as shown in Fig. 12.

Layer	Material	Concentration	Temperature (°C)	Speed (m/min)	Flow (ml/min)	T_{wet} (μm)
Substrate	Flextrode					
1st active layer	P3HT:PCBM	20:20 mg/ml	60	1.0	0.20	15
Compatibilizer	PEDOT F010:IPA	1:4 vol/vol	60	1.0	0.10	8
HTL	PEDOT 4083:IPA	1:2 vol/vol	60	1.0	0.30	23
ETL	ZnO	39 mg/ml	60	2.0	0.10	3.8
2nd active layer	P3HT:PCBM	20:20 mg/ml	60	1.0	0.08	6
Compatibilizer	PEDOT F010:IPA	1:4 vol/vol	60	1.0	0.10	8
HTL	PEDOT 4083:IPA	1:2 vol/vol	60	1.0	0.30	23
Conducting layer	PEDOT F10:IPA	1:1 vol/vol	60	1.0	0.40	31
Top electrode	Ag PV410		60	1.2		

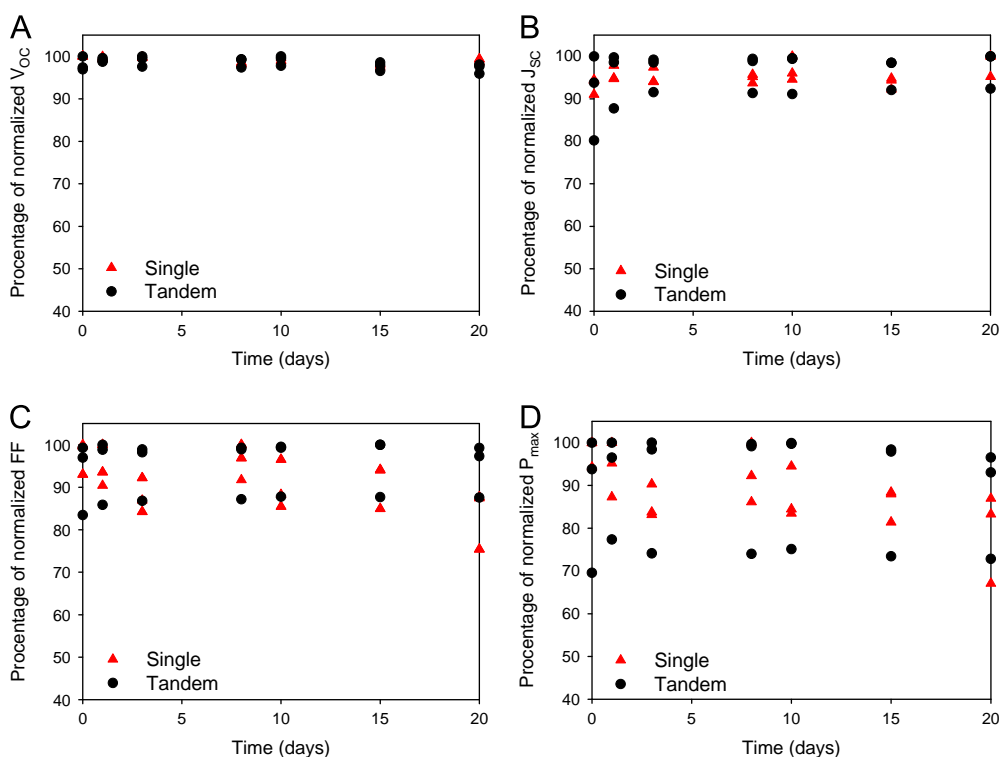


Fig. 13. A short accelerated shelf life stability study of 20 days of duration according to ISOS-D-2 conditions was performed to find if any increased degradation compared to single cell devices would be seen. No increased degradation was experienced for the tandem cells compared to the single cells, suggesting a stable interlayer. The figures are shown with normalized V_{oc} (A), J_{sc} (B), FF (C) and PCE (D).

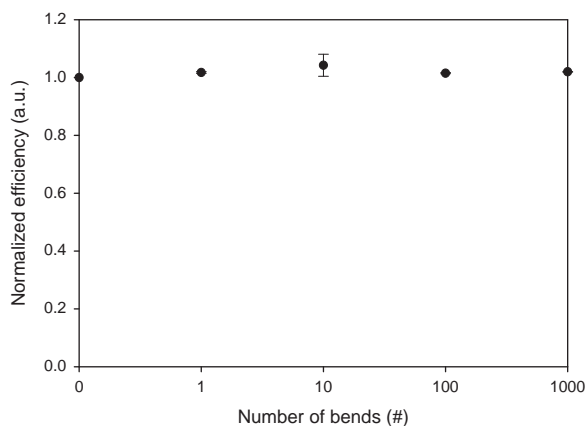


Fig. 14. Results of bending test of Amcor barrier encapsulated cells. Two samples were bended 0, 1, 10, 100 and 1000 times and *IV*-curves were recorded at each stage. The normalized efficiency shows that the bending has little influence on the performance of the cells for a range up to 1000 bends.

a couple of bending cycles [21]. In this case with the added number of layers and interfaces for the tandem stack there could be a higher risk of delamination or having layers cracking. The tandem cells however showed no signs of these effects, as seen in Fig. 14, suggesting that the stack, although being made up of twelve individual layers, have a good adhesion between the layers and that the layers are not damaged by crack formation or delamination during bending [22].

4. Conclusion

We have shown fully wet processed large area tandem solar cells comprising 12 layers on flexible substrates using only roll

processing techniques and highlight a technique to optimize the individual sub cells in the tandem structure by starting with the use of thick active layer thicknesses with a gradual reduction in thickness until the optimum is found. This was enabled through use of transparent electrodes on both sides enabling double sided illumination. Different tandem cell architectures have been prepared with variations in both active layer thicknesses and intermediate layer composition and thicknesses with *IV*- and *EQE*-tests performed to show the variation in the tandem cell performance. Finally, a stability study according to ISOS-D-2 was carried out to test the tandem solar cell stability compared to the single cell structure. We found that the tandem solar cells were as stable as the single junctions and that they seemed to exhibit less variation in performance.

Acknowledgments

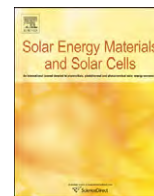
Henrik F. Dam and Thomas R. Andersen contributed equally to the work reported in this article. This work has been supported by Energinet.dk (Project no. 10728) and EU DP (J. no. 64012-0202). Partial financial support was also received from the European Commission as part of the Framework 7, from the EU Indian framework of the "Large cells" project that received funding from the European Commission's Seventh Framework Program (FP7/2007-2013. Grant nos. 261936 and INT/IRMC/EC-SOLAR/OISC/LARGE-CELLS:1/261936/2010), partial financial support was also received from the European Commission as part of the Framework 7 ICT 2009 collaborative project ROTROT (Grant no. 288565).

Appendix A. Supporting information

Supplementary data associated with this article can be found in the online version at <http://dx.doi.org/10.1016/j.solmat.2013.07.006>.

References

- [1] A. Hadipour, B. de Boer, P.W.M. Blom, Organic tandem and multi-junction solar cells, *Advanced Functional Materials* 18 (2008) 169–181.
- [2] T. Ameri, G. Dennler, C. Lungenschmied, C.J. Brabec, Organic tandem solar cells: a review, *Energy and Environmental Science* 2 (2009) 347–363.
- [3] R.R. Søndergaard, M. Hösel, F.C. Krebs, Roll-to-roll fabrication of large area functional organic materials, *Journal of Polymer Science Part B: Polymer Physics* 51 (2013) 16–34.
- [4] R. Søndergaard, M. Hösel, D. Angmo, T.T. Larsen-Olsen, F.C. Krebs, Roll-to-roll fabrication of polymer solar cells, *Materials Today* 15 (2012) 36–49.
- [5] N. Espinosa, M. Hösel, D. Angmo, F.C. Krebs, Solar cells with one-day energy payback for the factories of the future, *Energy and Environmental Science* 5 (2012) 5117–5132.
- [6] N. Espinosa, R. García-Valverde, A. Urbina, F.C. Krebs, A life cycle analysis of polymer solar cell modules prepared using roll-to-roll methods under ambient conditions, *Solar Energy Materials and Solar Cells* 95 (2011) 1293–1302.
- [7] N. Espinosa, R. García-Valverde, F.C. Krebs, Life-cycle analysis of product integrated polymer solar cells, *Energy and Environmental Science* 4 (2011) 1547–1557.
- [8] B. Azzopardi, C.J.M. Emmott, A. Urbina, F.C. Krebs, J. Mutale, J. Nelson, Economic assessment of solar electricity production from organic-based photovoltaic modules in a domestic environment, *Energy and Environmental Science* 4 (2011) 3741–3753.
- [9] N. Espinosa, R. García-Valverde, A. Urbina, F. Lenzmann, M. Manceau, D. Angmo, et al., Life cycle assessment of ITO-free flexible polymer solar cells prepared by roll-to-roll coating and printing, *Solar Energy Materials and Solar Cells* 97 (2012) 3–13.
- [10] M. Hösel, R.R. Søndergaard, M. Jørgensen, F.C. Krebs, Fast inline roll-to-roll printing for indium-tin-oxide-free polymer solar cells using automatic registration, *Energy Technology* 1 (2013) 102–107.
- [11] O. Hagemann, M. Bjerring, N.C. Nielsen, F.C. Krebs, All solution processed tandem polymer solar cells based on thermocleavable materials, *Solar Energy Materials and Solar Cells* 92 (2008) 1327–1335.
- [12] T.T. Larsen-Olsen, T.R. Andersen, B. Andreasen, A.P. Böttiger, E. Bundgaard, K. Norrman, et al., Roll-to-roll processed polymer tandem solar cells partially processed from water, *Solar Energy Materials and Solar Cells* 97 (2012) 43–49.
- [13] H.F. Dam, F.C. Krebs, Simple roll coater with variable coating and temperature control for printed polymer solar cells, *Solar Energy Materials and Solar Cells* 97 (2012) 191–196.
- [14] J.E. Carlé, T.R. Andersen, M. Helgesen, E. Bundgaard, M. Jørgensen, F.C. Krebs, A laboratory scale approach to polymer solar cells using one coating/printing machine, flexible substrates, no ITO, no vacuum and no spincoating, *Solar Energy Materials and Solar Cells* 108 (2013) 126–128.
- [15] J. Gilot, M.M. Wienk, R.A.J. Janssen, Measuring the external quantum efficiency of two-terminal polymer tandem solar cells, *Advanced Functional Materials* 20 (2010) 3904–3911.
- [16] E44 Committee, Test methods for measurement of electrical performance and spectral response of nonconcentrator multijunction photovoltaic cells and modules, ASTM International, 2010.
- [17] M.O. Reese, S.A. Gevorgyan, M. Jørgensen, E. Bundgaard, S.R. Kurtz, D.S. Ginley, et al., Consensus stability testing protocols for organic photovoltaic materials and devices, *Solar Energy Materials and Solar Cells* 95 (2011) 1253–1267.
- [18] T.T. Larsen-Olsen, E. Bundgaard, K.O. Sylvester-Hvid, F.C. Krebs, A solution process for inverted tandem solar cells, *Organic Electronics* 12 (2011) 364–371.
- [19] N. Li, T. Stubhan, D. Baran, J. Min, H. Wang, T. Ameri, et al., Design of the solution-processed intermediate layer by engineering for inverted organic multi junction solar cells, *Advanced Energy Materials* 3 (2013) 301–307.
- [20] C.-H. Chou, W.L. Kwan, Z. Hong, L.-M. Chen, Y. Yang, A Metal-Oxide, Interconnection layer for polymer tandem solar cells with an inverted architecture, *Advanced Materials* 23 (2011) 1282–1286.
- [21] S. Na, S. Kim, J. Jo, D. Kim, Efficient and flexible ITO-free organic solar cells using highly conductive polymer anodes, *Advanced Materials* 20 (2008) 4061–4406.
- [22] S.R. Dupont, M. Oliver, F.C. Krebs, R.H. Dauskardt, Interlayer adhesion in roll-to-roll processed flexible inverted polymer solar cells, *Solar Energy Materials and Solar Cells* 97 (2012) 171–175.



Letter

A laboratory scale approach to polymer solar cells using one coating/printing machine, flexible substrates, no ITO, no vacuum and no spincoating

Jon E. Carlé, Thomas R. Andersen, Martin Helgesen, Eva Bundgaard, Mikkel Jørgensen, Frederik C. Krebs*

Department of Energy Conversion and Storage, Technical University of Denmark, Frederiksborgvej 399, DK-4000 Roskilde, Denmark

ARTICLE INFO

Article history:

Received 6 July 2012

Received in revised form

3 September 2012

Accepted 6 September 2012

Available online 13 October 2012

Keywords:

Roll coating

Silver electrode printing

Flexo printing

Slot-die coating

ITO free

Vacuum free

ABSTRACT

Printing of the silver back electrode under ambient conditions using simple laboratory equipment has been the missing link to fully replace evaporated metal electrodes. Here we demonstrate how a recently developed roll coater is further developed into a single machine that enables processing of all layers of the polymer solar cell without moving the substrate from one machine to another. The novel approach to polymer solar cells is readily scalable using one compact laboratory scale coating/printing machine that is directly compatible with industrial and pilot scale roll-to-roll processing. The use of the techniques was successfully demonstrated in one continuous roll process on flexible polyethylene-terphthalate (PET) substrates and polymer solar cells were prepared by solution processing of five layers using only slot-die coating and flexographic printing. The devices obtained did not employ indium–tin–oxide (ITO) or vacuum evaporation steps making it a significant step beyond the traditional laboratory polymer solar cell processing methods involving spin coating and metal evaporation.

© 2012 Elsevier B.V. All rights reserved.

1. Introduction

The driving force for research within the field of polymer solar cells (PSCs) for several decades has been the huge potential of the technology to enable high volume solution processing under ambient conditions using fast roll-to-roll coating and printing [1] techniques which can make them commercially viable in terms of a very low production cost. However, even with the performance in terms of power conversion efficiency (PCE) and operational stability rapidly approaching the key targets, on a laboratory scale, research directed towards processing of large area solar cells has been very limited, possibly due to the economical aspect of acquiring and running the necessary machinery and the selective focus on reaching high PCEs. The majority of polymer solar cells reported to date comprise a tiny active area ($< 0.1 \text{ cm}^2$) and have been prepared by a combination of spin coating and vacuum evaporation on rigid glass substrates in a protective atmosphere. While, this approach has proven highly successful on the laboratory scale, with reported PCEs up to above 10%, these processing techniques are not roll-to-roll and industry compatible. Thus, novel processing methodologies that enable up-scaling of new developments to a realistic industrial

process are urgently needed for a faster and more direct transfer of PSCs from the laboratory to the larger scale coating facilities.

In this work we present a novel laboratory scale approach to polymer solar cells using one compact coating/printing machine (Fig. 1A), that enable the preparation of polymer solar cells in a directly scalable manner but on a very small scale. The machine enabled the solution processing of five layers on flexible substrates using slot-die coating and flexographic printing under ambient conditions. No ITO, no vacuum and no spin-coating was used in the process. Thus, the preparation of hundreds of fully functional PSCs could be performed in one continuous process within 2 h.

2. Experimental

Slot-die coating was performed for the first four layers of the polymer solar cells, and a small flexographic printing roll was employed for the back electrode, on a simple laboratory roll coater that comprised an improved version of the earlier described machine [2]. The coating station could either accept the slot-die head or the printing roller through a simple mount enabling exchange of coating method in less than a minute. For slot-die coating a head with a meniscus guide of 13 mm width was used for all the slot-die coating in this work as described earlier [2]. The back silver electrode was applied by flexographic printing with the same roll coater having a novel and compact

* Corresponding author. Tel.: +45 46 77 47 99.
E-mail address: frkr@dtu.dk (F.C. Krebs).

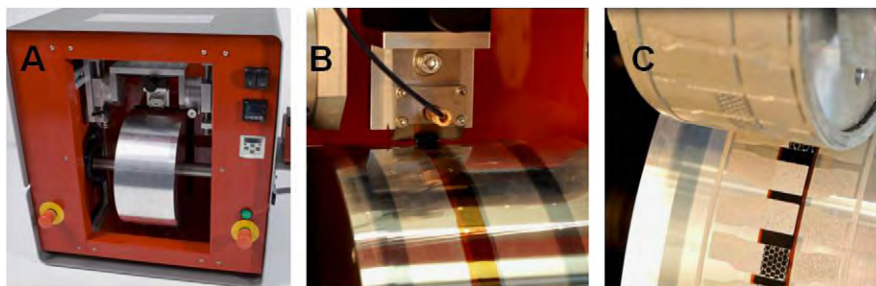


Fig. 1. (A) Picture of the small roll coater seen from the front, (B) slot-die coating of the active layer and (C) flexographic printing of the back silver electrode.

flexographic printing roll that comprised a metal cylinder with side registration. The motif was carried by a laser engraved rubber sleeve that could be fitted directly on the metal cylinder enabling facile exchange of the printing pattern (the outside diameter of the flexo sleeve was 12 inches). The coating machine shown in Fig. 1 is available from FOM Technologies.

2.1. Materials

Coating was performed on either pristine PET substrate or Flextrodes that comprise a highly conducting metal grid, semi-transparent conductor and hole blocking layer (freely available for academics from www.plasticphotovoltaics.com). The metal grid had a hexagonal pattern with a linewidth of 150 μm and a spacing of 2 mm. The height of the lines was 200 nm. The silver grid had a honeycomb structure with 13 mm wide stripes. Two types of highly conductive (HC) PEDOT:PSS was employed. For the front electrode (the firstly printed PEDOT:PSS electrode) we employed Clevis PH1000 from Heraeus diluted with isopropyl alcohol in the ratio 10:3 (w/w). The front PEDOT:PSS electrode had a sheet resistivity of 60–90 $\Omega \text{ square}^{-1}$ and the Flextrode with metal grid had sheet resistivity of 10 $\Omega \text{ Square}^{-1}$. For the back electrode we employed a thicker PEDOT:PSS (Clevis SV3 from Heraeus) also diluted with isopropyl alcohol to a viscosity of 300 mPa s. ZnO nanoparticles in acetone with a concentration of 55 mg/ml was employed for the electron transport layer. The active layer was composed of P3HT (electronic grade from Rieke) and 60PCBM (technical grade from Solenne BV). The PET substrate was Melinex ST506 obtained from Dupont–Teijin. The back silver grid was printed using a screen printing silver paste (PV410 from Dupont), different patterns were explored in this work (either a full silver or a honeycomb pattern). The sheet resistivity of the back PEDOT:PSS electrode was 60 $\Omega \text{ Square}^{-1}$ on its own and the sheet resistivity of the top silver electrode was 0.1 $\Omega \text{ Square}^{-1}$. The dry thickness of the top silver electrode was 6 μm .

2.2. Coating procedure

The pristine PET substrate was mounted on the roller using heat stable tape (3 M) and the procedure began by firstly slot-die coating a layer of PEDOT:PSS layer in the form of 13 mm wide stripes with a wet thickness of 20–40 μm . The coating was performed at a 70 $^{\circ}\text{C}$ roll temperature with a web speed of 0.4 m/min. This was followed by slot-die coating of zinc oxide acetone solution at a web speed of 0.8 m/min giving a wet thickness of 5 μm . The coated material was dried at a temperature of 70 $^{\circ}\text{C}$ affording an insoluble film of zinc oxide on top of the PEDOT:PSS layer. The active layer consisting of P3HT:PCBM (1:1, by weight) dissolved in chlorobenzene (40 mg/ml) was then coated with an offset of 2 mm from the PEDOT:PSS/ZnO electrode enabling electrical contact to be made to the first electrode (see Fig. 1B and schematic in Fig. 2). The flow of the solution was set to 0.1 ml/min and the web speed was varied to give different

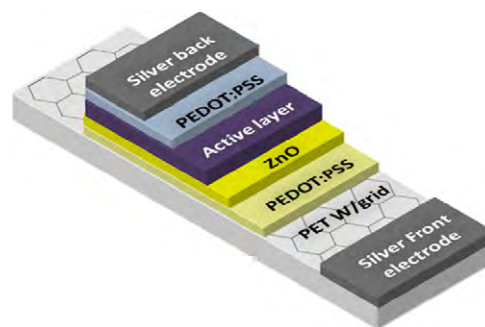


Fig. 2. Schematic illustration of a device with silver current collecting grid on top of a PET substrate. The active area of the devices in this study was 1 cm^2 .

thicknesses of the active layer. The back PEDOT:PSS layer was slot-die coated on the active layer with a further offset of 1 mm (to prevent shorting of the device). The coating was conducted at 80 $^{\circ}\text{C}$ with a web speed of 0.5 m/min affording a wet thickness in the range of 200–250 μm . The layer was dried on the roll for about 20 min. The back silver electrode was applied by flexographic printing of a heat curing silver paste PV410 (Dupont). The silver paste was added to the flexographic roll and further transferred to the substrate with a web speed of 1.2 m/min and roll temperature of 80 $^{\circ}\text{C}$. The completed solar cells were then removed from the roll and annealed at 140 $^{\circ}\text{C}$ in a hot air oven for 20 min before dividing the substrates into more than a hundred individual cells each with an active area of 1 cm^2 .

2.3. Test and measurement

Solar cells were measured with a Keithley 2400 sourcemeter under a KHS 575 solar simulator with an AM1.5G 1000 W/m^2 intensity.

3. Results and discussion

Preparation of the PSC devices explored in this work is illustrated in Fig. 1B and 1C. The first four layers were successfully slot-die coated by the use of a transparent front electrode, based on PEDOT:PSS (optionally with an underlying silver grid) as a solution processable alternative to ITO. The coating head used had a very small dead volume (< 50 μL) allowing use of a minimal amount of solution for coating (typically 1 mL is more than sufficient for a run), which makes this roll coater suitable as a test platform for new materials. During coating it is possible to adjust both the speed of the roll and the pump flow, hereby allowing a high degree of control over the wet thickness for each of the different layers. The system also allows for temperature control, in the range of 25–150 $^{\circ}\text{C}$, securing a fast and even drying of the films. A distinct advantage is that the roll is heated thus

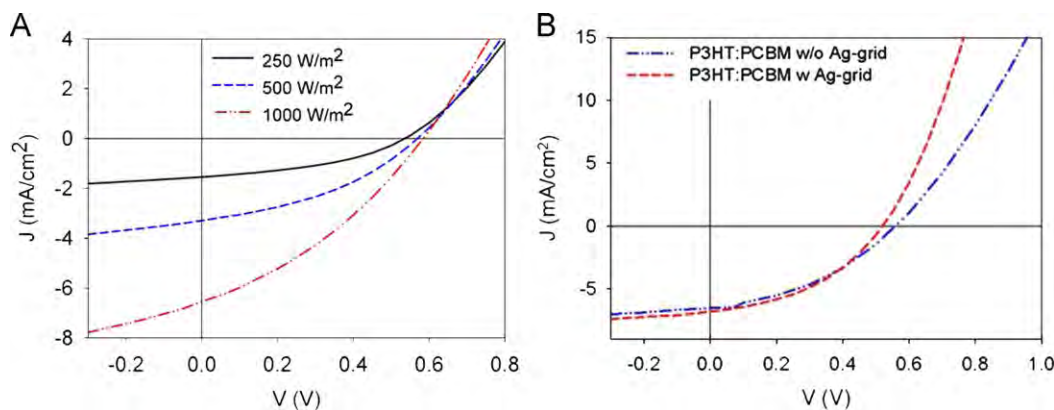


Fig. 3. J - V curves of PSC devices: (A) J - V curves of devices, without front silver grid, as a function of incident light intensity and (B) J - V curves of devices without and with front silver grid.

Table 1

Summary of the J - V data of devices without front silver grid at different light intensities.

Light intensity (W/m ²)	PCE (%)	V_{oc} (V)	J_{sc} (mA/cm ²)	FF (%)
1000	1.31	0.58	6.5	34.2
500	1.45	0.57	3.3	38.6
250	1.35	0.53	1.5	40.6

Table 2

Summary of the J - V data of the two different device types.

Anode	PCE (%)	V_{oc} (V)	J_{sc} (mA/cm ²)	FF (%)
PEDOT	1.4	0.56	6.4	39.5
Silver grid/PEDOT	1.5	0.52	6.7	42.4

enabling successful coating of materials that normally would gel during i.e. spin coating. The back silver electrode was applied by flexographic printing, using a commercially available silver paste, with several different types of patterns and sizes being possible through low cost laser engraving of the rubber sleeve. In a typical coating experiment several stripes were coated, spaced by around 4 cm, so that various process parameters could be altered in a single run. Using a five layer inverted solar cell device geometry such an experiment could be performed within 2 h in one continuous process including drying and cleaning.

The J - V curves of the PSC devices are shown in Fig. 3 (A and B) and the characteristics are given in Tables 1 and 2. For PSCs without front grid it was found that the devices were limited by extraction problems when operated under full sunlight due to the relatively high sheet resistivity of the front PEDOT:PSS electrode (70–90 Ω /square). By decreasing light intensity an improvement in performance was observed which is ascribed to an increase of the FF, as shown in Table 1.

The PSC device with silver front grid shows the highest PCE of 1.5% due to mainly higher current (6.7 mA/cm²) and FF (42.4%). This can be ascribed to a better conductivity of the anode when a honeycomb silver grid is added. On the other hand the grid results in shadow loss by covering some of the area. The total optical transmission through the substrate and grid structure is 70% compared to the substrate itself with a transmission of 85% but there is still an overall gain in short circuit current.

Compared to some of the most well documented examples of a fully R2R coated PSC, where PCEs around 2% are reported by employing ITO electrodes and better control of drying, a PCE of 1.5% obtained in this study is sufficient to validate this laboratory scale approach to PSCs as directly scalable to the large scale roll-to-roll equipment. In contrast to spin-coating this processing methodology makes the transition from lab to production faster/easier and enables optimization of the ink and processing directly at the lab scale with very low ink usage and waste. The avoidance of both ITO and vacuum steps is a significant advantage and the direct compatibility with roll-to-roll processing makes materials development potentially faster.

4. Conclusion

We successfully demonstrated a simple roll coating setup with a versatile platform for rapid exchange of the coating method. The coating machine enables the complete processing of ITO-free polymer solar cells on flexible polyester substrates without the use of vacuum and without moving the polyester substrate during the five processing steps employed here. The enabling feature was found to be the mounting of a compact flexographic printing roller that allow for printing of the silver back electrode in the same place as the slot-die coating head. We demonstrate that flexible P3HT:PCBM based polymer solar cells can be prepared entirely in air without vacuum steps and ITO while qualitatively similar performance can be achieved.

Acknowledgments

We thank Markus Hösel and Torben Damgaard-Nielsen for assisting in the design of the setup. Kristian Larsen and Torben Kjær are gratefully acknowledged for technical assistance and construction of the coating machine and coating/printing units.

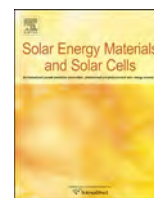
References

- [1] R. Søndergaard, M. Hösel, D. Angmo, T.T. Larsen-Olsen, F.C. Krebs, Roll-to-roll fabrication of polymer solar cells, *Materials Today* 15 (2012) 36–49.
- [2] H.F. Dam, F.C. Krebs, Simple roll coater with variable coating and temperature control for printed polymer solar cells, *Solar Energy Materials & Solar Cells* 97 (2012) 191–196.



Contents lists available at ScienceDirect

Solar Energy Materials & Solar Cells

journal homepage: www.elsevier.com/locate/solmat

The state of organic solar cells—A meta analysis



Mikkel Jørgensen^a, Jon E. Carlé^a, Roar R. Søndergaard^a, Marie Lauritzen^a,
 Nikolaj A. Dagnæs-Hansen^a, Sedi L. Byskov^a, Thomas R. Andersen^a,
 Thue T. Larsen-Olsen^a, Arvid P.L. Böttiger^a, Birgitta Andreasen^a, Lei Fu^b, Lijian Zuo^b,
 Yao Liu^c, Eva Bundgaard^a, Xiaowei Zhan^c, Hongzheng Chen^b, Frederik C. Krebs^{a,*}

^a Department of Energy Conversion and Storage, Technical University of Denmark, Frederiksborgvej 399, DK-4000 Roskilde, Denmark

^b State Key Laboratory of Silicon Materials, MOE Key Laboratory of Macromolecular Synthesis and Functionalization, Department of Polymer Science and Engineering, Zhejiang University, Hangzhou 310027, People's Republic of China

^c Beijing National Laboratory for Molecular Sciences, CAS Key Laboratory of Organic Solids, Institute of Chemistry, Chinese Academy of Sciences, Beijing 100190, People's Republic of China

ARTICLE INFO

Available online 13 June 2013

Keywords:

Polymer solar cells

All data reported until 2012

Statistical analysis

Comparison with other PV

Tandem cells

ABSTRACT

Solar cells that convert sunlight into electrical power have demonstrated a large and consistent growth through several decades. The growth has spawned research on new technologies that potentially enable much faster, less costly and environmentally friendly manufacture from earth abundant materials. Here we review carbon based solar cells through a complete analysis of all the data that has been reported so far and we highlight what can be expected from carbon based technologies and draw scenarios of how it can be made of immediate use.

© 2013 Elsevier B.V. All rights reserved.

1. Introduction

Organic photovoltaic (OPV) research has been in an exponential growth phase since the early reports [1–6] as witnessed by the number of papers produced yearly and the number of new scientists joining the field. This is naturally due to the pressing problem of finding sustainable energy solutions for the future, but perhaps also because the OPV technology is actually not very mature and possess a rich complexity offering many opportunities for research. This also has consequences for commercial exploitation, seemingly representing an uphill battle for an inferior PV technology having to compete with superior and established PV technologies that when taken together have to compete with many high performing renewable technologies such as wind energy and hydropower [7,8]. The OPV technology is attracting because it promises to be very low cost, light weight, produced from abundant materials and easily manufactured at high speed in large scale on simple roll-to-roll printing machinery [9–11]. On the other hand there are some evident hurdles to overcome: the present power conversion efficiency (PCE) is very low ($\leq 10\%$) while optimistic projections have been made [12,13] and the stability is also considered lacking [14,15]. Another problem that has not received much interest is the transition from square millimeter

sized scientific devices arduously prepared in the laboratory to large scale technical production. In many ways it seems that the scientific pursuit of OPV has developed into a race for the best efficiency number through clever schemes of optimizing the chemistry and device fabrication rather than the more distant goal of producing practically useful solar cells. One of the reasons is perhaps that it is by no means settled which materials should be used and what the optimum construction of the OPV device is. It can thus be viewed as one of the attractions (and pitfalls) of OPV research that almost infinite variation is possible. The interesting question is whether research in OPV is indeed justified or whether it is simply an oversold scientific idea? If it is not what can we realistically expect from it? And finally, how would or could we make use of its distinctive features?

2. Seeing OPV “en large”

The progress of photovoltaic technologies is often summed up in a simple diagram of efficiency *versus* time and shows an impressive learning curve for OPV [13], but it is based on a few hero cells and does not reflect the overall status of the field. It would be far more interesting to have all the data to give a comprehensive overview and to be able to extract information on different types of OPV with respect to composition and fabrication. Unfortunately, PV device parameters are not directly accessible in a central database, but are distributed in the ca. 9000 individual

* Corresponding author. Tel.: +45 46 77 47 99.
 E-mail address: frkr@dtu.dk (F.C. Krebs).

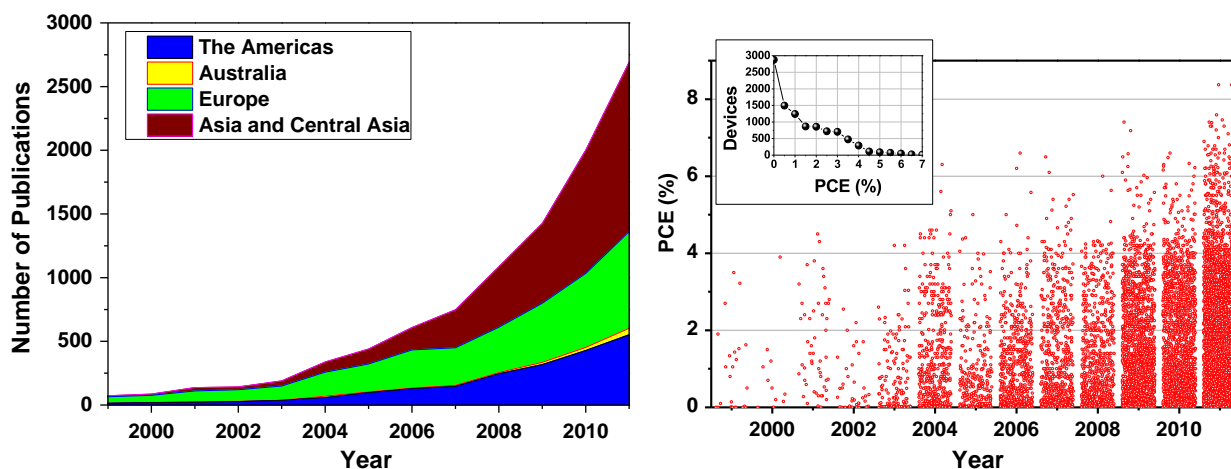


Fig. 1. Number of publications as a function of time with contributions from main countries (left). The PCE values obtained as a function of publication year (right). The inset show the distribution of PCE values.

scientific papers. We judged that this might be the last time that it would be feasible to collect these data by reading through each paper.¹ A search using the terms: “polymer solar cells” or “organic solar cells” were conducted in September 2011 using the Thomson Reuters Web of Knowledge database to compile a series of text files containing the bibliographic information including the digital object identifier (DOI) for each paper excluding review and conference proceeding papers; In total 8962 papers. An Excel database was constructed with a record for each solar cell device found in these papers. Each record has 26 fields comprising bibliographic information, materials used (polymers and acceptors), fabrication details and photovoltaic parameters of efficiency (PCE), open circuit voltage (V_{oc}), short circuit current density (J_{sc}), fill factor (FF), active area *etc.* The database was filled using a custom written program as a front to enter the data into the database read from each article. This resulted in a database of 10533 individual records of solar cells that are used as the basis for this paper. The process of reading papers and entering data took half a year with the help of a number of students and hired assistants. Recently, a smaller database study has been conducted on selected papers concerned with the P3HT:PCBM solar cell including 579 papers covering 2002–2010 [16]. Our aim was to construct a complete database covering all reports and we will in the following try to expose the actual state of OPV based on all publically available solar cell data rather than on single hero cells and also show that certain correlations appear some of which we believe are linked to PV based on carbon and others that may even reach beyond OPV to PV technologies at large.

3. The state of OPV

The search gave 8962 papers written by 15374 individual authors (by Jan 2012). Since year 2000 the growth has been exponential with over 2144 publications in 2011 from 6218 authors of which 5766 had not published in the previous years (in this field). In the beginning most of the contributions came from USA and European countries, but lately the Asia has taken lead. In this search the country of origin was taken from the address of the corresponding author. The exponential increase also means that about half of the authors have only contributed one paper and in the other end of the spectrum 169 (1%) authors have 25 or more papers and in total co-authored 4025 (45%) papers.

In Fig. 1 the PCE value of the individual 10533 solar cells are plotted against the year of submission for the paper. In most OPV papers the term “state of the art solar cells” are equated with the best or “hero” cells produced and these are normally used to indicate the status of the research field. It is clear that substantial progress is being made, but also that hero cells account for a very small part of the population and that they are not representative. Instead, the bulk of PCE values fall far below suggesting that these coveted results are actually rare exceptions. Remarkably, when the number of OPV devices is plotted as a function of PCE one does not get a normal distribution, but rather one that is skewed heavily toward zero PCE. This is in stark contrast to the study by Dang et al. [16] which only considered the maximum PCE for the limited and selected subset for P3HT:PCBM in 579 publications. One of the reasons is of course that the OPV field has become very complex with a huge number of possible variations in structure, chemical composition, fabrication history, interfacial layers *etc.* [17,18]. As a consequence many less performing devices are reported describing non-ideal choices. Some are also due to comparative studies varying different factors and others may simply reflect less competent procedures. It must also be a testament to how poorly defined and documented OPV production is. Even skilled workers may have a hard time duplicating hero cells because it involves factors that are simply unknown or not made public.

The PCE is a function of the product of the open circuit voltage (V_{oc}), short circuit density (J_{sc}) and fill factor (FF) divided by the incident power of the light source (P_i):

$$PCE = \frac{V_{oc} J_{sc} FF}{P_i} \quad (1)$$

When the PCE is plotted as a function of J_{sc} it appears that almost all OPV fall below a diagonal line corresponding to $PCE^{max} \sim 0.55 \times J_{sc}$ (Fig. 2, top left). Remarkably, the best inorganic solar cells also obey this rule except for gallium arsenide (GaAs) cells which have V_{oc} values above 1 V [19]. This limit to the PCE can be derived from the definition (Eq. (1)). For bulk hetero-junction type OPV the upper limit for V_{oc} is believed to be determined by the energy difference between the LUMO energy level of the polymer/organic molecule donor and the HOMO energy level of the acceptor material [20–22]. It is further reduced by the exciton binding energy and other factors. The fill factor of OPV devices vary greatly, but rarely exceeds 60%. It immediately follows that the factor of 0.55 is simply the product of V_{oc}^{max} and FF^{max} . It is not a strict physical limit that cannot be overcome, but as the results show it seems very hard to do so. The V_{oc}^{max} is also a linear function of the band gap which means that there is a trade-

¹ A recent search (Aug 2012) resulted in 13151 papers.

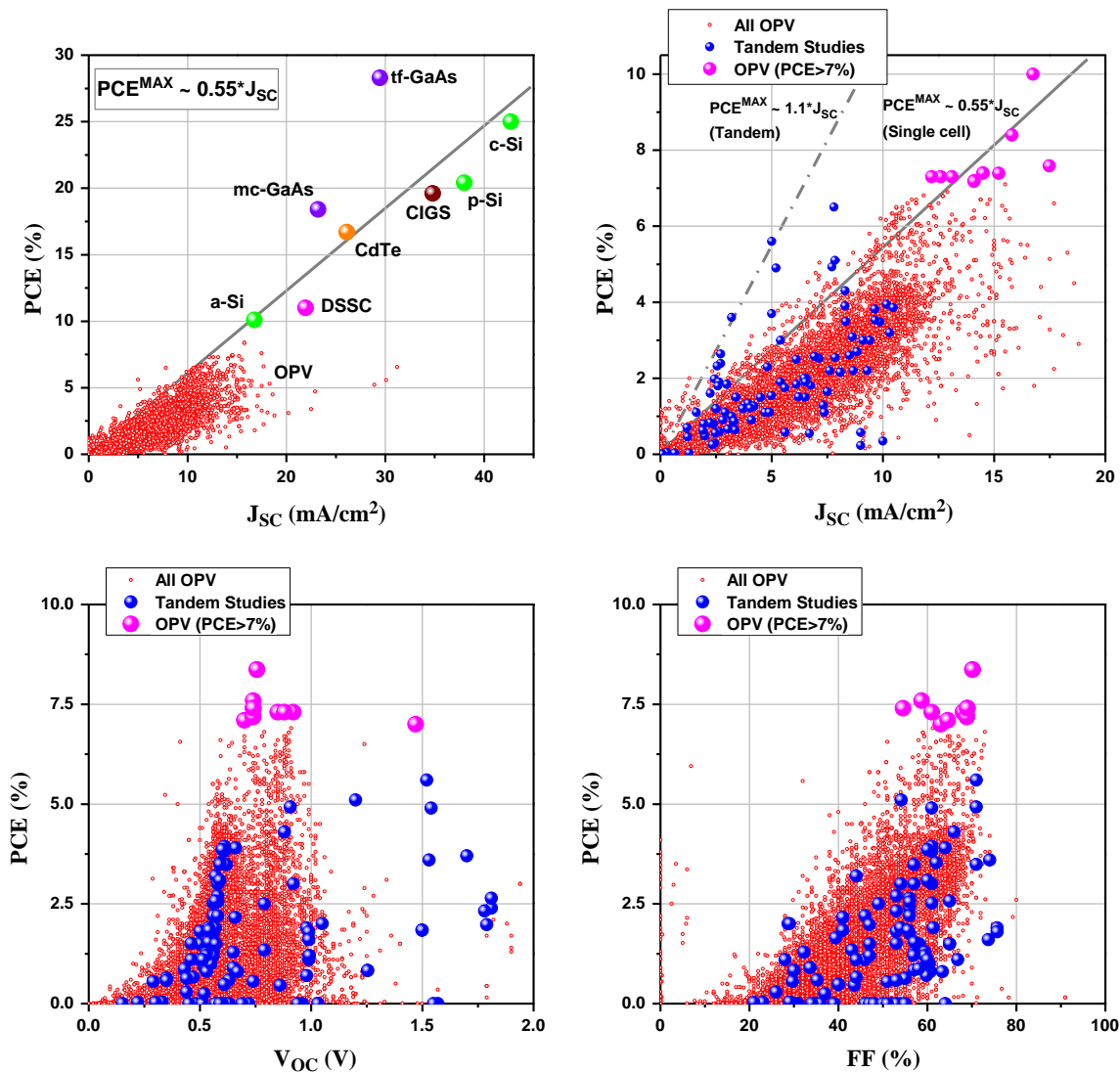


Fig. 2. Top left: A plot of PCE versus J_{SC} for all OPV data (small red circles) together with examples of the best inorganic PV devices (a-Si, p-Si, c-Si: amorphous, polycrystalline and crystalline silicon; DSSC: dye sensitized solar cell; mc-GaAs, tf-GaAs: multicrystalline and thin film Gallium Arsenide; CdTe: Cadmium Telluride; CIGS: Copper Indium Gallium Selenide). The line represents the correlation $PCE^{max} = 0.55 \times J_{SC}$. Top right: A close-up of the OPV region where values from tandem cell studies are marked as larger circles filled with blue color and hero cells with a PCE > 7% is marked by circles filled with magenta color (this group also contains a few tandem cells). The solid gray line show the correlation $PCE^{max} = 0.55 \times J_{SC}$, while the dash-dot line represents the correlation $PCE^{max} = 1.1 \times J_{SC}$ expected for tandem cells. Bottom left: The plot of PCE versus V_{OC} show a narrow distribution of V_{OC} rarely exceeding 1 V. Bottom right: PCE versus fill factor (FF). (For interpretation of the references to color in this figure legend, the reader is referred to the web version of this article.)

off in using low band gap polymers that harvest more low energy photons in that it reduces the possible V_{OC}^{max} [23]. The fill factor is a complex function of the electrical resistance elements in the device which in part depend on the sheet resistance of the electrodes [20]. A common solution has been to decrease the cell size to less than 1 mm² to minimize these losses [24], which would of course also limit their use in any practical application. Previous authors have reviewed the theoretical limits for the PCE of single cell OPV and estimated upper bounds of 10–20% [12,25].

4. Outliers

An escape from the limitations of single cells is to construct tandem cell devices with two cells stacked on top of each other. The top and bottom cells should ideally harvest complementary regions of the spectrum and could at best double the V_{OC} [26–30]. The effect would be to increase the slope to obtain: $PCE^{max} = 1.1 \times J_{SC}$ doubling

the possible efficiency. The number of papers describing tandem cells is still very small and the technical difficulties in the production of them seem to be very large [31–34]. Understandably, most of the cells reported are not optimal and it is yet impossible to judge if this correlation holds true. It is, however, intriguing that a few of the best small molecule OPVs actually follow this prediction very closely [35].

Due to the limited spectral absorption range of the active components of OPV it has proven very hard to increase J_{SC} beyond 15 mA/cm² [36]. These few (18) data points therefore deserve extra scrutiny. Chan et al. described two Copper Phthalocyanine/Rubrene based devices with staggering $J_{SC} = 22.9$ mA/cm², PCE = 4.72% and $J_{SC} = 30.1$ mA/cm², PCE = 5.58% [37]. Kim et al. used an optimized FTO electrode with the standard active layer mixture P3HT:PCBM to give four devices with J_{SC} 16.8–22.5 mA/cm² [38]. A few of these high J_{SC} data points are due to devices with low band gap materials. Chen et al. described a silole-benzothiadiazole based copolymer (DTS-BDT) ($J_{SC} = 16.5$ mA/cm²) [39]. Exchanging silicon for germanium Fei et al. obtained devices with $J_{SC} = 18.4$ and 18.6 mA/cm² [40]. In such cases

experimental detail concerning the light source and illumination condition would enable more in depth analysis.

5. Polymers and acceptors

Each record in our database also contained fields for a crude division of which polymers and acceptors were used. The polymers were subdivided into five categories: P3HT, MEH-PPV, MDMO-PPV, other polymers (mainly low band gap polymers) and none (usually molecular solar cells). Fig. 3 shows how the relative number of devices with these polymer categories are distributed for the J_{SC} and V_{OC} parameters.

The J_{SC} distribution for P3HT show a broad peak centered at 8 mA/cm² with a tail out to ca. 12.5 mA/cm² while the V_{OC} distribution show a very sharp peak at 0.6 V. If a fairly decent fill factor of 60% is chosen this would imply that P3HT containing devices should give PCE values in the range of 2.5–4.5%. In the case of the two other

polymer categories the J_{SC} distribution has no prominent peaks, but are rather dominated by a large population of low performance devices. For the “Other Polymers” category there is, however, a small peak around 14 mA/cm² which is due to low band gap polymers that can harvest a greater portion of the spectrum relative to P3HT [40–42]. This category is of course diverse and thus contains many examples of polymers that do not work well in OPV. In the V_{OC} distribution both the PPV and the “Other Polymer” categories show sharp peaks with PPV centered at 0.82 V while “Other Polymers” have two maxima at 0.63 V and 0.83 V. A similar subdivision was performed for different types of acceptor materials as shown in Fig. 4.

In the case of acceptor materials a somewhat larger selection were used to subdivide the data. Solar cells incorporating C60, C70, [60]PCBM and Bis [60]PCBM are mainly located in the lower left hand corner of the PCE versus J_{SC} plot, whereas those with [70]PCBM and ICBA stretch further up giving more efficient devices. The effect of the acceptor type on the V_{OC} can be seen in the plot of the relative number

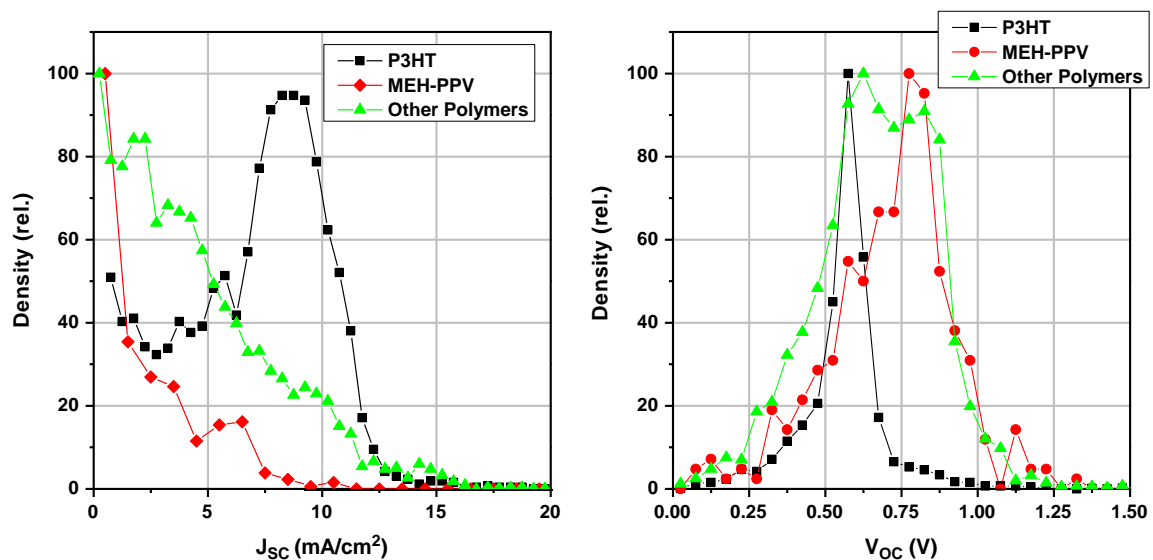


Fig. 3. Relative number of devices versus J_{SC} (left) and V_{OC} (right) for different polymer types.

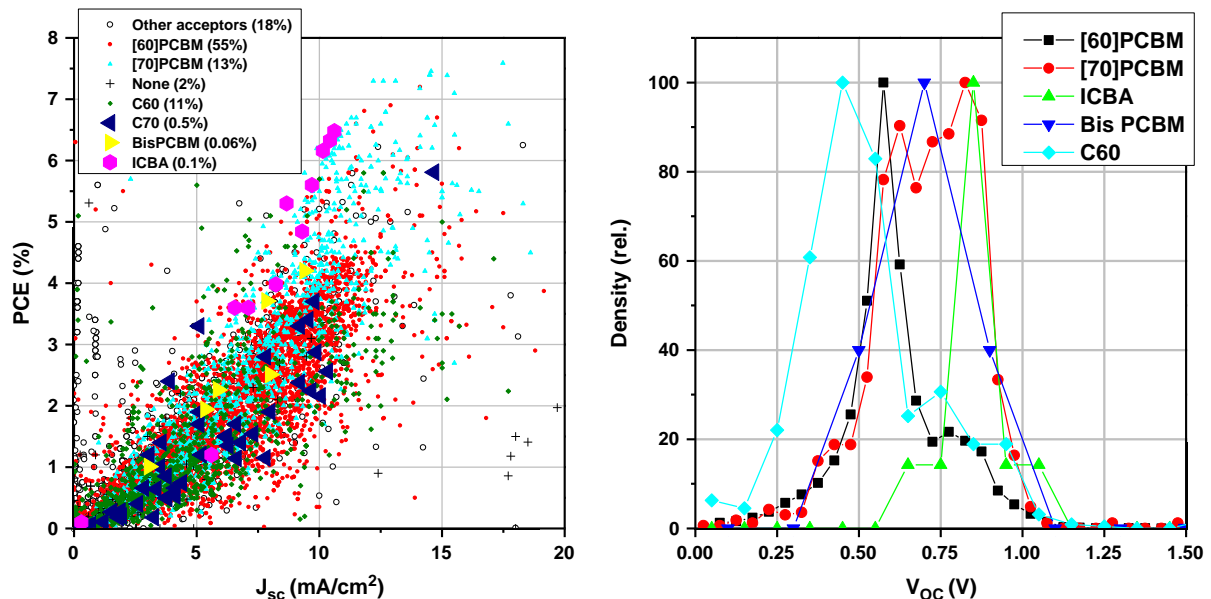


Fig. 4. PCE versus J_{SC} plot (left) and relative number of devices versus V_{OC} plot (right) for different types of acceptor materials used.

of devices versus V_{OC} (Fig. 3, right) where it is clear that C60 and [60]-PCBM give lower values than [70]-PCBM, PCBM, ICBA and Bis-PCBM.

The improvements in efficiency have been gained both in increased light harvesting resulting in a larger J_{SC} , but also by significantly increasing the V_{OC} . The main factors are obviously the shift from higher to lower band gap polymers and the choice of acceptors to match energy levels for maximizing the V_{OC} [43–46]. It is therefore interesting to look at the combined effects of the polymer and acceptor. We selected four categories: P3HT or other polymers with either [60] PCBM or [70]-PCBM. The result is shown in Fig. 5 as a plot of PCE versus J_{SC} for all four types of devices and in Fig. 5 as a plot of V_{OC} versus J_{SC} of the mean values of the four categories. Exchanging [60] PCBM for [70] PCBM increases both the J_{SC} and V_{OC} though the effect is larger for the “Other Polymer” types

($\Delta J_{SC} \sim 1.4 \text{ mA/cm}^2$, $\Delta V_{OC} \sim 0.15 \text{ V}$). This can probably be explained by assuming that many new low band gap materials (“Other Polymers”) have been engineered so that their energy levels have been optimized for [70] PCBM [47,48].

6. Annealing and additives

In most OPV devices the active layer responsible for photon absorption and carrier generation is of the bulk heterojunction type where the donor (polymer) and acceptor microphase separate into a bi-continuous network with a high internal surface where electron hole separation can take place and act as channels for transport of the two carrier types [49–52]. The optimum

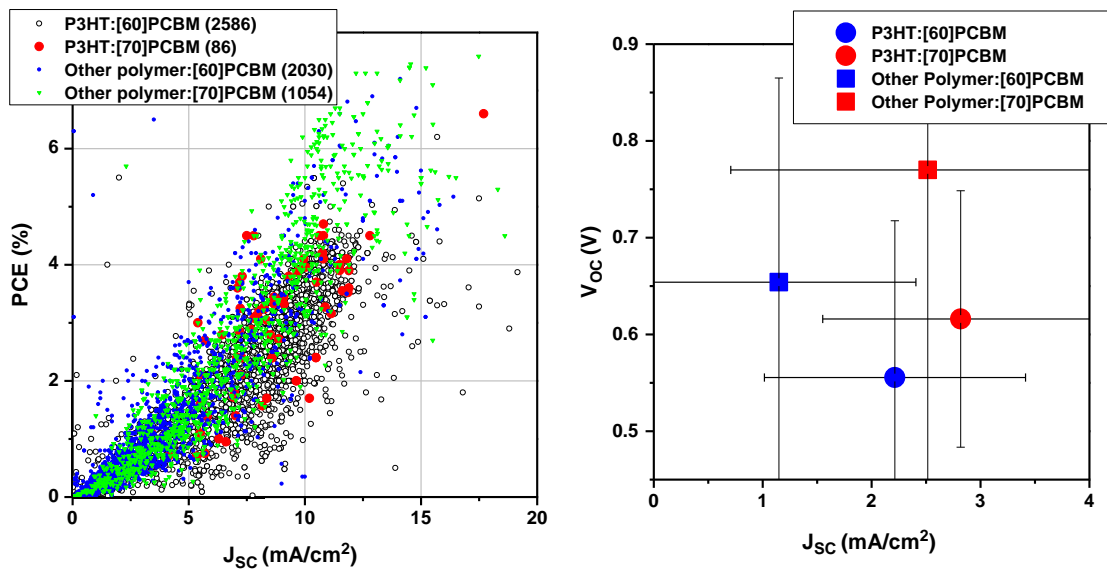


Fig. 5. Comparison of P3HT versus other polymers with either [60] PCBM or [70] PCBM.

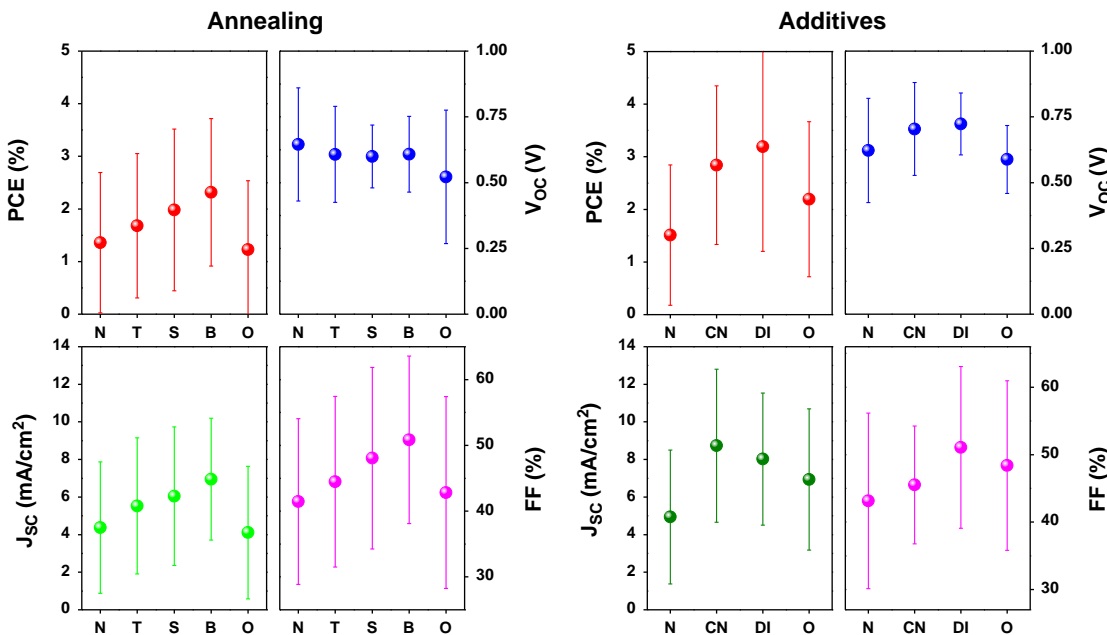


Fig. 6. Left: variation in mean values of solar cell parameters for devices annealed with different methods. (N: no annealing; T: temperature annealing; S: solvent annealing; B: both temperature and solvent annealing, O: Other annealing method). Right: variation of solar cell parameters with additives. (N: none; CN: 1-chloro-naphthalene; DI:1,8-diiodooctane; and O: other additive).

morphology may require some post treatment procedures and the most common method is to anneal the devices by heating them for a short period of time [53–55]. An alternative option is to expose the devices to solvent vapors that have been proposed to dissolve selectively into one of the components of the active layer mobilizing it enough to help the morphology to change [56–58]. A statistical analysis was carried out with the result shown in the plots in Fig. 6 left which clearly show that both temperature and solvent annealing increases PCE, mainly through increases in J_{SC} and FF, while V_{OC} is negatively affected.

Another popular stratagem is to use additives such as 1,8-diiodooctane or 1-chloronaphthalene to the active layer solution which increase the efficiency [45,59–62] as shown in Fig. 6 right. This time the better PCE is due to increases in all the parameters: V_{OC} , J_{SC} and FF. Molecular OPV devices account for 14% of the database where the active layer may be composed of discrete molecules of compounds such as phthalocyanines (CuPc, ZnPc), pentacene, tetracene, oligothiophenes [63–66]. Typical devices are constructed using chemical vapor deposition of these compounds sometimes creating gradients or mixtures of several of these to obtain bulk heterojunction type structures [67].

7. Normal versus inverted geometry

One of the important developments in OPV has been the shift from “normal” geometry of the OPV stack, where electrons exit from the top electrode (usually aluminum) and holes from the bottom (usually ITO), to the “inverted” geometry where electrons exit at the bottom and holes at the top [68–70]. This change allows (or determine) the use of other metals such as silver to be used as the top electrode which are much more resistant to oxygen and water [14,71,72]. The result is usually far more stable OPV devices that with proper encapsulation may even last for years alleviating the operational stability challenge [73–75]. The normal geometry is still by far the most common accounting for 90% even in 2011. It also still has a slight edge over the inverted geometry in terms of PCE and J_{SC} as seen in Fig. 7.

8. Fabrication methods and environment

The standard method of fabricating OPV is still using spin coating to apply thin layers of solutions such as the polymer: acceptor and PEDOT:PSS. The reason for its widespread use is of

course that it is a simple technology offering some control over the wet thickness of the film [76]. On the other hand it also constrains experiments to small individual rigid substrates which are far removed from any projected industrial production of OPV. Much of today's literature on OPV focuses on methods to optimize the efficiency and they may be hard to transfer from the laboratory to an industrial process [9]. So there is a real danger that much of this effort will have to be duplicated when a shift to roll-to-roll (R2R) fabrication methods occur. Most fabrication environments include a glovebox to minimize exposure to oxygen/water that are known to rapidly degrade devices [10,14,15]. Substrates are almost exclusively glass with a layer of ITO acting as one electrode. Finally nearly all fabrication methods involve a vacuum step such as evaporation of a metal electrode. R2R fabrication on flexible

Table 1
Fabrication methods and environment.

Fabrication method	Environment	Substrate	Vacuum	ITO
Spin Coating	86% Glovebox	90% Glass	99%	99%
Roll-to-roll (R2R)	0.5% Ambient air	10% Flexible	0.5%	
Unknown or other	13%			

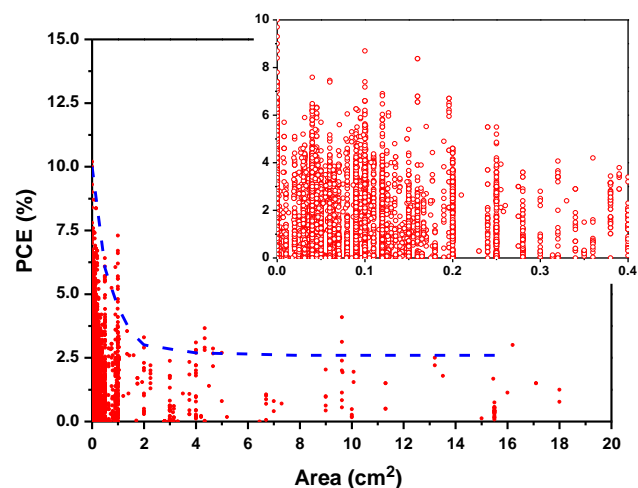


Fig. 8. A plot of the power conversion efficiency as a function of active area. The dotted blue curve is a guide to the eye. The insert is a zoom in on areas below 0.4 cm² that are very popular.

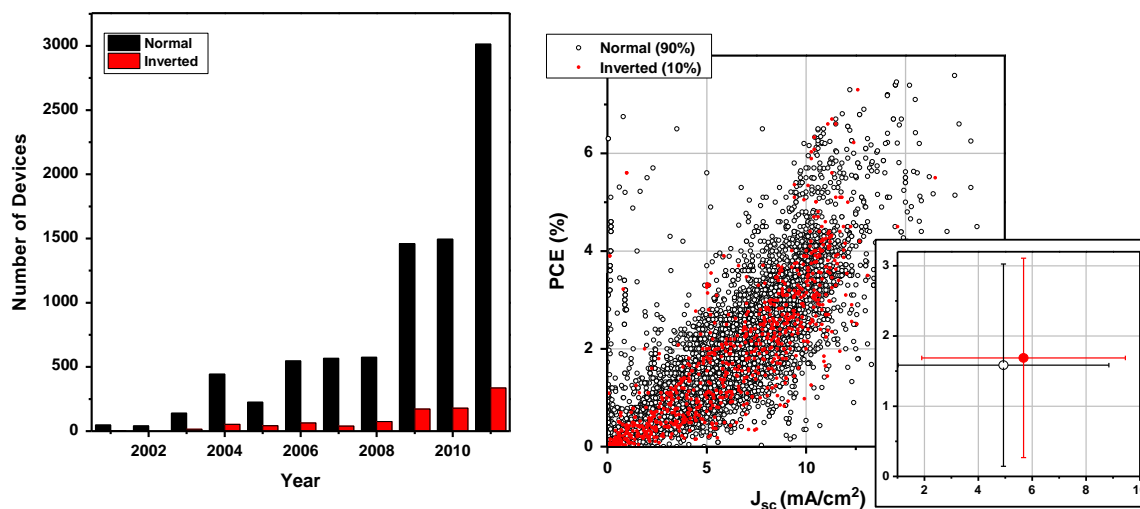


Fig. 7. Normal versus inverted geometry of the OPV stack. Number of devices per year (left). PCE versus J_{SC} (right).

substrates only account for 0.5% of the solar cell devices listed in the literature (Table 1). It must be mentioned, however, that at least one study has been carried out with R2R production of 10,000 solar cell modules (160,000 solar cells) made over a few days which is similar to the total number of devices in the present study [77]. This demonstrates the huge difference in production speed between these two modes of fabrication.

9. The active area of OPV

Mature photovoltaic technologies usually measure the device area in many square centimeters and upwards. Most OPV devices on the other hand are less than 0.2 cm² as shown in Fig. 8. One reason is the larger sheet resistivity of ITO compared to metals such as silver limiting the charge collection and thus also the efficiency [24]. Although the data is limited for device areas above 1 cm² it seems the efficiency falls off exponentially with size at very small active areas and stabilize at higher active areas. How the sheet resistivity influences the maximum obtainable PCE depends on the geometry of the device and use of metal bus bars to help charge collection [78]. In a typical layout this would lead to a more linear dependence between PCE and the area which does not seem in accordance with the data. Another factor that must be considered is the uncertainty in measuring the area correctly [79]. For a rectangular device with an area of e.g. 0.04 cm² which seems very popular this means accurately determining side lengths of 2 mm. Reporting the correct efficiency is not trivial involving both the accurate determination of the active area, the lamp power (if using a solar simulator) and the accurate measurement of small currents in an IV curve. This has led to a number of recommendations on how to perform and report these measurements [80]. Many authors advocate that exceptionally high efficiencies be checked by certified institutions such as NREL or Fraunhofer ISE and others. This is, however, a costly and time consuming practice that has not been widely adopted. A common practice is to use a shadow mask in front of the solar cell to define the illuminated area. This of course serves to define the active area and eliminate errors in harvesting light outside the active area, but still involves the accurate measurement of the aperture of the mask [81]. Other subtle errors are also introduced by this procedure due to the distance between the mask and the active layer and the amount of diffuse light from the lamp in comparison to the real sun which is outside the scope of this review [82–84]. The data suggests that it might be appropriate to also set a minimum standard area for the measurement of OPV efficiency. It is also striking that while most authors adhere to the promise of OPV as a low cost alternative to mature PV technologies the combined active area of all the laboratory scale OPV devices only cover 0.98 m² and the 86% of the devices which have an area of less than or equal to 0.2 cm² amount to only 0.04 m² in total.

10. Seeing the field of OPV from above

It is clear that the field of OPV has drawn an enormous number of researchers to it and from the analysis above it is also evident that the furtherance of the field will require some mode of direction other than what is in operation today. Currently the research carried out in the field is self-justified with a few exponents defining research targets through achievement of extreme values for a single parameter which is most often the efficiency but also the operational stability has been used as a metric [1,2,4–6,54,69,70,85,86]. In achieving those values which serve as a firm ground for competition the field is in near contradiction with the original vision of OPV. To recite the advantages of OPV (and perhaps also its purposes) they are large area, flexible solar cells with a thin outline prepared under

ambient conditions using fast modes of manufacture without the use of scarce elements such as indium, silver, gold or toxic solvents [87–89]. State-of-the-art OPV falls far from the vision in all these aspects [90]. The clearest conclusion to draw from the database study above (Fig. 8) is perhaps that the active area that one should as a minimum employ is 1 cm² and perhaps 4–5 cm² is a more conservative measure guaranteeing some level of scalability based on a report. It is, however, unreasonable to expect that scientists are willing to (or can) change the set of rules that are already in operation. It must also be borne in mind that this commonly practiced approach is linked to the questions of how good a value that can be achieved? but also to whom the result is addressed? The answer to the former question is still open while the data presented in Fig. 2 does show some clear boundaries. The answer to the latter question is that it is mostly for the scientists themselves in their isolated community. To change it, in the aim of widespread practical dissemination of OPV for energy production we would have to create a new and valiant purpose or indeed pursue the original purpose as per the vision of OPV. A second observation that might be partly linked to the active area is that OPV would seem to follow the empirical relationship plotted in Fig. 2 and thus imply that practical total area efficiencies for single junction carbon based PV will be around 5% (and perhaps 8% for tandem solar cells) when deployed over many square meters.

11. The new ground for competition

The most natural way to approach the vision of OPV would simply be to create meaningful energy with it and this would also resolve the challenge outlined above. The best measure of the usefulness of an energy technology is how fast it pays back the energy invested in it which is known as the energy payback time (EPBT) [91,92] and how many times it can do this in its service life known as the energy return factor (ERF) [91]. To be useful as a technology and do less harm to the environment requires that the ERF is significantly larger than one unless the technology in question (OPV) replaces something worse or more harmful [93]. The most obvious approach would be to measure the amount of electricity delivered to the electricity grid by reporting the reading from an electricity meter and relating it to the total area of the platform as exposed to the sun in a given geographical location. Clearly the area should be meaningful and on the order of square meters in an effort to allow for easy comparison to other PV technologies but also other renewable energy technologies. The calculation of the EPBT is achieved through life cycle analysis (LCA) and requires quite extensive knowledge of the process and also of the origin of all the ingredients entering the process leading to OPV [87,89,92–94]. Turning things upside down using such an approach may seem radical but is likely to be the necessary step up for OPV thus establishing whether it is indeed justifiably viewed as an energy technology or whether it is a phantom of scientific thinking.

12. What an OPV plant should look like and how it is different

Under the assumption given above that single junction carbon based solar cells will maximally yield 5% power conversion efficiency on the total area (for square meter sized panels) in a form that can be mass produced, it is possible to pose the question of how an OPV power plant should be constituted to be useful? Firstly, the general view is that solar parks based on crystalline silicon solar cells are barely profitable due to the performance which is viewed as low for the purpose (12–20%) unless the geographic location provides favorable conditions in the form of

a high degree of insolation or the local policy enables investment through favorable subsidy. It is thus clear that for a solar park based on OPV with the premise that the maximally achievable total area power conversion efficiency is 5% (8% on tandem architectures) will be unsuccessful if it is simply a deployment following the same methods as those currently employed for crystalline silicon solar cells [7,91]. This somber (but factual) view of the future of OPV will come true unless one takes specific advantage of the competitive edges that OPV does present while circumventing the distinct weaknesses that OPV admittedly also possess. To summarize, the weaknesses are linked solely to the power conversion efficiency [95–97] and the operational stability [14,90] and in the following we assume a total (large) area efficiency of 5% for single junctions and an operational lifetime under outdoor conditions of 5 years. The list of competitive edges of OPV compared to other solar cell technologies is long and even when compared to other renewable energy technologies OPV does have significant vantage points. The OPV technology is the only renewable energy technology that enables energy payback times of less than a few months, it is also the only technology that in spite of the relatively short service life potentially offer energy return factors in excess of 100 [91]. Finally, it is also the only energy technology that enables ultra-fast manufacture of a given energy producing unit [91]. This all implies that the OPV technology is already competitive and one can ask why it is not in use yet. The answer to this question is linked to the low performance and the consequent requirement for a large landmass. Also to make use of the advantages listed above the mode of deployment and the scaffold used for mounting the OPV has to be significantly different from traditional PV and clearly the landmass has to be available at very low cost. Arid regions that have no agricultural value are an obvious choice for PV and would be mandatory in the case of large scale deployment of OPV. Since insolation in such regions is usually high this would also be beneficial. One advantage of OPV is that it can be printed on flexible foil in near endless form [9] and if this property was employed in the deployment such that for instance a roll of solar cells was installed by simply rolling it out along a long fixed scaffold the installation rates would exceed panel based PV by several orders of magnitude such that the installation rate ideally matches the manufacturing rate. This implies that the installation would have to be achieved in an automated fashion and would also have to enable simultaneous de-installation for potential re-use while reinstalling new OPV at the end of the service life. The scaffold would of course be a lasting and reusable structure. We can thus outline how OPV should be installed to be useful and also highlight that this can already be realized with the currently available version of OPV. In the ultimate vision OPV is deployed in conjunction with other large renewable energy harvesting parks such as solar farms on- or off-shore thus minimizing infrastructure requirements and thus exploiting the synergy inherent in the complementarity between the different renewable energy technologies such as wind and solar power.

13. Conclusions

We compiled a database with all reported data for organic and polymer solar cells and found more than 10,000 recorded observations. We presented all these data in the context of photovoltaics in general and viewed single junction and tandem OPV. We also analyzed the effect of post processing treatments such as thermal annealing and solvent additives and viewed all these data. We found an enormous spread in data and that the reported high performance of OPV is resting on a few reports whereas the vast majority fall much lower and we conclude that the technological performance of OPV is much lower than the reported state-of-the-art. The possible reason for this is an observed exponential increase

in reported efficiency with decreasing active area and we propose that an active area $> 1 \text{ cm}^2$ should be employed to obtain meaningful data. To conclude, the polymer and organic solar cells have to rise to power in grid connected installations and focus should be turned to a gain in widespread use or alternatively we have to accept it as a stimulating scientific discipline serving the purpose of being a useful educational tool for the academic environment.

Acknowledgments

This work was supported the Danish National Research Foundation.

References

- [1] C.W. Tang, 2-Layer organic photovoltaic cell, *Applied Physics Letters* 48 (1986) 183–185.
- [2] S.E. Shaheen, C.J. Brabec, N.S. Sariciftci, F. Padinger, T. Fromherz, J.C. Hummelen, 2.5% efficient organic plastic solar cells, *Applied Physics Letters* 78 (2001) 841–843.
- [3] P. Peumans, S. Uchida, S.R. Forrest, Efficient bulk heterojunction photovoltaic cells using small-molecular-weight organic thin films, *Nature* 425 (2003) 158–162.
- [4] N.S. Sariciftci, L. Smilowitz, A.J. Heeger, F. Wudl, Photoinduced electron-transfer from A conducting polymer to buckminsterfullerene, *Science* 258 (1992) 1474–1476.
- [5] S. Morita, A.A. Zakhidov, K. Yoshino, Doping effect of buckminsterfullerene in conducting polymer: Change of absorption spectrum and quenching of luminescence, *Solid State Communications* 82 (1992) 249–252.
- [6] J.J.M. Halls, C.A. Walsh, N.C. Greenham, E.A. Marseglia, R.H. Friend, S.C. Moratti, A.B. Holmes, Efficient photodiodes from interpenetrating polymer networks, *Nature* 376 (1995) 498–500.
- [7] B. Azzopardi, C.J.M. Emmott, A. Urbina, F.C. Krebs, J. Mutale, J. Nelson, Economic assessment of solar electricity production from organic-based photovoltaic modules in a domestic environment, *Energy and Environmental Science* 4 (2011) 3741–3753.
- [8] T.D. Nielsen, C. Cruickshank, S. Foged, J. Thorsen, F.C. Krebs, Business, market and intellectual property analysis of polymer solar cells, *Solar Energy Materials and Solar Cells* 94 (2010) 1553–1571.
- [9] R. Søndergaard, M. Hösel, D. Angmo, T.T. Larsen-Olsen, F.C. Krebs, Roll-to-roll fabrication of polymer solar cells, *Materials Today* 15 (2012) 36–49.
- [10] Y. Galagan, I.G. de Vries, A.P. Langen, R. Andriessen, W.J.H. Verhees, S.C. Veenstra, J.M. Kroon, Technology development for roll-to-roll production of organic photovoltaics, *Chemical Engineering and Processing* 50 (2011) 454–461.
- [11] F.C. Krebs, J. Fyenbo, M. Jørgensen, Product integration of compact roll-to-roll processed polymer solar cell modules: methods and manufacture using flexographic printing, slot-die coating and rotary screen printing, *Journal of Materials Chemistry* 20 (2010) 8994–9001.
- [12] M.C. Scharber, D. Wühlbacher, M. Koppe, P. Denk, C. Waldauf, A.J. Heeger, C.L. Brabec, Design rules for donors in bulk-heterojunction solar cells—towards 10% energy-conversion efficiency, *Advanced Materials* 18 (2006) 789–794.
- [13] C.J. Brabec, S. Gowrisanker, J.J. Halls, D. Laird, S. Jia, S.P. Williams, Polymer-fullerene bulk-heterojunction solar cells, *Advanced Materials* 22 (2010) 3839–3856.
- [14] M. Jørgensen, K. Norrman, S.A. Gevorgyan, T. Tromholt, B. Andreasen, F.C. Krebs, Stability of polymer solar cells, *Advanced Materials* 24 (2012) 580–612.
- [15] N. Grosseord, J.M. Kroon, R. Andriessen, P.W.M. Blom, Degradation mechanisms in organic photovoltaic devices, *Organic Electronics* 13 (2012) 432–456.
- [16] M.T. Dang, L. Hirsch, G. Wantz, P3HT:PCBM, best seller in polymer photovoltaic research, *Advanced Materials* 23 (2011) 3597–3602.
- [17] G. Li, R. Zhu, Y. Yang, Polymer solar cells, *Nature Photonics* 6 (2012) 153–161.
- [18] S.R. Forrest, The path to ubiquitous and low-cost organic electronic appliances on plastic, *Nature* 428 (2004) 911–918.
- [19] H. Matsubara, T. Tanabe, A. Saegusa, S. Takagishi, T. Shirakawa, GaAs solar cell with GaInP window grown by all metalorganic source MOVPE, in: *Proceedings of the IEEE Photovoltaic Specialists Conference* vol. 2 (1994) pp. 1871–1873.
- [20] C. Winder, N.S. Sariciftci, Low bandgap polymers for photon harvesting in bulk heterojunction solar cells, *Journal of Materials Chemistry* 14 (2004) 1077–1086.
- [21] T.M. Clarke, J.R. Durrant, Charge photogeneration in organic solar cells, *Chemical Reviews* 110 (2010) 6736–6767.
- [22] S. Yamamoto, A. Orimo, H. Ohkita, H. Benten, S. Ito, H. Ohkita, Molecular understanding of the open-circuit voltage of polymer:fullerene solar cells, *Advanced Energy Materials* 2 (2012) 229–237.
- [23] R. Kroon, M. Lenes, J.C. Hummelen, P.W.M. Blom, B. de Boer, Small bandgap polymers for organic solar cells (polymer material development in the last 5 years), *Polymer Reviews* 48 (2008) 531–582.

- [24] J.D. Servaites, S. Yeganeh, T.J. Marks, M.A. Ratner, Efficiency enhancement in organic photovoltaic cells: consequences of optimizing series resistance, *Advanced Functional Materials* 20 (2010) 97–104.
- [25] Z.M. Beiley, M.D. McGehee, Modeling low cost hybrid tandem photovoltaics with the potential for efficiencies exceeding 20%, *Energy and Environmental Science* 5 (2012) 9173–9179.
- [26] L. Dou, J. You, J. Yang, C.C. Chen, Y. He, S. Murase, T. Moriarty, K. Emery, G. Li, Y. Yang, Tandem polymer solar cells featuring a spectrally matched low-bandgap polymer, *Nature Photonics* 6 (2012) 180.
- [27] S. Sista, Z. Hong, L.M. Chen, Y. Yang, Tandem polymer photovoltaic cells—current status, challenges and future outlook, *Energy and Environmental Science* 4 (2011) 1606–1620.
- [28] J.Y. Kim, K. Lee, N.E. Coates, D. Moses, T.Q. Nguyen, M. Dante, A.J. Heeger, Efficient tandem polymer solar cells fabricated by all-solution processing, *Science* 317 (2007) 222–225.
- [29] J. Gilot, M.M. Wienk, R.A.J. Janssen, Optimizing polymer tandem solar cells, *Advanced Materials* 22 (2010) E67–E71.
- [30] T. Ameri, G. Dennler, C. Lungenschmied, C.J. Brabec, Organic tandem solar cells: a review, *Energy and Environmental Science* 2 (2009) 347–363.
- [31] T.T. Larsen-Olsen, T.R. Andersen, B. Andreasen, A.P. Böttiger, E. Bundgaard, K. Norrman, J.W. Andreasen, M. Jørgensen, F.C. Krebs, Roll-to-roll processed polymer tandem solar cells partially processed from water, *Solar Energy Materials and Solar Cells* 97 (2012) 43–49.
- [32] A. Hadipour, B. de Boer, J. Wildeman, F.B. Kooistra, J.C. Hummelen, M.G. R. Turbiez, M.M. Wienk, R.A.J. Janssen, P.W.M. Blom, Solution-processed organic tandem solar cells, *Advanced Functional Materials* 16 (2006) 1897–1903.
- [33] A. Hadipour, B. de Boer, P.W.M. Blom, Organic tandem and multi-junction solar cells, *Advanced Functional Materials* 18 (2008) 169–181.
- [34] V. Shrotriya, G. Li, Y. Yao, C.W. Chu, Y. Yang, Transition metal oxides as the buffer layer for polymer photovoltaic cells, *Applied Physics Letters* 88 (2006) 073508-1–073508-3.
- [35] M. Riede, C. Uhrich, J. Widmer, R. Timmreck, D. Wynands, G. Schwartz, W. Gehr, D. Hildebrandt, A. Weiss, J. Hwang, S. Sundarraj, P. Erk, M. Pfeiffer, K. Leo, Efficient organic tandem solar cells based on small molecules, *Advanced Functional Materials* 21 (2011) 3019–3028.
- [36] Y. Li, Molecular design of photovoltaic materials for polymer solar cells: toward suitable electronic energy levels and broad absorption, *Accounts of Chemical Research* 45 (2012) 723–733.
- [37] M.Y. Chan, S.L. Lai, M.K. Fung, C.S. Lee, S.T. Lee, Doping-induced efficiency enhancement in organic photovoltaic devices, *Applied Physics Letters* 90 (2007) 089902-1–089902-2.
- [38] H. Kim, G.P. Kushto, R.C.Y. Auyeung, A. Piqué, Optimization of F-doped SnO₂ electrodes for organic photovoltaic devices, *Applied Physics A* 93 (2008) 521–526.
- [39] S. Chen, K.R. Choudhury, J. Subbiah, F. So, C.M. Amb, J.R. Reynolds, Photocarrier recombination in polymer solar cells based on P3HT and silole-based copolymer, *Advanced Energy Materials* 1 (2011) 963–969.
- [40] Z. Fei, J.S. Kim, J. Smith, E.B. Domingo, T.D. Anthopoulos, N. Stingelin, S. E. Watkins, J.S. Kim, M. Heeney, A low band gap co-polymer of dithienogermole and 2,1,3-benzothiadiazole by Suzuki polycondensation and its application in transistor and photovoltaic cells, *Journal of Materials Chemistry* 21 (2011) 16257–16263.
- [41] B.C. Thompson, J.M.J. Fréchet, Organic photovoltaics—polymer–fullerene composite solar cells, *Angewandte Chemie-International Edition* 47 (2008) 58–77.
- [42] J. Hou, H.Y. Chen, S.Q. Zhang, G. Li, Y. Yang, Synthesis, characterization, and photovoltaic properties of a low band gap polymer based on silole-containing polythiophenes and 2,1,3-benzothiadiazole, *Journal of the American Chemical Society* 130 (2008) 16144–16145.
- [43] E. Wang, L. Hou, Z. Wang, S. Hellström, F. Zhang, O. Inganäs, M.R. Andersson, An Easily Synthesized Blue Polymer for High-Performance Polymer Solar Cells, *Advanced Materials* 22 (2010) 5240–5244.
- [44] E.G. Wang, L. Wang, L.F. Lan, C. Luo, W.L. Zhuang, J.B. Peng, Y. Cao, High-performance polymer heterojunction solar cells of a polysilylfluorene derivative, *Applied Physics Letters* 92 (2008) 033307-1–033307-3.
- [45] T.Y. Chu, J. Lu, S. Beaupreü, Y. Zhang, J.R.ü. Pouliot, S. Wakim, J. Zhou, M. Leclerc, Z. Li, J. Ding, Y. Tao, Bulk heterojunction solar cells using thieno [3,4-c]pyrrole-4,6-dione and dithieno[3,2-b:2',3'-d]silole copolymer with a power conversion efficiency of 7.3%, *Journal of the American Chemical Society* 133 (2011) 4250–4253.
- [46] J. Yuan, Z. Zhai, H. Dong, J. Li, Z. Jiang, Y. Li, W. Ma, Efficient polymer solar cells with a high open circuit voltage of 1 V, *Advanced Functional Materials* (2012) 885–892.
- [47] M. Zhang, X. Guo, Y.F. Li, Synthesis and characterization of a copolymer based on thiazolothiazole and dithienosilole for polymer solar cells, *Advanced Energy Materials* 1 (2011) 557–560.
- [48] J.C. Bijleveld, A.P. Zoombelt, S.G.J. Mathijssen, M.M. Wienk, M. Turbiez, D.M. de Leeuw, R.A.J. Janssen, Poly(diketopyrrolopyrrole-terthiophene) for ambipolar logic and photovoltaics, *Journal of the American Chemical Society* 131 (2009) 16616.
- [49] S. Bertho, G. Janssen, T.J. Cleij, B. Conings, W. Moons, A. Gadisa, J. D'Haen, E. Goovaerts, L. Lutsen, J. Manca, D. Vanderzande, Effect of temperature on the morphological and photovoltaic stability of bulk heterojunction polymer: fullerene solar cells, *Solar Energy Materials and Solar Cells* 92 (2008) 753–760.
- [50] M. Drees, H. Hoppe, C. Winder, H. Neugebauer, N.S. Sariciftci, W. Schwinger, F. Schäffler, C. Topf, M.C. Scharber, Z. Zhu, R. Gaudiana, Stabilization of the nanomorphology of polymer–fullerene “bulk heterojunction” blends using a novel polymerizable fullerene derivative, *Journal of Materials Chemistry* 15 (2005) 5158–5163.
- [51] J.S. Moon, J.K. Lee, S. Cho, J. Byun, A.J. Heeger, “Columnlike” structure of the cross-sectional morphology of bulk heterojunction materials, *Nano Letters* 9 (2009) 230–234.
- [52] H. Hoppe, N.S. Sariciftci, Morphology of polymer/fullerene bulk heterojunction solar cells, *Journal of Materials Chemistry* 16 (2006) 45–61.
- [53] F. Padinger, R.S. Rittberger, N.S. Sariciftci, Effects of postproduction treatment on plastic solar cells, *Advanced Functional Materials* 13 (2003) 85–88.
- [54] W. Ma, C. Yang, X. Gong, K. Lee, A.J. Heeger, Thermally stable, efficient polymer solar cells with nanoscale control of the interpenetrating network morphology, *Advanced Functional Materials* 15 (2005) 1617–1622.
- [55] L.H. Nguyen, H. Hoppe, T. Erb, S. Günes, G. Gobsch, N.S. Sariciftci, Effects of Annealing on the Nanomorphology and Performance of Poly(alkylthiophene): Fullerene Bulk-Heterojunction Solar Cells, *Advanced Functional Materials* 17 (2007) 1071–1078.
- [56] G. Li, V. Shrotriya, Y. Yao, Y. Yang, Investigation of annealing effects and film thickness dependence of polymer solar cells based on poly(3-hexylthiophene), *Journal of Applied Physics* 98 (2005) 043704-1–043704-5.
- [57] M. Campoy-Quiles, T. Ferenczi, T. Agostinelli, P.G. Etchegoin, Y. Kim T.D. Anthopoulos, P.N. Stavrinou, D.D.C. Bradley, J. Nelson, Morphology evolution via self-organization and lateral and vertical diffusion in polymer: fullerene solar cell blends, *Nature Materials* 7 (2008) 158–164.
- [58] Y. Zhao, Z. Xie, Y. Qu, Y.H. Geng, L.X. Wang, Solvent-vapor treatment induced performance enhancement of poly(3-hexylthiophene): methanofullerene bulk-heterojunction photovoltaic cells, *Applied Physics Letters* 90 (2007) 043504-1–043504-3.
- [59] S.J. Lou, J.M. Szarko, T.J. Marks, L.X. Chen, S.J. Lou, J.M. Szarko, L. Yu, T.J. Marks, L.X. Chen, T. Xu, L. Yu, L.X. Chen, Effects of additives on the morphology of solution phase aggregates formed by active layer components of high-efficiency organic solar cells, *Journal of the American Chemical Society* 133 (2011) 20661–20663.
- [60] Y.Y. Liang, Z. Xu, J.B. Xia, S.T. Tsai, Y. Wu, G. Li, C. Ray, L.P. Yu, For the bright future-bulk heterojunction polymer solar cells with power conversion efficiency of 7.4%, *Advanced Materials* 22 (2010) E135–E138.
- [61] J. Peet, C. Soci, R.C. Coffin, T.Q. Nguyen, A. Mikhailovsky, D. Moses, G.C. Bazan, Method for increasing the photoconductive response in conjugated polymer/fullerene composites, *Applied Physics Letters* 89 (2006) 252105-1–252105-3.
- [62] J. Peet, J.Y. Kim, N.E. Coates, W.L. Ma, D. Moses, A.J. Heeger, G.C. Bazan, Efficiency enhancement in low-bandgap polymer solar cells by processing with alkane dithiols, *Nature Materials* 6 (2007) 497–500.
- [63] D.Y. Kim, F. So, Y. Gao, Aluminum phthalocyanine chloride/C60 organic photovoltaic cells with high open-circuit voltages, *Solar Energy Materials and Solar Cells* 93 (2009) 1688–1691.
- [64] T.S. van der Poll, J.A. Love, T.Q. Nguyen, G.C. Bazan, Non-basic high-performance molecules for solution-processed organic solar cells, *Advanced Materials* 24 (2012) 3646–3649.
- [65] S. Yoo, B. Domercq, B. Kippelen, Efficient thin-film organic solar cells based on pentacene/C60 heterojunctions, *Applied Physics Letters* 85 (2004) 5427–5429.
- [66] B. Walker, C. Kim, T.Q. Nguyen, Small molecule solution-processed bulk heterojunction solar cells, *Chemistry of Materials* 23 (2011) 470–482.
- [67] Y.Z. Lin, Y.F. Li, X.W. Zhan, Small molecule semiconductors for high-efficiency organic photovoltaics, *Chemical Society Reviews* 41 (2012) 4245–4272.
- [68] M. Niggemann, M. Glatthaar, P. Lewer, C. Müller, J. Wagner, A. Gombert, Functional microprism substrate for organic solar cells, *Thin Solid Films* 511–512 (2006) 628–633.
- [69] C. Waldauf, M. Morana, P. Denk, P. Schilinsky, K. Coakley, S.A. Choulis, C. J. Brabec, Highly efficient inverted organic photovoltaics using solution based titanium oxide as electron selective contact, *Applied Physics Letters* 89 (2006) 233517-1–233517-3.
- [70] M.S. White, D.C. Olson, S.E. Shaheen, N. Kopidakis, D.S. Ginley, Inverted bulk-heterojunction organic photovoltaic device using a solution-derived ZnO underlayer, *Applied Physics Letters* 89 (2006) 143517-1–143517-3.
- [71] M. Hermenau, M. Riede, K. Leo, S.A. Gevorgyan, F.C. Krebs, K. Norrman, Water and oxygen induced degradation of small molecule organic solar cells, *Solar Energy Materials and Solar Cells* 95 (2011) 1268–1277.
- [72] K. Norrman, M.V. Madsen, S.A. Gevorgyan, F.C. Krebs, Degradation patterns in water and oxygen of an inverted polymer solar cell, *Journal of the American Chemical Society* 132 (2010) 16883–16892.
- [73] S. Cros, R. de Bettignies, S. Berson, S. Bailly, P. Maise, N. Lemaitre, S. Guillerez, Definition of encapsulation barrier requirements: a method applied to organic solar cells, *Solar Energy Materials and Solar Cells* 95 (2011) 65–69.
- [74] F.C. Krebs, S.A. Gevorgyan, B. Gholamkhash, S. Holdcroft, C. Schlenker, M. E. Thompson, B.C. Thompson, D. Olson, D.S. Ginley, S.E. Shaheen, H. N. Alshareef, J.W. Murphy, W.J. Youngblood, N.C. Heston, J.R. Reynolds, S. J. Jia, D. Laird, S.M. Tuladhar, J.G.A. Dane, P. Atienzar, J. Nelson, J.M. Kroon, M. M. Wienk, R.A.J. Janssen, K. Tvingstedt, F.L. Zhang, M. Andersson, O. Inganäs, M. Lira-Cantu, R. de Bettignies, S. Guillerez, T. Aernouts, D. Cheyns, L. Lutsen, B. Zimmermann, U. Würfel, M. Niggemann, H.F. Schleiermacher, P. Liska, M. Grätzel, P. Lianos, E.A. Katz, W. Lohwasser, B. Jannon, A round robin study of flexible large-area roll-to-roll processed polymer solar cell modules, *Solar Energy Materials and Solar Cells* 93 (2009) 1968–1977.
- [75] C. Lungenschmied, G. Dennler, H. Neugebauer, S.N. Sariciftci, M. Glatthaar, T. Meyer, A. Meyer, Flexible, long-lived, large-area, organic solar cells, *Solar Energy Materials and Solar Cells* 91 (2007) 379–384.

- [76] K. Norrman, A. Ghanbari-Siahkali, N.B. Larsen, 6 Studies of spin-coated polymer films, Annual Reports on the Progress of Chemistry Section C: Physical. Chemistr 101 (2005) 174–201.
- [77] F.C. Krebs, J. Fyenbo, D.M. Tanenbaum, S.A. Gevorgyan, R. Andriessen, B. van Remoortere, Y. Galagan, M. Jorgensen, The OE-A OPV demonstrator anno domini 2011, Energy & Environmental Science 4 (2011) 4116–4123.
- [78] A. Manor, E.A. Katz, B. Hirsch, E.A. Katz, T. Tromholt, F.C. Krebs, Origin of size effect on efficiency of organic photovoltaics, Journal of Applied Physics 109 (2011) 074508-1–074508-9.
- [79] A. Cravino, P. Schilinsky, C.J. Brabec, Characterization of organic solar cells: the importance of device layout, Advanced Functional Materials 17 (2007) 3906–3910.
- [80] M.O. Reese, S.A. Gevorgyan, M. Jørgensen, E. Bundgaard, S.R. Kurtz, D.S. Ginley, D. C. Olson, M.T. Lloyd, P. Morvillo, E.A. Katz, A. Elschner, O. Haillant, T.R. Currier, V. Shrotriya, M. Hermenau, M. Riede, R. Kirov, G. Trimmel, T. Rath, O. Inganäs, F. Zhang, M. Andersson, K. Tvingstedt, M. Lira-Cantu, D. Laird, C. McGuinness, S. Gowrisanker, M. Pannone, M. Xiao, J. Hauch, R. Steim, D.M. DeLongchamp, R. Rösch, H. Hoppe, N. Espinosa, A. Urbina, G. Yaman-Uzunoglu, J.B. Bonekamp, A.J. J.M. van Breemen, C. Girotto, E. Voroshazi, F.C. Krebs, Consensus stability testing protocols for organic photovoltaic materials and devices, Solar Energy Materials and Solar Cells 95 (2011) 1253–1267.
- [81] H.J. Snaith, How should you measure your excitonic solar cells? Energy and Environmental Science 5 (2012) 6513–6520.
- [82] V. Shrotriya, G. Li, Y. Yao, T. Moriarty, K. Emery, Y. Yang, Accurate measurement and characterization of organic solar cells, Advanced Functional Materials 16 (2006) 2016–2023.
- [83] J.M. Kroon, M.M. Wienk, W.J.H. Verhees, J.C. Hummelen, Accurate efficiency determination and stability studies of conjugated polymer/fullerene solar cells, Thin Solid Films 403–404 (2002) 223–228.
- [84] S. Ito, H. Matsui, K.i. Okada, S.i. Kusano, T. Kitamura, Y. Wada, S. Yanagida, Calibration of solar simulator for evaluation of dye-sensitized solar cells, Solar Energy Materials and Solar Cells 82 (2004) 421–429.
- [85] G. Yu, J. Gao, J.C. Hummelen, F. Wudl, A.J. Heeger, Polymer photovoltaic cells—enhanced efficiencies via a network of internal donor-acceptor heterojunctions, Science 270 (1995) 1789–1791.
- [86] G. Li, V. Shrotriya, J.S. Huang, Y. Yao, T. Moriarty, K. Emery, Y. Yang, High-efficiency solution processable polymer photovoltaic cells by self-organization of polymer blends, Nature Materials 4 (2005) 864–868.
- [87] N. Espinosa, R. García-Valverde, A. Urbina, F. Lenzmann, M. Manceau, D. Angmo, F.C. Krebs, Life cycle assessment of ITO-free flexible polymer solar cells prepared by roll-to-roll coating and printing, Solar Energy Materials and Solar Cells 97 (2012) 3–13.
- [88] F.C. Krebs, All solution roll-to-roll processed polymer solar cells free from indium-tin-oxide and vacuum coating steps, Organic Electronics 10 (2009) 761–768.
- [89] R. Garca-Valverde, J.A. Cherni, A. Urbina, Life cycle analysis of organic photovoltaic technologies, Progress in Photovoltaics 18 (2010) 535–558.
- [90] G. Dennler, M.C. Scharber, C.J. Brabec, Polymer-fullerene bulk-heterojunction solar cells, Advanced Materials 21 (2009) 1323–1338.
- [91] N. Espinosa, M. Hösel, D. Angmo, F.C. Krebs, Solar cells with one-day energy payback for the factories of the future, Energy and Environmental Science 5 (2012) 5117–5132.
- [92] D. Yue, P. Khatav, F. You, S.B. Darling, Deciphering the uncertainties in life cycle energy and environmental analysis of organic photovoltaics, Energy and Environmental Science 5 (2012) 9163–9172.
- [93] N. Espinosa, R. García-Valverde, F.C. Krebs, Life-cycle analysis of product integrated polymer solar cells, Energy and Environmental Science 4 (2011) 1547–1557.
- [94] C.J.M. Emmott, A. Urbina, J. Nelson, Environmental and economic assessment of ITO-free electrodes for organic solar cells, Solar Energy Materials and Solar Cells 97 (2012) 14–21.
- [95] L.J.A. Koster, V.D. Mihailetchi, P.W.M. Blom, Ultimate efficiency of polymer/fullerene bulk heterojunction solar cells, Applied Physics Letters 88 (2006) 093511-1–093511-3.
- [96] K.M. Coakley, M.D. McGehee, Conjugated polymer photovoltaic cells, Chemistry of Materials 16 (2004) 4533–4542.
- [97] G. Dennler, M.C. Scharber, T. Ameri, P. Denk, K. Forberich, C. Waldauf C.J. Brabec, Design rules for donors in bulk-heterojunction tandem solar cells-towards 15% energy-conversion efficiency, Advanced Materials 20 (2008) 579–583.